UNIVERSIDAD AUTÓNOMA DE MADRID
Facultad de Ciencias
Departamento de Física Teórica

# Tests of color dynamics and precision measurements of $\alpha_s$ using jet production in DIS with the ZEUS detector at HERA

Submitted in partial fullfilment of the requirements
for the degree 'Doctor en Ciencias Físicas' by

Marcos Jiménez
Supervisors : Claudia Glasman and Juan Terrón

12/05/2008

UNIVERSIDAD AUTÓNOMA DE MADRID
Facultad de Ciencias
Departamento de Física Teórica

# Tests de la dinámica de color y medidas de precisión de $\alpha_s$ usando la producción de jets en DIS con el detector ZEUS en HERA

Entregado como requisito parcial de el título
de 'Doctor en Ciencias Físicas' por

Marcos Jiménez
Directores de tesis : Claudia Glasman and Juan Terrón

12/05/2008

*Este trabajo está dedicado a mis padres*

*O God, I could be bounded in a nutshell and count myself a king of infinite space..*
Hamlet (Act I, Scene ii).

# Introduction

Jet production in the deep inelastic scattering (DIS) of an electron (positron)[1] and a proton (ep $\rightarrow$ jets + X) probes the partonic structure of the proton and allows the study of the dynamical properties of the strong interactions. The elementary particles that interact through the strong force, the quarks and the gluons, are believed to be the constituents of all hadronic matter. Thus, Quantum Chromodynamics (QCD), the theory that describes them, can be tested in lepton hadron colliders such as HERA. This document presents two recent analyses of jet production in neutral current (NC) DIS carried out in the context of the ZEUS Collaboration, both of which represent stringent tests of perturbative QCD (pQCD).

The first of them consists of improved measurements of inclusive-jet cross sections, which, as will be discussed, are important by themselves, but moreover allow a precise determination of the strong coupling ($\alpha_s$) at HERA. That analysis concludes with a high-precision comparison of the measured scale dependence of $\alpha_s$ with that predicted by pQCD, in what constitutes a compelling test of this theory.

The second analysis is a study of the underlying gauge symmetry structure of the strong interactions by means of angular correlations among the final-state jets in three-jet events. It is shown in this analysis that angular-correlation variables similar to those defined for $e^+e^-$ annihilation at LEP to extract the color factors using four-jet events can also be devised for HERA physics. The measurements have been compared to theoretical predictions based on different gauge symmetry groups and good agreement is found with those corresponding to SU(3). This is the first analysis at HERA that unveils the color factors.

In Chapter 1 the main aspects of pQCD are introduced with some supporting experimental verification. We will show there that the non-Abelian character of QCD is an essential feature of the theory since it leads to the self-coupling of the gluons and ultimately to asymptotic freedom, the decrease of the strong coupling at shorter distances. The role of HERA in understanding the proton and grounding QCD experimentally is emphasized to provide the proper context in which to introduce the two jet analyses.

All the measurements have been carried out using data from the ZEUS detector at HERA. HERA is an electron proton synchrotron collider with a center-of-mass energy of $\sqrt{s} = 320$GeV, giving way to momentum transfers between the electron and the constituents of the proton well within the predictive capabilities of pQCD. ZEUS is a multipurpose detector at one of the interaction points of HERA. It consists of a number of different detectors layered around the collision vertex, whose aim is

[1] From now on, whenever the word electron shows up, it will actually represent either an electron or a positron

to record as much information as possible about the collisions. Thus, ZEUS is a powerful tool for the study of QCD. A detailed description of the ZEUS detector is provided in Chapter 2.

In Chapter 3 we will delve into the pQCD calculations made to be compared to the measured jet observables. These observables are inclusive-jet cross sections and angular-correlations in NC DIS. A detailed study of the uncertainties affecting the theoretical calculations is also presented. Monte Carlo (MC) generators are used to understand and correct the jet measurements for detector effects. These simulations are also discussed in Chapter 3.

In Chapter 4 we will see how the data samples were selected through a carefully designed trigger system and how these samples compare to the MC simulations. The comparisons legitimize the use of the MC simulations for estimating the systematic uncertainties in the measurements and obtaining the necessary corrections to the jet cross sections presented in Chapter 5.

The final results for the inclusive-jet analysis, including the $\alpha_s$ determinations and the scale dependence of the coupling, are presented in Chapter 6. The results for the analysis of angular correlations in three-jet events and the sensitivity of the measurements to the underlying symmetry of the strong interactions are presented in Chapter 7. A brief summary and outlook of the two analyses are provided in the last chapter.

The data used in the analyses presented here were collected during the running period 1998-2000, when HERA operated with protons of energy $E_p = 920$ GeV and electrons or positrons of energy $E_e = 27.5$ GeV, and correspond to an integrated luminosity of $81.7 \pm 1.8$ pb$^{-1}$, of which 16.7 pb$^{-1}$ (65.0 pb$^{-1}$) was for $e^-p$ ($e^+p$) collisions.

*The results presented in this document are based on several analyses:*

- Measurement of inclusive and dijet cross sections in neutral current deep inelastic scattering at high $Q^2$ [1];
- Measurement of the jet-radius dependence of inclusive jet cross sections in neutral current deep inelastic scattering at high $Q^2$ and determination of $\alpha_s$ [2];
- Measurement of angular correlations in three-jet production in neutral current deep inelastic scattering at high $Q^2$ [3];
- Determination of a combined value of $\alpha_s$ from HERA jet data [4];

- Measurement of inclusive-jet cross sections in neutral current deep inelastic scattering at high $Q^2$ with HERA II data (analysis in progress).

*They have been presented by the author in the following conferences:*

1 'Jet correlations at HERA',
invited talk on behalf of the ZEUS Collaboration,
International Europhysics Conference on High Energy Physics (EPS 2005),
Lisbon, Portugal,
July 2005;

2 'Jet cross sections in NC DIS and determination of $\alpha_s$ at HERA',
invited talk on behalf of the ZEUS Collaboration,
XIV International Workshop on Deep Inelastic Scattering and QCD (DIS 2006),
Tsukuba, Japan,
April 2006;

3 'Jets and $\alpha_s$ measurements in DIS at HERA',
invited talk on behalf of the H1 and ZEUS Collaborations,
International Conference on the Structure and Interactions of the Photon including the 17th International Workshop on Photon-Photon Collisions (PHOTON 2007),
Paris, France,
July 2007;

4 'Jet measurements and determinations of $\alpha_s$ at HERA',
invited talk on behalf of the H1 and ZEUS Collaborations,
Rencontres de Moriond, QCD and High Energy Interactions,
La Thuile, Italy,
March 2008.

This work has been carried out in the frame of the ZEUS Collaboration through the High Energy Physics Group of the Universidad Autónoma de Madrid. The author was financially supported by the Spanish Ministry of Education and Science.

# Introducción

La producción de chorros hadrónicos (jets) en la dispersión profundamente inelástica (DIS) entre un electrón (positrón) y un protón ($ep \rightarrow jets + X$) revela la estrutura partónica interna del protón y permite el estudio de las propiedades dinámicas de las 'interacciones fuertes'. Es sabido que las partículas elementales que interactúan mediante la fuerza fuerte, los quarks y los gluones, son los constituyentes de toda la materia hadrónica. Así, la Cromodinámica Cuántica (QCD), que es la teoría que las describe, puede ser sometida a estudios en colisionadores de altas energías hadron-lepton, como lo es HERA. Este documento presenta dos análisis recientes en los que se han llevado a cabo tests exigentes de QCD perturbativa (pQCD) mediante la producción de jets mediada por corrientes neutras (NC) en DIS.

El primero de ellos consiste en medidas de gran precisión de la constante de acoplo fuerte ($\alpha_s$), el parámetro fundamental de QCD a energías grandes. Estas medidas, además de proveer una mejora en la capacidad predictiva de pQCD, también ponen a prueba la predicción teórica de la dependencia de $\alpha_s$ con la escala de la energía. El segundo análisis es un estudio de la estructura gauge subyacente en las interacciones fuertes. Este estudio se ha realizado mediante el diseño y la medida de observables de correlación angular entre los jets del estado final en sucesos de tres jets. Los observables diseñados son sensibles al grupo gauge de simetría subyacente y por lo tanto pueden discernir entre posibles teorías basadas en grupos gauge diferentes, proporcionando así un test directo de QCD.

En el primer capítulo se presentan los aspectos generales de pQCD respaldados por su verificación experimental. Ahí veremos que el carácter no Abeliano de QCD es una propiedad esencial de la teoría, ya que da lugar al auto-acoplo de los gluones y a la libertad asintótica, que es la disminución de $\alpha_s$ a distancias menores. El rol de HERA en el entendimiento del protón y en la fundamentación experimental de QCD es enfatizado en este capítulo para proporcionar el contexto en el cual se presentan los dos análisis de producción de jets.

Todas las medidas han sido hechas en el contexto de la Colaboración ZEUS con el detector de ZEUS en HERA. HERA es un sincrotrón que colisiona electrones y protones a una energía de centro de masas de $\sqrt{s} = 320$ GeV, dando lugar a transferencias de momento entre el electrón y los constituyentes del protón dentro del rango predictivo de pQCD. ZEUS es un detector multipropósito situado en uno de los puntos de interacción de HERA. Este detector consiste de un número de componentes situados alrededor del vértice de la colisión, cuyo propósito es obtener tanta información como sea posible sobre las partículas resultantes. Es por lo tanto una herramienta muy útil para el estudio de QCD. El capítulo 2 contiene una descripción detallada del detector ZEUS.

Los cálculos de pQCD hechos para obtener la predicción teórica para los observables de jets se presentan en el Capítulo 3. Las medidas con las cuales se comparan los cálculos son de secciones eficaces de jets que, como veremos, son observables particularmente adecuados para llevar a cabo tests de pQCD. En este capítulo también se describen los generadores de Monte Carlo, que han sido usados para entender y corregir las medidas por los efectos del detector.

En el Capítulo 4 se presenta la selección de las muestras de datos, que como se explica ahí, se consigue a través de un sistema de 'triggers' específicamente diseñado para hacer medidas de jets en NC DIS. Este capítulo también contiene comparaciones de las muestras de datos con las simulaciones de Monte Carlo. Estas comparaciones legitimizarán el uso de las simulaciones de Monte Carlo para la estimación de las incertidumbres sistemáticas que afectan a las medidas así como la obtención de los factores de corrección necesarios para las secciones eficaces de jets.

Los resultados finales del análisis de producción inclusiva de jets, incluyendo las determinaciones de $\alpha_s$ y el test de su dependencia con la escala de la energía, se muestran el Capítulo 6. Los resultados del análisis de las correlaciones angulares en sucesos de tres jets y la sensibilidad de las medidas a la simetría subyacente se presentan en el Capítulo 7. El último capítulo contiene un resumen y las perspectivas futuras de los análisis contenidos en este documento.

Las muestras de datos usados en los análisis presentados aquí fueron tomadas durante el período 1998-2000, en el cual HERA proporcionaba protones de energía $E_p = 920$ GeV y electrones o positrones de energía $E_e = 27.5$ GeV, y que corresponden a una luminosidad integrada de $81.7 \pm 1.8$ pb$^{-1}$, de la cual 16.7 pb$^{-1}$ (65.0 pb$^{-1}$) era para colisiones $e^- p$ ($e^+ p$).

*Los resultados de este documento se basan en varios análisis:*

- Measurement of inclusive and dijet cross sections in neutral current deep inelastic scattering at high $Q^2$ [1];
- Measurement of the jet-radius dependence of inclusive jet cross sections in neutral current deep inelastic scattering at high $Q^2$ and determination of $\alpha_s$ [2];
- Measurement of angular correlations in three-jet production in neutral current deep inelastic scattering at high $Q^2$ [3];
- Determination of a combined value of $\alpha_s$ from HERA jet data [4];
- Measurement of inclusive-jet cross sections in neutral current deep inelastic

scattering at high $Q^2$ with HERA II data (analysis in progress).

*Los resultados han sido presentados por el autor en las siguientes conferencias:*

1 'Jet correlations at HERA',
invited talk on behalf of the ZEUS Collaboration,
International Europhysics Conference on High Energy Physics (EPS 2005),
Lisbon, Portugal,
July 2005;

2 'Jet cross sections in NC DIS and determination of $\alpha_s$ at HERA',
invited talk on behalf of the ZEUS Collaboration,
XIV International Workshop on Deep Inelastic Scattering and QCD (DIS 2006),
Tsukuba, Japan,
April 2006;

3 'Jets and $\alpha_s$ measurements in DIS at HERA',
invited talk on behalf of the H1 and ZEUS Collaborations,
International Conference on the Structure and Interactions of the Photon including the 17th International Workshop on Photon-Photon Collisions (PHOTON 2007),
Paris, France,
July 2007;

4 'Jet measurements and determinations of $\alpha_s$ at HERA',
invited talk on behalf of the H1 and ZEUS Collaborations,
Rencontres de Moriond, QCD and High Energy Interactions,
La Thuile, Italy,
March 2008.

Este trabajo ha sido desarrollado en la Colaboración ZEUS a través del grupo de Altas Energías de la Universidad Autónoma de Madrid. El autor ha sido financiado por el Ministerio de Educación y Ciencia.

# Contents

# Chapter 1

# Introduction

This chapter presents the theoretical background and motivation for the two jet production analyses that are the object of this document. As mentioned in the introduction, the first of these analyses consists of measurements of inclusive-jet production in NC DIS. These measurements provide a direct connection with the hard, fundamental physics responsible for the structure of the proton and are used to test pQCD and to extend our knowledge of protonic structure. Moreover, they also yield precision determinations of $\alpha_s$ and its energy-scale dependence .

The second analysis also uses measurements of jet production in NC DIS but with the aim of obtaining a transparent method for studying the underlying gauge symmetry of the strong interactions. In this case, the emphasis is not placed on inclusive-jet production, but rather on subtle angular correlations among the hadronic jets in the final state of three-jet events that are sensitive to the internal symmetry of the interactions.

The first analysis will be refered to the '$\alpha_s$ analysis' throughout this document, whereas the second will be refered to as the 'angular-correlations' analysis. This chapter provides a theoretical introduction to pQCD with an emphasis on its color structure, the scale-dependence of $\alpha_s$ and the proton parton distribution functions. The theoretical introduction and experimental evidence provided is not meant to be exhaustive, but rather to serve as a sufficient background and motivation for the two jet analises which are introduced at the end.

## 1.1 Deep inelastic scattering and the parton model

An electron beam is a well known tool to probe the inner structure of a proton. The idea is that the inner structure determines the scattering distributions of the electrons and can thus be determined from it. In order for this recipe to work, however,

the interactions between the probe and the partons must be understood and, to second order, also those among the partons themselves. Phase-space regions where the proton structure is well determined from previous experiments can be used to test the theory, whereas regions where the theory is precise in its predictions can be used to further determine the proton structure. In QED quarks and leptons interact through the exchange of a virtual photon. For this reason the four-momentum squared, $Q^2$, of the mediator boson is often viewed as the squared energy scale of the process. Since $E \sim 1/\lambda$, $1/\sqrt{Q^2}$ is also the distance scale at which the hadron is being resolved.

At low values of $Q^2$ (large distances), a proton behaves like a charged, point-like object. With increasing $Q^2$ it can be excited to resonant states. If $Q^2$ is sufficiently large the proton breaks appart, revealing its inner structure. This regime is called Deep Inelastic Scattering (DIS). Fig. 1.1 shows a pictorial view of a general DIS process ($ep \rightarrow e + X$) mediated by a neutral virtual boson ($\gamma, Z^0$) and it is termed neutral current (NC) DIS. The momentum transfer betwen the incoming electron and proton leads to a scattered electron plus a (possibly) complicated hadronic final state. The hadronic final state consists of both the products of the hard interaction of the boson with the struck parton and the 'remnant' of the proton. The figure

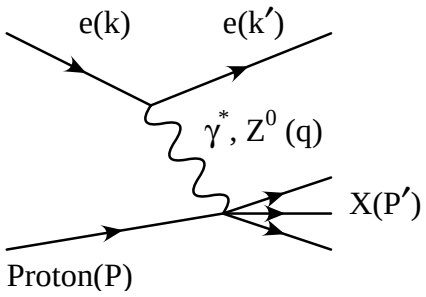


Figure 1.1: Pictorial representation of a NC DIS event.

shows the available four-momenta in the interaction, which can be used to build Lorentz-invariant observables with which to express cross sections:

$$Q^2 = -q^2 = (k - k')^2 \qquad x = \frac{-q^2}{2P \cdot q} \qquad y = \frac{P \cdot q}{P \cdot k} = \frac{Q^2}{sx} \tag{1.1}$$

Any two of these three observables are sufficient to describe the kinematics of a DIS event. If the proton was made up of only quarks, then the variable $x$ would be the fraction of the proton's momentum carried by the struck quark. This model is called the quark-parton model (QPM). The variable $y$ is a measure of the inelasticity of the event, it can be expressed in terms of $s$, the center-of-mass (CM) energy of the collision. Finally $Q^2$, the four-momentum transfer, is the squared difference between the four momenta of the incoming and outgoing leptons. Before expressing

the $(ep \to e + X)$ cross section in terms of these variables, let us write down its general form [5]

$$d\sigma \sim L^e_{\mu\nu} W^{\mu\nu}, \tag{1.2}$$

where $L^e_{\mu\nu}$ represents the lepton tensor which we know from QED and $W^{\mu\nu}$ serves to express our ignorance of the target structure. We can build the most general form of $W^{\mu\nu}$ using the independent four-momenta, $g^{\mu\nu}$ and $\epsilon^{\mu\nu\alpha\beta}$. Then in the limit $\frac{M^2}{Q^2} \to 0$ where the parton masses can be ignored, we can express the general NC DIS cross section $(ep \to e + X)$ as:

$$\frac{d^2\sigma}{dxdQ^2} = \frac{4\pi\alpha^2}{xQ^4}[xy^2 F_1 + (1-y)F_2 + y(1-\frac{1}{2}y)xF_3] \tag{1.3}$$

The functions $F_i$ are used to parametrize the proton's structure. $F_3$ is a parity violating contribution which becomes non-negligible only at high $Q^2$, where Z mediated events have a sizeable effect. Sometimes the combination

$$F_L \to F_2 - 2xF_1 \tag{1.4}$$

called the longitudinal structure function is used and corresponds to the absorption of a longitudinally polarized photon by a quark. In this case the cross section is a function of $F_2$, $F_L$, and $F_3$. In the QPM a massless quark cannot absorb a longitudinally polarized photon and $F_L$ can be neglected, so that with this parametrization only $F_2$ remains.

The DIS experiments of the late 60's at SLAC provided the first evidence for the point-like constituent structure of hadrons, consistent with the QPM [6]. Fig. 1.2 shows these early results, where the measured structure functions are observed to loose their dependence on $Q^2$. If $Q^2$ is interpreted as the resolution of the probe, then the scaling of the structure functions simply reflects the fact that a point will not look otherwise by an increase in resolution. It can be shown that in this case the structure functions will depend only on the dimensionless quantity $\omega = \frac{2q\cdot P}{Q^2}$:

$$F_2(x, Q^2) \to F_2(\omega) \tag{1.5}$$

Thus, the SLAC experiment gave the first view into the proton structure, which to a first approximation was the QPM. The basic idea of the QPM is that in the NC DIS process $(ep \to e + X)$ the virtual boson interacts with one of the quark constituents of the proton. A frame is chosen (the proton infinite-momentum frame) such that relativistic time dilation slows down the rate at which quarks interact with each other and the struck quark is essentially free during the interaction with the virtual boson. The interaction can then be expressed as the incoherent sum of scattering probabilities from single free quarks:

$$\frac{d^2\sigma}{dxdQ^2} = \sum_{i=1}^{n_f} \int d\xi f_i(\xi)(\frac{d^2\sigma'}{dxdQ^2}) \tag{1.6}$$

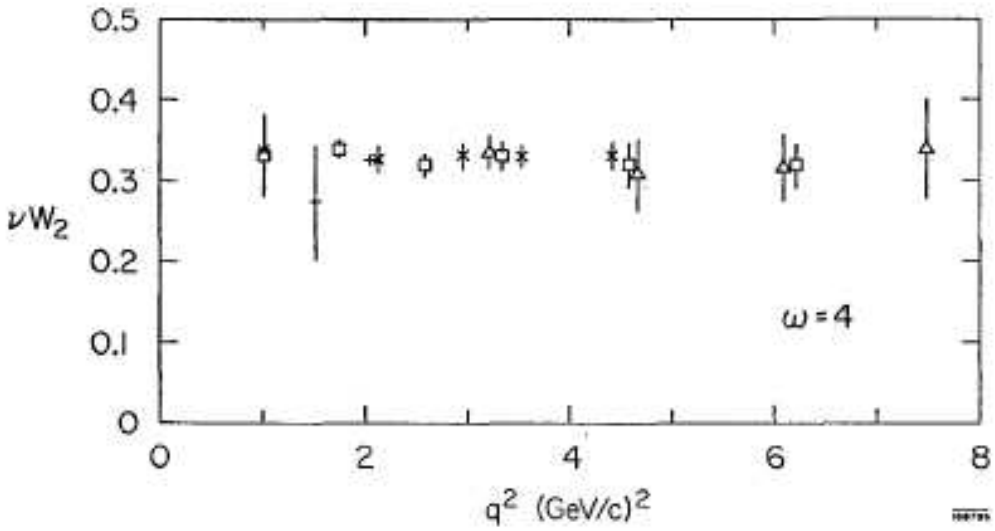


Figure 1.2: The scale invariance of the proton form factor $\nu W_2$ as first discovered by the SLAC DIS experiment.

The functions $f_i(\xi)$ are called the parton distribution functions (PDFs) and here represent the probability of finding a quark of type $q$ with a fraction $\xi$ of the proton's momentum, and the cross section in the integrand is that of the elastic process $eq \to eq$. From this QPM equation the relationship between the structure functions and the parton distribution functions follows ($F_L$ vanishes)

$$2xF_1(x) = F_2(x) = \sum_{i=1}^{n_f} e_i^2 x f_i(x), \tag{1.7}$$

and thus measurements of the structure functions allow the determination of the quark PDFs. During the very early DIS experiments carried out in the 70's, good agreement was found between the data and the QPM; however, if one integrated the measured momentum of the quark PDFs it was found that:

$$\int \sum_{i=1}^{n_f} x f_i(x) dx \sim 0.5 \tag{1.8}$$

Only about half of the momentum of the proton could be accounted for by the quarks in the QPM. The electromagnetic probe could not detect possible neutral partons within the proton. The full machinery of QCD, however, was able provide

a satisfactory explanation of the missing momentum through the couplings of its neutral gauge bosons, the gluons. In fact, QCD predicts a contribution not only from gluons, but also to some degree from a whole sea of particles resulting from $g \to q\bar{q}$ processes that intrinsically accompany the three valence quarks. The equations for the PDFs shown so far are only the first-order approximation to the structure functions from the viewpoint of pQCD. The missing momentum problem can in retrospect be seen as the first indirect evidence for the existence of the gluons and the sea. But before looking at the PDFs in more detail lets delve into the formalism of the theory.

## 1.2 The Quantum Field Theory of Color Dynamics

A Quantum Field Theory can be characterized by its Lagrangian density. The Feynman rules required for any perturbative prediction can be derived from it. In the quantum field theory of color dynamics, QCD, the Lagrangian density has the form [7]:

$$\mathcal{L}^{QCD}[\alpha_0, m_f] = \mathcal{L}_{invar} + \mathcal{L}_{gauge} + \mathcal{L}_{ghost}, \tag{1.9}$$

The gauge-fixing and ghost densities, $\mathcal{L}_{gauge}$ and $\mathcal{L}_{ghost}$, are added to solve the problem of quantizing $\mathcal{L}_{invar}$ and will not be covered here. The Lagrangian is a function of the quark and gluon fields, the bare coupling $\alpha_0$ and the quark masses $m_f$. At energies that are large compared to $m_f$ the masses can be ignored and in perturbative expansions in terms of Feynman diagrams the (renormalized) coupling $\alpha_s$ is left as the only undetermined parameter of the theory. Therefore $\alpha_s$ plays a central role from both the theoretical and experimental points of view. The classical density $\mathcal{L}_{invar}$ is, explicitly

$$\mathcal{L}_{invar} = \sum_{flavours} \bar{q}_a \left[\gamma^\mu D_\mu - m_f\right]_{ab} q_b - \frac{1}{4} F^A_{\alpha\beta} F_A^{\alpha\beta}, \tag{1.10}$$

where the sum runs over the different flavours of quarks. The fields $q_a$ $(a = 1, 2, 3)$ form a basis of the triplet representation of SU(3). It is assumed that only color singlet states of SU(3) can be detected with present-day detectors. Apart from reproducing the observed hadronic spectrum, this assumption accounts for not having observed the quark fields of QCD in isolation, despite their abundance as the constituents of most of the matter around us.

The QCD Lagrangian is built with SU(3) local gauge invariance as the guiding principle. Thus, eight gluon fields are needed to construct the covariant derivative $D_\mu$:

$$D_\mu = \delta_\mu + i g_s T_a G^a_\mu \tag{1.11}$$

| *Group* | $C_A$ | $C_F$ | $T_F$ |
|---|---|---|---|
| U(1) | 0 | 1 | 1 |
| $U(1)^3$ | 0 | 1 | 3 |
| SU(N) | $N$ | $(N^2-1)/2N$ | 1/2 |
| SU(3) | 3 | 4/3 | 1/2 |

Table 1.1: Casimir factors for some common gauge groups

Here the $T_a$ are the generators of SU(3) and the index 'a' runs over the dimensions of the SU(3) Lie Algebra, $(N_c^2 - 1 = 8)$. The gluon fields $G_\mu^a$ are coupled to the quark fields through the covariant derivative $D_\mu$ with strength $g_s$. Gluon fields obey their own Lagrangian. This is the final $-\frac{1}{4}F_{\alpha\beta}^A F_A^{\alpha\beta}$ piece, where the field strength tensor $F_{\alpha\beta}^A$ is given by:

$$F_{\alpha\beta}^A = \partial_\alpha G_\beta^A - \partial_\beta G_\alpha^A - g_s f^{ABC} G_\alpha^B G_\beta^C \ , \tag{1.12}$$

Here the indexes $A, B, C$ run over the eight color degrees of freedom of the gluon field. The $f^{ABC}$ are the gauge group structure constants which would vanish for an Abelian theory. For a non-Abelian group such as SU(3), however, they do not vanish, leading to a central property of QCD, the self-coupling of the gluon. Thus, symbolically the QCD Lagrangian contains the following pieces:

$$\mathcal{L} = \bar{q}q + G^2 + g_s \bar{q}qG + g_s G^3 + g_s^2 G^4 \tag{1.13}$$

They correspond, pictorially, to the the Feynman diagrams in Fig. 1.3. Notice the presence of the triple and quadruple gluon vertices. This is the distinguishing characteristic of QCD.

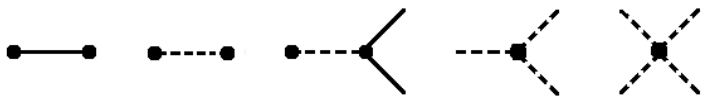

Figure 1.3: Feynman diagrams of the terms in the QCD Lagrangian, from eq. 1.13

The gauge symmetry also determines the relative strengths of the different vertices. Standard books [8] can be consulted for a derivation of the Feynman rules from the Lagrangian density. Here it suffices to say that the eigenvalues of the Casimir operators of the gauge group multiply the contributions to the scattering amplitude from the different vertices, as pictured in Fig. 1.4. The color factors $C_F$,$C_A$,

and $T_F$ represent the fundamental strengths of the gluon radiation from quarks, the triple-gluon vertex, and the gluon splitting into a quark-antiquark vertex. These 'color factors' are unique to a symmetry group and can be used to identify it. The

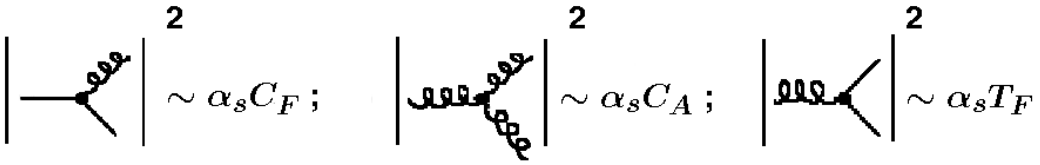


Figure 1.4: The relative squared amplitudes of the vertices of the theory are dictated by the underlying symmetry group through the color factors.

dynamics of the theory is governed by the underlying symmetry group through its color factors. For example, if the QCD Lagrangian was made invariant under a group other than $SU(3)$, say the Abelian $U(1) \otimes U(1) \otimes U(1)$, then the strength of the gluon self-coupling vertices would vanish by virtue of $C_A = 0$. Table 1.1 shows the color factors for different symmetry groups. They can be obtained in terms of the group generators $t^r_{ab}$ and its structure constants $f^{rst}$ by the relations:

$$t^r_{ab} t^r_{bc} = \delta_{ac} C_F, \qquad f^{rst} f^{rsu} = \delta^{tu} C_A, \qquad t^r_{ab} t^s_{ba} = \delta_{rs} T_F \tag{1.14}$$

One possible way to test QCD is to design observables that are sensitive to the color-factor configuration. The color factors have been measured experimentally in $e^+e^-$ annihilation at LEP through angular correlations among the final-state jets. These measurements are discussed in depth in the next section. Note that the 'angular-correlations' analysis presented in this document opens the same venue of research in $ep$ scattering at HERA.

### 1.2.1 Experimental verification of the gauge structure of QCD in $e^+e^-$ collisions

Investigations of the triple-gluon vertex have been carried out at LEP (see, for example [9–19]), using angular correlations in four-jet events from $Z^0$ hadronic decays. Consider the diagrams shown in Fig 1.5 for four-parton final states of Z decays. Gluons can either be radiated off quarks directly or they can emerge from the splitting of a virtual gluon. Since the characteristic diagrams contain the vertices of Fig 1.4, the total four-jet cross section is sensitive to the color factors. Extracting the color factors from the total four-jet cross section is however not direct since this amplitude is also sensitive to $\alpha_s \equiv \frac{g_s^2}{4\pi}$. An alternative method would be to measure the

contributions directly by counting how many $q\bar{q}gg$ final states there are with respect to $q\bar{q}q'\bar{q}'$. This proves difficult in practice, since the final-state partons hadronize into jets before they can be detected. Quarks and gluons result in final-state jets of different morphology, but the efficiency in the identification of the jet with the originating parton spoils the transparency of this method.

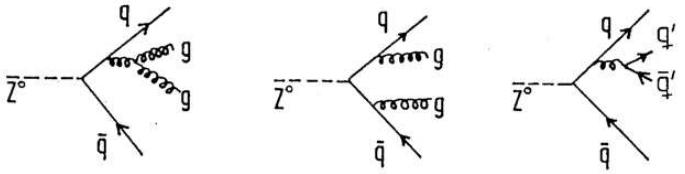


Figure 1.5: LEP 4-jet representative Feynman diagrams. Gluons can either be radiated off quarks or they emerge from the splitting of a virtual gluon. The final states are angularly correlated.

There is an altogether different venue which offers a direct way of studying the gauge symmetry. The final-state jets are angularly correlated according to the type of process which produced them. This is due to helicity conservation at the vertices. Reconsider Fig. 1.5. The virtual gluons that are radiated from almost back-to-back $q\bar{q}$ pairs in Z decays are predominantly polarised longitudinally along the $q\bar{q}$ direction. They can therefore decay only into gluon pairs along this axis with total spin 0, but not into secondary $q\bar{q}$ pairs, the spins of which add up to 1. However, projected onto an axis perpendicular to the flight direction, the virtual gluon spin is just $\pm 1$, so that this state can decay into a $q\bar{q}$ pair along this direction but not into a pair of transverse gluons.

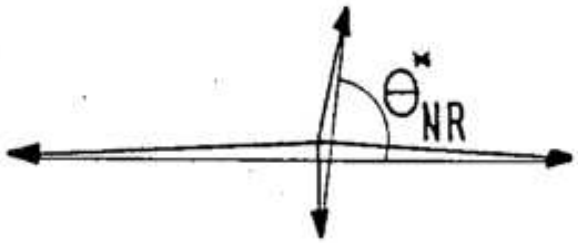


Figure 1.6: The $\Theta_{NR}$ angle used at LEP to discern the color factors at work in the strong interactions. Other angles based on the same principles were devised for this kind of analysis.

With these extreme cases in mind, the variable $\Theta_{NR}$ is defined as the the polar

angle between the axes spanned by the two primary quark-jets and the two gluons (or the secondary quarks in the case of $q\bar{q}q'\bar{q}'$) as shown in Fig. 1.6. This angle should be sensitive to the relative contribution of the different vertices. Experimentally the axes are defined for jets ordered according to their energies, such that the two most energetic jets are taken to be the primary quark jets. The angle $\Theta_{NR}$ is thus defined as the polar angle between the axes spanned by the two high-energy and the two low-energy jets, a definition which matches the previous one. In more detail, it can be shown [20] that the angular distributions in the rest frame of the virtual gluon are linear in $cos^2\Theta_{NR}$:

$$\begin{aligned} q\bar{q}q'\bar{q}' &\sim 1 - cos^2(\Theta_{NR}) \\ q\bar{q}gg &\sim cos^2(\Theta_{NR}) \end{aligned} \tag{1.15}$$

Quark final states are suppressed relative to gluon final states by a factor $\sim \frac{1}{N_C}$ because more color combinations can contribute for octet gluons than for triplet quarks. Thus, a small number of quark jets and a vanishing number of gluon jets are produced with large values of $\Theta_{NR}$. In contrast, many gluon jets are produced with small polar angles and no quark jets. Therefore, the distribution in $cos(\Theta_{NR})$ is very

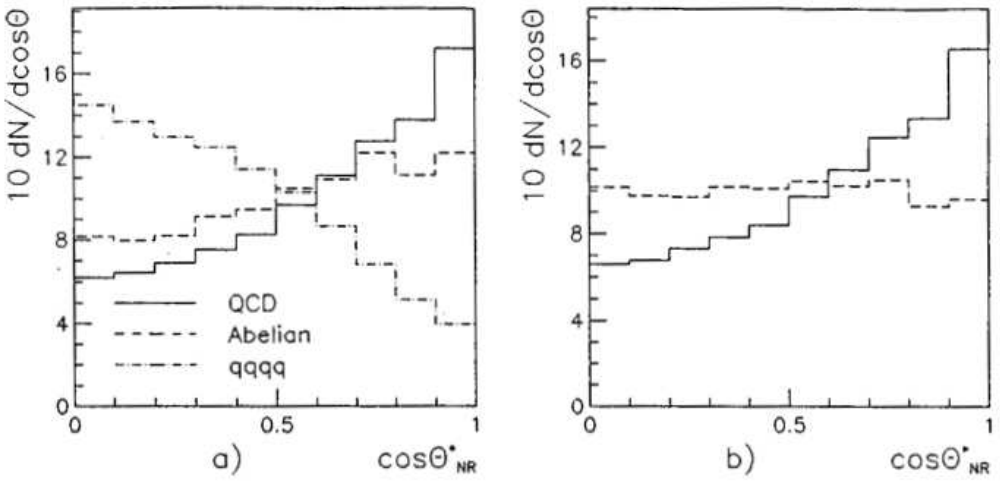


Figure 1.7: The distributions of $\cos\theta_{NR}$, (a) separately for the final states $q\bar{q}gg$ and $q\bar{q}q'\bar{q}'$ in QCD and the Abelian model, and (b) for all subprocesses summed up.

sensitive to the relative contribution from the $ggg$ coupling, since any deviation from the canonical QCD color factor would strongly affect the prediction for this angular distribution. Fig. 1.7 shows the prediction for the $cos(\Theta_{NR})$ angular-correlation in $e^+e^-$ annihilation. The distribution predicted by pQCD is compared to an Abelian model based on $U(1) \otimes U(1) \otimes U(1)$. As shown, the variable is well suited to

discern between the two models. A precision measurement of this distribution would reveal which model is correct. In fact, this variable has been used to obtain direct extractions of the color factors [21], the results of which are shown in Fig. 1.8. Note that the variable $cos(\Theta_{NR})$ is only one of several angular-correlation variables

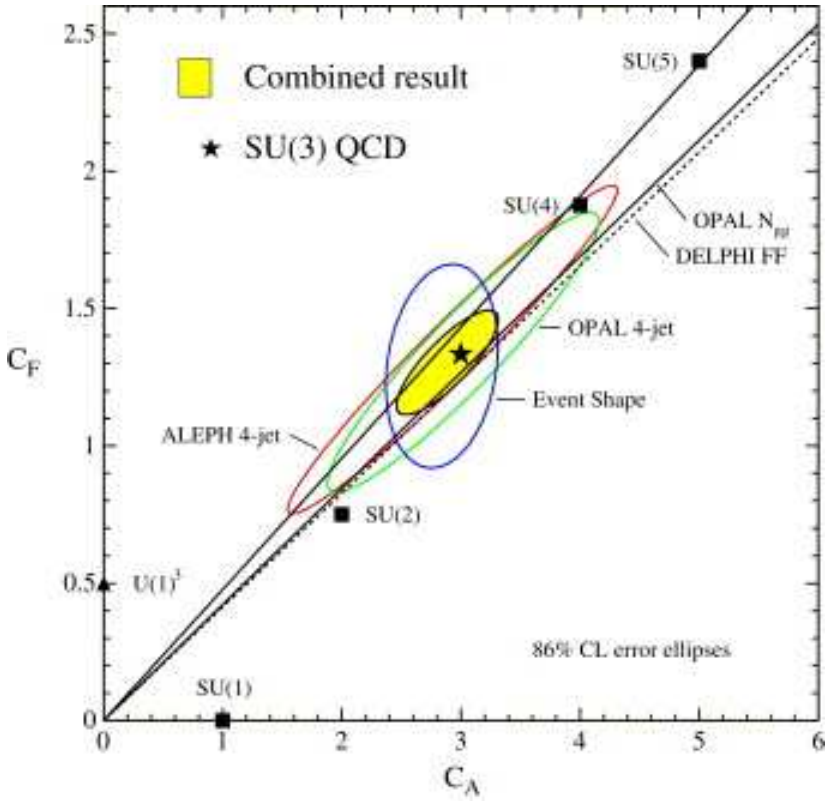


Figure 1.8: Combined result for the direct determination of the underlying symmetry of the strong interactions in $e^+e^-$ annihilation at LEP using angular correlations among four-jet final states.

defined at LEP for this type of analysis. The other variables are based on similar principles and will not be covered here.

### 1.2.2 Loop corrections and the running of the strong coupling

The previous section shows how the gauge-symmetry assumption of QCD can be grounded experimentally using angular-correlation variables. The color factors are also involved in the scale dependence (running) of $\alpha_s$. In Quantum Field Theory higher-order loop contributions, like the ones shown in Fig. 1.9, diverge logarithmically. The divergent loop contributions can be interpreted as corrections to the bare coupling $\alpha_0$, the coupling that appears in the Lagrangian. This means the effective coupling the experimentalist measures can be taken as $\alpha_0$ times a series

of loop corrections. The loop effects depend on $Q^2$ and therefore transform a nu-

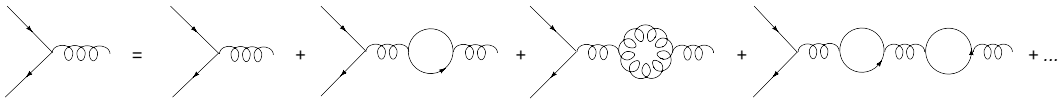

Figure 1.9: Divergent loop corrections to the coupling in QCD. The self-gluon contributions are responsible for the sign of the $\beta$ function, resulting in asymptotic freedom.

merical parameter, the 'bare coupling', into a function of $Q^2$, an 'effective coupling' $\alpha_s(Q)$. Loop divergences are dealt with by re-parametrizing (renormalizing) the theory with respect to a given, in principle arbitrary renormalization scale $\mu$. To all orders the prediction is independent of the arbitrary choice of $\mu$, but at fixed order one would want to choose $\mu$ such that in the finite perturbative expansion the effective coupling most closely resembles the one the experimentalist measures. In terms of the renormalizability of the theory, the important point is that once the theory is reparametrized in terms of a reference $\alpha_s(\mu)$, the value of $\alpha_s(Q)$ measured by the experimentalist does not depend on the particular process. The experimental measurements of $\alpha_s$ are by convention compared at $\alpha_s(M_Z)$, although they are obtained from a wide range of energy scales. Thus, the comparisons are in reality a test of the prediction for the running of $\alpha_s$.

The propagator (vacuum) loops of the theory are related to the possible couplings of the theory. The specific way in which the coupling depends on $Q^2$ is determined by the gauge symmetry of the Lagrangian through the effect of the particular loop contributions to the running. To see how this works, lets consider how the scale dependence of the coupling is obtained. In a renormalizable Quantum Field Theory such as QCD the coupling is the solution to the renormalization group equation for the $\beta$-function, the function that characterizes the dependence of $\alpha_s$ on the renormalization scale $\mu$ [7]:

$$\mu\frac{\delta(\alpha_s)}{\delta\mu} = 2\beta(\alpha_s) = -\frac{\beta_0}{2\pi}\alpha_s^2 - \frac{\beta_1}{4\pi^2}\alpha_s^3 - ...; \qquad \beta_0 = 11 - \frac{2}{3}n_f \qquad \beta_1 = 51 - \frac{19}{3}n_f, \tag{1.16}$$

where $n_f$ is the number of quarks with mass less than the energy scale $\mu$. In order to solve this equation for $\alpha_s$ a constant of integration must be introduced, which is the value of $\alpha_s$ at a given scale. This value is obtained experimentally and as we mentioned is conventionally taken at $\alpha_s(M_Z)$. In QED only fermionic loop corrections analogous to the fermionic loops in Fig. 1.9, which have a 'screening' effect, contribute to the $\beta$-function. In Fig. 1.9 we see, however, that QCD because of the gluon self-coupling also contains gluonic loops and these dominate over the $n_f$ fermion 'screening' loops, causing an overall 'anti-screening' effect such that the color charge leaks out into the cloud of virtual particles surrounding the color source.

At leading-logarithmic order, the series in Fig. 1.9 can be summed to give

$$\alpha_s(Q) = \frac{\alpha_s(\mu)}{1 - \frac{1}{4\pi}\beta_0\alpha_s(\mu)log(\frac{Q^2}{\mu^2})}, \tag{1.17}$$

where $\beta_0 = 11 - \frac{2}{3}n_f$ is the first term in the expansion of the $\beta$-function, and gives an overall positive valued contribution to the denominator. The first piece of $\beta_0$ comes from the self-coupling gluon loops and dominates (in a world with less than 16 flavours) over the $\frac{2}{3}n_f$ fermion loop contributions. Herein lies the reason the self-coupling of the gluons leads, through the anti-screening gluon loops, to asymptotic freedom, a crucial aspect of QCD. Moreover, at decreasing $Q^2$ the running increases, suggesting that the confinement of quarks and gluons within color-singlet hadronic states is also contained in QCD. Confinement is only suggested but not proven by pQCD since the perturbative approach relies heavily on the (asymptotic) convergence of the perturbative series around $\alpha_s$, compromised and eventually lost at large distances. The scale at which pQCD breaks down is called $\Lambda_{QCD}$ and corresponds to the hadron scale ($\sim$ 220 MeV). Since it will be useful in later discussions, the two-loop expression for $\alpha_s(Q)$ in terms of $\Lambda_{QCD}$ is [22]:

$$\alpha_s(Q) = \frac{4\pi}{\beta_0 \ln(Q^2/\Lambda^2)}[1 - \frac{2\beta_1}{\beta_0^2}\frac{\ln[\ln(\frac{Q^2}{\Lambda^2})]}{\ln(\frac{Q^2}{\Lambda^2})}] \tag{1.18}$$

Eq. 1.18 gives a precise theoretical prediction for the running of $\alpha_s$ which depends on the particular vacuum loops of the theory. Fig. 1.10 shows the scale dependence of $\alpha_s$ for different values of $\alpha_s(M_Z)$. The central dashed line and the shaded area in Fig. 1.10 represent curves of the dependence of $\alpha_s$ on $Q$ which are theoretically possible without regard to experimental data. Although pQCD predicts how the running will be, a single curve like those in Fig. 1.10 is singled out experimentally by measuring $\alpha_s$ at a given scale. The validity of QCD is not tested by a single $\alpha_s$ measurement, but rather by showing that determinations of $\alpha_s$ from a variety of processes proving different scales all lie on the same curve.

### 1.2.3 The scaling violations of the structure functions and the factorization property of QCD

We have already shown how the non-Abelian character of QCD shows up in angular-correlation variables and also determines the scale dependence of the coupling. Now we return to the DIS regime of $ep \to e + X$ where we left off in the first section, to see how the gauge structure of the theory also reveals itself through the structure functions. In terms of pQCD, the QPM formula 1.7 is the zeroth-order term in the expansion of $F_2$ as a power series in $\alpha_s$. To include the $O(\alpha_s)$ corrections, we also

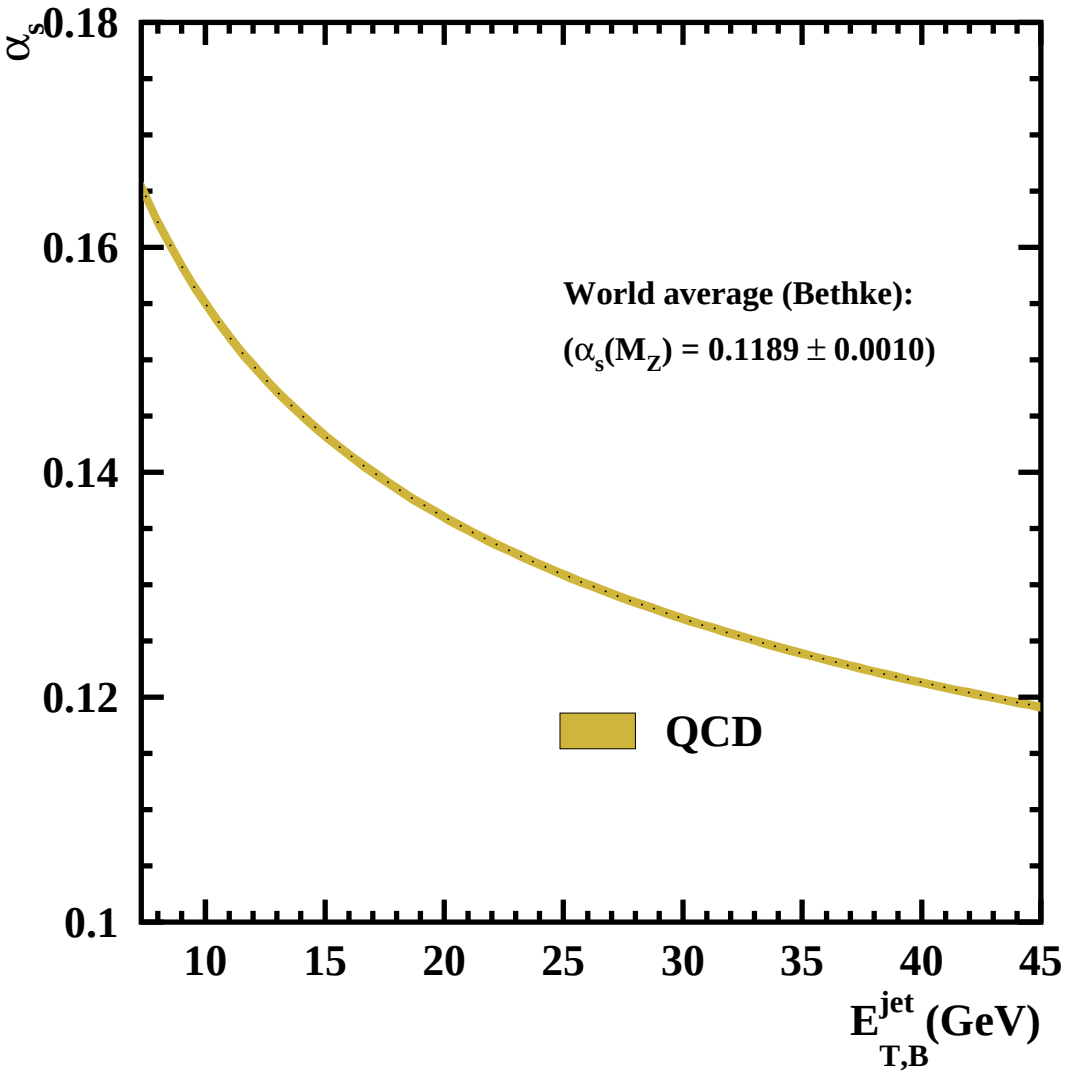


Figure 1.10: Perturbative QCD prediction for the scale dependence of $\alpha_s$ for three different values of $\alpha_s(M_Z)$:0.1179,0.1189 and 0.1199, corresponding to the current world average.

have to take into account subprocess diagrams such as that in Fig. 1.11, where there is an initial-state emission of a gluon. This type of diagram has a singularity in the collinear gluon limit. Let $P_{qq}(z)$ be the probability of a quark emitting a gluon such that it becomes a quark with a momentum reduced by a fraction $z$ with respect to the parent quark. For simplicity we develop the formalism for now only with this contribution. The rest will be added at the end. Then the new expression for the structure function after including the initial-state radiation diagram is [5]:

$$\frac{F_2(x,Q^2)}{x} = \sum_i e_i^2 \int \frac{d\xi}{\xi} q(\xi)[\delta(1-\frac{x}{\xi}) + \frac{\alpha_s}{2\pi} P_{qq}(\frac{x}{\xi}) \log \frac{Q^2}{\mu_F^2})] \qquad (1.19)$$

Here $q(\xi)$ is the quark distribution function. The scale $\mu_F$ is a lower limit on the transverse momentum introduced as an artificial cut-off to regularize the divergent

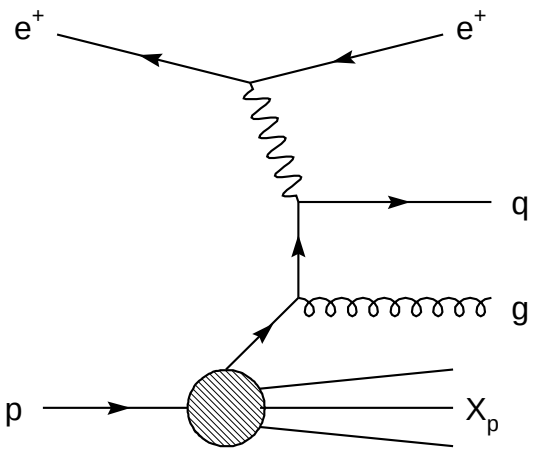


Figure 1.11: Initial-state emission of a gluon.

integral that results from the collinear ($k_T \to 0$) gluon emission. We may now regard Eq. 1.19 as the first two terms in a power series for $F_2$ around $\alpha_s$. The $\log \frac{Q^2}{\mu_F^2}$ factor represents a logarithmic deviation of the scale-invariance of the QPM structure function, eq. 1.7. The 'logarithmic violation' which results from the presence of gluon emission is a historically important prediction of pQCD.

Recall that the logarithmic contribution to Eq. 1.19 is divergent. This divergence can be treated in a manner analogous to the divergent contributions to the coupling from loop corrections. As with the bare coupling $\alpha_0$, we can regard $q_0(y)$ as an unmeasurable, bare distribution. The collinear singularities can then be 'factorized' into the definition of the quark distribution at a factorization scale ($\mu_F$), the scale at which we regularize the divergent integrals. The effective quark distribution thus acquires a scale dependence with $\mu_F$: $q_0(x) \to q(x, \mu_F^2)$. The collinear divergence can be considered as a long-distance, non-perturbative effect to the calculation. By 'absorbing' it into the PDFs, it becomes part of a measurable quantity. This recipe will only work if the 'factorization' of the PDFs can be done at all orders and the resulting quark distributions are universal. It can be shown that this is indeed the case [23], a characteristic known as the 'factorization property' of QCD.

The prediction for $F_2$ should be independent of the factorization scale, therefore the theoretical expression for the quark distribution must satisfy a renormalization group equation. Applying the same machinery as for $\alpha_s(Q)$, the dependence of $q(x, Q^2)$ on $Q^2$ ($\mu_F$ is typically set equal to $Q^2$, the scale at which the proton is being resolved) can be obtained and gives the integro-differential equation [5]:

$$\frac{d}{d \log Q^2} q(x, Q^2) = \frac{\alpha_s}{2\pi} \int \frac{d\xi}{\xi} q(\xi, Q^2) P_{qq}(\frac{x}{\xi}). \tag{1.20}$$

This is the famous DGLAP equation describing the scale-dependent evolution of the PDFs. It is analogous to the $\beta$-function of $\alpha_s$ which describes the evolution of $\alpha_s(Q)$. Eq 1.20 is only the one loop expression. As with $\alpha_s$, the theory has provided the functional dependence of the PDFs with $Q^2$, resulting in an infinite family of possible curves. A single PDF curve from these must be singled out by experiment. Having determined the value of the PDFs experimentally at some scale, the theory is then able to predict their values at all $Q^2 \gg 1$ GeV$^2$. Note that the evolution of the PDFs with the scale is again governed by the vertices of the theory and, thus, by the color factors.

We have shown that DIS can provide direct evidence for the existence of the gluon through measurements of the scaling violations of the structure functions. The HERA *ep* collider is particularly suited for $F_2$ measurements since it gives access to a wide range of phase-space in $x$ and $Q^2$. In particular, it extends to the low $x$ regime, where, as we will see, the gluon and sea quark PDFs are dominant. Fig. 1.13 shows measurements of $F_2$ made by the ZEUS Collaboration at HERA [24]. The measurements of the structure function over a wide range of $Q^2$ for different $x$ values are compared in the figure to NLO QCD predictions based on the same data. The measured structure functions clearly exhibit logarithmic violations of the scale invariance, evidencing the presence of the characteristic vertices of pQCD. In the

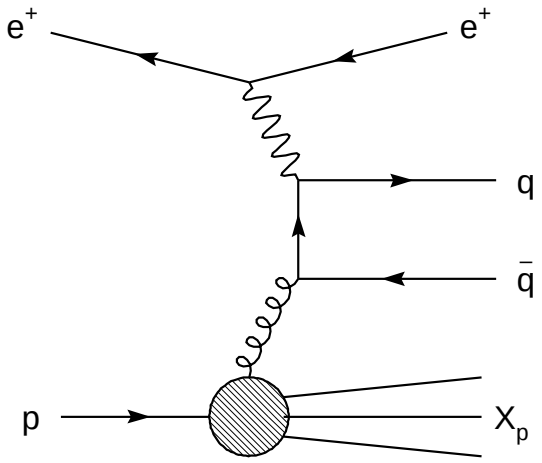


Figure 1.12: The presence of the gluon field induces a sea quark distribution arising from gluon splittings into $q\bar{q}$ pairs.

discussion so far we have glossed over a couple of points:

- A diagram similar to Fig. 1.11 gives a final-state collinear divergence, but it cancels out with the one loop contributions.

- There is also a divergence from a soft ($E \to 0$) gluon being emitted at very small energies. This divergence cancels out with the one loop contributions.

The presence of the gluon field induces a sea quark distribution arising from gluon splittings into $q\bar{q}$, as shown in Fig. 1.12. This type of process will contribute to $F_2$ with a term $P_{qg}$ multiplied by the gluon distribution, where $P_{qg}$ represents the probability of a gluon splitting into a $q\bar{q}$ pair. The complete evolution equation for a quark density is:

$$\frac{dq_i(x,Q^2)}{d\log Q^2} = \frac{\alpha_s}{2\pi}\int \frac{d\xi}{\xi}(q_i(\xi,Q^2)P_{qq}(\frac{x}{\xi}) + g(\xi,Q^2)P_{qg}(\frac{x}{\xi})) \tag{1.21}$$

The DGLAP equations are a key ingredient in global QCD fits to extract the PDFs of any hadron, which themselves are necessary for any pQCD calculation of an observable in a reaction involving incoming hadrons. The next section elaborates on this point.

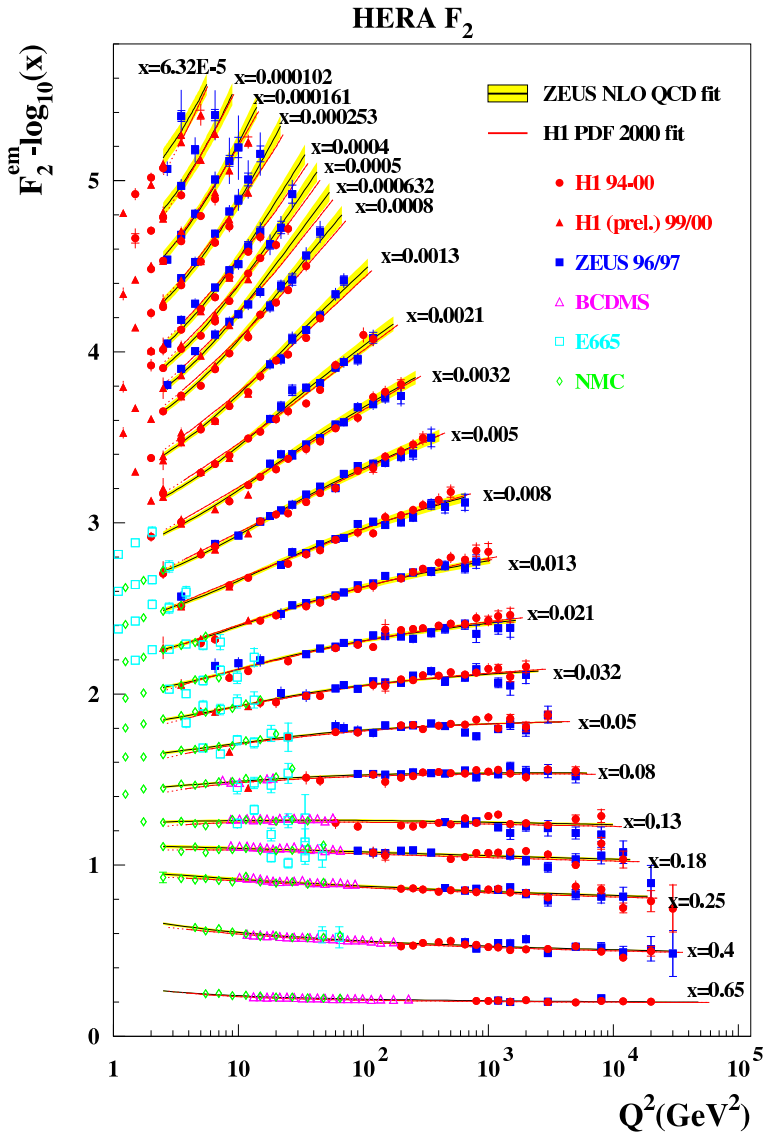


Figure 1.13: Summary of measurements of $F_2$. For better visibility, the results for different values of $x$ were multiplied with the given factors of 2i.

## 1.3 Jet measurements in NC DIS and determinations of $\alpha_s(M_Z)$ at HERA

HERA physics covers a wide range of momentum transfers ($Q^2$) and is therefore useful for both constraining the proton PDFs and testing the perturbative regime of QCD. The knowledge gained at HERA has a universal character due to the factorization property of QCD. In general, the factorization property allows a NC DIS cross section to be expressed as the convolution of the proton PDFs with calculable pQCD matrix elements:

$$\sigma(P_1, P_h) = \sum_i \int d\xi \cdot f_i(\xi, \mu_F^2) \cdot \hat{\sigma}(P_1, \xi P_h, \alpha_s(\mu_R), \mu_R, \mu_F). \tag{1.22}$$

The matrix elements represent the short-distance, hard part of the interaction. The PDFs contain the long-range non-perturbative part of the interaction and must be determined experimentally. Fig. 1.14 shows determinations of the PDFs made by the ZEUS Collaboration at HERA [25]. In regions where the uncertainty of the PDFs is large, improved cross-section measurements can help reduce this uncertainty when included in the global QCD fits. By the same token, regions where the PDFs are well constrained allow for measurements of cross sections with small uncertianties, providing a powerfull tool to study QCD.

As seen in Fig. 1.14, the ZEUS collaboration has performed a global QCD analysis using ZEUS data alone to obtain the PDFs. Lets sketch how such an analysis proceeds.

- A reference value $Q_0$ is chosen and the PDFs are parametrized at that value, $q(x, Q_0)$;
- These distributions are then evolved numerically, using the DGLAP equations, to obtain values of the $F_i(x, Q^2)$ or any other pQCD observables in the kinematic regions where they are measured;
- A global numerical fit (ZEUS-JETS) is performed to determine the 'best' values for the parameters, including $\Lambda_{QCD}$, in terms of how well the evolution matches the measurements.

Such fits have also been done by other collaborations like MRST [26] or CTEQ [27], where a wide set of structure-function data from a number of different experiments is fitted. The MRST and CTEQ global fits find tensions among the different data sets and threfore a rigorous statistical treatment to obtain the PDF uncertainties is not possible.

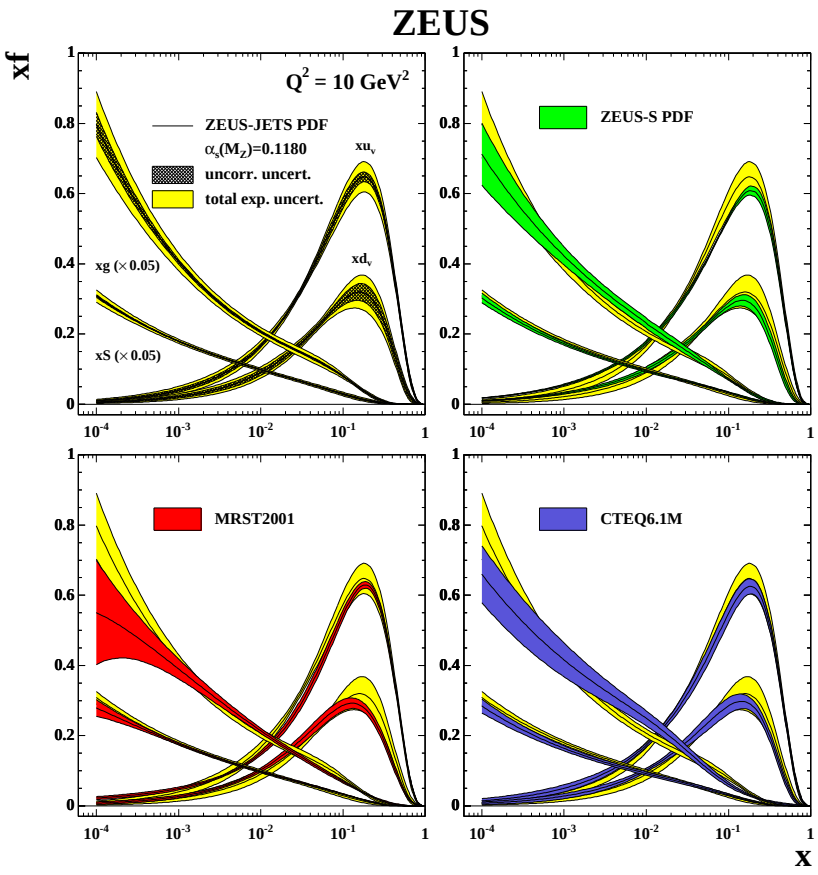


Figure 1.14: The PDFs as functions of $x$ at $Q^2 = 10$ GeV$^2$ as determined in a global QCD fit made by the ZEUS Collaboration (ZEUS-JETS, upper left plot). The fit includes also jet data. For comparison, the PDFs extracted using ZEUS plus fixed-target data (ZEUS-S, upper right plot) and those obtained by MRST (MRST2001, lower left plot), or CTEQ (CTEQ6.1M, lower right plot) are also shown. The total experimental uncertainty bands are shown for each PDF set.

The ZEUS-JETS fit has the advantage that the uncertainties from all the data sets used in the fits are well understood and, in that sense, the statistical treatment is more reliable, although at the expense of restricting the fit to ZEUS data alone. Most of the information for the PDFs in global fits, restricted to ZEUS data or not, is given by measurements of the total DIS cross sections as functions of $x$ and $Q^2$. As we showed in eq. 1.3, the total cross section depends on $F_2$ which can itself be expressed in terms of the quark and gluon PDFs. Therefore the measurements of $F_2$ shown in Fig. 1.13 are of particular importance in global fits. Nonetheless the gluon PDF contribution enters only indirectly for these measurements and other means of constraining it are necessary. With this in mind the ZEUS Collaboration studied the impact of including jet cross-section measurements to constrain the gluon PDF and

found they helped constrain its uncertainty substantially in the mid-to-high $x$ region. The PDFs from the ZEUS-JETS fit, shown in Fig. 1.14, are compared with those extracted using ZEUS plus fixed-target data and found to be in agreement. The ZEUS-JETS PDFs are also compatible with those obtained in the global analyses by MRST or CTEQ. Note that the gluon and sea PDFs dominate in the low $x$ region. The fact that the evolution equations can simultaneously fit different processes over a wide range in $x$ and $Q^2$ is a compelling test of pQCD.

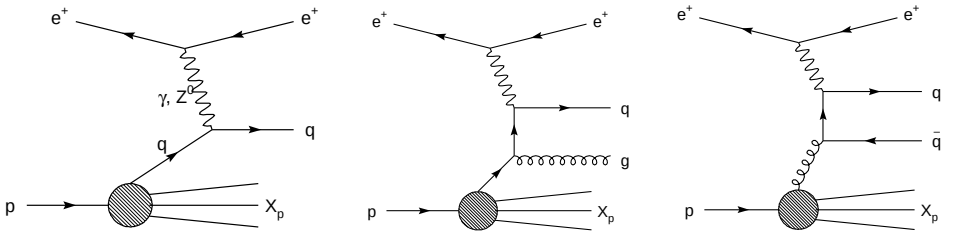


Figure 1.15: Diagrams that contribute to the production of jets in NC DIS at HERA

.

Let us now consider the other piece of eq. 1.22, the hard-scattering matrix elements. We will be mostly interested in the production of jets in NC DIS. At $O(\alpha_s)$ in $ep$ collisions, there are three characteristic diagrams which contribute to jet production. They are shown in Fig. 1.15. The first diagram corresponds to the QPM, sensitive to the quark PDFs. The second is gluon radiation by the struck quark (QCD Compton) and contains a QCD vertex or sensitivity to $\alpha_s(M_Z)$. This diagram dominates the cross section at high $Q^2$, where both the theoretical and PDF uncertainties are small. Measurements of inclusive-jet cross sections in regions dominated by the QCD Compton diagram render the most precise determinations of $\alpha_s(M_Z)$. The third diagram is called boson-gluon fusion (BGF) and is both directly sensitive to $\alpha_s$ and to the gluon PDF. The contribution from the BGF diagram is responsible for precision jet production measurements being able to constrain the gluon PDF in global QCD fits. The BGF contribution is greater at lower $Q^2$ because, as we have seen, at lower $x$ the gluon PDF plays a dominant role ($Q^2$ is correlated to $x$ in HERA physics). Although the gluon PDF is constrained in the low $x$ region by structure function data, the jet data provide a tighter constraint on the gluon PDF in the mid- to high-x region. The gluon PDF is entangled with the value of $\alpha_s(M_Z)$, but this is not an issue since at high $Q^2$, where QCDC dominates, jet data allow a determination of $\alpha_s(M_Z)$ independently of gluon density. Fig. 1.16 shows the gluon PDF uncertainties resulting from the ZEUS global fit with and without the inclusion of the jet cross-section data. The uncertainties are substantially reduced as a result of including the jet data.

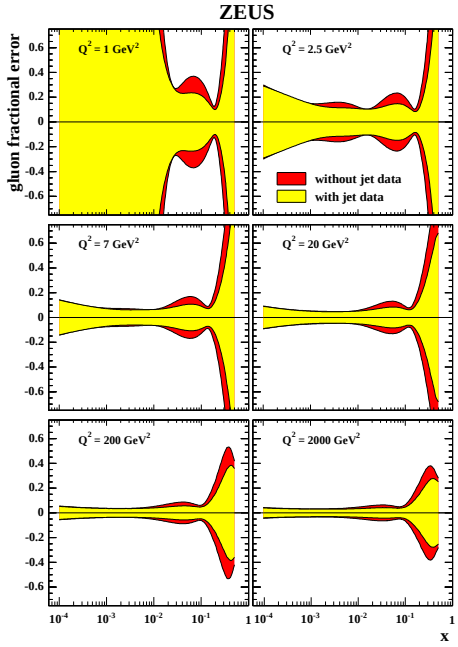


Figure 1.16: Relative uncertainties in the gluon PDF resulting from a global QCD fit using ZEUS data alone with and without the inclusion of the jet data. A substantial reduction in the gluon PDF uncertainties is observed in the mid-to-high $x$ region when the jet data is included.

The full potential of jet measurements goes well beyond constraining the PDFs, however. Historically, the definition of a resolvable jet of hadrons that can be applied to both the theory and the data is what allowed access to the short-distance physics, providing the connection between pQCD and the experiment. For example, the first direct evidence of gluon radiation came from the observation of three-jet events in 1979 by the JADE, Mark-J, TASSO and PLUTO experiments at the 30∼35 GeV $e^+e^-$ collider PETRA, at DESY [28]. Another example is the four-jet rates measured at LEP, used to extract the color factors.

The study of jet production in $ep$ collisions at HERA has been well established as a testing ground of perturbative QCD providing precise determinations of the strong coupling constant, $\alpha_s$, and its scale dependence. The jet observables used to test pQCD included dijet [29–31], inclusive-jet [30, 32, 33] and multijet [34, 35] cross sections in neutral current NC DIS.

The purpose of this document is to cover two new examples with which jet rates in NC DIS have been used to study pQCD with the ZEUS detector at the HERA collider:

- Measurements of inclusive-jet cross sections in NC DIS are used to make precise determinations of $\alpha_s(M_Z)$ and measure its scale dependence. The jet

reconstruction algorithm is also studied in this analysis.

- Three-jet measurements in NC DIS are used to investigate variables that show sensitivity to the underlying symmetry of the strong interactions, in analogy with the LEP analyses.

Before delving into these two studies, it is important to define what is meant by a jet and to choose a reference frame that is optimal for these particular analyses.

### 1.3.1 The definition of a jet

The view into the small-distance hard interaction that jet measurements provides is inevitably clouded by the subsequent long distance showering and eventual hadronization of the primary quarks and gluons. The effect of the long distance processes on the identification of the hadronic state with the partonic state can be minimized with a suitable definition of a jet. The aim is to obtain a precise picture of the short distance dynamics, well into the predictive regime of pQCD. The algorithm used to reconstruct the jet must take into account the dynamics of the collision and its possible backgrounds. For example, collisions where a hadron is involved in the initial state, such as $ep$ collisions differ in overall event structure from the purely electromagnetic ones of $e^+e^-$ collisions in that neither all the partons in the initial state nor all the hadrons in the final state participate in the hard scattering.

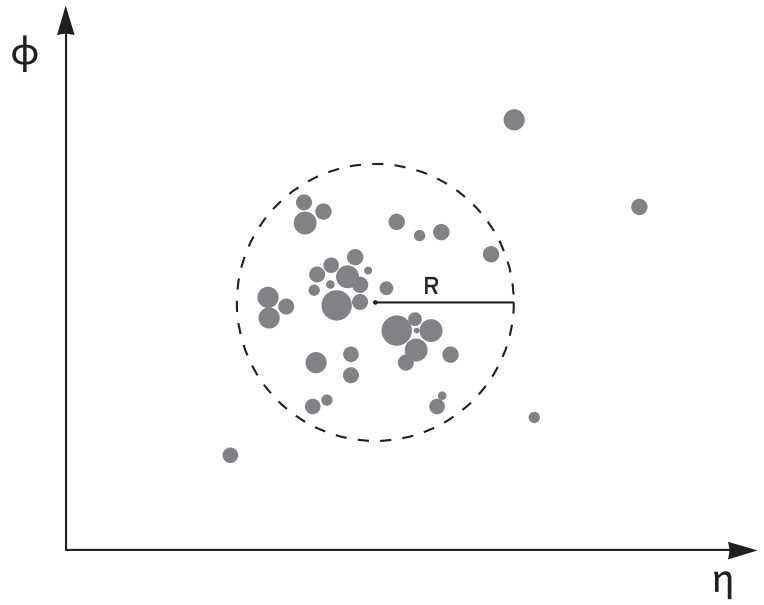


Figure 1.17: The 'jet radius' parameter R is the maximum distance in the $(\eta, \phi)$ plane at which two particles get combined in the $k_T$ clustering algorithm. It is conventional to set R=1, although this might not be the optimal choice for all analyses.

It is important for the jet algorithm to exploit the particular characteristics of this type of collisions in order to distinguish the final state of the hard interaction from the rest of the hadronic matter present. HERA *ep* collisions are characterized by the presence of a 'beam remnant' composed of the initial state radiation of the scattered parton together with the remnants of the spectator partons. The beam remnant has low transverse energy with respect to the beam axis. In other types of collisions the global aspect of the event can be different. For example, in $p\bar{p}$ collisions the soft interactions among the spectator partons lead to an underlying event resulting in an isotropic distribution of energy in the detector, whereas in $e^+e^-$ collisions all the hadronic matter in the final state originates from the hard interaction.

Thus, the optimal algorithm used to reconstruct hadronic jets depends on the experiment. There are, nevertheless, several requirements that a jet algorithm should at a minimum satisfy. From both a theoretical and experimental point of view, a jet-finding algorithm needs to be collinear and infrared safe. This means that in the case when the $E_T$ of an emitted parton is close to 0 or when a parton divides into collinear partons the emitted particles are recombined into the same jet. The jet algorithm should be as insensitive as possible to the hadronization of the originating partons. Finally, the jets should be reconstructed in a suitable reference frame to help maximize the distinction between the hard scattering event and any background hadronic activity, such as the presence of a beam remnant.

At HERA, the CM frame depends on the kinematics of an individual event, and thus the jet algorithm should emphasize the use of longitudinally invariant observables. For this reason the natural variables to use in this case are the transverse momentum ($E_T$), pseudorapidity ($\eta$), and azimutal angle ($\phi$) of the jet, where:

$$E_T = E \sin\theta \qquad \text{and} \qquad \eta = -\ln\left[\tan\left(\theta/2\right)\right] \tag{1.23}$$

Consider an *ep* collision which has resulted in some distribution of particles in the final state, each of which is identified by its 4-momentum $p^\mu$. We assume the scattered electron has been identified and omitted from the input list to the jet reconstruction. The $k_T$ algorithm [36] proceeds according to the following steps:

- For every pair of particles i and j, the distance between the two particles is defined as:
$$d_{ij} = min(E_{T,i}, E_{T,j})^2 \left[(\eta_i - \eta_j)^2 + (\phi_i - \phi_j)^2\right], \tag{1.24}$$
- For every particle i, the quantity is also defined:
$$d_i = E_{T,i}^2 \cdot R^2, \tag{1.25}$$

where $R$ is a parameter of the algorithm which plays the role of a jet radius in the $(\eta, \phi)$ plane, as pictured in Fig. 1.17 It is the maximum distance at which two particles are combined in the algorithm.

- The smallest value of all $(d_{ij}, d_i)$ is considered. If this is one of the $d_{ij}$'s then the two particles are merged into a new one following a given recombination scheme. If the minimum is one of the $d_i$'s, then that cluster is considered as a *protojet* and no longer considered for clustering;

- The procedure is repeated until no remaining cluster is left and all the particles have been assigned to protojets. At each iteration, one particle is removed, so the number of iterations is always equal to the original number of final-state particles;

- Finally, from the sample of protojets, the final jets are selected by imposing a cut on $E_T$ which sets the scale to distinguish the hard and the soft processes, and a cut on $\eta$, due to the detector geometrical acceptance.

The particles are treated as massless objects and so are the resulting reconstructed jets. In the analyses presented here, the recombination scheme for the particles at each step, known as the Snowmass convention [37], is

$$E_{T,k} = E_{T,i} + E_{T,j} \qquad \eta_k = \frac{1}{E_{T,k}}(\eta_i E_{T,i} + \eta_j E_{T,j}) \qquad \phi_k = \frac{1}{E_{T,k}}(\phi_i E_{T,i} + \phi_j E_{T,j}). \tag{1.26}$$

The above definition provides a QCD-motivated implementation of the jet requirements. It allows the inclusion of the proton remnant in the beam jet while associating with jets the soft radiation accompanying the hard parton scattering. Since the distance is weighted by the minimum $E_T$ it does not combine soft emissions into fake jets. The collinear divergence is taken care of since a collinear emission will be recombined with its parent parton, while experimentally the finite resolution of the detector will not differentiate between a hadron and its collinear decay products. From a theoretical point of view, the jet algorith should allow the jet cross sections to be written in factorizable forms such that each structure function can be split into its jet contributions. It has been shown that this is accomplished only by a class of algorithms such as the $k_T$ cluster algorithm and only when the jets are reconstructed in a particular family of reference frames. Studies have demonstrated that the $k_T$ cluster algorithm in the longitudinally invariant inclusive mode [38] is at present the method to reconstruct jets in $ep$ collisions for which the smallest uncertainties are achieved.

The Breit frame belongs to this class and is particularly suited to QCD studies, as we now discuss.

### 1.3.2 The Breit frame of reference

In *ep* collisions, at lowest order the interacting quark will hadronize into a jet, independently of the value of $\alpha_s$. Thus, in wanting to extract $\alpha_s$ from jet measurements, one would like to select a sample of jet events such that the QPM contribution is suppressed. Moreover, the jet recognition should also be insensitive to the beam remnant. Thus, an ideal reference frame is one where one can trivially distinguish hard interaction jets from the beam remnant as well as $\alpha_s$-sensitive jet production from the QPM contribution. The Breit frame [39] is defined such that the struck quark in the QPM bounces back along the beam direction with equal but opposite momentum. It differs from the hadronic CM frame only by a longitudinal boost. In such a frame, neither the jet initiated by the struck quark, nor the remnant jet have any $E_T$, as depicted in Fig 1.18. The production of jets with $E_T$ in the Breit frame is sensitive to $\alpha_s$ at lowest order and excludes both the beam remnant and the QPM contribution in a natural way. Therefore the Breit frame is ideal for QCD studies using jets. Formally, the Breit frame is defined as the frame where the virtual

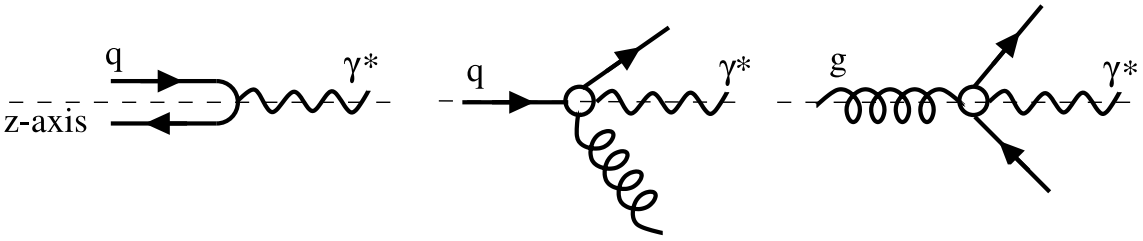


Figure 1.18: Diagrams contributing to jet production as viewed in the Breit frame. The Born process does not contribute with jets having $E_{T,\mathrm{B}}^{\mathrm{jet}} > 0$. From left to right, the Born, QCDC and BGF processes.

boson is completely space-like (i.e. its energy is zero) and has no $E_T$ in the beam direction. The Lorentz transformation from the laboratory to the Breit frame can be specified in terms of the virtual boson's 4-momentum ($q^\mu$), and therefore depends on the kinematics of a given event. The transformation matrix can be applied to the four momenta of all the particles in the final state so that the jet reconstruction using the $k_T$ clustering algorithm can be carried out in this frame. Since the Breit frame aligns the struck quark with the virtual boson, the scattering angle of the struck quark in the laboratory ($\gamma$) characterizes the transformation. In the extreme case where $\gamma \to 180°$, the transformation from the laboratory to the Breit frame is just the unit matrix. In cases where $\gamma$ is small, the transformation will considerably deviate from and distort the laboratory frame. The characteristics of the detector in the Breit frame must be understood, since the distance in the $\eta - \phi$ plane used by the $k_T$ clustering algorithm might become small in comparison to detector cell sizes

in the Breit frame. We will delve deeper into this subject in chapter 4. Finally, the Breit frame is particularly suited because it belongs to a class of reference frames (of which the hadronic CM and the laboratory frames are not members) such that resummed calculations for jet obervables are possible.

### 1.3.3 Extracting $\alpha_s(M_Z)$ from inclusive-jet measurements in NC DIS in the Breit frame

A value of $\alpha_s$ can be obtained from a jet cross-section measurements by the following procedure. The dependence of the theoretical predictions on the assumed value for $\alpha_s(M_Z)$ is parametrized according to a simple polynomial:

$$[\frac{d\sigma}{dA}](\alpha_s(M_Z)) = C_1\alpha_s(M_Z) + C_2\alpha_s(M_Z)^2 \tag{1.27}$$

This parametrization is then fitted to theoretical predictions made at NLO in pQCD using a range of different assumed values for $\alpha_s(M_Z)$. Self-consistency requires that the assumed value of $\alpha_s(M_Z)$ be made the same both in the parametrizations of the PDFs used and in the matrix elements. Once the polynomial dependence of the theoretical prediction on $\alpha_s(M_Z)$ is obtained, the polynomial is solved for the value of $\alpha_s(M_Z)$ that reproduces the measured cross section. The method is pictured in Fig. 1.19.

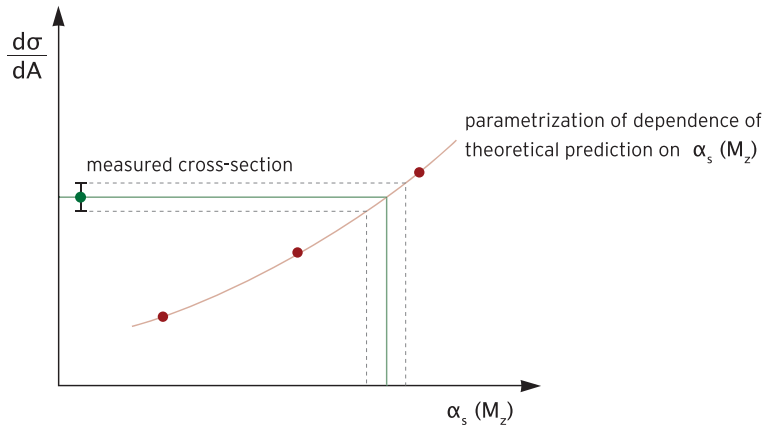


Figure 1.19: Method for extracting $\alpha_s(M_Z)$ from the measured cross sections. The dependence of the theoretical prediction on $\alpha_s(M_Z)$ is parametrized according to a polynomial. Afterwards the polynomial is solved for the measured value of the cross section.

Experimental determinations of $\alpha_s(M_Z)$ have been motivated in this chapter as one of the most comprehensive and stringent ways to test QCD. It has also been emphasized that the precision of these measurements is correlated with the precision with which pQCD is able to make predictions. Jet production has allowed a number

of precise determinations of $\alpha_s$ and its scale dependence at HERA. This stems from the fact that jet production with high $E_T$ in the Breit frame is sensitive to $\alpha_s$ at lowest order and that it relates the pQCD partonic predictions to the measured hadronic final state in a way that is insensitive to the long-range hadronization process. The jet measurements used in the past include dijet, inclusive-jet and multijet cross sections in NC DIS, and dijet, inclusive-jet and multijet cross sections in photoproduction (i.e $Q^2 = 0$). Fig. 1.20 shows a number of determinations of $\alpha_s$ made at HERA. They are consistent with each other as well as with the world average. The jet observables that yield $\alpha_s(M_Z)$ with the smallest overall uncertainties are inclusive-jet cross sections in NC DIS. Thus, it makes sense to try

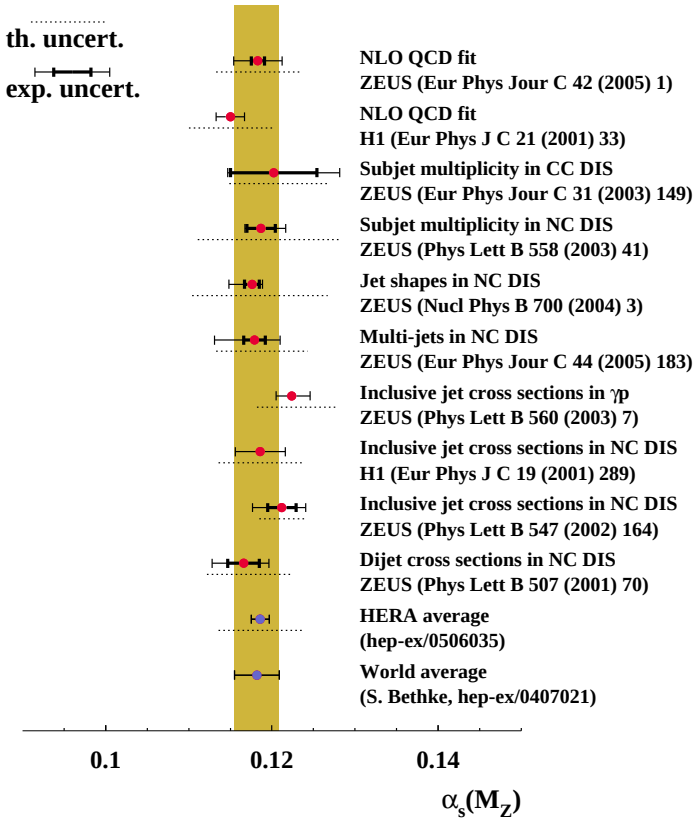


Figure 1.20: A compilation of determinations of $\alpha_s(M_Z)$ made at HERA.

to pursue this venue further. The '$\alpha_s$ analysis' presented in the rest of the chapters of this document encompasses the following studies:

- New measurements of inclusive-jet cross sections with increased statistics have been made as functions of $Q^2$, $E^{jet}_{T,B}$, $\eta^{jet}_B$, and $E^{jet}_{T,B}$ for different regions of $Q^2$;
- The dependence of the differential as well as the total inclusive-jet cross sections

on the jet-radius R has been studied and a range of validity for this parameter has been established;

- The inclusive-jet cross-section measurements with respect to $Q^2$ and $E_{T,\mathrm{B}}^{\mathrm{jet}}$ have been used to make new determinations of $\alpha_s(M_Z)$. A region has been identified which yields the value of $\alpha_s(M_Z)$ with the smallest uncertainties obtained thus far by the ZEUS Collaboration;

- The extracted values of $\alpha_s$ have been used to test its scale dependence over a wide range of $E_{T,B}^{jet}$ and $Q^2$.

The jet cross-section measurements represent a compelling test of QCD when compared to the NLO pQCD predictions in $Q^2$ and $E_{T,B}^{jet}$. They are expected to show sensitivity to the gluon PDF through the BGF process and should be included in future global QCD fits. These measurements also provide a well understood environment on which to study the $k_T$ cluster jet algorithm. The conventional value for the jet radius (R=1) in the $k_T$ clustering algorithm might not be optimal for certain analyses at the LHC where, for example, the identification of a heavy particle decaying into jets that emerge close in phase space might require lower values of R [40]. The objective of this study is to determine a region of validity for the jet radius, R. By region of validity what is meant is that the systematic and theoretical uncertainties involved for a given choice of R do not prevent the analysis, and that quantities derived from the jet measurements such as the value of $\alpha_s(M_Z)$ do not depend on R.

### 1.3.4 Three-jet cross sections in NC DIS in the Breit frame and angular-correlation variables

The study of the underlying symmetry of the strong interactions through angular-correlation variables carried at LEP has inspired a similar analysis for *ep* collisions at HERA. The 'angular-correlations' analysis presented in this document is the first of its kind at HERA and opens a new venue through which to test QCD. It turns out that *ep* physics is from this analysis' point of view substantially different to $e^+e^-$ physics. The adaptation to *ep* physics of this type of analysis is not straightforward, since a number of complications arise which in some cases reduce the sensibility of the angular variables to the underlying symmetry.

At HERA, the triple-gluon vertex appears already at LO for three-jet final-state production. The theoretical expression for the three-jet cross section at LO can be separated into four terms according to the color factors they contain:

$$\sigma_{ep\to 3jets} = C_F^2 \cdot \sigma_A + C_F C_A \cdot \sigma_B + C_F T_F \cdot \sigma_C + T_F C_A \cdot \sigma_D \qquad (1.28)$$

Two issues absent in $e^+e^-$ that need to be confronted in $ep$ interactions arise immediately. First, the scale evolution of the available PDF fits is parametrized assuming SU(3) as the underlying symmetry and could introduce a color dependence in the calculations. Second, in the LEP analyses the characteristic energy scale is $M_Z$ and is the same for all the events; as a result, there is no dependence on the running of $\alpha_s$. In $ep$ collisions at HERA, the production of jets of high $E^{jet}_{T,B}$ in the Breit frame has $E^{jet}_{T,B}$ or $Q^2$ as the characteristic scale for the process, introducing a sensitivity on the running of $\alpha_s$ and therefore to the symmetry group assumed in the running. The aim of this analysis is to see the effect of the underlying gauge symmetry exclusively on the angular correlations of the final-state jets. Thus, in this analysis we would like to study observables which are as insensitive as possible to the symmetry-dependent evolution of the PDFs and $\alpha_s$. For these reasons, the cross sections are normalized to the total cross section, such that only the shape of the distributions in the variables is of relevance. This choice of observable has the benefit of ridding itself from most of the dependence on the evolution of the PDFs and $\alpha_s(M_Z)$, as well as on the magnitude of $\alpha_s$ itself. In order to suppress any residual dependence on the scale evolution, the region of phase can be constrained if necessary in such a way as to restrict the running of $\alpha_s$ and the PDFs, while retaining the sensitivity of the angular-correlation variables to the underlying gauge symmetry. Three-jet cross sections in NC DIS in the Breit frame are measured in NC DIS and their distributions in terms of these variables are shown and compared to different theoretical models.

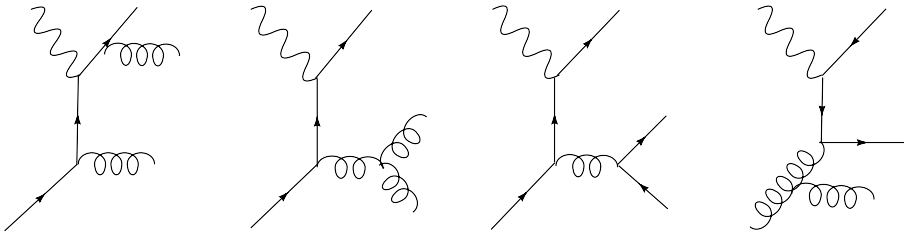

Figure 1.21: Examples of tree-level Feynman diagrams for three-jet production in $e^{\pm}p$ collisions at HERA contributing to $\sigma_A$ ($C_F \times C_F$), $\sigma_B$ ($C_F \times C_A$), $\sigma_C$ ($C_F \times T_F$) and $\sigma_D$ ($T_F \times C_A$), respectively.

The Feynman diagrams shown in Fig. 1.21 are characteristic of each of the four subprocess cross sections that compose the right-hand side of eq.1.28. The first diagram is the double-gluon Bremstrahlung from a quark line. This diagram is analogous to the double-gluon Bremstrahlung diagrams from $e^+e^-$ except that the quark is now in the initial state. This can be seen by simply rotating the diagram. The second and third diagrams are analogous to the $e^+e^-$ diagrams in the same way: they contain the triple-gluon vertex and the gluon splitting into a $q\bar{q}$ pair,

respectively. The fourth diagram also contains a triple-gluon vertex associated to an initial-state gluon from the proton. For three-jet production in *ep* collisions, an angle $\Theta_H$ is defined in analogy with $\Theta_{NR}$, as the angle between the plane formed by the incoming proton beam (which corresponds to the initial-state quark direction) and the primary jet (the one with the highest $E_{T,B}^{jet}$) and the plane formed by the lowest $E_{T,B}^{jet}$ jets [41]. This angle should be sensitive to the relative contributions from the second and third types of diagrams, following the same arguments as in the discussion of the LEP analysis.

The method relies heavily not only on how the correlations among the final-state jets differ in shape, but also on the magnitude of each sub-process cross section. Two requirements must be met in order to make an angular variable valid for this sort of study:

- The angular correlation must have a distinctive distribution for each type of sub-process;
- The relative magnitude of the subprocess cross section must be large enough that its signature contribution to the shape of the cross section is visible.

The variables that have been devised to carry out this program at HERA are (See Fig. 1.22):

- $\theta_H$, the angle between the plane determined by the highest transverse energy jet and the beam and the plane determined by the two lowest transverse energy jets [41];
- $\cos\alpha_{23}$, which is inspired by the variable $\alpha_{34}^{e^+e^-}$ for $e^+e^- \to 4jets$, is defined as the angle between the two lowest transverse energy jets. See Fig. 1.22;
- $\beta_{KSW}$, which is inspired by the Korner-Schierholz-Willrodt angle $\phi_{KSW}^{e^+e^-}$ for $e^+e^- \to$ 4jets, is defined as

$$cos(\beta_{KSW}) = cos\left[\frac{1}{2}(\angle[(\vec{p_1}\times\vec{p_3}),(\vec{p_2}\times\vec{p_B})] + \angle[(\vec{p_1}\times\vec{p_B}),(\vec{p_2}\times\vec{p_3})])\right],$$

  where $\vec{p}_i, i = 1, ..., 3$ is the momentum of jet $i$ and $\vec{p}_B$ is a unit vector in the direction of the beam; the jets are ordered according to decreasing transverse energy;
- $\eta_{max}^{jet}$, the maximum pseudorapidity of the three jets with highest transverse energy.

These angular-correlation variables are with the exception of $\eta_{max}$ analogous to the ones used in LEP analyses. The jet correlations could be distorted by the boost

to the laboratory frame and for this reason the jets are reconstructed in the Breit frame of reference. The angular-correlation variables presented above are shown to be sensitive to the underlying symmetry and can be used to distinguish among theories with different gauge symmetries.

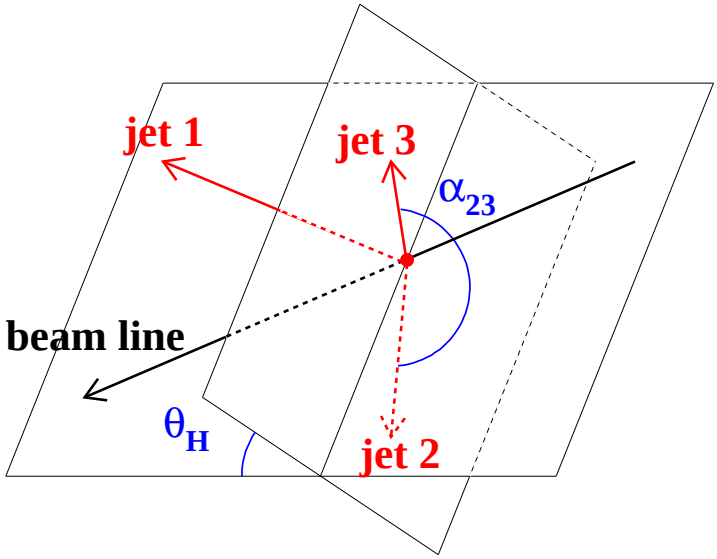


Figure 1.22: Three-jet angular-correlation variables $\Theta_H$ and $\alpha_{23}$

# Chapter 2

# The HERA collider and the ZEUS detector

## 2.1 The Hadron Electron Ring Accelerator

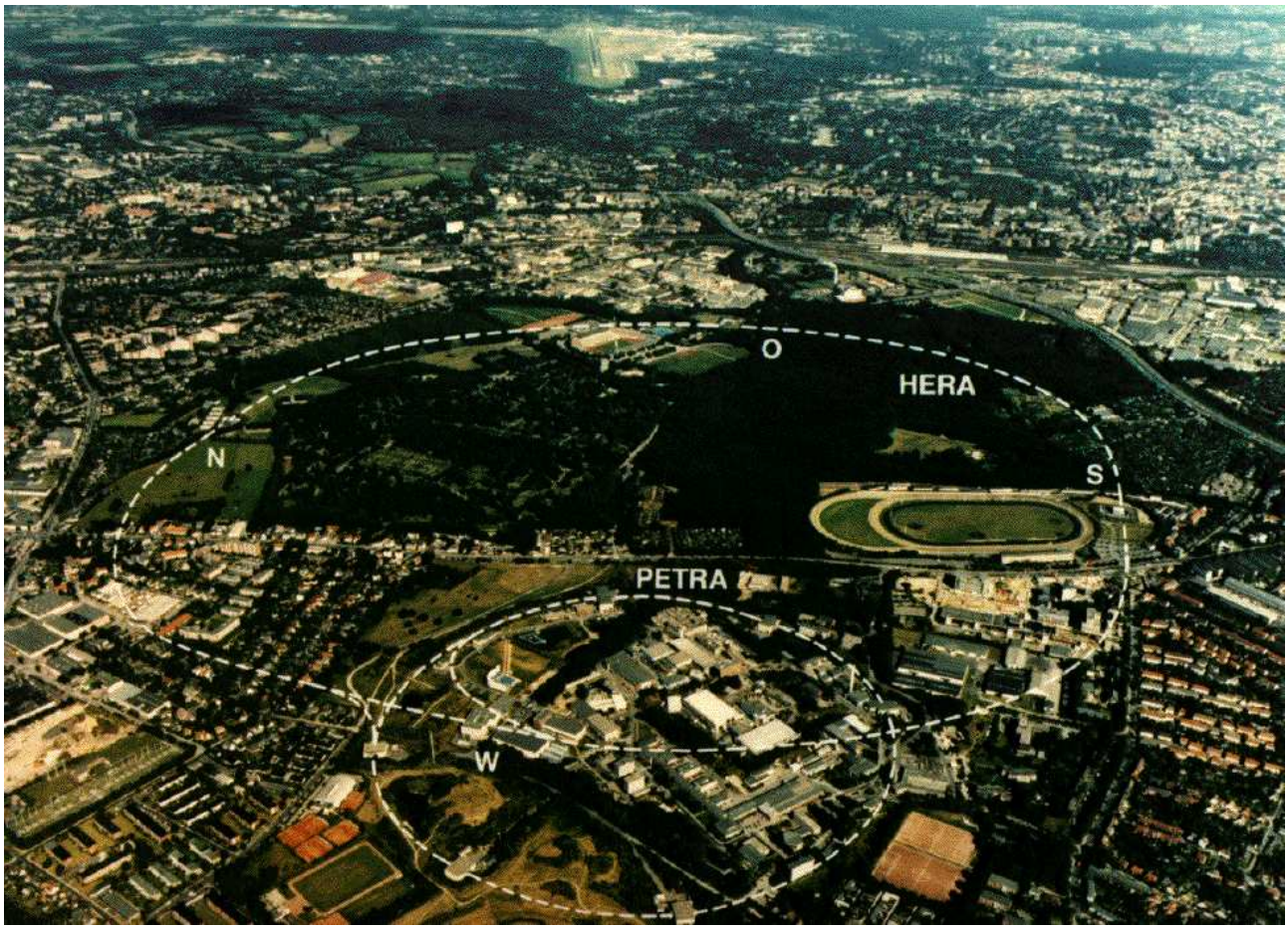


Figure 2.1: View of DESY.

The HERA (Hadron Elektron Ring Anlage) collider is located at DESY in Ham-

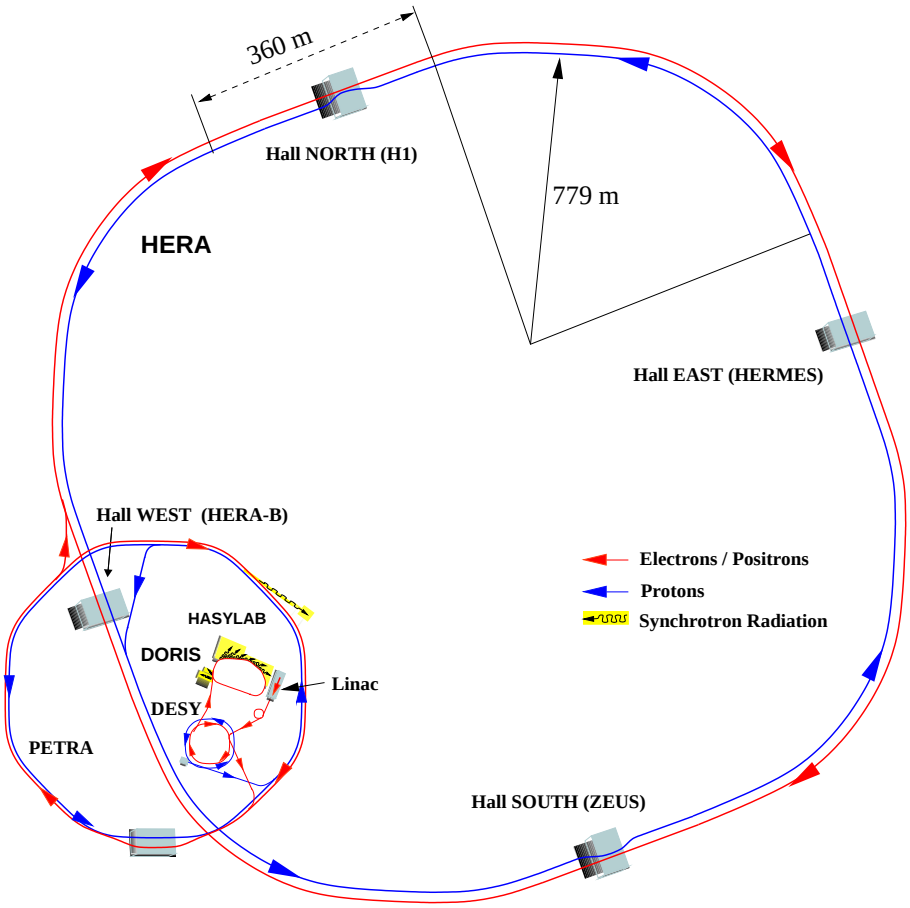


Figure 2.2: The HERA accelerator complex. Four experiments are located in the experimental halls : South (ZEUS), West (HERA-B), North (H1), and East (HERMES).

burg, Germany. It offers unique opportunities to explore the structure of the proton as it is the first *ep* collider in the world. Figure2.1 shows an aerial view of DESY and the surrounding area including the location of the two largest accelerators HERA and PETRA.

HERA was approved in 1984 and first collisions were observed in 1991. Operations for physics started in 1992 and ended in 2007. HERA consists of one storage ring for protons and one for electrons. The design energy is 30 GeV for electrons and 820 GeV for protons. Each storage ring consists of four 90° arcs connected by 360 m long straight sections and is located (10–25) m below ground. Superconducting magnets are used for the proton storage ring. Four experimental halls (North, South, East, West) are situated in the middle of the straight sections. The two collider experiments, H1 and ZEUS, are located in the northern and southern experimental halls, respectively. In both interaction regions electrons and protons collided head-on at zero crossing angle. Two fixed-target experiments, HERMES

and HERA-B, have been installed in the eastern and western experimental halls, respectively. They made use of only the HERA electron (HERMES) and proton (HERA-B) beams, respectively. HERMES [42] is investigating the spin structure of the nucleon and HERA-B [43] aimed to study the $\mathcal{CP}$-violation in the $B^0\overline{B^0}$-system. Figure 2.2 shows the layout of the HERA collider, the four experimental halls and the system of pre-accelerators used at DESY. In a first step, electrons and protons were accelerated using linear accelerators. A small storage ring PIA (Positron-Intensity-Accumulator) was used in between the linear accelerator and DESY II to accumulate electrons until sufficient intensity was reached. In a next step, the particles were injected into DESY II (electrons) and DESY III (protons). After injection into PETRA and further acceleration, electrons and protons were injected into HERA. From 1995 to 1997 positrons were used instead of electrons because severe lifetime problems of the electron beam were observed. The reason was most likely the capturing of positively-charged dust which originated from ion getter pumps from the HERA electron vacuum system by the electron beam [44]. With the installation of new pumps in the winter shutdown 1997/1998 the problem was significantly reduced and HERA switched back to electrons in 1998. Several HERA parameters from the 1997 runing period and the corresponding design values are given in Table 2.1. The data used in the analyses presented here were collected during the running period 1998-2000, when HERA operated with protons of energy $E_p = 920$ GeV and electrons or positrons of energy $E_e = 27.5$ GeV, and correspond to an integrated luminosity of $81.7 \pm 1.8$ pb$^{-1}$, of which 16.7 pb$^{-1}$ (65.0 pb$^{-1}$) was for $e^-p$ ($e^+p$) collisions.

## 2.2 The ZEUS Detector

The ZEUS detector [45] is a general purpose magnetic detector designed to study various aspects of electron-proton scattering. It has been in operation since 1992 until 2007 and consists of various sub-components to measure the hadrons and leptons in the final-state and, therefore, to characterize the final-state in terms of energy, direction, and type of the produced particles.

The coordinate system of the ZEUS detector is a Cartesian right-handed coordinate system. The origin ($(X, Y, Z) = (0, 0, 0)$) is located at the nominal interaction point. The Z-axis points in the proton beam direction, the Y-axis upwards, and the X-axis horizontally towards the center of HERA. The polar (azimuthal) angle $\theta$ ($\phi$) is determined relative to the positive Z-axis (X-axis). With this definition the polar angle of the incoming electron beam is 180° and that of the incoming proton beam is 0°. The +Z-direction is referred as the *forward*, and the –Z-direction as the

| HERA parameters | Design Values | | Values of 1997 | |
|---|---|---|---|---|
| | $e^{\pm}$ | p | $e^{+}$ | p |
| Circumference (m) | 6336 | | | |
| Energy (GeV) | 30 | 820 | 27.6 | 821.2 |
| Center-of-mass energy (GeV) | 314 | | 301 | |
| Injection energy (GeV) | 14 | 40 | 12 | 40 |
| Energy loss per turn (MeV) | 127 | $1.4 \cdot 10^{-10}$ | 127 | $1.4 \cdot 10^{-10}$ |
| Current (mA) | 58 | 160 | 36 | 78 |
| Magnetic field (T) | 0.165 | 4.65 | 0.165 | 4.65 |
| Number of bunches | 210 | 210 | 174+15 | 174+6 |
| Bunch crossing time (ns) | 96 | | | |
| Horizontal beam size (mm) | 0.301 | 0.276 | 0.200 | 0.200 |
| Vertical beam size (mm) | 0.067 | 0.087 | 0.054 | 0.054 |
| Longitudinal beam size (mm) | 0.8 | 11 | 0.8 | 11 |
| Specific luminosity ($cm^{-2}s^{-1}mA^{-2}$) | $3.6 \cdot 10^{29}$ | | $5.0 \cdot 10^{29}$ | |
| Instantaneous luminosity ($cm^{-2}s^{-1}$) | $1.6 \cdot 10^{31}$ | | $1.45 \cdot 10^{31}$ | |
| Integrated luminosity per year ($pb^{-1}/a$) | 35 | | 36.5 | |

Table 2.1: HERA parameters. In 1997 HERA operated with 174 colliding bunches, 15 positron-pilot bunches and 6 proton-pilot bunches.

*backward* direction.

The ZEUS detector consists of the main detector located around the nominal interaction point and several small detectors positioned along the beam line in both positive and negative Z-directions. The main detector is shown in Figs. 2.4 and 2.5 along and perpendicular to the beam direction, respectively. The design is asymmetric with respect to the Z-axis because of the large forward-backward asymmetry of the final-state system. The difference in the energy of the electron beam (27.5 GeV) and proton beam (920 GeV) results in a center-of-mass system which is moving in the direction of the proton beam relative to the laboratory frame.

The inner part of the main detector consists of the tracking system enclosed by a superconducting solenoid which produces an axial magnetic field of 1.43 T. The CTD, a cylindrical drift chamber, surrounds the beam pipe at the interaction point. In order to provide additional means of track reconstruction in the forward (backward) direction, the CTD was supplemented by the FTD (RTD). The FTD consists of three sets of planar drift chambers with transition radiation detectors (TRD) in between. The RTD is one planar drift chamber with three layers. The vertex detector VXD measures the event vertex and possibly secondary vertices and improves the momentum and angular resolution of charged particles as determined with the CTD alone. In 1994 high voltage problems and damage due to synchrotron

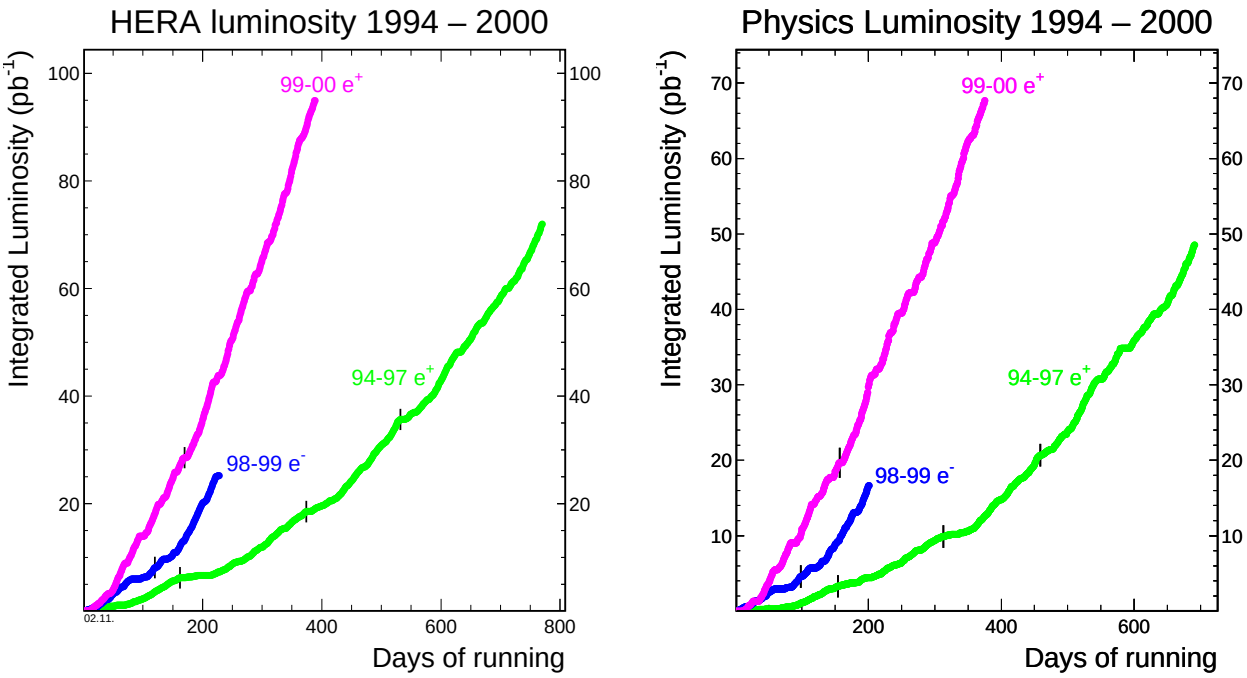


Figure 2.3: Integrated luminosity delivered by HERA in the different running periods (left plot) and the one taken with the ZEUS detector (right plot). The latter is used for physics analysis.

radiation caused part of the VXD to be off and it was removed.

The high resolution uranium calorimeter (UCAL) encloses the tracking detectors. It is subdivided into the forward (FCAL), barrel (BCAL), and rear (RCAL) parts.

The UCAL in turn is surrounded by an iron yoke made of 7.3 cm thick iron plates. The yoke serves two purposes: it provides a return path for the solenoid magnetic field flux and, in addition, is instrumented with proportional chambers. The latter design feature makes it possible to measure energy leakage out of the UCAL. The yoke is therefore referred to as the backing calorimeter (BAC). As the yoke is magnetized to 1.6 T by copper coils, it is used to deflect muons. In order to detect and measure the momentum of muons, limited streamer tubes are mounted surrounding the iron yoke in the barrel (BMUI, BMUO) and the rear (RMUI, RMUO) regions. As the particle density and the muon momentum in the forward direction is higher than in the barrel and rear directions due to the energy difference of the electron and proton beams, the muon chambers in the forward direction are designed differently. Limited streamer tubes mounted on the inside of the iron yoke (FMUI) and drift chambers and limited streamer tubes mounted outside the iron yoke (FMUO) are used for this purpose. Two iron toroids provide a toroidal magnetic field of 1.7 T. In the backward direction at $Z = -7.3\,\mathrm{m}$, a veto

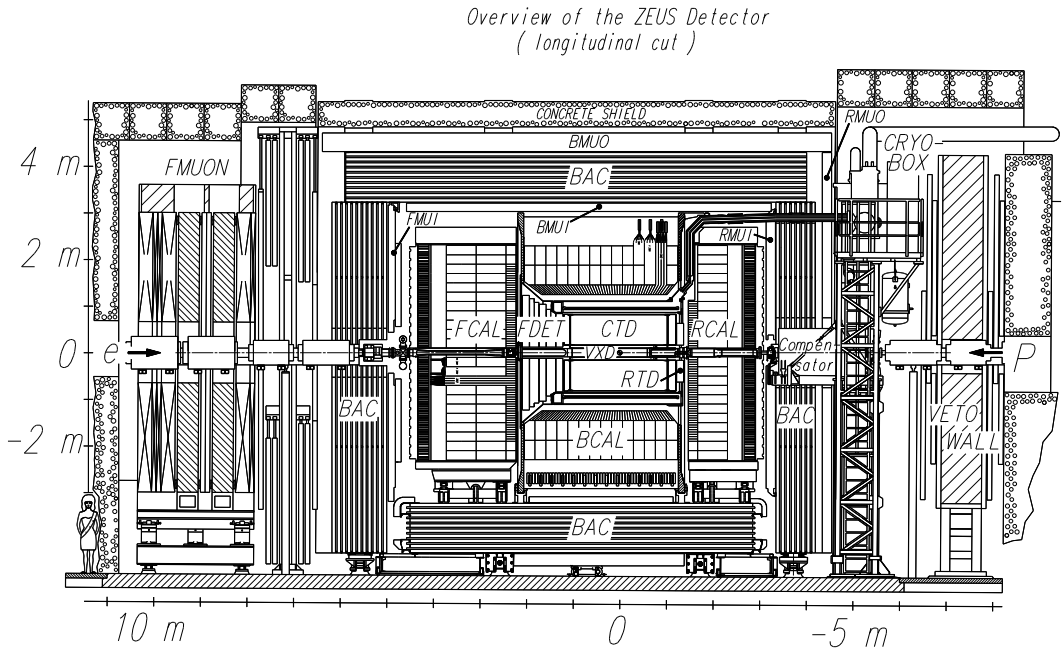


Figure 2.4: View of the ZEUS detector along the beam direction.

wall outside the detector composed of iron and scintillation counters is used to reject background events dominated by proton-beam-gas reactions.

### 2.2.1 The Central Tracking Detector

The tracking system of the ZEUS detector consists of the forward, central and rear tracking devices, which operate under a high magnetic field of 1.43 T to achieve a high resolution for high momentum tracks. All the tracking quantities used in this analysis are provided by the Central-Tracking Detector (CTD) [46]. The CTD is a cylindrical drift chamber which provides a high-precision measurement of the direction and transverse momentum of charged particles and of the event vertex. The position resolution in $r - \phi$ is about $230\,\mu$m and the transverse momentum resolution is

$$\frac{\sigma(p_t)}{p_t} = 0.0058 \cdot p_t(\mathrm{GeV}) \oplus 0.0065 \oplus \frac{0.0014}{p_t}\,, \tag{2.1}$$

where the first term corresponds to the resolution of the hit positions, the second term to smearing from multiple scattering within the CTD and the last term to multiple scattering before the CTD. The position of the interaction point in $X$ and $Y$ is measured with a resolution of 0.1 cm and in $Z$ with a resolution of 0.4 cm.

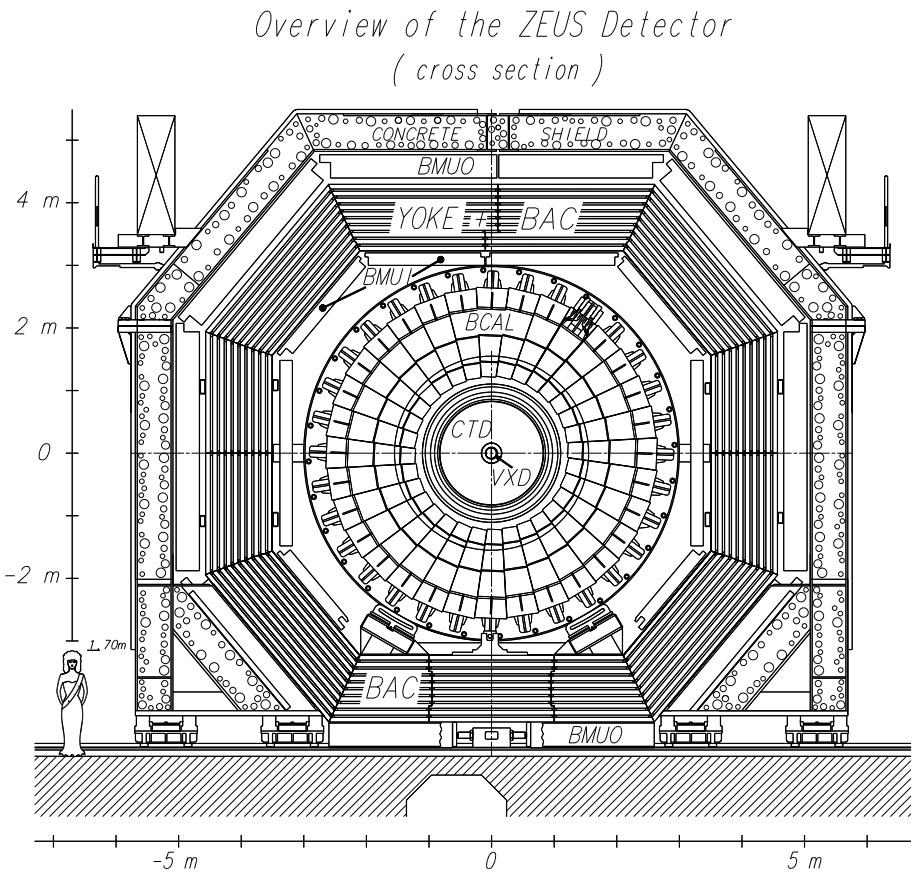


Figure 2.5: View of the ZEUS detector perpendicular to the beam direction. See text for a description of the components.

The CTD is filled with a mixture of argon, $CO_2$ and ethane. Particle identification is possible by measurements of the mean energy loss dE/dx of charged particles within the tracking detector. The CTD covers a polar angle of $15° < \theta < 164°$ and the full range of the azimuthal angle $\phi$. Its active volume has a length of 205 cm, an inner radius of 18.2 cm, and an outer radius of 79.4 cm.

The CTD is designed as a multi-cell superlayer chamber and subdivided into eight sections and nine superlayers. One octant is shown in Fig. 2.6. The CTD consists of 576 cells with each cell being equipped with eight sense wires. The number of cells increases from 32 in the innermost superlayer to 96 cells for the outermost superlayer. Every other superlayer has its sense wires rotated by a certain angle with respect to the beam axis. The angles for each superlayer are given in Fig. 2.6. With this configuration, the $Z$ position of a track can be reconstructed with an accuracy of aproximately 2 mm.

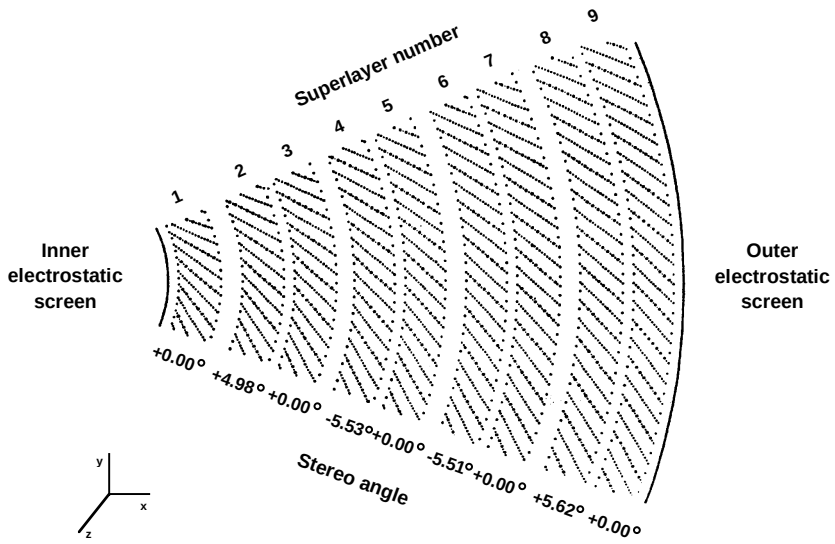


Figure 2.6: Layout of a CTD octant. Each octant has nine superlayers with the even numbered ones declined with respect to the beam axis ('Stereo angle').

### 2.2.2 The Uranium-Scintillator Calorimeter (UCAL)

Calorimeters in particle physics measure the energy of particles by their absorption in a medium that becomes ionized or excited through shower processes. The ZEUS calorimeter (UCAL) has been designed as a sampling calorimeter, where absorber layers alternate with scintillator layers, which are the optical readout. The calorimeter is required to be hermetic with a nearly full solid-angle coverage and to have a good hadronic energy resolution by achieving an equal response to electromagnetic and hadronic particles.

The UCAL is divided into three parts, which cover different polar angles [47–49]. All parts of the calorimeter, FCAL ($2.2° < \theta < 39.9°$), BCAL ($36.7° < \theta < 128.1°$), and RCAL ($128.1° < \theta < 176.5°$) are built of alternating layers of 3.3 mm thick depleted uranium and 2.6 mm thick plastic scintillator plates (SCSN38). The natural radioactivity of $^{238}$U is used as a reference signal to calibrate the readout channels to a precision of $< 0.2\%$.

Uranium is an advantageous absorber for hadron calorimetry, since it provides a high yield of spallation neutrons which impart the energy to the hydrogen nuclei of the scintillator. Together with an additional contribution of photons from neutron capture of the uranium, this helps to compensate the signal loss of hadrons arising from the loss of binding energy, nuclear fission fragments and from undetected decay products. Electrons and photons do not suffer such losses as they interact predominantly with the atomic electrons and not with the nuclei. The ratio between the

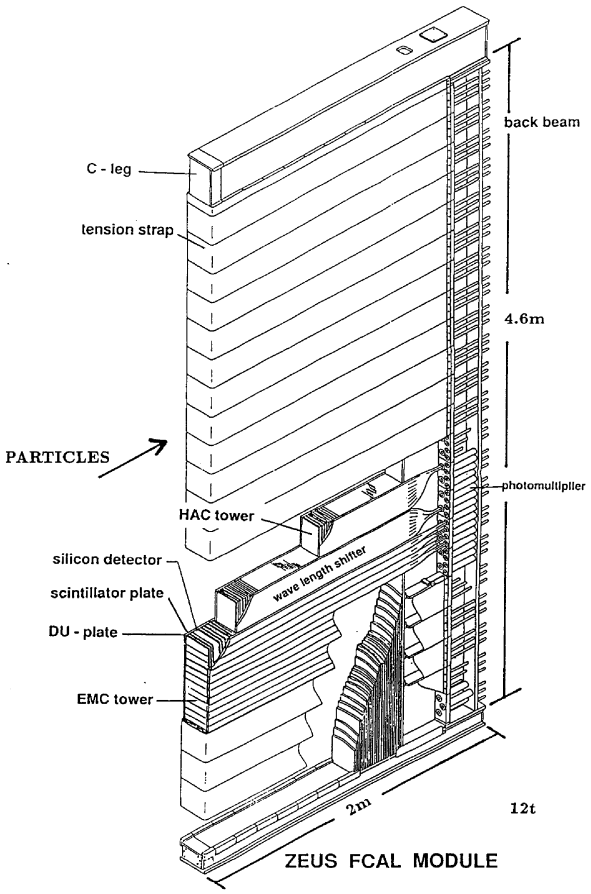


Figure 2.7: Layout of a FCAL module. The UCAL modules are subdivided into one electromagnetic (EMC) and two hadronic (HAC1,HAC2) sections, which in turn are divided into cells. A cell is read out on two opposite sides by one wavelength shifter each.

pulse heights of electrons and hadrons, $e/h$, which has been achieved is

$$e/h \;=\; 1.00 \;\pm 0.03 \tag{2.2}$$

The three calorimeter parts are subdivided into modules. The modules are transversally separated into towers, and the towers in turn longitudinally into electromagnetic (EMC) and hadronic sections (HAC). The design of an FCAL module is shown in Fig. 2.7. The FCAL and RCAL modules are planar and perpendicular with respect to the beam axis (see Fig. 2.4), while the BCAL modules are wedge-shaped and projective in the polar angle. The calorimeter modules are further segmented into cells. The cell dimensions are 20cm×20cm for hadronic cells and 5cm×20cm (10cm×20cm) for electromagnetic cells in the FCAL and BCAL (RCAL). The design of the three calorimeter parts takes into account the different particle densities and energies due to the asymmetric electron and proton beam energies. Each EMC section is segmented transversally into four cells (two in RCAL), while a HAC tower is

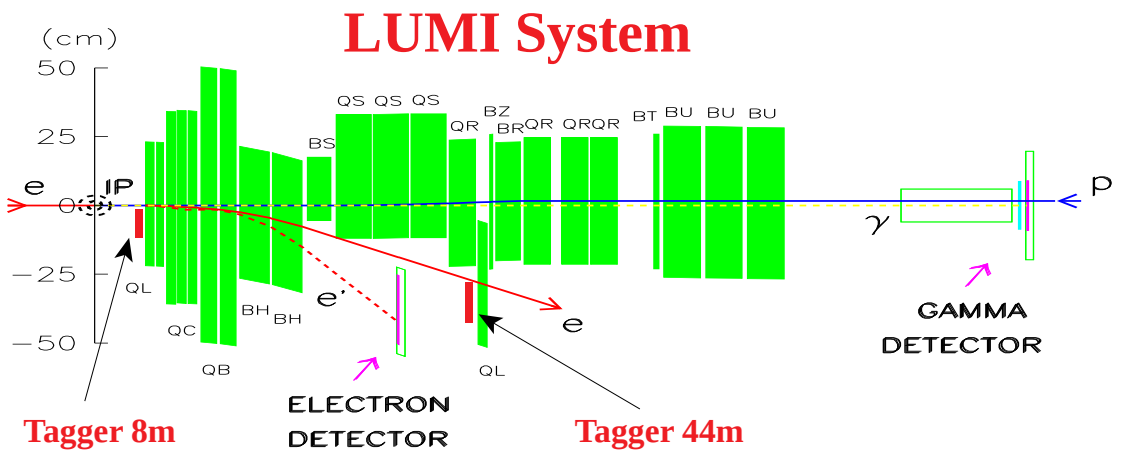


Figure 2.8: Location of ZEUS detectors in negative Z-direction. Shown are the gamma (LUMIG) and electron detectors (LUMIE) used for the luminosity measurement.

not divided transversally. They are instead longitudinally subdivided into two (one in RCAL) hadronic cells (HAC1, HAC2). Each cell is read out on two opposite sides. This is done on each side by a wavelength shifter coupled to one photomultiplier tube. The information of both photomultiplier tubes is used to provide a limited reconstruction of the position of the measured particle and to check the uniformity of the readout.

The single particle energy resolution for electrons and hadrons was determined in test-beam experiments to be $\sigma_E/E = 0.18/\sqrt{E}$ and $\sigma_E/E = 0.35/\sqrt{E}$ respectively, where $E$ is mesured in GeV.

## 2.3 The luminosity measurement

The luminosity, $\mathcal{L} \equiv N/\sigma$, relates the number of events $N$ with the cross section $\sigma$. A precise determination of the luminosity is essential for any cross section measurement in a high-energy physics experiment. The luminosity of $ep$-collisions at HERA is measured by observing the rate of hard bremsstrahlung photons from the Bethe-Heitler process $ep \to e\gamma p$ [50]. As the theoretical cross section is known to an accuracy of 0.5% from QED calculations, a precise measurement of the photon rate permits a precise determination of the $ep$-luminosity at HERA.

Figure 2.8 shows the layout of the HERA magnet system and the ZEUS luminosity detectors in the backward (–Z)-direction. In the case of ZEUS, this is done by two lead/scintillator electromagnetic calorimeters at Z = −34 m (LUMIE) and Z = −107 m (LUMIG). Photons with $\theta_\gamma < 0.5$ mrad originating from the Bethe-

Heitler process $ep \to e\gamma p$ are detected by the LUMIG detector [51, 52]. The energy resolution of the LUMIG detector was measured under test-beam conditions to be $18\%/\sqrt{E}$. It was also determined that the carbon/lead filter placed in front of the detector to shield it against synchrotron radiation degrades the resolution to $23\%/\sqrt{E}$. The impact position of incoming photons can be determined with a resolution of 0.2 cm in $X$ and $Y$, because at a depth of $7X_0$ 1 cm wide scintillator strips are installed within the LUMIG detector. The LUMIG detector is also used to determine the electron-beam tilt and to measure photons from initial-state radiation.

The LUMIE calorimeter [51, 52] at Z = −35 m detects electrons in the limited energy range from 7 to 20 GeV which are produced under polar angles of less than 5 mrad with respect to the electron-beam direction. These electrons are deflected by the HERA magnet system and leave the beam pipe at Z = −27 m through an exit window similar to the one in front of the LUMIG detector. The LUMIE detector has an energy resolution of $18\%/\sqrt{E}$ under test-beam conditions. It was initially designed to measure the electrons of the Bethe-Heitler process $ep \to e\gamma p$ at the same time as the photons of this process are measured in the LUMIG detector. It was found that this was not necessary to have a precise measurement of the luminosity.

## 2.4 The ZEUS trigger and data acquisition systems

The short bunch crossing time at HERA of 96 ns, equivalent to a rate of about $10^7$ crossings per second, is a technical challenge and puts stringent requirements on the ZEUS trigger and data acquisition systems. The total interaction rate, which is dominated by background from upstream interactions of the proton beam with residual gas in the beampipe, is of the order 10 - 100 kilo-events per second (10 - 100 kHz) while the rate of $ep$ physics events in the ZEUS detector is of the order of a few Hz [53, 54]. Other background sources are electron-beam gas collisions, beam halo and cosmic events.

ZEUS employs a sophisticated three-level trigger system in order to select $ep$ physics events efficiently while reducing the rate to a few Hz. A schematic diagram of the ZEUS trigger system is shown in Fig. 2.9.

The First Level trigger (FLT) is a hardware trigger, designed to reduce the input rate below 1 kHz. Each detector component has its own FLT, which stores the data in a pipeline, and makes a trigger decision within 2 $\mu$s after the bunch crossing. The decision from the local FLTs are passed to the Global First Level Trigger (GFLT), which decides whether to accept or reject the event, and returns this decision readout within 4.4 $\mu$s. The typical information available at FLT are CAL activity (total transverse energy, missing transverse momentum,...), CTD tracks

(number of tracks,...), hits in the muon chambers, etc.

If the event is accepted, the data is fully digitalized and transferred to the Second Level Trigger (SLT). The trigger signals at the SLT have a better resolution than those at the FLT. Moreover, some information is first available at the SLT like CAL timings, which are useful in rejecting non-*ep* background events. The SLT is designed to reduce the rates to the order of 50-100Hz. Each detector component has its own SLT, which passes a trigger decision to the Global Second trigger (GSLT) [55].

If the event is accepted by the GSLT, all detector components send their data to the Event Builder (EVB), which combines all the data of an event into a single record of ADAMO [56] database tables. This is the data structure on which the Third Level Trigger (TLT) code runs. The TLT is software based and runs part of the offline reconstruction code. It is designed to reduce the rate to a few Hz.

## 2.5 Event reconstruction and analysis

The scheme of the ZEUS offline and Monte Carlo (MC) simulation programs is shown in Fig. 2.10. Events from the real detector or simulated events are reconstructed by the program ZEPHYR, where the signals of the different components are calibrated and highly complex tasks, like tracking reconstruction, are performed. After processing the raw data, the user has access to the raw and reconstructed quantities via the program EAZE. In the framework of EAZE, the user writes his own analysis program in either Fortran or C. It is used to reconstruct relevant quantities and perform selection cuts. Subsets of the data or MC simulated events can be saved for further analysis. The program LAZE is an event-display program which allows graphical viewing of various aspects of an event including the tracks of charged particles in the CTD, energy depositions in the CAL, and other component-related quantities. To allow fast access to specific types of events during reconstruction, it is checked whether each event meets one of the conditions designed by the ZEUS analysis groups. If a specific condition is met, a flag called a DSTBIT is set. Before analyzing detailed component information in the user's EAZE program, the events can be preselected by requiring certain DSTBITS. This allows a faster loop over the whole data sets since only those events are processed further.

Simulated MC events are generated using the program AMADEUS (named ZDIS in previous versions) which contains a shell environment to steer a number of MC generator programs. The output data is stored in the same (ADAMO) format as the data from the real detector and passed to the ZEUS detector simulation program MOZART, based on the CERN GEANT program [57]. A simulation of the ZEUS trigger chain is done by the program ZGANA. Interfaces between the programs

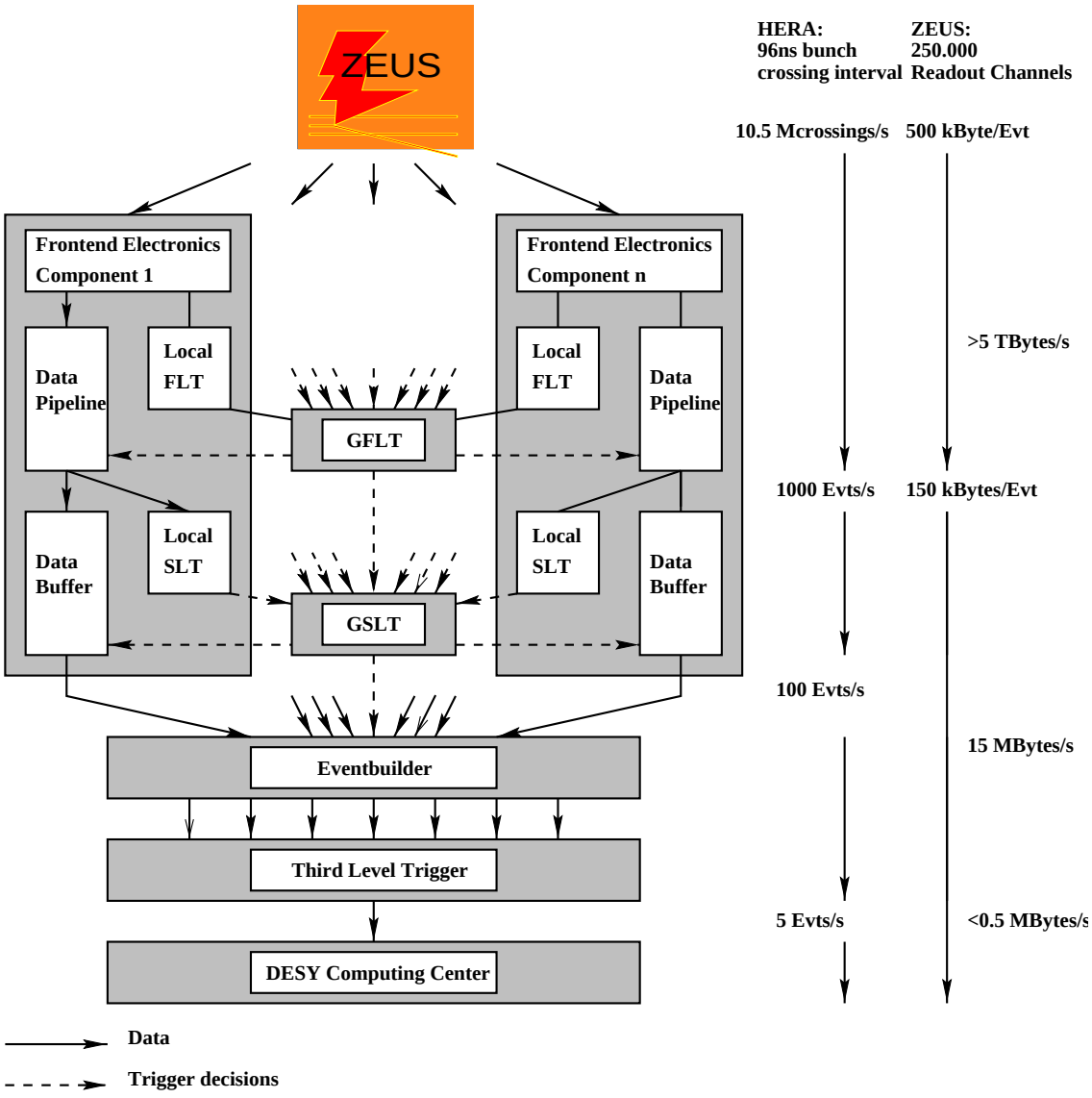


Figure 2.9: Schematic diagram of the ZEUS trigger and data acquisition systems.

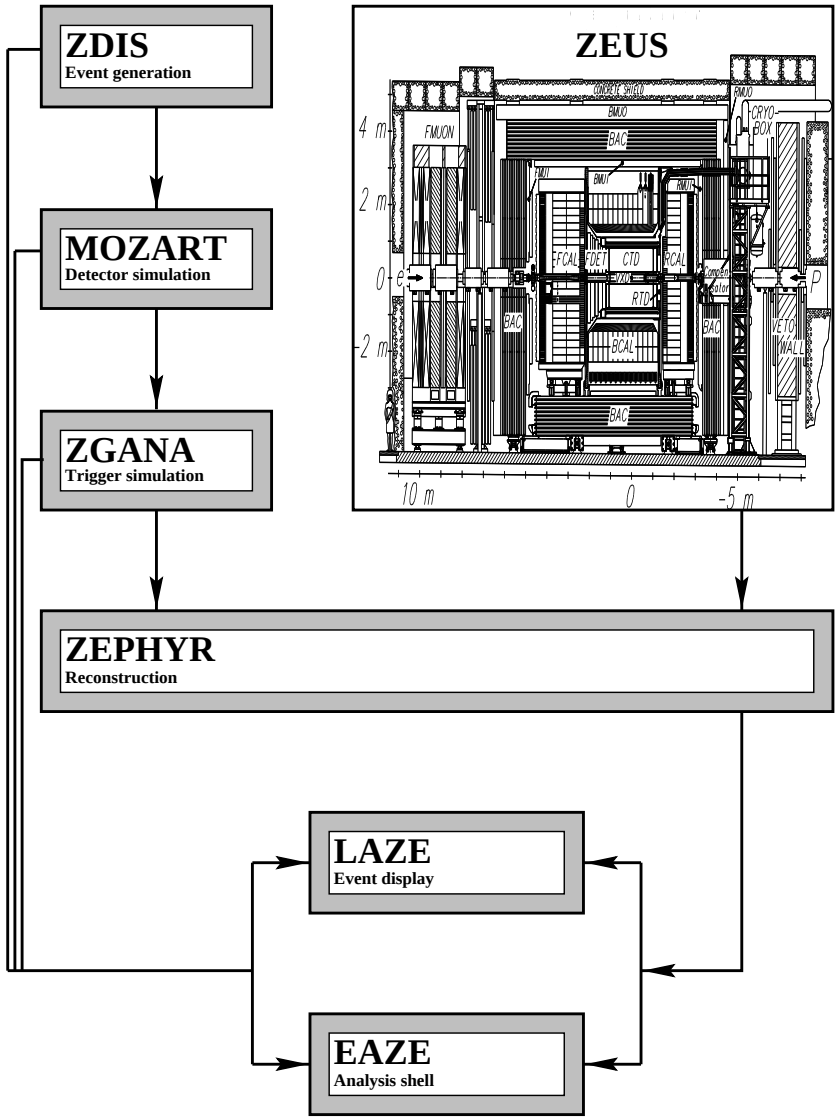


Figure 2.10: Interrelationship of the ZEUS offline and Monte Carlo (MC) simulation programs.

used for MC generation and the programs EAZE and LAZE provide specific MC information such as generated kinematic quantities, vertices and particles to the user. An overview of the physics analysis environment of the ZEUS experiment can be found in [58].

## 2.6 Event and detector simulation

In order to correct the data for trigger and detector effects, a full Monte Carlo simulation is required. This can be split in two pieces. First, an event generator, which calculates the scattering processes at hadron level from given matrix elements. Using hadronisation models, the final-state particles are obtained as a list of 4-vectors. This is what we mean by *generator-level*. In the second step, these particles are passed to a full simulation of the trigger and detector, yielding output in the form of ADAMO tables, which can be treated in the same way as the data. This is called *detector-level*.

Events from the event generator are processed by the MOZART package. This is a GEANT-based program which simulates the response of each detector component, based on the current knowledge of the ZEUS detector from both physics studies and test-beam results. Each particle interaction with dead material and detector component is simulated, including effects of digitization of the signals and known sources of noise. The ZGANA package simulates the trigger response to the event, based on the component signals, and them ZEus PHYsics Reconstruction (ZEPHYR) package performs the full offline reconstruction using all calibration constants. The Monte Carlo events simulated are then written in an identical format as the data taken with the ZEUS detector.

# Chapter 3

# Theoretical calculations and event generators

## 3.1 Introduction

Complete perturbative calculations for jet cross-sections in $ep$ scattering are available in most cases only to next-to-leading (NLO). The amount of work associated to making these calculations increases factorially with each order. The calculations available are coded into computer programs that allow users to obtain theoretical predictions in a straightforward way. DISENT [59] is one of such programs and has been used extensively to calculate inclusive and three-jet cross-sections at $O(\alpha_s^2)$ for the analyses presented here. Certain parameters, such as the renormalization and factorization scales ($\mu_R$ and $\mu_F$) or the proton PDFs are not given by the theory. The influence of these choices on the theoretical predictions is related to the theoretical uncertainties as discussed in this chapter. Recently calculations at $O(\alpha_s^3)$ for three-jet production have become available through the program NLOJET++ [60]. This program has been used to study the $O(\alpha_s^3)$ contribution to the three-jet angular-correlation predictions. At $O(\alpha_s^2)$ it has been used to cross-check DISENT.

We saw in Chapter 1 that a suitable definition of a jet connects the hadronic energy distributions measured in detectors with the partons that are the final states of perturbative QCD calculations. Despite the validity of this approach it is important to study the effect of the hadronization process on the jet production predictions in order to obtain a more accurate comparison between the theory and the data. This is accomplished by first complementing the fixed-order calculations with enhanced regions from higher-orders, leading to a 'parton cascade' picture. As we will discuss later, there are two available parton cascade models, the Color Dipole Model [61] and the Parton Shower Model [62]. The parton shower is calculated up to a soft scale. After the parton shower is completed the hadronization of the partons must

be simulated. The hadronization does not change the overall properties of the event such as the jet energy or angular distributions, since it is a process that happens at a soft energy scale of $\sim 300$ MeV. The Lund String Model [63] and the Cluster Model [64] are two available hadronization models. The programs that simulate the fixed-order calculations along with the parton shower and the subsequent hadronisation are called 'Monte Carlo event generators' and play an important role in particle physics and in particular in the analyses presented here.

It is also necessary to understand the detector with which the measurements were made in order to know their precision and to determine any bias introduced by the detecting device. A simulation of the detector has been developed for this purpose and is interfaced with the event generators. The output of the simulation can be submitted to the data triggering chain and reconstructed in the same way as the data. This tool allows the experimentalist to study the reconstruction of any observable by feeding a known generated distribution to the detector simulation and studying its outcome.

## 3.2 Theoretical predictions in pQCD

As outlined in Chapter 1, the basic equation to be solved is eq. 1.22, the convolution of the matrix elements at some fixed order with the experimentally determined proton PDFs. The integrals in eq. 1.22 are not solved exactly by computer programs, but approximated by the normalized sum of N randomly generated 'events' in the phase space:

$$\sigma \sim \frac{1}{N} \sum_{event}^{N} \sum_{j\ parton\ i} f_i(\xi_j, \mu_F = Q_j^2) \cdot \hat{\sigma}(\xi_j, Q_j^2, \alpha_s(\mu_R = Q_j^2), \mu_R = Q_j^2, \mu_F = Q_j^2) \tag{3.1}$$

In the limit where $N \to \infty$, the sum approximates the exact solution. In practice, the number of events generated (N), is determined by how well the particular computer program converges to the final answer. In the program DISENT, for example, $10^8$ events were enough to make the statistical fluctuations negligible. In NLOJET++, on the other hand, it was necessary to generate $\sim 10^9$ events to get a comparable statistical uncertainty.

The $k_T$ clustering algorithm can be applied to any set of four-momenta. In particular, it has been applied to the partonic final states of each 'event' during an 'inclusive cross-section' calculation in order to simultaneously obtain differential three or inclusive-jet cross-section predictions in terms of the kinematic or jet variables.

In perturbative QCD there are several elements of the calculations which are

not set by the theory and must be provided by the user. The proton PDFs, or the value of $\alpha_s(M_Z)$ are examples of experimentally determined ingredients to the calculations. The renormalization and factorization scales are also not set by the theory and must be chosen by the user to make the calculations possible. Here is a list of choices made for the theoretical calculations:

- The calculations are performed in the $\overline{\text{MS}}$ renormalization and factorization schemes using a generalized version [59] of the subtraction method [65];
- The number of flavours is set equal to five;
- The choice of factorization scale was chosen to be $\mu_F = Q$;
- For the choice of renormalization scale calculations with different choices were made; For the $\alpha_s$ analysis the default was $\mu_R = E^{jet}_{T,B}$, but cross checks were made with $\mu_R = Q$, the default choice for the angular-correlations analysis;
- The ZEUS-S [24] parametrizations of the proton PDFs were used as default;
- The strong-coupling constant, calculated at two loops, was set always equal to that of the proton PDFs; In the default case it was the same one used for the ZEUS-S parametrizations, $\Lambda_{\overline{\text{MS}}} = 226$ MeV, corresponding to $\alpha_s(M_Z) = 0.118$.

**The jet observables**

The observables calculated for the $\alpha_s$ analysis were inclusive-jet cross sections in terms of $E^{\text{jet}}_{T,\text{B}}$ and $Q^2$ with the jet radius choices of R=0.5, 0.7 and 1. For the angular-correlations analysis, the observables calculated were three-jet cross sections in terms of $\Theta_H$, $\cos\alpha_{23}$, $\cos\beta_{ksw}$, and $\eta^{jet}_{max}$, normalized to the total three-jet cross section. The cross-sections were in both analyses calculated for the $Q^2 > 125$ GeV$^2$ region, with all jets having an $-2 < \eta^{\text{jet}}_{\text{B}} < 1.5$ and all events being in the $|\cos\gamma_h| < 0.65$ region. Only jets with $E^{\text{jet}}_{T,\text{B}} > 8$ GeV were considered for the inclusive-jet cross sections. For the angular-correlations analysis only those events having at least three jets with at least one of the jets having $E^{\text{jet}}_{T,\text{B}} > 8$ GeV and the other two $E^{\text{jet}}_{T,\text{B}} > 5$ GeV were considered for the cross section calculations.

## 3.3 Sources of theoretical uncertainty in the cross-section predictions

The previous section outlined the different inputs that the user must provide in order to obtain pQCD predictions. The scales $\mu_R$ and $\mu_F$ are 'arbitrary' paramaters

that are not given by the theory and need to be especified in a calculation. The dependence of an observable on $\mu_R$ and $\mu_F$ can be used to estimate the uncertainty in its prediction incurred by truncating the perturbative series at fixed order. Naturally, the experimentally determined value of $\alpha_s(M_Z)$ and the proton PDFs introduce an experimental uncertainty which propagates and also constitutes part of the uncertainty in the theoretical predictions.

**Theoretical uncertainty from that due to higher-order contributions**

As mentioned, the theoretical calculations are not carried out to all orders in perturbative QCD. If $\mu_R$ is chosen as the characteristic scale for the process, then one expects that by constraining the calculations to higher scales the convergence of the perturbative expansion will be improved. Recall the renormalization group equation:

$$\frac{d\sigma}{d\mu_R} = \frac{d}{d\mu_R}[\sum_{N=0}^{\infty} \alpha_s(\mu_R)^N \cdot \hat{\sigma}_N(x, Q^2, \mu_R)] = 0 \tag{3.2}$$

Since the scale-dependence of $\alpha_s$ converges to a given curve at higher orders, the factors that multiply $\alpha_s^N$ must compensate for $\alpha_s(\mu_R)$ in order to make eq. 3.2 true. This cancellation does not happen term by term, but rather the dependence of the $\mathrm{N}^{\mathrm{th}}$ term on $\mu_R$ is partially compensated by the $\mu_R$-dependence of the $(\mathrm{N}+1)^{\mathrm{th}}$ term. At fixed order, however, the $\mu_R$-dependence of the predicted cross-section is used to gauge the error margin incurred by having truncated the series. It is conventional to vary $\mu_R$ by a factor of two up and down for this purpose. The resulting variation in the prediction is taken as the uncertainty resulting from the lack of knowledge of higher-order contributions. It should be noted that this is merely a convention, and cannot be taken full-heartedly as the true error incurred by having truncated the series at fixed order.

This uncertainty is minimized by restricting the calculations to high energy scales, where the relatively weaker strength of $\alpha_s$ improves the convergence of the perturbative series. This is one of the main reasons we found $d\sigma/dE_{T,B}^{jet}$ and $d\sigma/dQ^2$ at high $E_{T,B}^{jet}$ and high $Q^2$ to be good jet observables for tests of pQCD. Figs. 3.1 and 3.2 show an estimate of the relative theoretical uncertainty for the predictions of $d\sigma/dQ^2$ and $d\sigma/dE_{T,B}^{jet}$ coming from varying $\mu_R$ from $\mu_R = E_{T,B}^{jet}/2$ to $\mu_R = 2E_{T,B}^{jet}$. The $\mu_R$ related uncertainty is below $\pm 7\%$ at low $Q^2$ and aslo at low $E_{T,B}^{jet}$ and decreases to less than $\pm 5\%$ for $Q^2 > 250$ GeV$^2$ for $R = 1$. For smaller radii, the estimated uncertainty is smaller(higher) at low(high) $Q^2$ than for $R = 1$. For $R = 1.2$, Fig. 3.1 shows how this uncertainty increases up $\pm 10\%$ for $Q^2 \sim 500$ GeV$^2$.

Fig. 3.3 shows the relative $\mu_R$-scale uncertainty for the inclusive-jet differential cross sections with respect to $E_{T,B}^{jet}$ for different regions of $Q^2$. It is below $\pm 7\%$ at

low $Q^2$ and low $E_{T,B}^{jet}$ and decreases to about $\pm 5\%$ in the highest $Q^2$ region.

For the three-jet angular correlations analysis we are interested only in the shapes of the distributions, therefore the normalized cross sections are used. Normalized cross sections have the advantage that the correlated uncertainties in the numerator and denominator partially cancel out. Fig. 3.4 shows the relative $\mu_R$-scale uncertainty for the normalized cross sections with respect to $\Theta_H$, $\cos\alpha_{23}$, $\cos\beta_{ksw}$, and $\eta_{max}^{jet}$. The uncertainties are typically below 5%. In the lower $\cos\alpha_{23}$ region, the uncertainty is large, signaling that there could be large contributions from higher orders there.

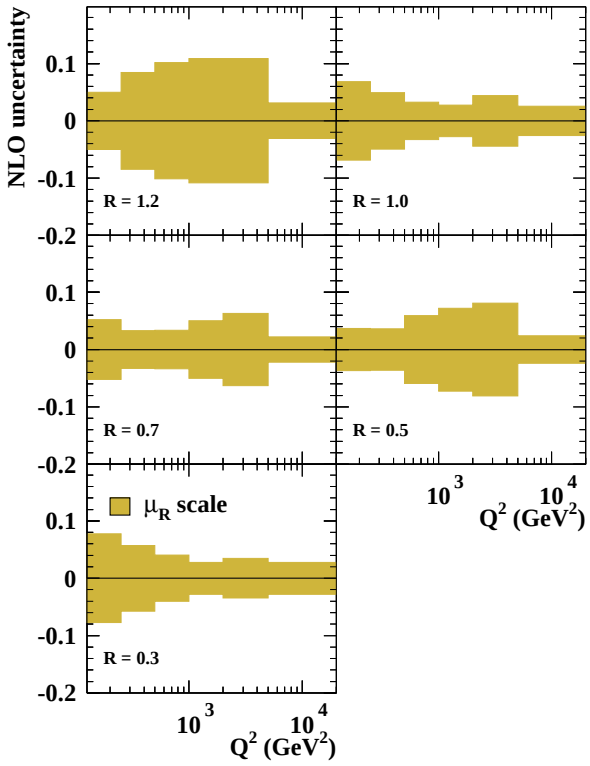


Figure 3.1: Estimate of the relative theoretical uncertainty in $d\sigma/dQ^2$ from terms beyond $O(\alpha_s^2)$. The uncertainty is shown for different choices of the jet-radius. The uncertainty gets large for $R > 1$.

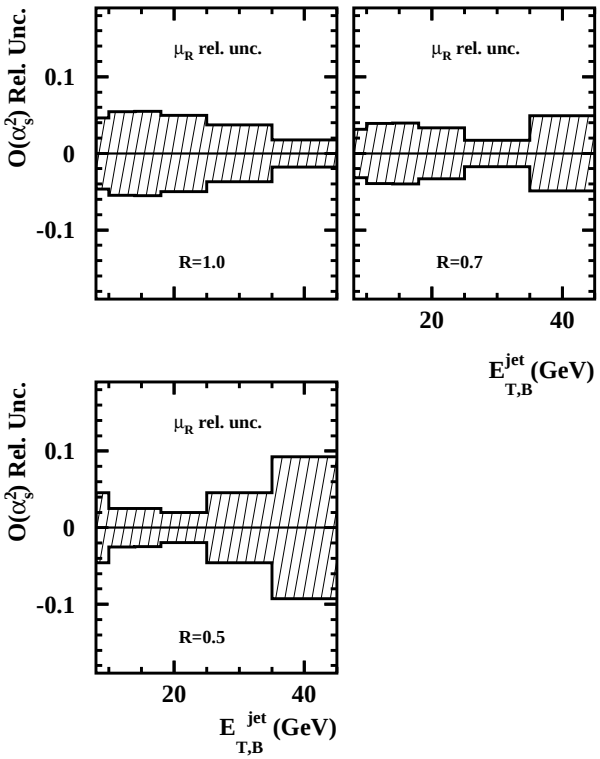


Figure 3.2: Estimate of the relative theoretical uncertainty in $d\sigma/dE^{jet}_{T,B}$ from terms beyond $O(\alpha_s^2)$.

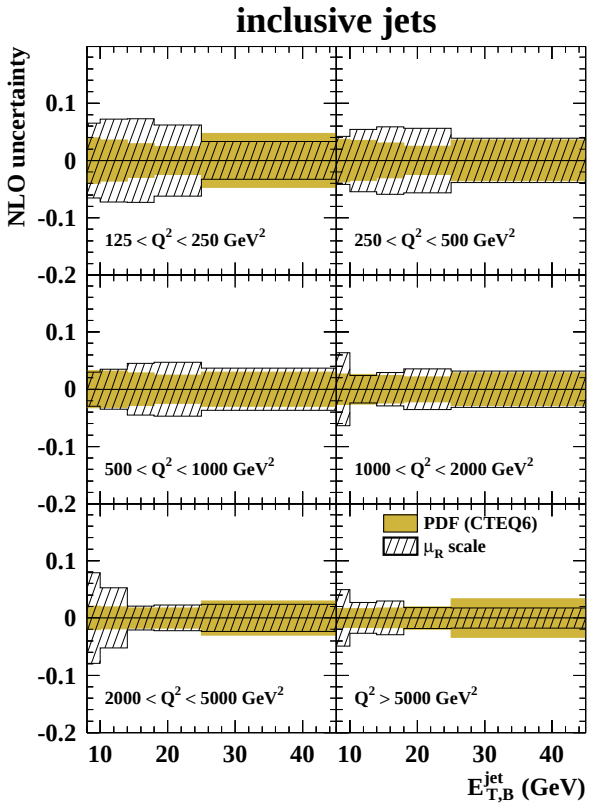


Figure 3.3: Estimate of the relative theoretical uncertainty in $d\sigma/dE^{jet}_{T,B}$ for different regions of $Q^2$ from terms beyond $O(\alpha_s^2)$. The $\mu_R$-scale uncertainty is compared to the uncertainty coming from that in the proton PDFs. In some regions the uncertainty from the proton PDFs dominates the overall uncertainty. This signals that these measurements can help constrain the PDFs when included in global QCD fits. These calculations are for R=1.

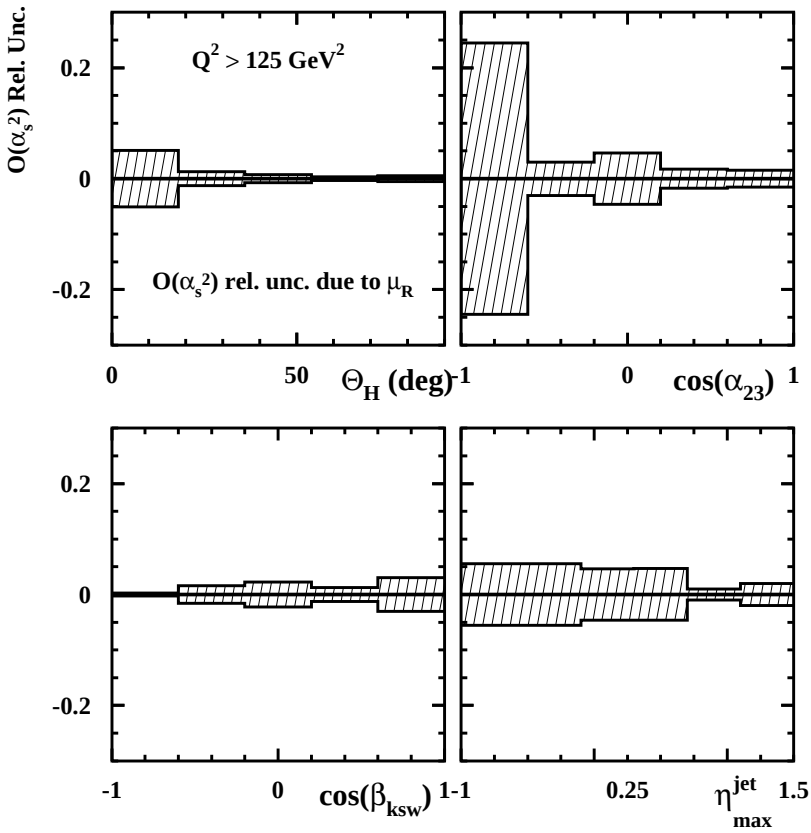


Figure 3.4: Estimate of the relative theoretical uncertainty in the three-jet normalized differential cross sections with respect to $\Theta_H$, $\cos\alpha_{23}$, $\cos\beta_{ksw}$, and $\eta^{jet}_{max}$ from terms beyond $O(\alpha_s^3)$. Note that in the low $\cos\alpha_{23}$ region the uncertainty is relatively large.

**Theoretical uncertainty from that of $\alpha_s(M_Z)$**

The value of $\alpha_s(M_Z)$ is not given by the theory and has to be determined experimentally. The world average for this value is currently determined with an uncertainty of $\sim 1\%$ [66]. In order to estimate the uncertainty in the predictions due to that in the value of $\alpha_s(M_Z)$, the calculations were repeated for different $\alpha_s(M_Z)$ values. The proton PDF parametrizations made with the corresponding $\alpha_s(M_Z)$ variants were used.

For the default ZEUS-S case $\alpha_s(M_Z) = 0.119$ and the calculations were repeated using ZEUS-S$\uparrow\uparrow$ with $\alpha_s(M_Z) = 0.121$ and ZEUS-S$\downarrow\downarrow$ with $\alpha_s(M_Z) = 0.117$. The relative difference between the 'up' and 'down' calculations was taken as the uncertainty from that in $\alpha_s$. The relative difference was then scaled to reflect the current uncertainty in the world average of $\alpha_s(M_Z)$ ($\pm 0.0010$). Fig 3.5 and Fig. 3.6 show the relative uncertainties for $d\sigma/dQ^2$ and $d\sigma/dE^{jet}_{T,B}$, which in all cases were below 2%. Fig 3.7 shows the relative uncertainties for the angular-correlation variables. In this case they are almost an order of magnitude smaller than for the inclusive-jet analysis, since the correlated uncertainties partially cancel out in the normalized cross section.

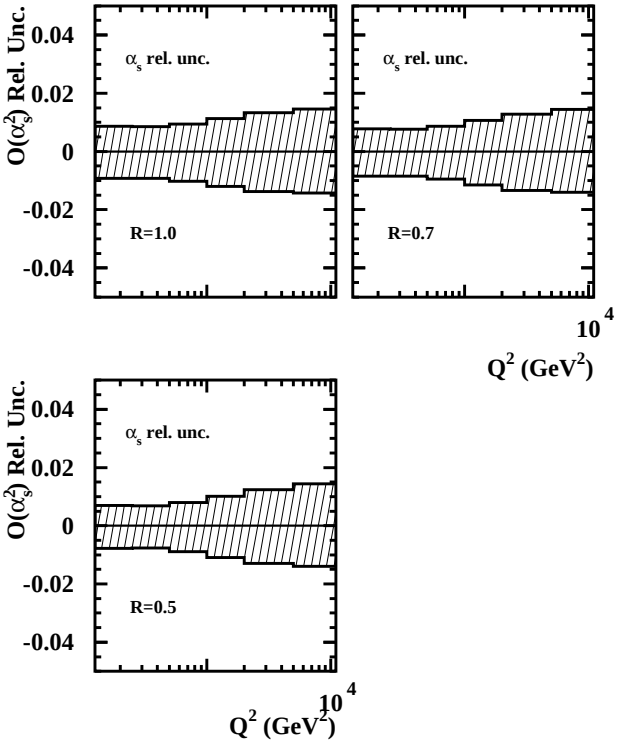


Figure 3.5: Estimate of the relative theoretical uncertainty in $d\sigma/dQ^2$ from that in $\alpha_s(M_Z)$.

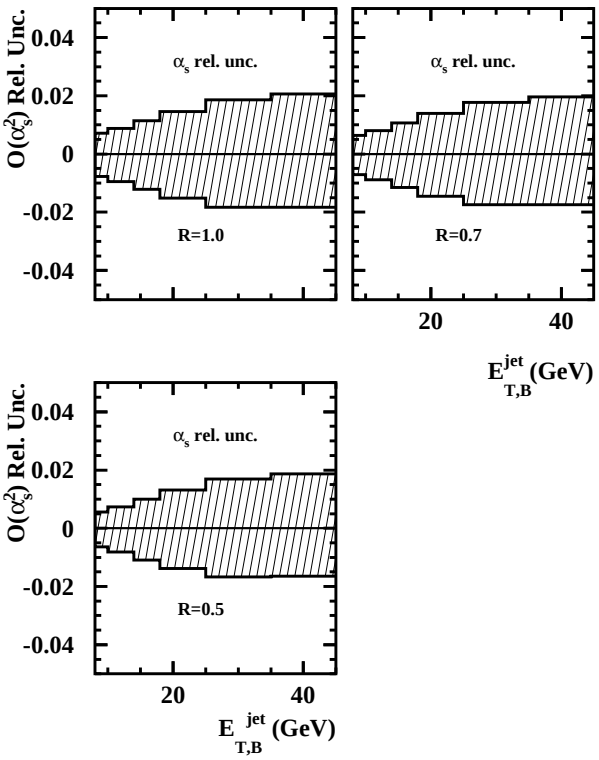


Figure 3.6: Estimate of the theoretical uncertainty $d\sigma/dE^{jet}_{T,B}$ from that in $\alpha_s(M_Z)$.

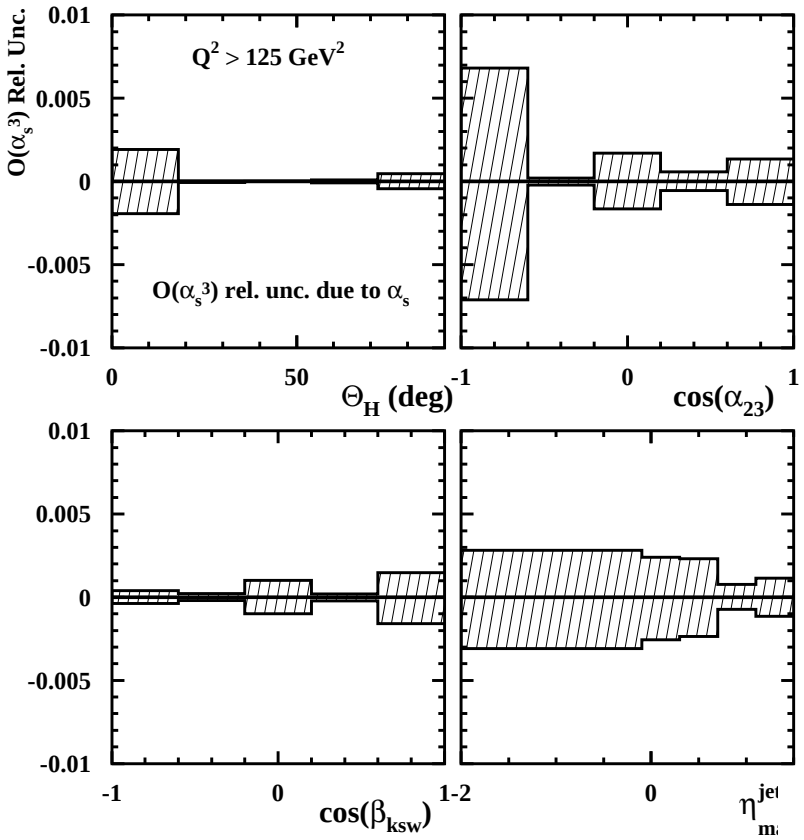


Figure 3.7: Estimate of the relative theoretical uncertainty in the three-jet normalized differential cross sections with respect to $\Theta_H$, $\cos\alpha_{23}$, $\cos\beta_{ksw}$, and $\eta^{jet}_{max}$ from that in $\alpha_s$.

**Theoretical uncertainty from that in the proton PDFs**

The uncertainty in the prediction of any observable due to those in the proton PDFs can be obtained in a systematic way using the Hessian method [67, 68]. In order to allow users to apply this method a 'set of PDF sets' which characterizes the variance from each of the parameters used in the global QCD fit has to be provided. This set is obtained by the collaborations that make the QCD global fits in the following way:

- In the Hessian method the $\chi^2$ used to determine the best fit of the PDFs is expanded quadratically about its global minimum;
- The Hessian matrix, the matrix of second derivatives of the $\chi^2$ involved in the expansion, is diagonalized to obtain a set of orthonormal eigenvectors that span the parameter-space;
- With this basis the relevant neighborhood around the global minimum, used to estimate the uncertainty in parameters of the fit, corresponds to the interior of a hypersphere of radius T, where T is a 'tolerance' parameter;
- The variations of each parameter along the eigenvector direction about the global minimum of the $\chi^2$ are used to define an 'eigen set' of PDF sets which serves as a general 'PDF sets' basis; This basis can be used to estimate uncertainties of observables coming from those in the parametrization in the proton PDFs;
- To find the uncertainty all that is needed is to calculate the observable $2 \times N$ times, where N is the number of parameters in the PDF parameter space, and then apply the following general formula:

$$(\delta V)^2 = \frac{1}{4}\sum_{i=1}^{n}[V(a_i^+) - V(a_i^-)]^2 \tag{3.3}$$

- Eq. 3.3 is the sum of the squared differences between an observable, such as a cross section, calculated using the PDF eigenset corresponding to the positive variation of a parameter ($a_i^+$), and the same observable calculated using the PDF eigenset corresponding to the negative variation ($a_i^-$).

Eq. 3.3 takes into account the uncertainty in theoretical calculations of an observable due to that in each of the parameters of the parametrization of the PDF sets. The statistical restrictions on the tolerance T, the radius around the minimum about which the $\chi^2$ is allowed to vary, must be relaxed in order to account for

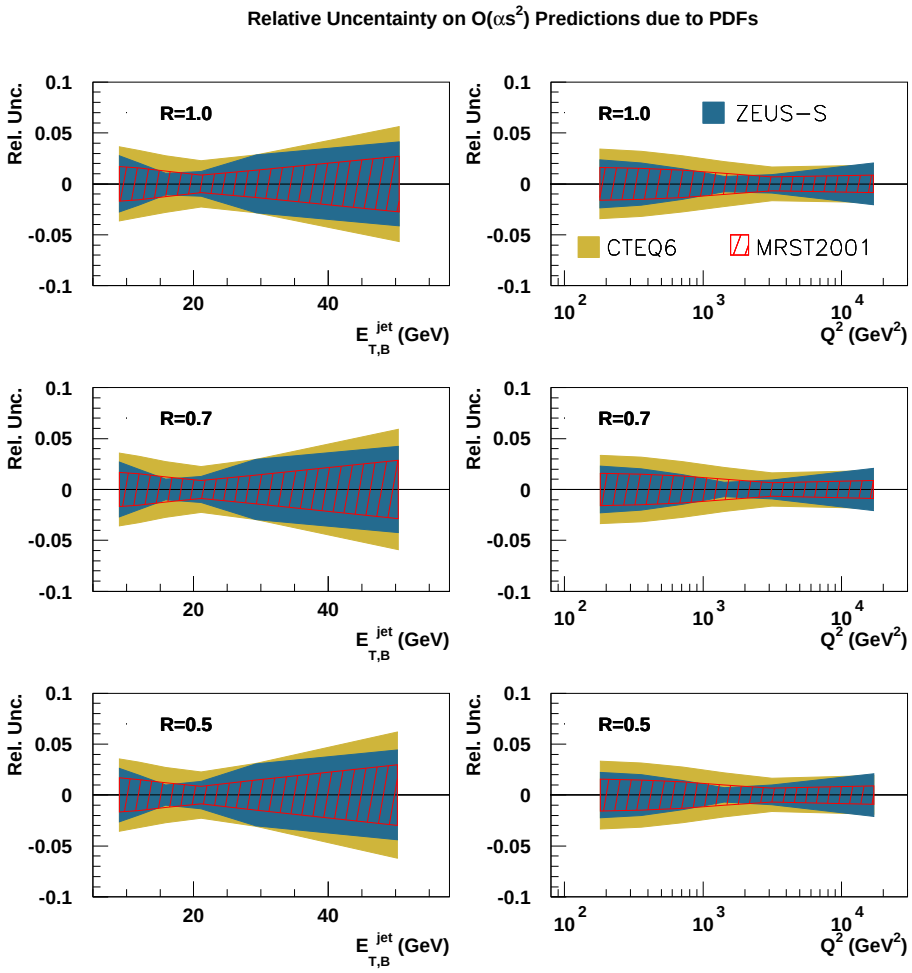


Figure 3.8: The relative uncertainty in the inclusive-jet cross sections due to those in the PDF parametrizations.

inconsistencies in the data sets that are being fitted. At the end, the general eq. 3.3 will yield an error for an observable that is $\propto$ T.

Fig. 3.8 shows the uncertainties in the inclusive-jet cross-section predictions due to those in the proton PDFs. These uncertainties where obtained by carrying out the calculations for every set of the 'eigen PDF sets' and then applying eq. 3.3. For the CTEQ PDFs the tolerance parameter was set to $T = \sqrt{100}$ [69], and the resulting uncertainties are larger than those of the MRST Collaboration, who used $T = \sqrt{50}$ [67]. In comparison to these, the ZEUS-S global fit has the advantage of using input data sets for the fits whose uncertainties are under control, making a rigorous statistical treatment possible. We found that the uncertainties in the MRST sets were comparable to that of the ZEUS-S sets. For this reason, the ZEUS-S sets were the ones used for the published results.

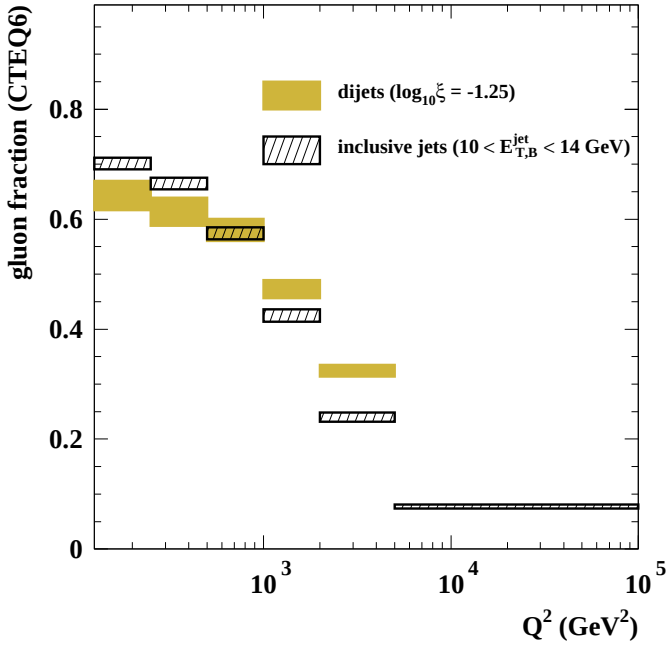


Figure 3.9: The relative contribution of gluon-induced events (BGF) to the inclusive-jet cross section. The hatched area represents the uncertainty in the calculations due to that in the proton PDFs (CTEQ6). The gluon fraction increases and becomes dominant at lower $Q^2$.

Returning to Fig. 3.3, we found that the uncertainties due to the PDFs are the dominant uncertainties in some regions of the phase space, including the low $Q^2$ regions, where the contribution from gluon-induced events becomes large. This is interpreted as a signature that measurements of inclusive-jet cross sections, which also have a small overall experimental uncertainty, can help constrain the gluon PDF when included in a global QCD fit. Furthermore, Fig. 3.9 shows that the fraction of the events that correspond to gluon-induced events (BGF) is important, especially in the lower $Q^2$ region, evidencing the sensitivity of this type of measurements to the gluon PDF.

Fig. 3.10 shows the relative uncertainties in the angular correlation normalized cross sections due to the PDFs. Due to the normalization they are in general much smaller than for the $d\sigma/dE^{jet}_{T,B}$ or $d\sigma/dQ^2$ predictions and in most cases negligible.

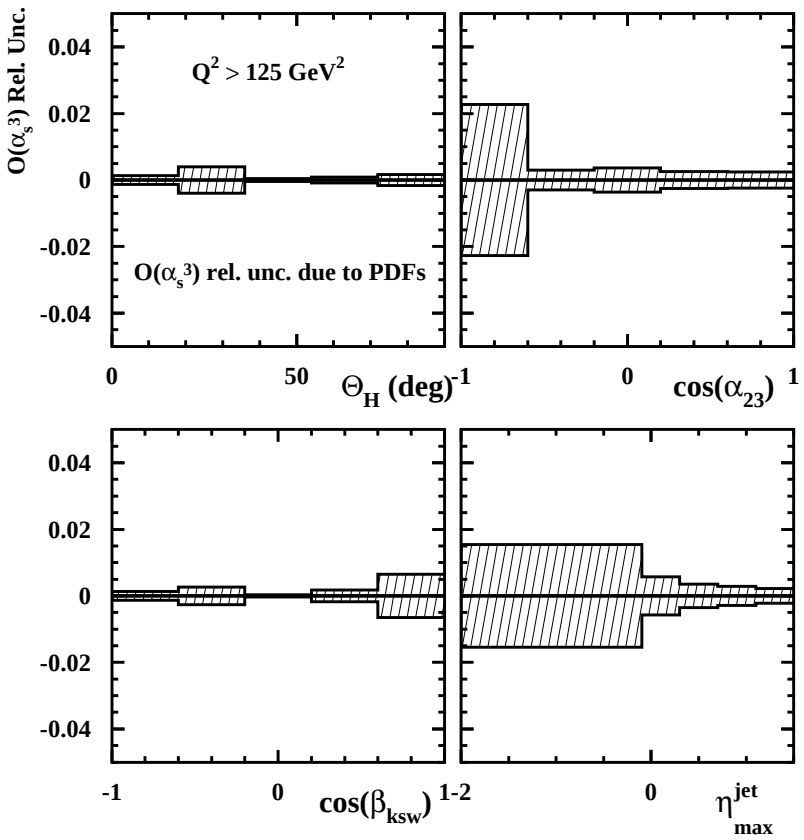


Figure 3.10: Estimate of the relative theoretical uncertainty in the three-jet normalized differential cross sections with respect to $\Theta_H$, $\cos\alpha_{23}$, $\cos\beta_{ksw}$, and $\eta^{jet}_{max}$ from that in the proton PDFs.

**Theoretical uncertainty from the choice of factorization scale $\mu_F$**

The dependence of the cross sections on $\mu_F$ is smaller than in the other parameters considered so far because in the DGLAP equations 1.21 the PDFs do not evolve as steeply with $Q^2$ as $\alpha_s$ does in the phase-space region of interest. As we will show in the next chapter (see Fig. 4.19), the $x$ region covered by our data samples is $0.004 \lesssim x \lesssim 0.3$, which we know from Fig. 1.13 corresponds to a region where the variation of $F_2$ with $Q^2$ is small. In these analyses $\mu_F$ has been varied from $\mu_F = Q/2$ to $\mu_F = 2 \times Q$ to estimate the uncertainty in the predictions due to the choice of the factorization scale. Since the dependence of $F_2$ with $Q^2$ is rather flat for our phase-space region this uncertainty was found to be negligible in comparison to the other theoretical uncertainties and is not shown for that reason.

## 3.4 Sensitivity of the angular-correlation variables to the underlying symmetry

We showed in eq. 1.28 that the three-jet cross-section in NC DIS can be expressed as a sum of the color factors times sub-process matrix elements

$$\sigma_{ep\to 3jets} = C_F C_F \cdot \sigma_A + C_F C_A \cdot \sigma_B + C_F T_F \cdot \sigma_C + T_F C_A \cdot \sigma_D, \tag{3.4}$$

where both $\sigma_B$ and $\sigma_D$ contain contributions from the triple-gluon vertex (TGV) characteristic of QCD. The aim of this analysis is to study how the underlying symmetry of the theory is reflected in angular correlations among the jets in three-jet events. In particular, we would like to find sensitivity independently of other sources of 'color sensitivity', such as $\alpha_s(\mu_R)$ or the PDF evolution. One way to gain independence from these other sources is to use the normalized cross sections:

$$\sigma_{\mathrm{N,i}}(\frac{C_A}{C_F}, \frac{T_F}{C_F}) = \frac{\sigma_i}{\sigma_T} = \frac{\sigma_A^i + \frac{C_A}{C_F} \cdot \sigma_B^i + \frac{T_F}{C_F} \cdot \sigma_C^i + \frac{T_F}{C_F}\frac{C_A}{C_F} \cdot \sigma_D^i}{\sum_j^N \sigma_j(\frac{C_A}{C_F}, \frac{T_F}{C_F}) \cdot \Delta x_j} \tag{3.5}$$

where $\sigma_i$ represents the differential cross-section integrated over bin $i$, the $\Delta x_i$ is the bin-width of bin $i$ and $\sigma_T$ is the differential cross-section integrated over the whole phase-space. Normalizing the cross sections has several advantages:

- The dependence on the absolute value of the cross-section is lost, leaving only the shapes of the angular correlations, which is the object of interest;
- Apart from that in $\alpha_s$, other correlated dependencies between the numerator and denominator cancel out to a large extent, such as those from the PDFs;
- The correlated theoretical and experimental uncertainties also cancel out to a large extent. We have already shown that the theoretical uncertainties are greatly reduced in some regions;
- From eq. 3.4 we see that the color dependence has been reduced to that on the two color-factor ratios $\frac{C_A}{C_F}$ and $\frac{T_F}{C_F}$.

The sensitivity of the angular-correlation variables is reflected in how distinct the individual sub-process normalized cross-sections are with respect to each other. A very distinct shape for $\sigma_B$ or $\sigma_D$ is desirable since these sub-process cross sections contain the TGV. The sensitivity to a particular vertex will depend on both the characteristics of the individual sub-process shapes as well as on their overall contribution to the cross section, i.e a small contribution is still difficult to spot even if it has a distinct shape.

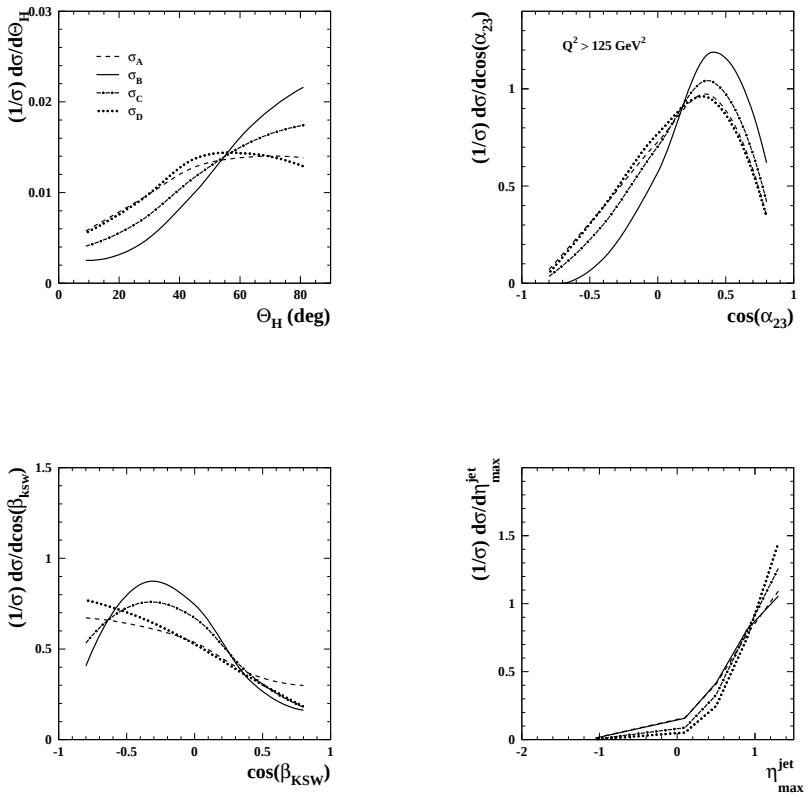


Figure 3.11: The different sub-process normalized cross-sections are shown for the variables $\Theta_H$, $\cos\alpha_{23}$, $\cos\beta_{ksw}$, and $\eta^{jet}_{max}$. In the $\Theta_H$, $\cos\alpha_{23}$, $\cos\beta_{ksw}$ cases the shape is very distinct for the $\sigma_B$ which contains the TGV. For the variable $\eta^{jet}_{max}$ the most distinguishable shape is that of $\sigma_D$, which also contains the TGV. The calculations where done at $O(\alpha_s^2)$ using the program NLOJET++.

Fig. 3.11 shows the theoretical predictions at $O(\alpha_s^2)$ obtained using the program NLOJET++. The figure shows that the shape of $\sigma_B$, which contains the TGV, is very distinct from the rest in the variables $\Theta_H$, $\cos\alpha_{23}$, $\cos\beta_{ksw}$. The shape of $\sigma_D$, which is also sensitive to the presence of the TGV, is distinguishable in the $\eta^{jet}_{max}$ variable. The four angular-correlation variables shown here are the most sensitive found after an exhaustive scan of these types of variables for three-jet configurations in *ep* NC scattering.

In order to make these predictions possible, in DISENT the color components in the calculations were identified and disentangled, so as to compute the different contributions. In NLOJET++ this approach proved impossible, since some of the color factors are wired into the calculations in an irretrieveable way. Nevertheless it

is possible to carry out NLOJET++ calculations with different SU(N) groups. This was done, as discussed in more detail in Chapter 7, with enough choices of SU(N) to solve eq. 3.5, with the sub-process cross sections left as unknowns. In this way the cross-section predictions were obtained at $O(\alpha_s^2)$ using NLOJET++. At $O(\alpha_s^3)$ eq. 3.5 must be modified as more color configurations come into play, making the identification of the color factors a more challenging task which has not yet been carried out.

In eq. 3.5 we saw how the cross-section prediction can be resolved into its different color components. The information about the underlying symmetry group is contained in the color factors. The sub-process normalized cross sections are independent of the symmetry group and are general for a range of gauge theories with other invariances. There is, however, a residual dependence on the color factors through the running of $\alpha_s$ and the PDF evolution, as we will discuss later.

From eq. 3.5 it is clear how to obtain the predictions for other group invariances-simply replace the color factors of SU(3) with those of any other group. The symmetry groups considered for this analysis are: SU(3), SO(3), SU(N$\rightarrow\infty$), U(1)$\otimes$U(1)$\otimes$U(1), and $C_F = 0$. The choice of $C_F = 0$ does not actually correspond to any group and is used as an extreme choice.

Fig. 3.12 shows the normalized cross-section predictions using NLOJET++ at $O(\alpha_s^2)$ for the variables $\Theta_H$, $\cos\alpha_{23}$, $\cos\beta_{ksw}$, and $\eta_{max}^{jet}$ for different underlying symmetry group assumptions. The bottom plots show the relative difference between an alternate group prediction and the QCD prediction. As can be seen in the plots, the angular-correlation variables are sensitive to the color factors. For all the variables the choice $C_F = 0$ deviates dramatically from SU(3). The variable $\eta_{max}^{jet}$ can be used to distinguish SU(N$\rightarrow\infty$), while U(1)$\otimes$U(1)$\otimes$U(1) gives a different prediction to SU(3) most noticeably in the variables $\Theta_H$, $\cos\beta_{ksw}$, and $\eta_{max}^{jet}$.

The question arises as to why the variables do not show the same dramatic discernability between non-Abelian QCD and the Abelian choice of U(1)$\otimes$U(1)$\otimes$U(1) as for the LEP analyses in $e^+e^-$ data. The reason lies on the particular characteristics of HERA physics. Take the $\Theta_H$ variable as an example. This variable, as is the case in $e^+e^-$, is designed to distinguish between different contributions from the $\sigma_B$ and $\sigma_C$ types of diagrams, which contain $g \rightarrow gg$ and $g \rightarrow q\bar{q}$ vertices, respectively. The predicted relative sub-process contributions at HERA are $\sigma_A : 23\%$, $\sigma_B : 13\%$, $\sigma_C : 39\%$, $\sigma_D : 25\%$. Thus, although the $\sigma_B$ contribution has a distinct shape, the sensitivity to this vertex is suppressed by the small relative contribution of $\sigma_B$. The other sub-process cross-section with a TGV is $\sigma_D : 25\%$, but the TGV appears in the initial state as a result of the gluon content of the proton, and the correlation is somewhat smeared.

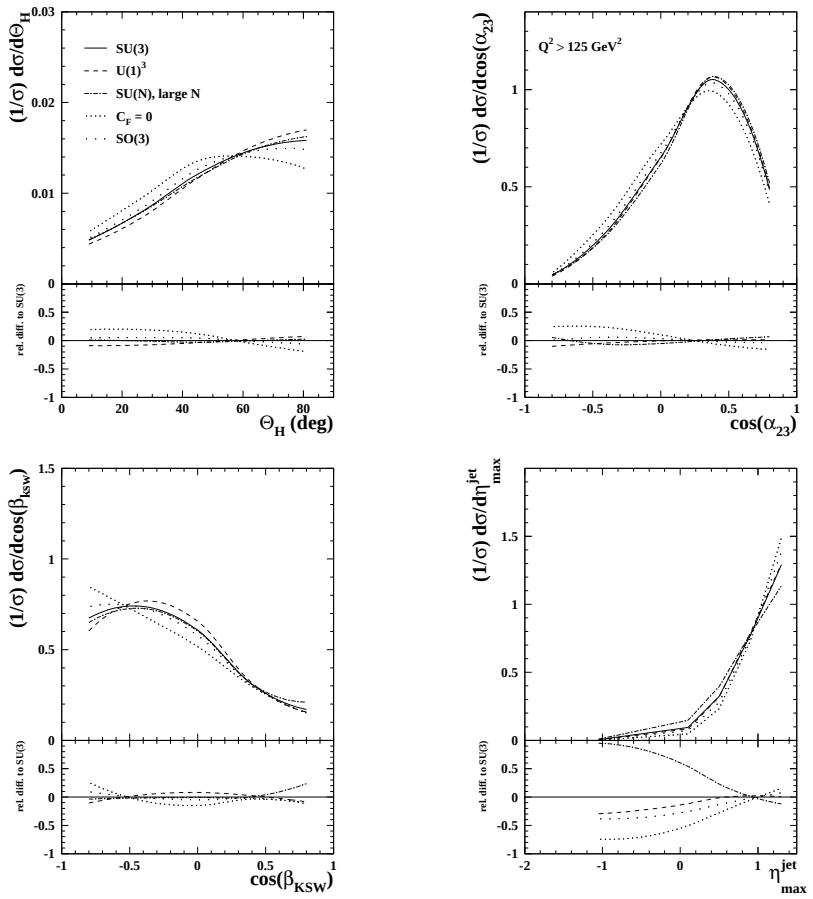


Figure 3.12: The normalized cross-section predictions using NLOJET++ at $O(\alpha_s^2)$ are shown for the variables $\Theta_H$, $\cos\alpha_{23}$, $\cos\beta_{ksw}$, and $\eta_{max}^{jet}$ for different underlying symmetry group assumptions. The bottom plots show the relative difference between the al alternate group prediction and the QCD prediction. The angular-correlation variables are sensitive to the color factors.

### 3.4.1 Additional sources of color dependence in the theoretical predictions

We have shown that the theoretical predictions involve both the evolution of the coupling and of the proton PDFs with the energy scale. The equations that govern these evolutions are determined by the color factors of SU(3) and can introduce a 'color bias' in the predictions. If all the bin regions for a given angular-correlation variable have the same distribution of $Q^2$, then there is complete cancellation of the $Q^2$ dependence. If the bins have different $Q^2$ distributions, then the $Q^2$ dependence is not totally correlated in the numerator and denominator and will does not cancel completely. In this case a dependence on the evolution of $\alpha_s(\mu_R)$ or the proton

PDFs would still be observed. Since the PDF evolution is rather flat with $Q^2$ for our phase-space region, this dependence is expected to be suppressed relative to that in $\alpha_s(\mu_R)$.

The distributions in $Q^2$ for every bin of $\Theta_H$, $\cos\alpha_{23}$, $\cos\beta_{ksw}$, and $\eta^{jet}_{max}$ were calculated using the MEPS MC event generator discussed in Section 3.5. They are shown in Figs. 3.13 through 3.16. These figures revealed that the variable $\eta^{jet}_{max}$ has a bin-dependent $Q^2$ distribution. Therefore, the dependence of the cross-section on the energy scale $\mu_R$ or $\mu_F$ does not cancel neatly in the normalized cross-sections for $\eta^{jet}_{max}$, despite the normalization.

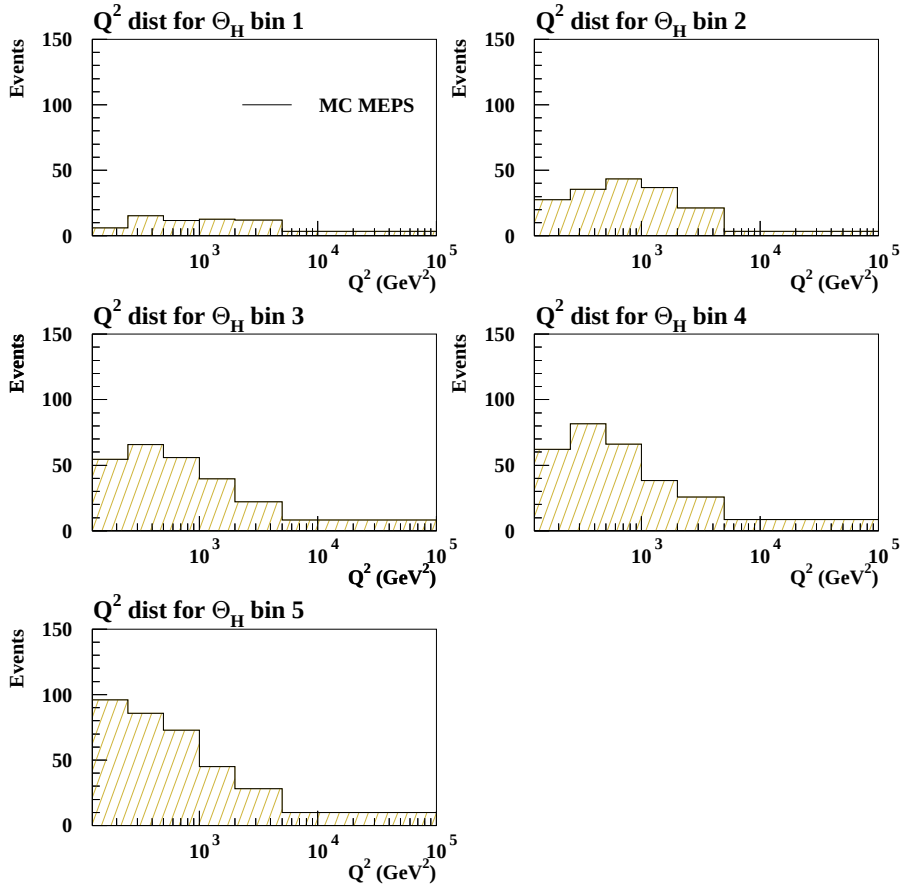


Figure 3.13: The distribution in $Q^2$ for each bin in $\Theta_H$ as predicted by the LEPTO MC.

The dependence of the cross-section predictions on the evolution of $\alpha_s(\mu_R)$ and the PDFs was studied by fixing their scale dependence in the calculations. For example, fixing $\mu_R$ fixes $\alpha_s(\mu_R)$ to a single value. The dependence of the normalized cross-sections on the running is then estimated by comparing the 'fixed $\mu_R$' calculation to

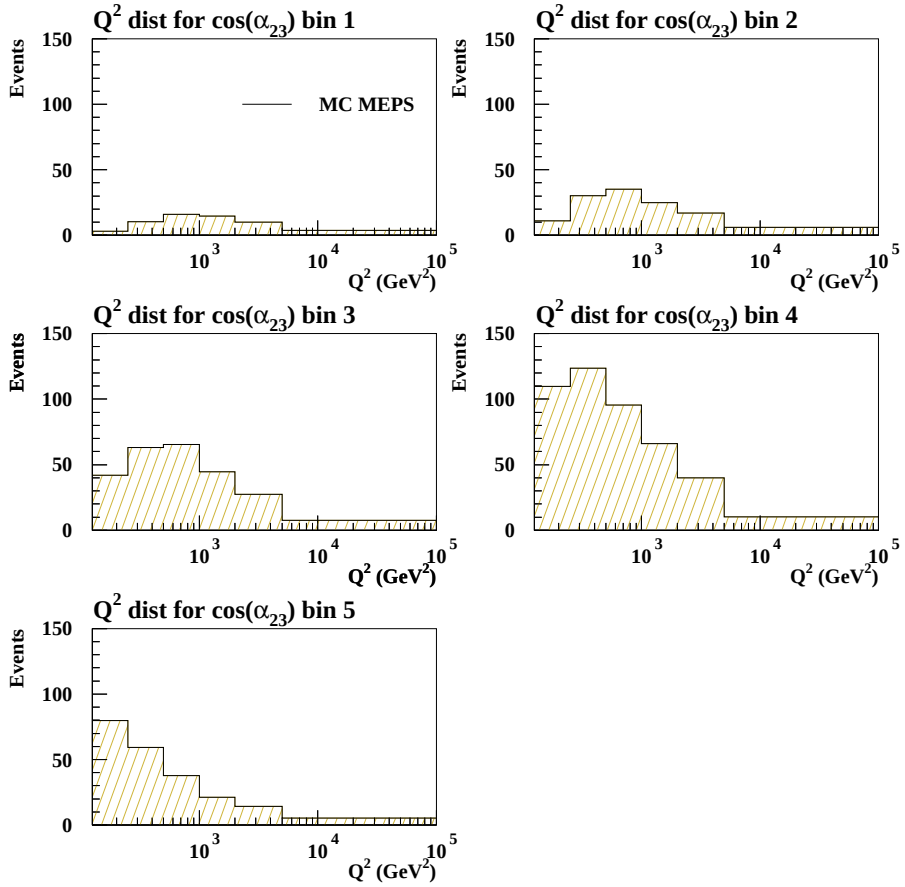


Figure 3.14: The distribution in $Q^2$ for each bin in $\cos\alpha_{23}$ as predicted by the LEPTO MC.

the default one. For the case of the PDFs, $\mu_F$ was fixed. The constant value chosen for $\mu_F^2$ and $\mu_R^2$ was the average $Q^2$ in the data $< Q^2 >$. Fig. 3.17 shows the relative difference between the $O(\alpha_s^2)$ predictions for $\Theta_H$, $\cos\alpha_{23}$, $\cos\beta_{ksw}$, and $\eta_{max}^{jet}$ done with $\mu_R = \sqrt{< Q^2 >} = \sqrt{982}$ GeV and the default ones where $\mu_R = Q$. The same figure shows a similar comparison for the calculations done with $\mu_F = \sqrt{< Q^2 >}$. A couple of things become clear from these figures. The angular variables are much more sensitive to the running of $\alpha_s$ than to the PDF evolution. In fact, this test shows that any residual dependence on the color factors used for the PDF evolution can be safely neglected for the normalized cross sections. As expected from the distributions in $Q^2$, the variable $\eta_{max}^{jet}$ shows the biggest sensitivity to the running of $\alpha_s$. In the lower $\eta_{max}^{jet}$ region, the relative difference increases to $\sim 40\%$.

Lets look at Fig. 3.18, which is very similar to Fig. 3.17 except that now the

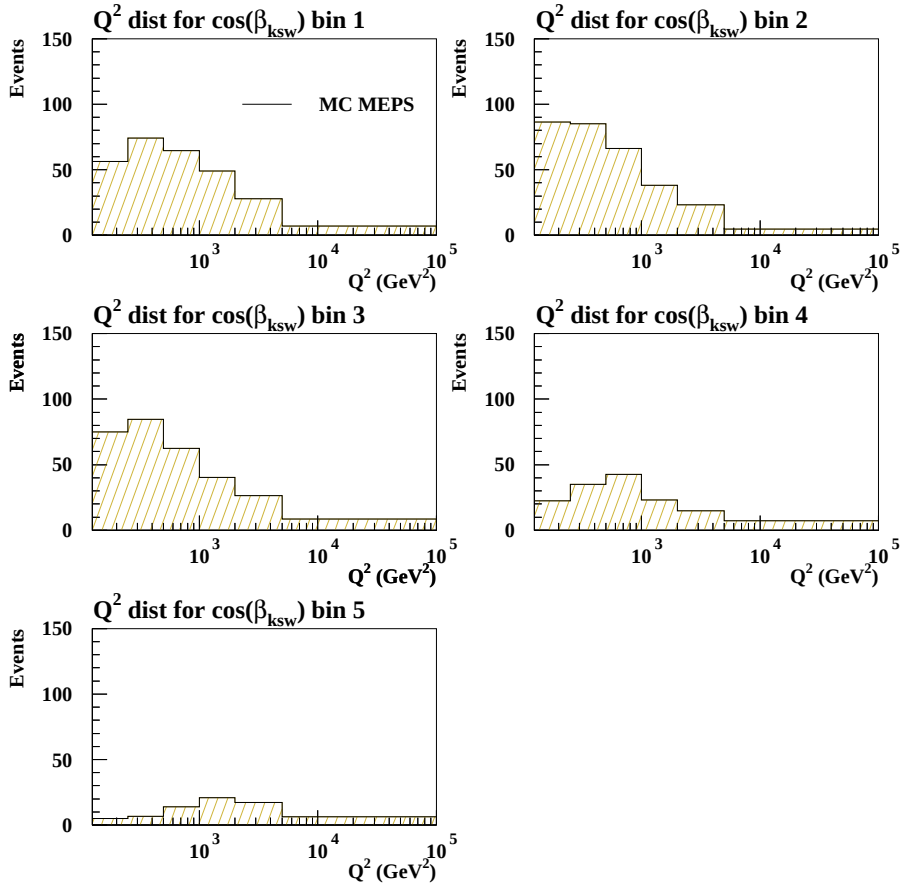


Figure 3.15: The distribution in $Q^2$ for each bin in $\cos\beta_{ksw}$ as predicted by the LEPTO MC.

calculations are done to $O(\alpha_s^3)$ instead of LO. The dependence of the predictions on the PDF evolution is still small, while the dependence with the running of $\alpha_s$ is substantially reduced. This can be understood by considering that the running of $\alpha_s$ at $N^{th}$ order is partially compensated by the matrix elements at $(N+1)^{th}$ order. At $O(\alpha_s^3)$ we have:

$$\sigma(x, Q^2, \mu_R) = \alpha_s^2(\mu_R) \cdot \hat{\sigma}_2(x, Q^2) + \alpha_s^3(\mu_R) \cdot \hat{\sigma}_3(x, Q^2, \mu_R) \tag{3.6}$$

where the dependence of the first term on $\mu_R$ is partially compensated by the second term.

In summary, we found that the PDF evolution does not introduce a bias, while the evolution of $\alpha_s$ introduces an additional sensitivity to the color factors in some phase-space regions for those angular variables where the cancellation is not complete. We also found that going to a higher-order calculation rids the angular vari-

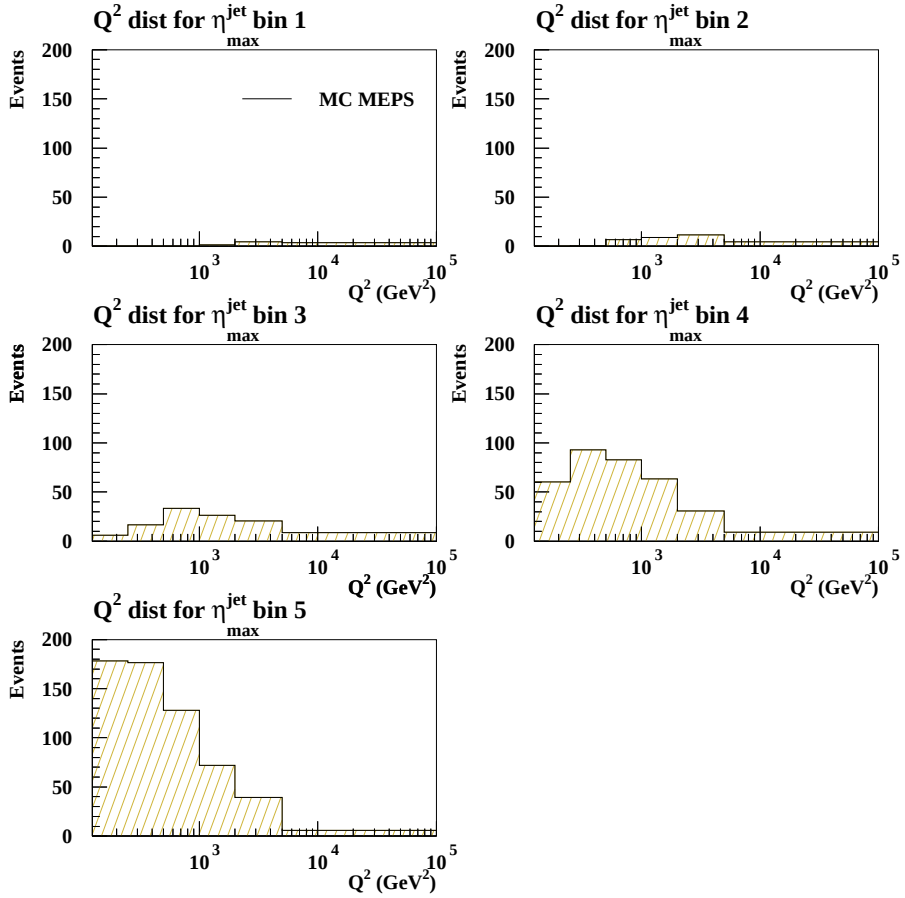


Figure 3.16: The distribution in $Q^2$ for each bin in $\eta^{jet}_{max}$ as predicted by the LEPTO MC. The different $\eta^{jet}_{max}$ bins populate different regions of $Q^2$, leading to a more noticeable effect of $\alpha_s(\mu_R)$ and PDF evolution on the normalized cross sections.

ables of this residual sensitivity on the color factors from $\alpha_s(\mu_R)$. Moreover, one could simply exclude some regions in the angular variables in order to supress such a dependence in a fit to the color factors.

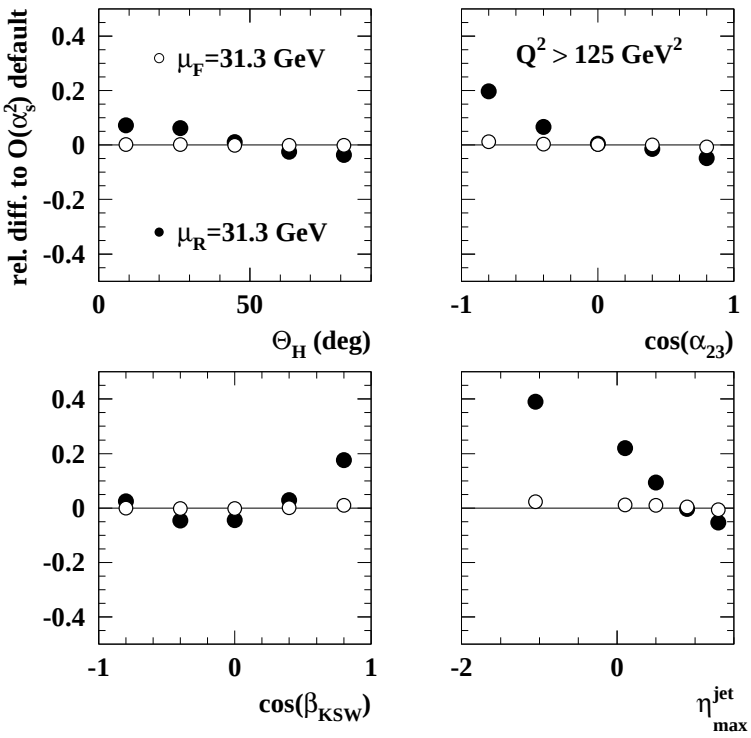


Figure 3.17: Relative difference between the predictions made at $O(\alpha_s^2)$ for the angular-correlation normalized cross sections with $\mu_R = \sqrt{< Q^2 >}$ and the predictions with $\mu_R = Q$. The relative difference with the predictions with $\mu_F = \sqrt{< Q^2 >}$ is also shown. The effect of the PDF evolution on the predictions is small, while that of the running of $\alpha_s$ is not negligible in some areas such as the low $\eta^{jet}_{max}$ region.

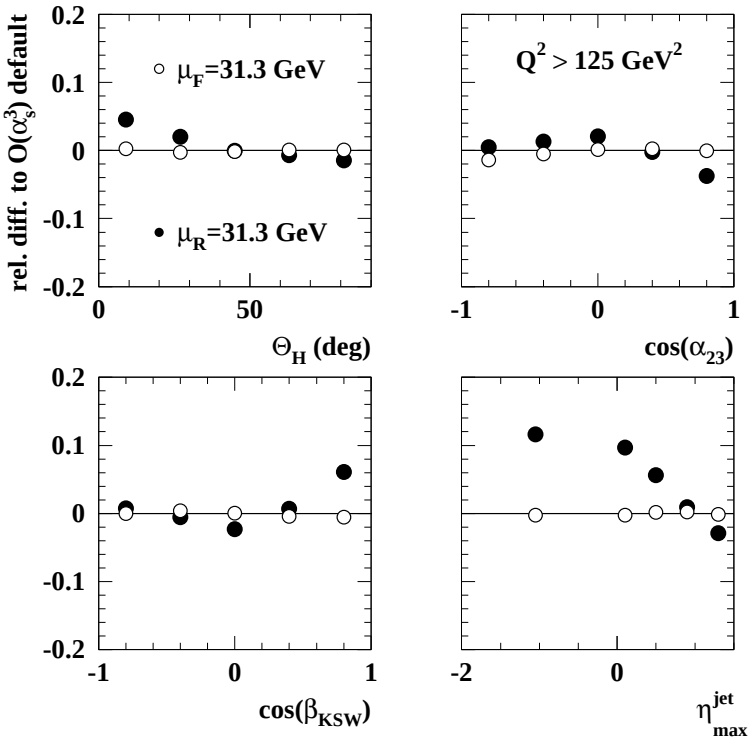


Figure 3.18: Relative difference between the $O(\alpha_s^3)$ predictions for the angular-correlation normalized cross sections with $\mu_R = \sqrt{< Q^2 >}$ with $\mu_R = Q$. The relative difference with $\mu_F = \sqrt{< Q^2 >}$ is also shown. The dependence with the PDF evolution is small, while the dependence with the running of $\alpha_s$ is reduced at NLO.

### 3.4.2 A restricted phase-space region for the study of the angular-correlation variables

Another way to rid the predictions from the 'color bias' introduced by the running of $\alpha_s$ or the PDF evolution is simply to restrict the phase-space such that $\alpha_s$ and the PDFs have no leaway to evolve. This approach is complementary to going to higher orders and has also been carried out in this analysis. The phase-space region to which the cross-sections are constrained is not arbitrary. If we consider that the $\eta^{jet}_{max}$ distribution in $Q^2$ has the most dramatic impact in terms of making this variable sensitive to the running of $\alpha_s$, then it makes sense to use this distribution, shown in Fig. 3.16, to determine the new restricted phase-space. From Fig. 3.16 we see that if the $Q^2$ region is constrained to $500 < Q^2 < 5000$ GeV$^2$ then the loss in statistics is minimized while the distributions in $Q^2$ are fairly similar within this restricted region. Fig. 3.19 shows the resulting dependence on the running of $\alpha_s$ and the PDF evolution at LO. As expected, the dependence is substantially reduced by restricting the phase-space to this region. Fig. 3.20 shows the dependencies for the restricted region in $Q^2$ at NLO. As we can see, going to $O(\alpha_s^3)$ and simultaneously restricting the phase-space region minimizes any residual dependence of the distributions on the running of $\alpha_s$.

Finally, it was verified that the angular-correlation variables still showed sensitivity to the underlying symmetry in the new phase-space region. This was done as before, by looking at the distributions of the sub-process normalized cross-sections in a symmetry group independent way. The results are shown in Fig. 3.22, where it can be seen that the variables have not lost sensitivity to the underlying symmetry. Figs. 3.23 through 3.25 show the theoretical uncertainties due to those in higher orders ($\mu_R$), $\alpha_s(M_Z)$ and the PDFs, respectively, at $O(\alpha_s^3)$ using NLOJET++. They are similar to those for the wider phase-space region $Q^2 > 125$ GeV$^2$.

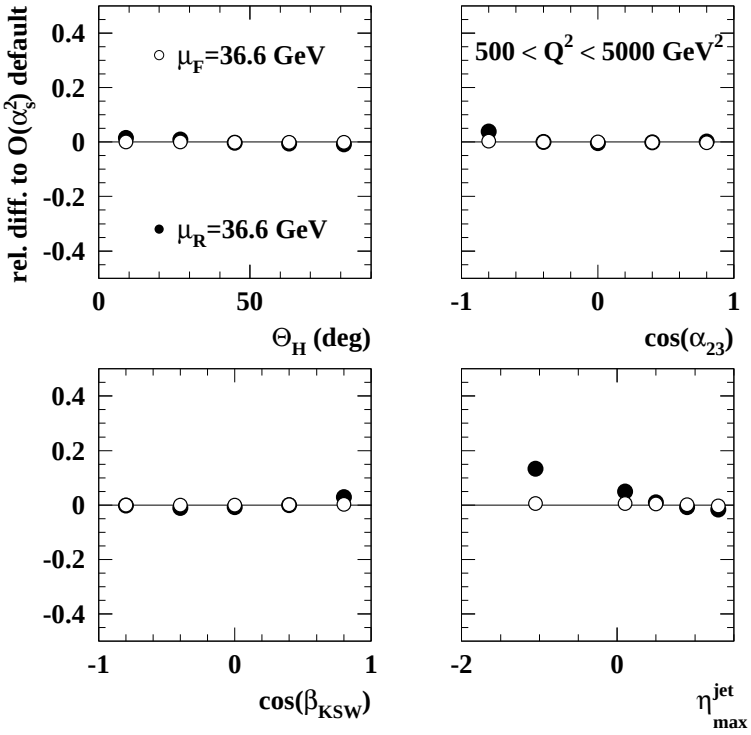


Figure 3.19: Relative difference between the $O(\alpha_s^2)$ predictions for the angular-correlation normalized cross sections with $\mu_R = \sqrt{< Q^2 >}$ and those with $\mu_R = Q$. The relative difference with $\mu_F = \sqrt{< Q^2 >}$ is also shown. The phase-space region has been restricted to $500 < Q^2 < 5000$ GeV$^2$. The dependence of the predictions on the running of $\alpha_s(\mu_R)$ is substantially reduced.

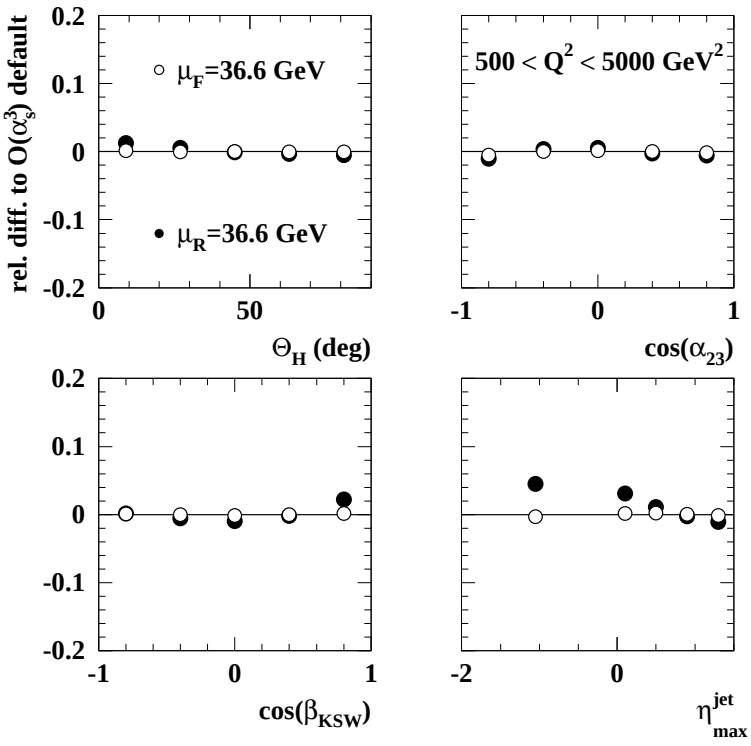


Figure 3.20: Relative difference between the $O(\alpha_s^3)$ predictions for the angular-correlation normalized cross sections with $\mu_R = \sqrt{< Q^2 >}$ and those with $\mu_R = Q$. The relative difference with $\mu_F = \sqrt{< Q^2 >}$ is also shown. The phase-space region has been restricted to $500 < Q^2 < 5000$ GeV $^2$. The dependence of the predictions on $\alpha_s(\mu_R)$ is substantially reduced.

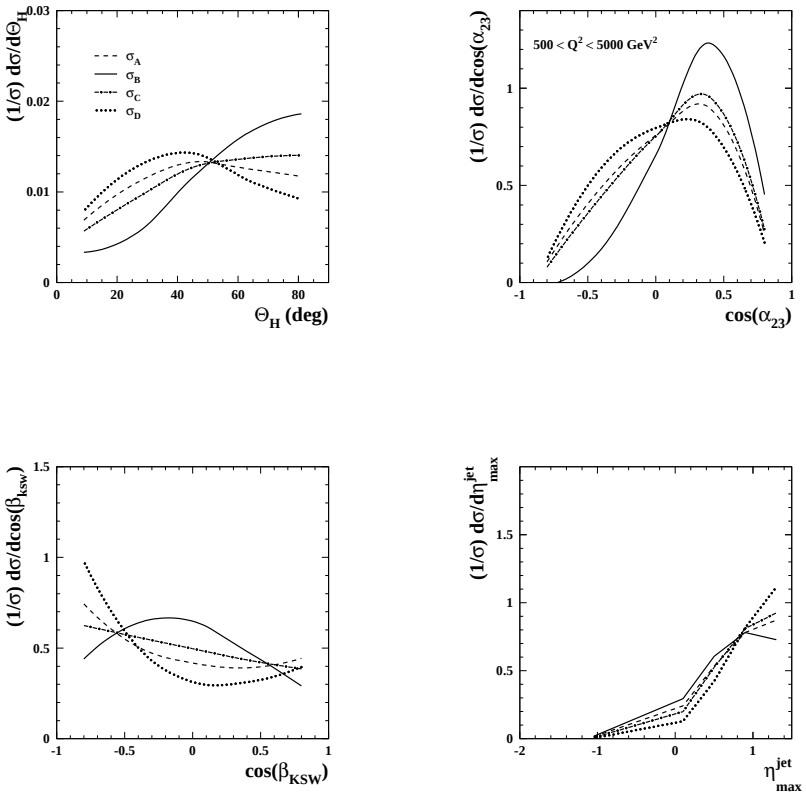


Figure 3.21: The different sub-process normalized cross-sections are shown for the variables $\Theta_H$, $\cos\alpha_{23}$, $\cos\beta_{ksw}$ and $\eta^{jet}_{max}$ for the restricted region $500 < Q^2 < 5000$ GeV$^2$. In the $\Theta_H$, $\cos\alpha_{23}$ and $\cos\beta_{ksw}$ cases the shape is very distinct for the $\sigma_B$, which contains the TGV. For the variable $\eta^{jet}_{max}$ the most distinguishable shape is that of $\sigma_D$, which also contains the TGV. The calculations where done at $O(\alpha_s^2)$ using the program NLOJET++.

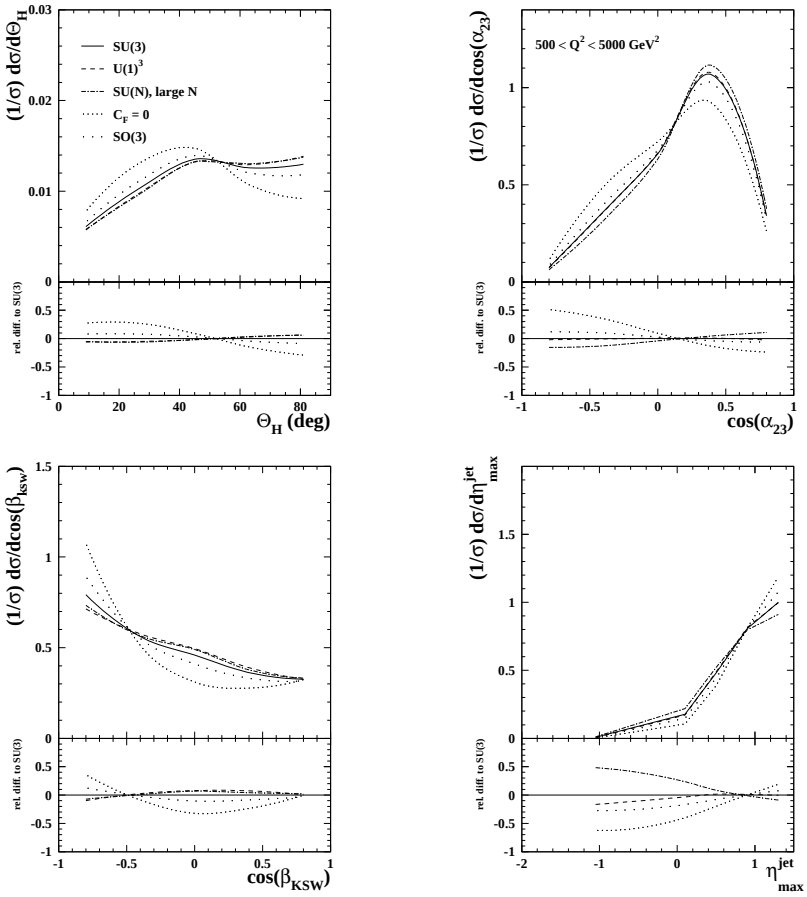


Figure 3.22: The normalized cross-section predictions using NLOJET++ at $O(\alpha_s^2)$ are shown for the variables $\Theta_H$, $\cos\alpha_{23}$, $\cos\beta_{ksw}$ and $\eta^{jet}_{max}$ for different underlying symmetry group assumptions for the restricted region $500 < Q^2 < 5000$ GeV$^2$. The bottom plots show the relative difference between an alternate group prediction and the QCD prediction. The angular-correlation variables are sensitive to the color factors.

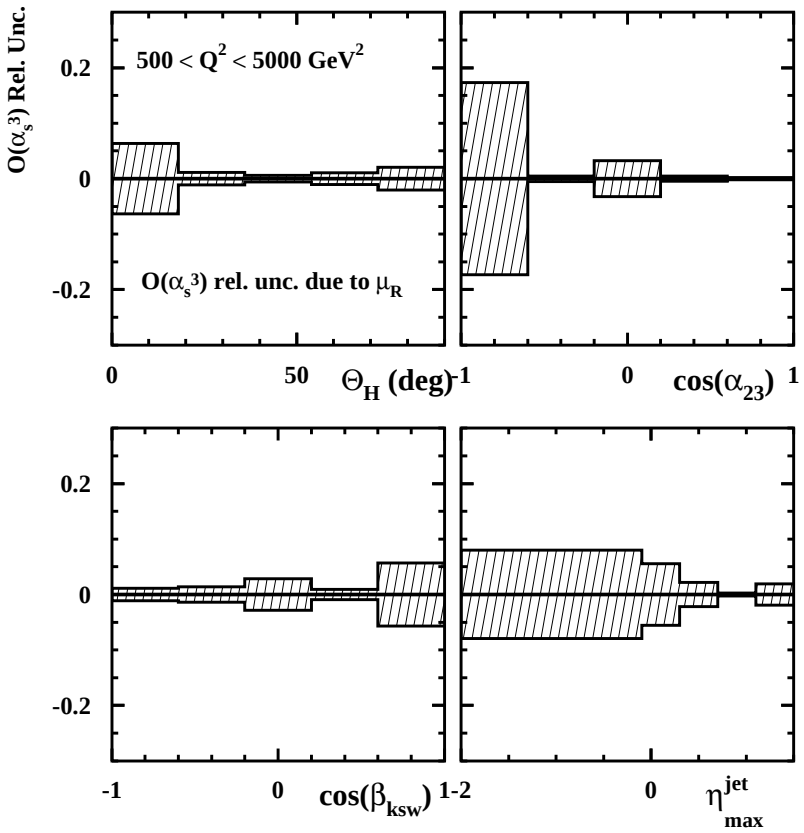


Figure 3.23: Estimate of the relative theoretical uncertainty in the three-jet normalized differential cross sections with respect to $\Theta_H$, $\cos\alpha_{23}$, $\cos\beta_{ksw}$ and $\eta^{jet}_{max}$ from terms beyond $O(\alpha_s^3)$.

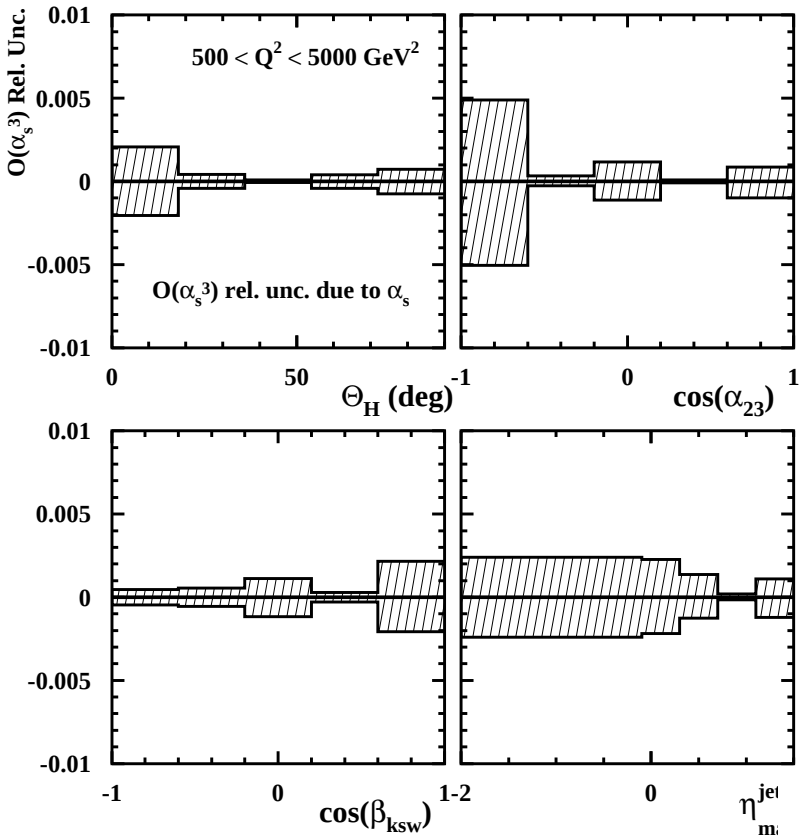


Figure 3.24: Estimate of the relative theoretical uncertainty in the three-jet normalized differential cross sections with respect to $\Theta_H$, $\cos\alpha_{23}$, $\cos\beta_{ksw}$ and $\eta^{jet}_{max}$ from that in $\alpha_s$.

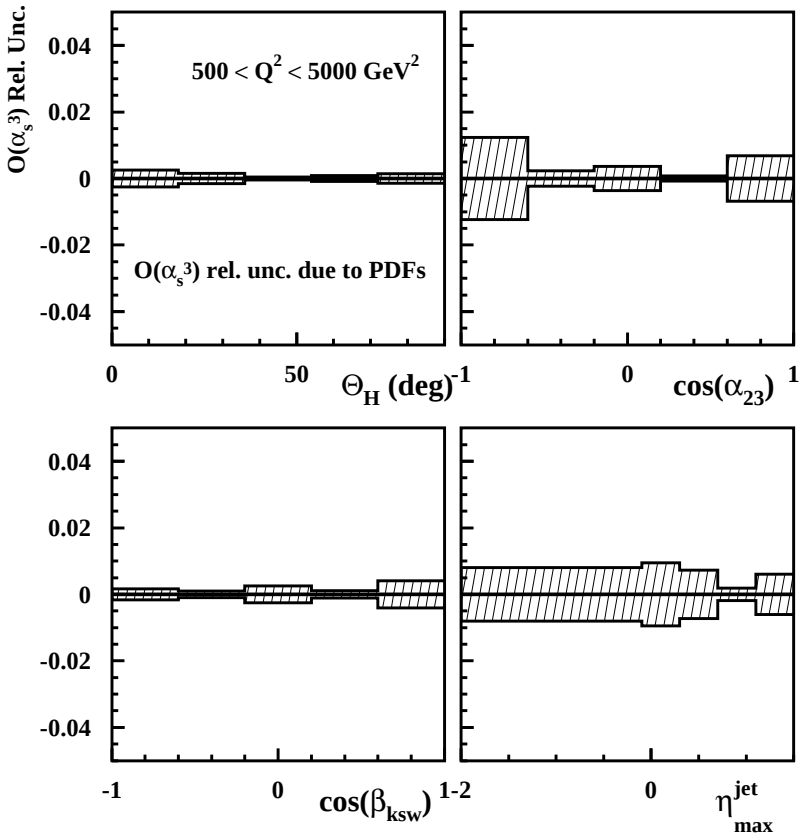


Figure 3.25: Estimate of the relative theoretical uncertainty in the three-jet normalized differential cross sections with respect to $\Theta_H$, $\cos\alpha_{23}$, $\cos\beta_{ksw}$ and $\eta^{jet}_{max}$ from that in the PDFs.

### 3.4.3 $O(\alpha_s^2)$ vs $O(\alpha_s^3)$ theoretical predictions for the three-jet angular-correlations analysis

The effect of including an additional order for the calculations in the angular-correlations analysis has been studied. We will see in subsequent chapters how the $O(\alpha_s^2)$ and $O(\alpha_s^3)$ calculations compare to the data. Here a simple comparison between the $O(\alpha_s^2)$ and the $O(\alpha_s^3)$ is shown, along with the total theoretical uncertainty for the calculations shown as a band. Note that the total theoretical uncertainty also includes that due to the modelling of the parton cascade, discussed later in this chapter. Fig. 3.26 (Fig. 3.27) show the normalized cross-section predictions using NLOJET++ at $O(\alpha_s^2)$ and $O(\alpha_s^3)$ for the variables $\Theta_H$, $\cos\alpha_{23}$, $\cos\beta_{ksw}$, and $\eta_{max}^{jet}$ in the region $Q^2 > 125$ GeV$^2$ ($500 < Q^2 < 5000$ GeV$^2$). The bottom plots show the relative difference between the $O(\alpha_s^2)$ and $O(\alpha_s^3)$ predictions with the band being the total uncertainty in the $O(\alpha_s^3)$ predictions. As we can see, the theoretical uncertainties, which have a large contribution from the $\mu_R$-related uncertainty, are large where the $O(\alpha_s^2)$ and $O(\alpha_s^3)$ differ most, as one would expect.

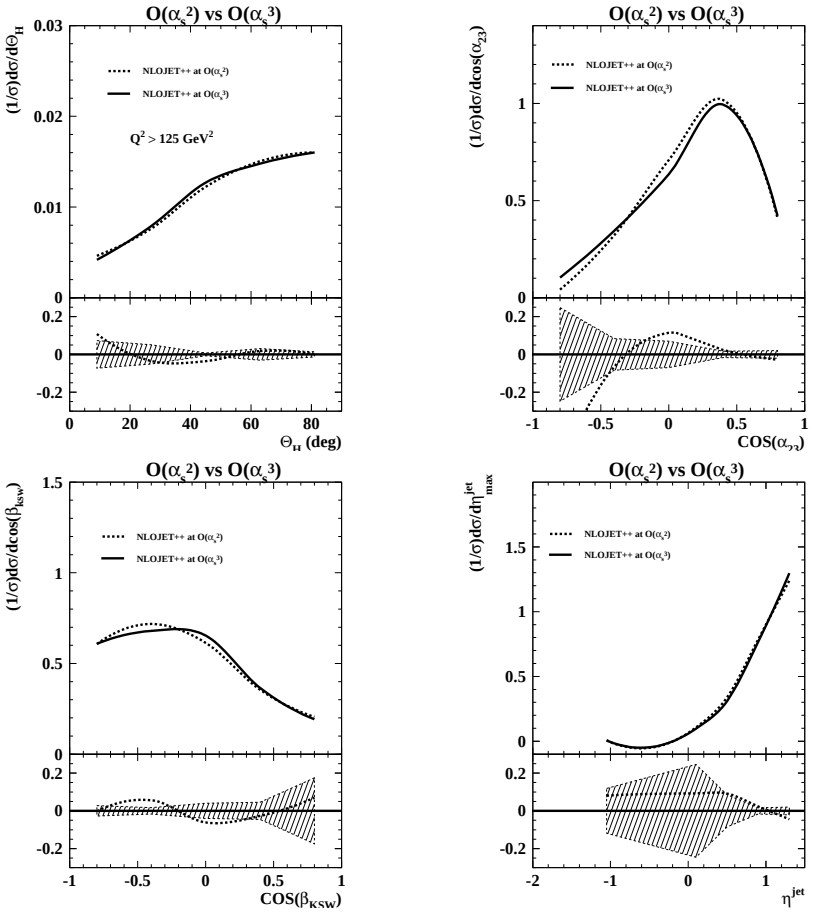


Figure 3.26: The normalized cross-section predictions using NLOJET++ at $O(\alpha_s^2)$ and $O(\alpha_s^3)$ are shown for the variables $\Theta_H$, $\cos\alpha_{23}$, $\cos\beta_{ksw}$ and $\eta^{jet}_{max}$ in the region $Q^2 > 125$ GeV$^2$. The bottom plots show the relative difference between the $O(\alpha_s^2)$ and $O(\alpha_s^3)$ predictions with the band being the total uncertainty in the $O(\alpha_s^3)$ predictions.

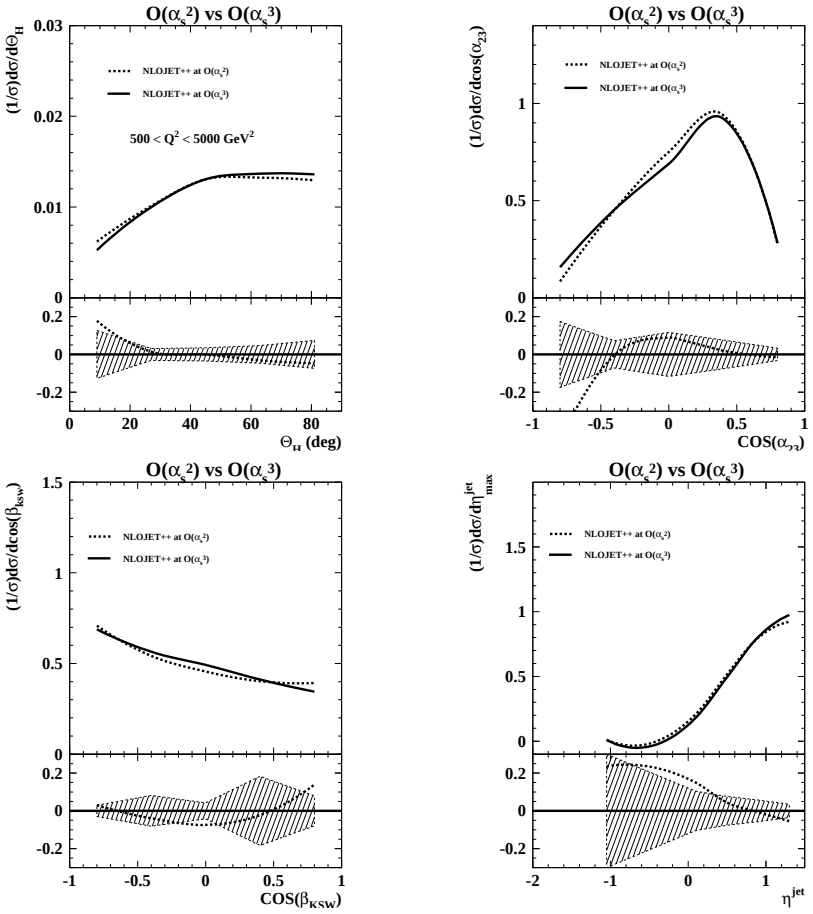


Figure 3.27: The normalized cross-section predictions using NLOJET++ at $O(\alpha_s^2)$ and $O(\alpha_s^3)$ are shown for the variables $\Theta_H$, $\cos\alpha_{23}$, $\cos\beta_{ksw}$ and $\eta^{jet}_{max}$ in the region $500 < Q^2 < 5000$ GeV$^2$ GeV$^2$. The bottom plots show the relative difference between the $O(\alpha_s^2)$ and $O(\alpha_s^3)$ predictions with the band being the total uncertainty in the $O(\alpha_s^3)$ predictions.

## 3.5 Monte Carlo event generators

The definition of a jet observable allows one to compare the hard scattering predictions with the hadronic distributions measured in detectors. It is however necessary to model the hadronization of outgoing partons in order to improve this comparison. The modelling of the hadronization has another advantage. It can be interfaced with a simulation of the detector, giving an essential tool to understand the data better. In fact, modelling the physics and the experimental setup has a deeper significance, since on the one hand encapsulates our present knowledge of the physics, and on the other it allows us to learn from the experiment by comparisons to the data. The uses of event generators in the context of jet analyses are:

- To study the reconstruction of the jet observables as shown in Chapter 4. There we will see studies of the resolution and possible bias of the detector on the observables;
- To understand other reconstruction issues related to the geometry of the detector as seen in different reference frames; in particular, a study of the appropriate $\cos\gamma_H$ region to be used for jet analyses in the Breit frame is shown in Chapter 4;
- To study the purity and efficiency of the sample selection, as shown in Chapter 5;
- To obtain correction factors, such as hadronization or electroweak effects, to be applied to the pQCD calculations in order to improve the comparison with the data, as shown in Chapter 5;
- To estimate the sources of systematic uncertainties in the measurements, as shown in Chapter 5.

The usefulness of this tool relies on how well the simulation is able to describe the data distributions. In the next chapter comparisons of the distributions of the MC simulation to those of the data sample are amply shown. The remainder of this chapter is devoted to laying out the basic components of event generators in DIS.

The ideal would be to be able to reproduce the distributions in the data directly from first QFT principles and interface this with the detector simulation. The hadronization process, however, takes place at an energy scale where perturbative QCD is no longer applicable and one must resort to phenomenological models to simulate soft processes. The Lund String Model [63] is one such example. It can be supplemented directly to the pQCD fixed-order calculations, but in this case the resulting jets would be narrower than those observed in data. The situation is

substantially improved when fixed-order pQCD is supplemented with higher-order resummed contributions. This approach can be pictured as a parton cascade produced by the interacting partons. They give a more realistic partonic state with which the subsequent hadronization can produce more realistic jets. The basic elements of a MC event generator are outlined below, using Fig. 3.28 as a reference:

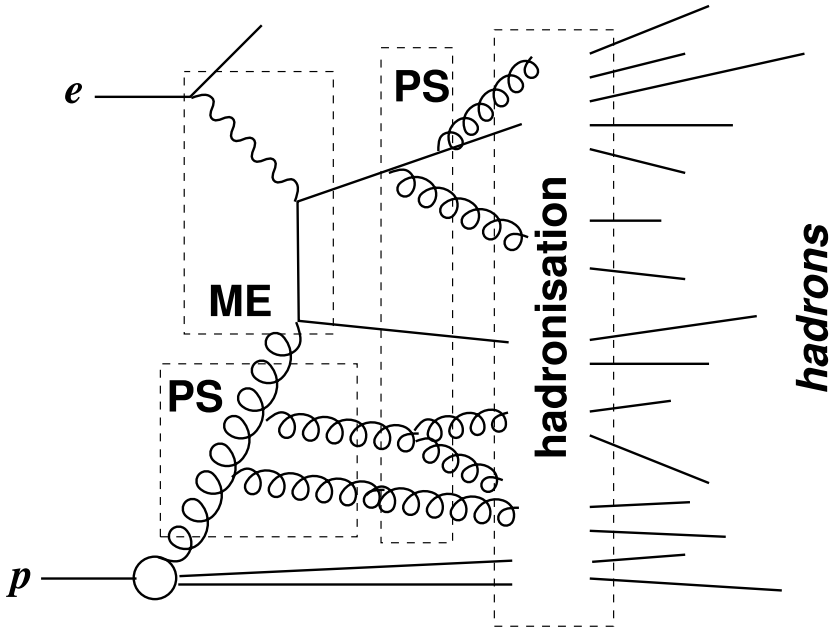


Figure 3.28: Schematic representation of a Monte Carlo event generator. The matrix elements are supplemented by an initial and final-state parton shower before hadronization. The final hadrons can then be interfaced with a detector simulation.

- ***Complete pQCD calculations*** : The starting point of the MC simulation is the generation of the partonic distributions for the variables and processes of interest. They are generated using complete pQCD calculations at a given order in perturbation theory. For the MC event generators currently available at HERA, these calculations are only done at $O(\alpha_s)$.

- ***QED and QCD radiation*** (***Parton cascade***) : With the partonic distributions in hand, it is still possible to evolve the system further through pQCD. In the Parton Shower Model the scattered colored partons emit (branch into) more partons, who can again branch. Thus, these radiative contributions can be pictured as a parton cascade. The branchings follow DGLAP evolution. In the Color-Dipole Model the radiation is viewed as coming from the two colored antennae formed by the the struck parton and the proton remnant. QED radiation is also simulated and can have interesting effects in the final-state, but it does not participate in the hadronization process. The snapshot of the

MC-generated final-state partons after the parton cascade is defined as the 'MC parton level'.

- ***Hadronization*** : The MC parton level provides a well-suited input for the hadronization. A hadronization model is then applied and the partonic level is evolved by a soft process into colorless hadrons, the 'MC hadron level'. It is important to note that the hadronization model does not alter the global properties of the jets, which have already been determined by more energetic processes in the hard scattering and parton cascade.

- ***Remnant*** A DIS event contains a characterisctic 'proton remnant' in the forward region composed of the 'spectator partons' that have not taken part in the hard interaction. If the scattered parton is colored, so will the remnant system. The color connection with the remnant also has to be simulated and can have a detectable effect on the hadronization process.

- ***Detector simulation*** : Once the hadronization level is obtained, the event simulation is complete and can be submitted to a detector and trigger simulation programs, which output the events in the same format as the data and can be directly compared to it.

### 3.5.1 The parton cascade

The pure matrix element approach to the parton cascade has some problems, not the least of which is that the amount of work associated increases factorially with each order. The available MC programs for jet production in NC DIS only contain complete pQCD calculations to $O(\alpha_s)$. Moreover, there are certain enhanced higher-order contributions which cannot be ignored if one wants to obtain reasonable jets from an $O(\alpha_s)$-based calculation. One solution is to supplement the fixed-order calculations with the enhanced part of higher-order contributions summed to all orders, leading to the parton cascade picture already mentioned. The two models available for its implementation are described below.

#### The matrix element plus parton shower (MEPS) approach

The Parton Shower Model (PS) [62] supplements the fixed-order calculations with multiple branchings. This can be pictured as in Fig. 3.29, where the parton cascade is taken into account for both the initial and final-state hard-interacting partons. In the final state the evolving partons are time-like, and the shower moves to smaller scales with each branching, until a cut-off scale is reached beyond which pQCD is no longer applicable and the shower is stopped ($\sim$ 1GeV). In the initial state an

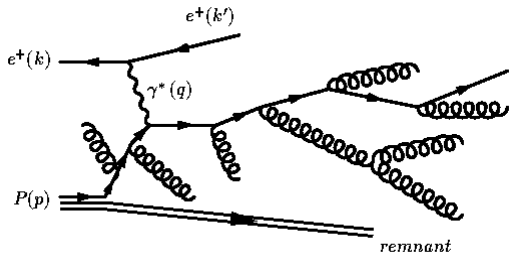


Figure 3.29: Schematic representation of the Parton Shower Model, in which initial and final-state small-angle radiation is resummed to all orders.

incoming quark from the proton, initially with a virtual mass-squared $-m_0$ and carrying a fraction $x_0$ of the proton's momentum, evolves to more virtual masses and lower momentum fractions with successive small-angle emissions. Eventually it participates in a hard-scattering process at a scale $Q^2$. In order to make the computation more efficient for the initial-state parton cascade, the PS is evolved backwards in time starting from the scale $Q^2$. This avoids evolving forward to unuseful virtualities.

**The color-dipole model (CDM)**

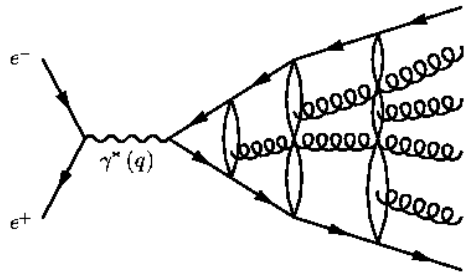


Figure 3.30: Schematic representation of the Color-Dipole Model, in which the parton cascade stems from the radiation of a dipole system. In DIS, the dipole is formed between the struck parton and the proton remnant.

In the color-dipole model [61] the cascade is not separated into initial and final-state emissions. Rather, the outgoing quark is viewed as forming part of a dipole system with the proton renmant. The emission of a gluon can be treated as radiation from this color dipole, and to a good approximation the emission of a second, softer gluon can be treated as radiation from two independent dipoles, one between the $q$ and $g$ and one between the $g$ and $\bar{q}$. In the CDM, this is generalized so that the emission of a third, still softer, gluon is given by three independent dipoles, and so

on (see Fig.3.30). This model was originally implemented for $e^+e^-$ where the picture was two radiating color anteannae formed by the outgoing quarks. The model has to be modified for DIS since the proton remnant has a transverse size. Moreover, this model only takes into account the possibility of QCD Compton-like events. The contribution of BGF-like processes is taken into account by implementing a procedure to correct for the first emission of the cascade.

### 3.5.2 Hadronization models

So far we have discussed the calculation of the matrix elements and the higher-order parton-cascade approach. Both of these processes can be calculated using perturbative QCD down to a soft scale beyond which it is no longer applicable. Since perturbative calculations are not possible, we are forced to rely on phenomenological models to complete the hadronization of the outgoing partons. This is necessary in the context of understanding and correcting the data for possible biases introduced by the experimental setup. Moreover, modelling the hadronization is important in terms of improving the comparison between the predictions and the data. There are two models available to implement the hadronization, the Lund String Model and the Cluster Fragmentation Model. They are briefly discussed here.

#### The Lund String Model

In this model the color field between the partons at the end of the parton shower is represented as a one-dimensional massless relativistic string. The string has a $q$ or $\bar{q}$ at each end, as shown in Fig. 3.31. It acts as a confining potential roughly linear with its length. Gluons are represented as momentum-carrying 'kinks' in the string. As quarks move apart the string gains length and energy which leads to fragmentation of the string through the appearance of new $q\bar{q}$ pairs. The string is fragmented iteratively according to the recipe:

$$f(z) \sim \frac{1}{z}(1-z)^a exp(-b\frac{m_T^2}{z}) \tag{3.7}$$

where $z$ is the fraction of the quantity $E + p_L$ of the parent string piece taken by its daughter, $m_T = \sqrt{p_T^2 + m^2}$, 'transverse' and 'longitudinal' refer to the string axis, and $a$ and $b$ are parameters. Momentum transverse to the string axis, $p_T$, is introduced in an *ad hoc* fashion using a Gaussian probability distribution. A large number of additional parameters is used to fine-tune the relative production of particles such as strange, pseudoscalar, and vector mesons.

For the jet analysis, the important part of the hadronization process is that its effect is mostly to 'smear' the energy already configured into a jet by the parton

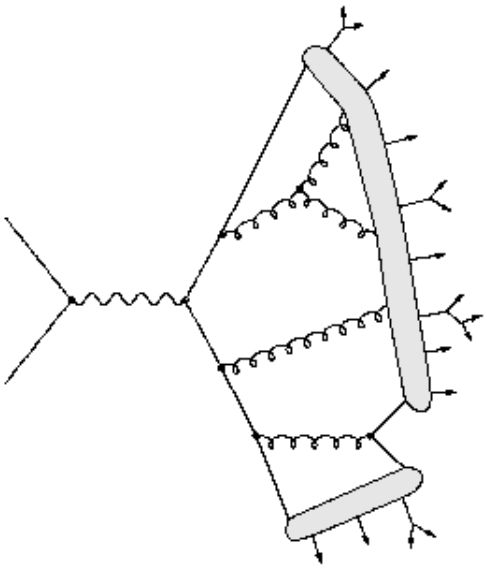

Figure 3.31: Schematic representation of the Lund String Model, in which quarks separate forming strings whose tension is roughly linear with its length until $q\bar{q}$ pairs from the vacuum break them into new sets of strings.

cascade. The jet radius discussed in Chapter 1 plays an important role here, since the more this paramater is reduced (as we will see), the more that jet production becomes sensitive to the 'smearing' effect of the hadronization.

**The Cluster Fragmentation Model**

The Cluster Fragmentation Model has been used in previous similar jet analyses in order to cross-check the corrections obtained with the Lund String Model approach. This model is implemented in the HERWIG [64] MC event generator. The analysis presented here relied on this previous check with HERWIG. In HERWIG, at the end of the parton cascade pairs of partons are associated into colorless clusters as shown in Fig. 3.32. These clusters then undergo phase-space decay to produce stable pions, kaons, and baryons. Clusters with mass larger than a parameter $M_{cl}$ are split into two before the phase-space decay. Additional parameters control the properties of heavy hadron decay.

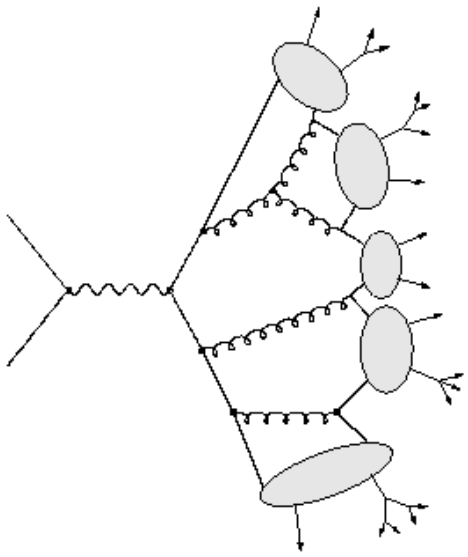

Figure 3.32: Schematic representation of the Cluster Fragmentation Model.

## 3.6 Detector Simulation

The final-state particles of each MC-generated event are processed through a ZEUS-detector simulation program which is based on GEANT 3.13 [70]. The GEANT program includes the response of the detector components and the interaction of particles in dead material. The generated events are passed through the detector simulation, subjected to the same trigger requirements as the data, and processed by the same reconstruction and offline programs. The output of the MC generators, after the detector simulation, is referred to as the 'detector level'. It is in the same format as the actual ZEUS data.

### 3.6.1 The LEPTO Monte Carlo generator

Since the angular correlations three-jet in NC DIS in the Breit frame sample is a sub-sample of the one used for the $\alpha_s$ analysis, the MC samples generated for these analyses were the same ones. From these, particular sub-samples were then selected for each analysis.

There are several event generators available for jet production in NC DIS at HERA. The LEPTO program [62] is the one used for the jet analyses presented here. The hard-scattering calculations are based on the leading-order electroweak cross section for the underlying parton level scattering and include QCD corrections using exact matrix elements. The PDFs are provided using the standard library

PDFLIB, which contains the information for most parametrizations of the proton densities.

LEPTO does not provide electroweak corrections. The HERACLES [71] program calculates first-order electroweak corrections and is interfaced to LEPTO via a program called DJANGOH [72].

After the hard scattering process has been calculated, there are two options for the parton shower, corresponding to the two models discussed previously. In LEPTO one can select to do the calculations using the 'Matrix Elements Plus Parton Shower' (MEPS) option or the Color-Dipole Model (ARIADNE-CDM) option [61]. Although in both cases the calculations are done by LEPTO, the sample generated by using the MEPS option is referred to sometimes as a 'LEPTO MC sample', while the sample generated using the CDM option is referred to as an 'ARIADNE MC sample'. Once the parton radiation is completed, the hadronization is performed with the Lund Model as implemented in JETSET [73–75]. After the fragmentation process, the final-state hadrons are provided and the simulated event can be used or fed into the detector simulation for further studies.

### 3.6.2 Technical details of the samples generated for the angular correlations and $\alpha_s$ analyses

Several MC samples were generated to determine the response of the detector to jets of hadrons and the correction factors necessary to correct the cross-sections for purity and efficiency. These samples were generated with at least five times the luminosity in the data to avoid statistical uncertainties. The generated events were passed through the GEANT 3.13-based ZEUS detector and trigger-simulation programs. They were reconstructed and analysed by the same program chain as for the data.

Neutral current DIS events including radiative effects were simulated using HERACLES 4.6.1 program with the DJANGOH 1.1 interface to the hadronization programs. HERACLES includes corrections for initial and final-state radiation, vertex and propagator terms, and two-boson exchange. The QCD cascade is simulated using the color-dipole model (CDM) including the leading-order (LO) QCD diagrams as implemented in ARIADNE 4.08. The CTEQ5D proton PDFs were used for these simulations. Fragmentation into hadrons is performed using the Lund string model as implemented in JETSET. The jet search was performed on the MC events using the energy measured in the CAL cells in the same way as for the data.

## 3.7 Comparisons of the MC parton level with DISENT and NLOJET++

One of the things for which MC simulations are used is to study the effects of the hadronization on the final-state partons of pQCD. This translates to obtaining 'hadronization correction' factors to be applied to the theoretical calculations in order to improve the comparison with the data.

It can be argued that the legitimacy of this procedure is compromised if the parton level of the MC, which includes the parton cascade, does not compare well to the calculations which it aims to correct for hadronization. Moreover, a focus of concern in the $\alpha_s$ analysis could be the following. If a MC is used that contains an assumed value of $\alpha_s(M_Z)$ in order to obtain correction factors, then a bias could be introduced on the $O(\alpha_s^2)$ prediction used to parametrize the dependence of the theory on the assumed value of $\alpha_s(M_Z)$ in order to extract $\alpha_s(M_Z)$. This bias will be very small since, as shown in Chapter 5, the hadronization correction factor is a fraction of two quantities that depend on the value $\alpha_s(M_Z)$, and thus the dependence cancels out to a large extent.

Fig. 3.33 shows a comparison of $d\sigma/dE_{T,B}^{jet}$ and $d\sigma/dQ^2$ at $O(\alpha_s^2)$ using the program DISENT, with the MC parton level obtained using the MEPS and CDM parton cascades. Both the MEPS and CDM options of LEPTO provide a fair description of the higher-order contribution for these observables. For this reason the hadronization corrections have been implemented to the $O(\alpha_s^2)$ predictions using the average of the values obtained with MEPS and CDM.

Fig. 3.34 shows a comparison of $d\sigma/dE_{T,B}^{jet}$ for different bins of $Q^2$ at $O(\alpha_s^3)$ using DISENT with the MC parton level using CDM. Although only the CDM option is shown, both the MEPS and CDM options of LEPTO provide a reasonable description of the higher-order contribution for these observables. Again the hadronization corrections have been implemented to the $O(\alpha_s^2)$ predictions using the average of the values obtained with MEPS and CDM.

It is interesting to test how well the angular-correlations are reproduced by the parton cascade, where the $O(\alpha_s)$ matrix elements in the MC models contain only BGF and QCD Compton, and thus no events with three jets in the Breit frame. The third jet in three-jet events in the MC is a result solely of the cascade. Since the branchings are those of pQCD there should be a fair simulation of the angular correlation distributions, except for the case in wich the third jet is emitted at large angles.

Fig. 3.35 shows a comparison of the $O(\alpha_s^2)$ and $O(\alpha_s^3)$ predictions using NLOJET++ and the MC predictions at parton level with different underlying parton

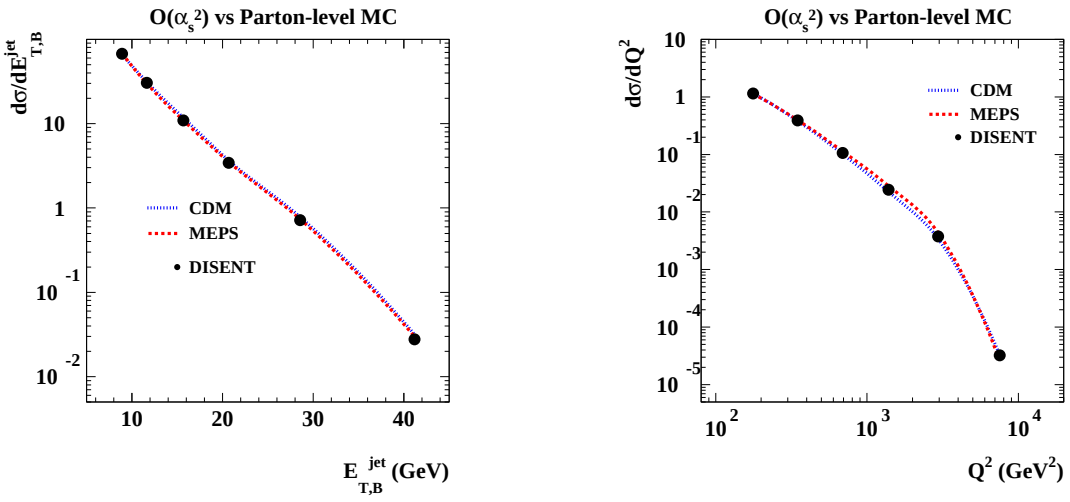


Figure 3.33: Comparison of the $O(\alpha_s^2)$ predictions using DISENT and the MC predictions at parton level with the CDM and MEPS parton cascade models.

cascade models. The distributions are shown for $\Theta_H$, $\cos\alpha_{23}$, $\cos\beta_{ksw}$, and $\eta^{jet}_{max}$ for the region of $Q^2 > 125$ GeV$^2$. The MC model with the MEPS parton cascade generally reproduces better the NLOJET++ predictions. The hadronization corrections were obtained using MEPS alone. The MC model with the CDM cascade was used as a systematic cross-check. Fig. 3.36 shows the same comparison for the restricted region of $500 < Q^2 < 5000$ GeV$^2$ with similar conclusions.

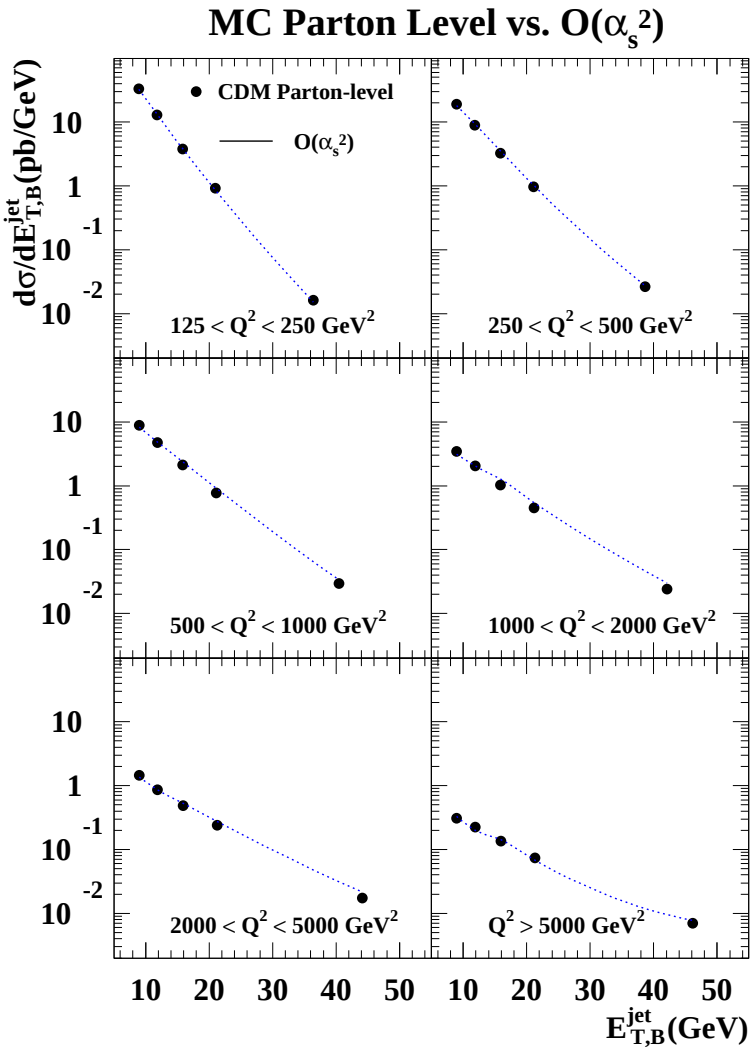


Figure 3.34: Comparison of the $O(\alpha_s^2)$ predictions using DISENT and the MC predictions at parton level with the CDM parton cascade model.

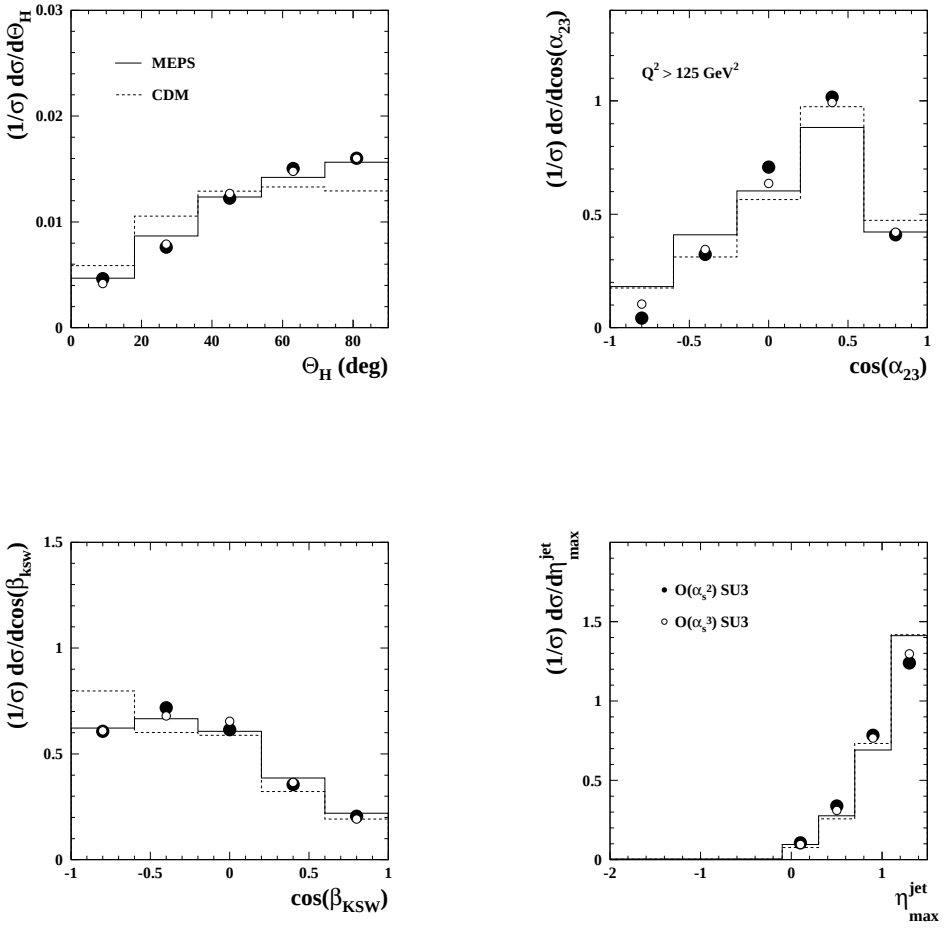


Figure 3.35: Comparison of the $O(\alpha_s^2)$ and $O(\alpha_s^3)$ predictions using NLOJET++ and the MC predictions at parton level with different underlying parton shower models. The distributions are shown for $\Theta_H$, $\cos\alpha_{23}$, $\cos\beta_{ksw}$ and $\eta^{jet}_{max}$ for the region of $Q^2 > 125$ GeV$^2$.

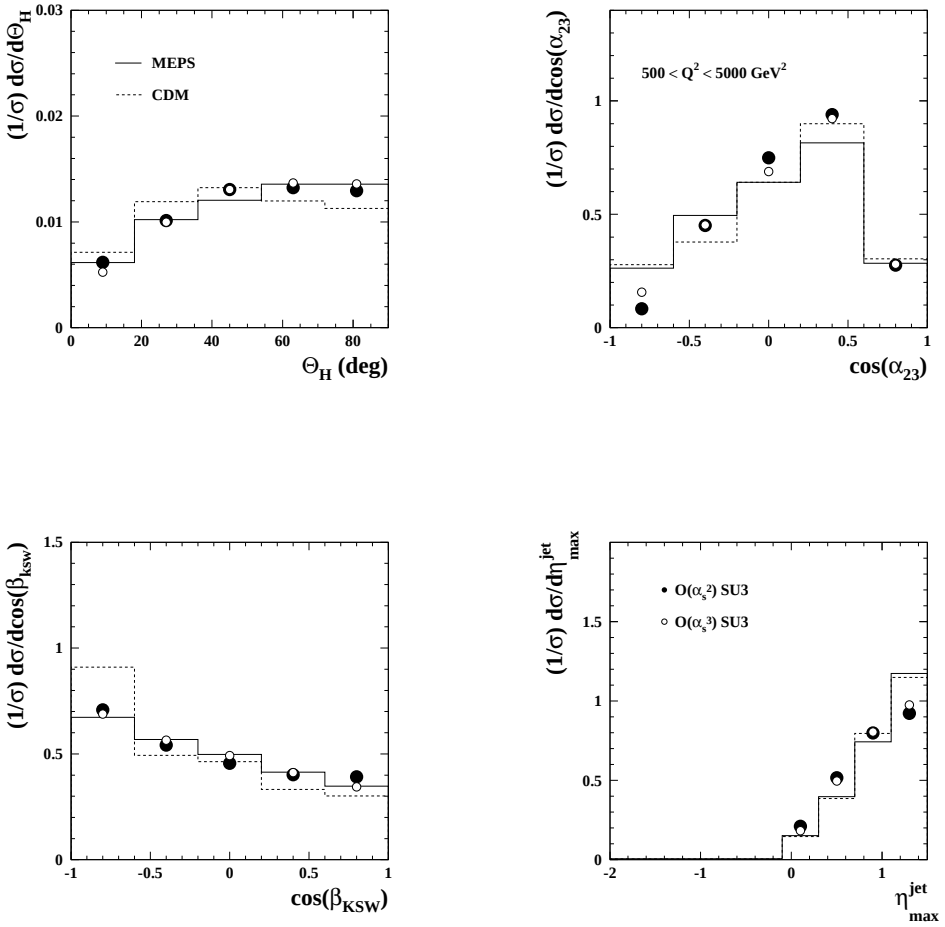


Figure 3.36: Comparison of the $O(\alpha_s^2)$ and $O(\alpha_s^3)$ predictions using NLOJET++ and the MC predictions at parton level with different underlying parton shower models. The distrubitions are shown for $\Theta_H$, $\cos\alpha_{23}$, $\cos\beta_{ksw}$ and $\eta_{max}^{jet}$ for the region of $500 < Q^2 < 5000$ GeV$^2$.

### 3.7.1 Theoretical uncertainties due to the parton cascade and hadronization models

The modelling of the parton cascade and the hadronization introduces a model dependence in the predictions. The theoretical uncertainty on the hadronization model has been estimated in previous analyses by comparing the predictions obtained using CDM with those of HERWIG and have been found to be small. This is expected since the hadronization does not have a large effect on the global properties of the jet. The parton cascade takes place at a larger energy scale and is expected to have a larger impact on the jet variables.

Fig. 3.37 and Fig. 3.38 show the estimated uncertainty due to this model dependence in the inclusive-jet cross sections. To correct the $O(\alpha_s^3)$ cross sections in this case, the average of MEPS and CDM was used and the uncertainty was calculated as half the difference between the predictions. As can be seen in the plots, these uncertainties are always below 5% for this analysis. For the angular-correlations analysis, the corrections obtained using MEPS were used. Figs. 3.39 and 3.40 show the relative theoretical uncertainties on the modelling of the parton cascade for the angular-correlation normalized cross sections. While in general we find that these uncertainties are small, in some regions they are dominant, such as the lower $\eta_{max}^{jet}$ region. In a rigorous fit, it would be desirable to exclude the lower $\eta_{max}^{jet}$ region for this reason.

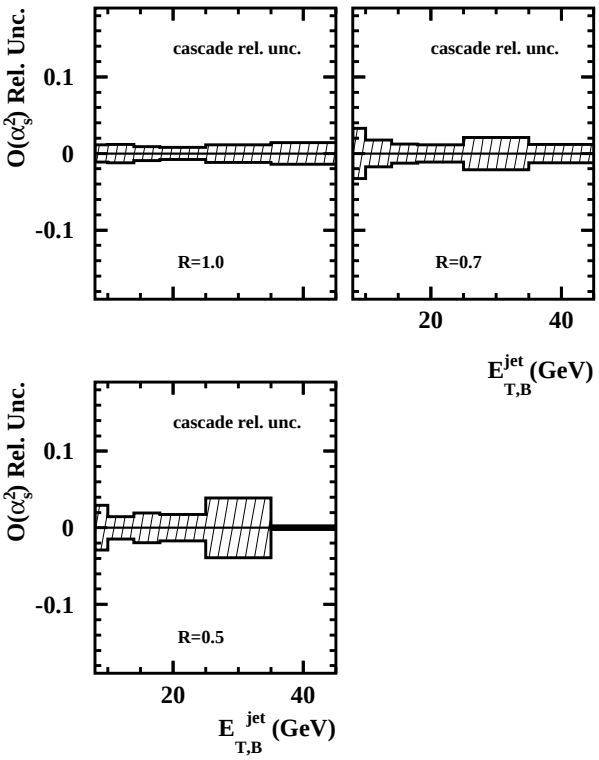


Figure 3.37: Estimate of the relative theoretical uncertainty in the inclusive-jet differential cross sections with respect to $E^{jet}_{T,B}$ on the modelling of the parton cascade.

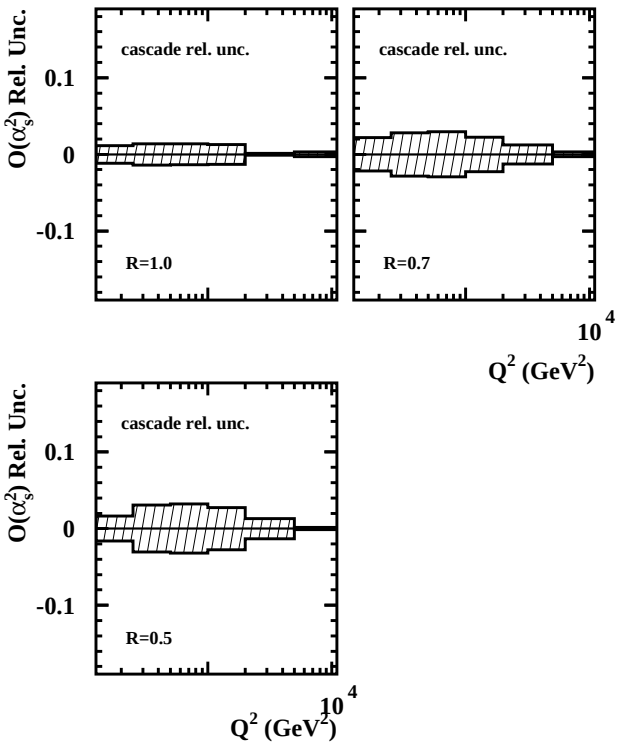


Figure 3.38: Estimate of the relative theoretical uncertainty in the inclusive-jet differential cross sections with respect to $Q^2$ on the modelling of the parton cascade.

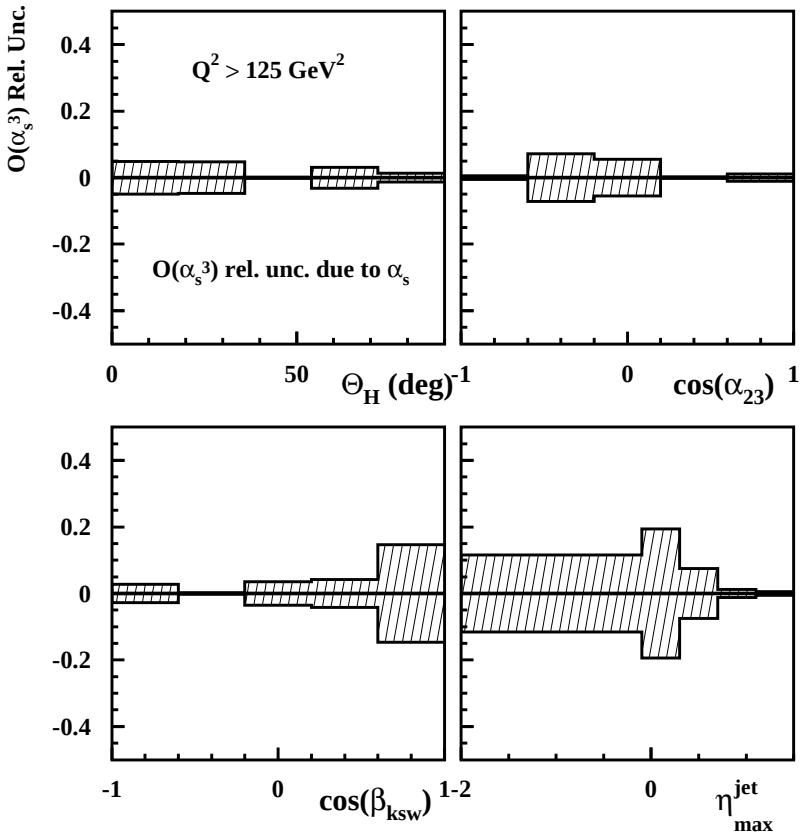


Figure 3.39: Estimate of the relative theoretical uncertainty in the three-jet normalized differential cross sections with respect to $\Theta_H$, $\cos\alpha_{23}$, $\cos\beta_{ksw}$ and $\eta^{jet}_{max}$ on the modelling of the parton cascade.

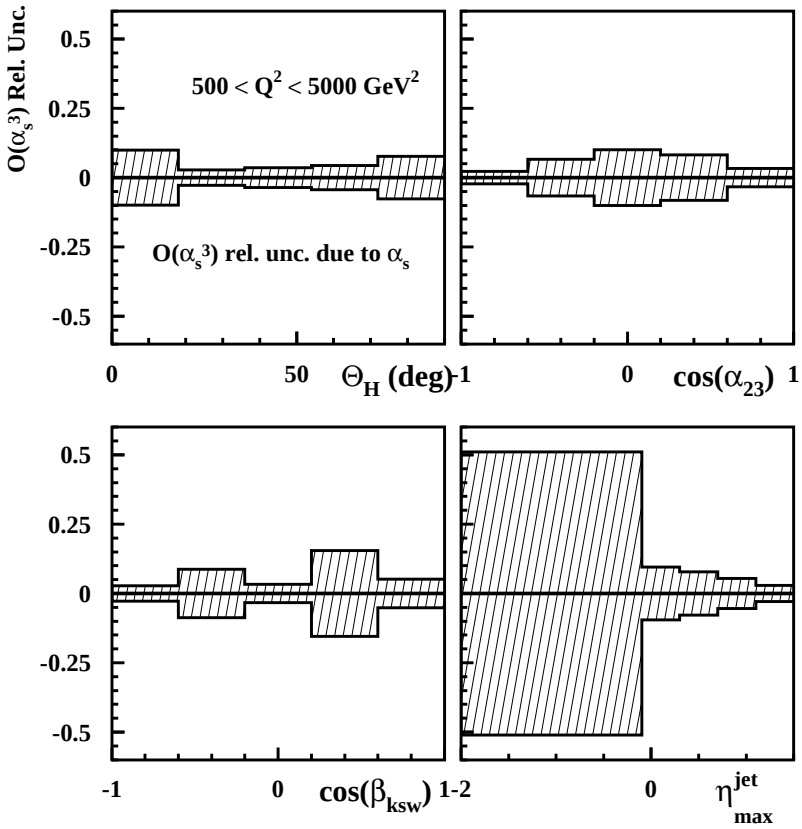


Figure 3.40: Estimate of the relative theoretical uncertainty in the three-jet normalized differential cross sections with respect to $\Theta_H$, $\cos\alpha_{23}$, $\cos\beta_{ksw}$ and $\eta^{jet}_{max}$ on the modelling of the parton cascade.

# Chapter 4

# Event selection and variable reconstruction

## 4.1 Introduction

This chapter contains a description of the NC DIS data samples used for the jet analyses. The events included in each jet-data sample are selected using a trigger system which was designed for this type of analyses. The three characteristic properties an event must have in order to be included in the sample are:

- Balanced transverse momentum;
- The presence of a scattered electron;
- The presence of at least one high $E_{T,B}^{jet}$ jet.

The main detector component used for the selection is the UCAL. UCAL cell energy deposits are taken as the 'particle' four-momenta fed into the jet reconstruction and electron finder algorithms. The CTD also plays an important role in terms of track and vertex reconstruction.

There are several known backgrounds to the selection of a NC DIS sample: photoproduction events (PHP), charged-current (CC) DIS events, beam-gas related events and cosmic rays. In order to remove these backgrounds carefully designed 'cleaning cuts' are applied in the selection. The same cuts are applied to the MC simulation.

Jet analyses naturally require that especial attention be paid to the proper reconstruction of jets, for which:

- The detector resolution of the jet variables $E_{T,B}^{jet}$, $\eta_{\mathrm{B}}^{\mathrm{jet}}$ and $\phi_B^{jet}$ has to be known and any alteration to these variables introduced by the detector needs to be corrected for;

- The energy scale of the jets has to be known and needs to be well simulated by the MC;
- The regions of the UCAL where the reconstruction of the jets is not sufficiently good have to be identified and excluded in the selection (both in the laboratory and in the Breit frame).

These three points necessitate the use of a MC simulation, as discussed in the previous chapter. The legitimacy of using the MC simulations rests on their ability to properly reproduce the distributions in the data for all the observables used in the analyses. The MC samples are generated with minimal bias restrictions and then submitted to exactly the same selection criteria as the data. Comparison plots between the distributions in the data and in the MC samples are usually the starting point of any analysis. The 'control plots' for the distributions in the data and MC samples are presented at the end of this chapter.

## 4.2 Data samples

Three data samples were selected for the jet analyses presented in this document:

- A data sample consisting of NC DIS events at high $Q^2$ with at least one high $E_T$ jet in the Breit frame based on $81.7 \pm 1.8$ pb$^{-1}$ of integrated luminosity collected with the ZEUS detector during the 1998-2000 (HERA I) running period. This data sample was used for:
  - Making inclusive-jet cross-section measurements of $d\sigma/dE^{jet}_{T,B}$ and $d\sigma/dQ^2$;
  - Making measurements of inclusive-jet cross sections in $d\sigma/dE^{jet}_{T,B}$ for different regions of $Q^2$ to be used as input to global PDF fits.
  - Studying the dependence on the jet-radius parameter in the $k_T$ clustering algorithm;
  - Extracting $\alpha_s(M_Z)$ and measuring its scale dependence. This data sample was also used in combination with H1 in order to produce a first combined HERA $\alpha_s(M_Z)$ determination;
  - There are 19,908 events in this sample after the selection discussed in this chapter for R=1. For R=0.7 there are 16,231 events and for R=0.5 there are 12,934 events.
- A data sample consisting of events at high $Q^2$ with at least three jets with high $E_T$ in the Breit frame based on $81.7 \pm 1.8$ pb$^{-1}$ collected with the ZEUS detector during the 1998-2000 (HERA I) running period. This data sample

was used for measuring angular-correlations of the three jets and testing the underlying symmetry group; There are 1095 events in this sample.

- A data sample collected with the ZEUS detector during the 2004-2007 (HERA II) running period. During those years HERA operated with polarized electrons or positrons. This sample corresponds to an integrated luminosity of 370 $pb^{-1}$. This is an analysis in progress whose aim is to improve upon the results of the other two analyses by using HERA II data.
  - To obtain even more stringent tests of pQCD;
  - To obtain the 'ultimate' determination of $\alpha_s(M_Z)$ and PDFs from HERA;
  - To obtain enough data statistics to make an extraction of the color factors possible in the three-jet analysis;
  - There are 91,555 events in this sample.

## 4.3 Event selection

Two inclusive-jet NC DIS samples were selected using the HERA I and HERA II running periods, respectively. From the HERA I running period sample, a subsample with more restrictive jet criteria, namely the presence of at least three jets of high $E_T$ in the Breit frame, was selected. This was the sample used for the three-jet angular-correlations analysis. As already outlined in the introduction, the main properties of a NC DIS event are: balanced transverse momentum, the presence of a scattered electron, and the presence of jets in the final state. The following sections contain an outline of the specific trigger chain and the selection cuts used. These are divided into:

- ***Online selection***: triggers implemented during the online data-taking. These are more inclusive cuts in order to avoid the loss of valuable physics data and to minimize CPU time during data taking;
- ***Offline selection***: The selection includes full jet and scattered electron reconstruction. It also includes all the 'cleaning cuts' employed to reject backgrounds.

### 4.3.1 Online selection

The trigger selection chain is implemented online. It was designed to select NC DIS events with the highest possible efficiency. Thus, the cuts imposed at the different trigger levels are not overly exclusive and involve only the short calculations allowed

by CPU constrains. The computations involved in the selection become more refined as the CPU time available increases going up the trigger chain.

**First Level Trigger**

At the FLT level, minimum overall UCAL energy deposits were required. The conditions imposed:

- $E^{FLT}_{EMC} > 10$ GeV or
- $E^{FLT} > 15$ GeV or
- $E^{FLT}_{BEMC} > 3.4$ GeV or
- $E^{FLT}_{REMC} > 2.0$ GeV or
- $E^{FLT}_{T} > 11.6$ GeV

Additionally, it was demanded that the event has at least one good track found by the CTD FLT.

**Second Level Trigger**

At the SLT, the following conditions were imposed:

- A reconstructed vertex with $-60\text{cm} < z_{vtx} < 60\text{cm}$. This cut removed events which occured far from the interaction region, since the detector response could be very different for such events. This cut also removed beam-gas related events;
- $E - p_z > 8.0$ GeV,where $E$ and $p_z$ are the energy and the longitudinal momentum of the event, determined from energy deposits in the UCAL. For a NC interaction of massless particles, $E - p_z = E_e + E_p + p_{z,e} - p_{z,p} = 2E_e = 2 \times 27.5$ GeV, so that events with $E - p_z << 55$ GeV are associated with PHP or CC interactions;
- $E^{cone}_T > 8.0$ GeV, where $E^{cone}_T$ is the sum of transverse energy in all UCAL cells outside a cone of 10° around the FCAL beampipe;
- $E - p_z > 12$ GeV or $p_z/E < 0.95$ to further reduce the contamination from beam-gas interactions.

**Third Level Trigger**

The following conditions were imposed at the TLT:

- The number of 'bad tracks' had to be smaller than 6. A 'bad track' was defined as a track which is long enough for a good reconstruction (i.e. it has more than 5 hits in axial superlayers and more than 5 hits in stereo superlayers, and more than 20 hits in total) and points to a very backward vertex ($z_{vtx} < -75$cm). The cut on the number of 'bad tracks' suppressed proton beam-gas background events, which usually contain forward-going tracks coming from the backward region;

An event was required to fulfill at least one of the following conditions at the TLT:

- $E_T^{cone} > 25$ GeV;
- The time available at the TLT level permitted the application of a jet-finding algorithm. Events with at least one jet of $E_{T,jet} > 10$ GeV and $\eta_{jet} < 2.5$ were retained. The jet algorithm was applied over all the cells in the UCAL, including those that would be associated with the electron candidate, so that the electron candidate was usually identified as a jet at this point;
- $p_z/E < 1.0$ and two or more jets with $E_{T,jet} > 6$ GeV and $\eta_{jet} < 2.5$.

As described in the experimental setup, during the offline reconstruction of the events some additional requirements were imposed and stored in a bit structure (DST bits). However, no further requirements were applied at this level for the jet analyses.

### 4.3.2 Offline selection

At this stage a NC DIS sub-sample was selected from the available ZEUS data sample on tape through the particular trigger selection just described. This sub-sample was stored in a format called 'ntuple', which basically consists of arrays containing all the relevant information for the specific analysis for each event. After the trigger online selection a sample was obtained containing a very 'inclusive' NC DIS selection of jets, whose purity and efficiency can be further improved, and whose phase-space region has yet to be restricted to the given analysis. Further requirements were imposed to select the final sample as follows.

**Identification of the scattered electron- the SINISTRA electron finder**

A neural network approach was developed based on the showering properties of the electron in the segmented UCAL. The aim is to best identify the electromagnetic

particles using only the information from the UCAL and to separate them from the single hadrons or jets of particles for which the pattern of energy deposits in the UCAL can look quite similar, especially at low energies.

It was found that electrons and background populate different regions in a multi-dimensional configuration space parametrized by the variables characterizing the shower. These variables relate, for example, to the width and depth of the shower. The particular values for this variable for the case of an electron shower were determined using a neural network approach, trained using Monte Carlo samples for both electrons and hadrons. A high efficiency was found for electron identification.

The algorithm used in these analyses for the electron identification based on this neural network approach is called SINISTRA [76]. The algorithm proceeds by merging together groups of cells according to pre-defined criteria. Each cell is merged with the adjacent cell of highest energy; This clustering procedure associates cells which most likely come from a single particle shower. A cluster is defined to be composed of no more than $3 \times 3$ cells. A candidate cluster for an electron is called an island. The input variables are the energies registered in the corresponding island and the neural network projects the information into one output variable $P$, which is interpreted as the probability that the island originates from the scattered electron ($P \sim 1$) or is of hadronic origin ($P \sim 0$).

It is possible to define the electron four-momentum using the constituent cells and weighting their respective positions with their energies. Using the energy and position, the four-momentum of the island is reconstructed. Each island was associated a probability. The one with the largest probability was taken as the scattered electron.

Efficiency and purity studies of the electron candidates have shown that an optimal selection required an associated probability of at least $P > 0.9$ and that the probability given by SINISTRA was reliable if the island had an energy larger than 10 GeV. These were the requirements imposed on the identified scattered electron for the events in the NC DIS samples.

To improve the purity and efficiency of the electron candidate, three additional cuts were imposed:

- $y_e < 0.95$, where $y_e = 1 - E'_e(1 - \cos\theta_e)/(2E_e)$ and $E'_e$ ($\theta_e$) is the energy (polar angle) of the electron candidate. This condition removed events in which fake electron candidates were found in the FCAL;

- the total energy not associated with the electron candidate within a cone of radius 0.7 units in the pseudorapidity-azimuth ($\eta - \phi$) plane around the electron direction should be less than 10% of the electron energy. This condition

removed photoproduction and DIS events in which part of a jet was falsely identified as the scattered electron;

- for $20^\circ < \theta_e < 140^\circ$, the fraction of the electron energy within a cone of radius 0.3 units in the $\eta - \phi$ plane around the electron direction should be larger than 0.9; for $\theta_e < 20^\circ$, the cut was raised to 0.98. This condition removed events in which a jet was falsely identified as the scattered electron;

Note that although some algorithms make use of tracking information, in SINISTRA it is not necessary.

**Signal selection**

Even after the electron identification, there can still be substantial backgrounds in the sample; sometimes photons, jets, or other isolated particles are mis-identified as the scattered electron. One such background is photoproduction, defined at HERA as an event with a $Q^2 \leq 1$ GeV$^2$. Another background is 'beam-gas events'. Molecules can leak into an imperfect vacuum and cause collisions near the interaction point that may 'look' like nominal interactions. These types of collisions can be identified by a large number of 'bad tracks' in the CTD not stemming from the primary vertex. Finally, Charged-Current (CC) mediated events in DIS give a neutrino in the final state and can be characterized by missing transverse momentum in the detector and the absence of a scattered electron.

Here is a list of the 'cleaning cuts' applied to suppress the contribution from specific backgrounds:

- $p_T/\sqrt{E_T} < 2.5$ GeV$^{1/2}$, where $p_T$ is the missing transverse momentum as measured with the UCAL ($p_T \equiv \sqrt{p_X^2 + p_Y^2}$) and $E_T$ is the total transverse energy in the UCAL. This cut removed charged-current DIS events, cosmic rays and beam-related background;

- Using the definition of a bad track already given, the number of bad tracks is required to be less than 5. The presence of many bad tracks in the detector is typical of an event produced by a beam-gas interaction;

- $38 < (E - p_Z) < 65$ GeV, where $E$ is the total energy as measured in the UCAL, $E = \sum_i E_i$ and $p_z$ is the z-component of the vector $\vec{p} = \sum_i E_i \vec{r_i}$. In both cases the sum runs over all UCAL cells, $E_i$ is the energy of the UCAL in cell $i$ and $\vec{r_i}$ is a unit vector along the line joining the reconstructed vertex and the geometric centre of the cell $i$. This cut removed events with large initial-state radiation and further reduced the background from photoproduction;

- A cut in $-34cm < z_{vtx} < 34cm$. This cut removed events whose vertex is far from the nominal interaction region. These events were removed because the detector response to events far from the nominal interaction region can be different;

- There can be background from elastic Compton processes ($ep \to ep\gamma$), since the $\gamma$ or the electron could be falsely identified as a jet. In these events there are two electromagnetic clusters in the UCAL, thus two SINISTRA electron candidates can be found. Cuts on energy and isolation are applied as for the first candidate. If there was a second candidate that passes these cuts and the energy on the whole UCAL excluding that belonging to the two candidates was found to be less than 4 GeV, the event was rejected.

**Phase-space region and jet selection**

The phase-space of the analyses was defined in terms of $Q^2$ and $\cos\gamma_h$, where $\cos\gamma_h$ is defined by

$$\cos\gamma_h = \frac{(1-y)xE_p - yE_e}{(1-y)xE_p + yE_e} \tag{4.1}$$

The variable $\cos\gamma_h$ is the cosine of the scattered parton polar angle in QPM events. The variable $\cos\gamma_h$ is reconstructed via

$$cos\gamma_h = \frac{(\sum_h p_{xh})^2 + (\sum_h p_{yh})^2 - (\sum_h (E-p_z)_h)^2}{(\sum_h p_{xh})^2 + (\sum_h p_{yh})^2 + (\sum_h (E-p_z)_h)^2}, \tag{4.2}$$

where the sums run over all the UCAL cells not associated to the electron candidate. At the detector level, $Q^2$ was reconstructed using the double-angle method,

$$Q^2_{DA} = 4 \cdot E_e^2 \frac{\sin\gamma_h(1+\cos\theta_e)}{\sin\gamma_h + \sin\theta_e - \sin(\theta_e+\gamma_h)}, \tag{4.3}$$

where $\theta_e$ is the angle of the scattered electron. The double-angle method does not involve final-state electron or jet energies and was shown to exhibit better reconstruction properties since it does not involve the energy information or its uncertainty from the UCAL.

A cut of $Q^2_{DA} \geq 125$ GeV$^2$ was used to select a region that is well into the DIS regime. For the angular correlations analysis, a second sub-sample was also selected using $500 \leq Q^2_{DA} \leq 5000$ GeV$^2$. The 'hadronic' $\gamma_h$ was restricted to $-0.65 \leq \cos\gamma_h \leq 0.65$. The lower limit of this cut avoided a region with limited acceptance due to the requirement on the energy of the scattered electron, while the upper limit was chosen to ensure good reconstruction of the jets in the Breit frame.

Additional selection cuts designed to improve on the reconstruction of the jets were applied:

- jets with low transverse energy in the laboratory frame ($E^{jet}_{T,L} < 2.5$ GeV) have not been included in the final sample; this cut removed a small number of jets for which the uncertainty on the energy corrections was large;

- events were removed from the sample if any of the jets was in the backward region of the detector ($\eta^{\rm jet}_{\rm L} < -2$). This requirement removed events in which a radiated photon from the electron was misidentified as a hadronic jet in the Breit frame;

- The distance in $\eta - \phi$ plane from the electron of any jet was required to be less than one;

- $E^{\rm jet}_{T,\rm B} > 8$ GeV;

- $-2 < \eta^{\rm jet}_{\rm B} < 1.5$.

For the $\alpha_s$ analysis, every event was required to have at least one jet with $E^{jet}_{T,B} > 8$ GeV. For the three-jet analysis, every event was required to have at least three jets, of which at least one must have $E^{jet}_{T,B} > 8$ GeV and the other two $E^{jet}_{T,B} > 5$ GeV. The final jet selection was implemented after the jet energy scale and $E^{jet}_{T,B}$ loss caused by the detector were corrected for as explained in the next sections.

## 4.4 Jet reconstruction using the UCAL

The UCAL is the main detector component used to carry out the identification of jets. Jets are reconstructed using the $k_T$ clustering algorithm in the Breit frame with the UCAL cell four-momenta as the initial 'input set of partcles'. A four-momentum, $p^\mu$ was associated to each cell, where $p^0$ corresponds to the energy deposit in the cell and $\vec{p}$ was determined by treating the cell as a massless particle and its position to be at its center. In order to reconstruct jets in the Breit frame, the four-momenta of the cells in the UCAL not associated to the electron candidate were transformed into the Breit frame, where the $k_T$ cluster algorithm is applied.

It is important to quantify the resolution of the detector to the jet variables and any bias the dead material in front of the UCAL may introduce to their measurement. It is also necessary that the energy scale of the jets be the same in the data and MC samples. To ensure that this is the case, studies of the energy-scale in the UCAL for the data and MC simulations were carried out through for each of the analyses. This section describes both of these studies.

| $\eta_{\rm L}^{\rm jet}$ region | Energy-scale corrections |
|---|---|
| [-2.0,0.0] | 0.993 |
| [ 0.0,1.0] | 0.995 |
| [ 1.0,1.5] | 0.988 |
| [ 1.5,2.0] | 1.013 |
| [ 2.0,3.0] | 1.019 |

Table 4.1: Energy-scale correction factors applied to the $E_{T,L}^{jet}$ of the jets in the data for the HERA I analyses.

### 4.4.1 Jet energy scale corrections

The energy scale uncertainty of the UCAL coupled with differences in the hadronic final state between the data and MC simulations has traditionally been the dominant systematic uncertainty in jet measurements. Energy-scale uncertainties of $\pm(3-5)\%$ lead to uncertainties of $\sim \pm(10-20)\%$ in the cross-section measurements. Neutral current deep inelastic scattering events with high $Q^2$ provide a means to calibrate the UCAL energy scale. QPM-type of events, in which the final state consists of the scattered electron back-to-back with one jet were used to calibrate the UCAL. Since the total $E_T = 0$ the electron's $E_T$ $(= p_{T,DA})$ must compensate the jet's $E_T$. Notice that the quantity $p_{T,DA}$ is obtained using the 'double angle' method which relies solely on the angular position and not on the UCAL energies. The idea is that the ratio $R = \frac{E_{T,L}^{jet}}{p_{T,DA}}$ should be the same in the MC and in the data, a necessary condition to validate the usage of the MC simulation in terms of obtaining acceptance correction factors.

Thus, the double ratio $R' = \frac{R^{DATA}}{R^{MC}}$ was used as an energy-scale correction factor to level the data jet energy scale with that of the MC simulation. In order to take into account the fact that the offset between data and MC may depend on the region of the detector, these factors were obtained as a function of $\eta_{\rm L}^{\rm jet}$. Table 4.1 shows the $\frac{1}{R'}$ factors applied to correct the $E_{T,L}^{jet}$ of the jets in the data. The values shown are for the HERA I jet analyses (the corresponding correction factors for the HERA II analyses were also obtained).

### 4.4.2 Detector bias and resolution

In order to know the precision with which jet measurements can be made and to see any biases introduced by the detector, comparisons of the hadronic system before and after the simulation of the detector were made. The quantities $E_{T,\rm B}^{\rm jet}$, $\phi_B^{jet}$ and $\eta_{\rm B}^{\rm jet}$ were obtained for each jet at hadron and detector levels in order to study

the correlation and relative differences. This procedure required a 'jet matching' algorithm to identify the jets at the hadron level with the corresponding ones at detector level for a given simulated event.

The correlation between the hadron and detector level of the MC simulation is a measure of the resolution and the bias on the jet variables introduced by the detector. The better the correlation, the better the resolution. Any bias introduced by the detector was identified as a deviation from a perfect correlation. The spread of the correlation reflects the detector resolution. Figs. 4.1 through 4.6 show the correlation between the hadron and detector levels for the jet variables in the $\alpha_s$ analysis for different jet radii. As expected, the detector does not alter the position of the jets, but they however loose $E_{T,L}^{jet}$ as they go through dead material in front of the UCAL. Moreover, there is no particular dependence on the jet radius. Figs. 4.7 through 4.10 show the correlation between the hadron and detector levels for angular-correlation variables in the three-jet analysis. While there is no bias, the reconstruction of these variables is not as good as for the $E_{T,\mathrm{B}}^{\mathrm{jet}}$, $\phi_B^{jet}$ and $\eta_{\mathrm{B}}^{\mathrm{jet}}$ variables, although still reasonable. The energy loss was corrected for by using the method described below.

The jet-energy loss and resolution of the jet variables can be quantified by means of a gaussian fit to the relative difference between the hadronic level and the detector level $E_{T,\mathrm{B}}^{\mathrm{jet}}$. The procedure to obtain a set of correction factors to correct for the loss of $E_{T,\mathrm{B}}^{\mathrm{jet}}$ in the detector is the following:

- Standard cuts were applied at the hadron level to select the jets in the MC sample. At the detector level, the cuts were relaxed in order to allow for a wider phase-space;

- For each event, the jets at hadron and detector levels were matched. The matching procedure involves calculating, for each event, the distance between each of the jets at hadron level and all the jets at detector level in the $\eta - \phi$ plane,

$$\Delta[hd] = \sqrt{(\eta_{\mathrm{L}}^{\mathrm{jet}}(CAL) - \eta_{\mathrm{L}}^{\mathrm{jet}}(HAD))^2 + (\phi_L^{jet}(CAL) - \phi_L^{jet}(HAD))^2}. \quad (4.4)$$

  The smallest distance found matched the two jets, if this distance is smaller than 1. The procedure was repeated until all the jets were matched or no pair of jets is left for which the distance is less than 1;

- The mean value $< E_{T,L}^{jet}(CAL) >$ as a function of $E_{T,L}^{jet}(HAD)$ was parametrized by a straight line, or set of straight lines if necessary. The fitted function has the form

$$E_{T,L}^{jet}(CAL) = m \cdot E_{T,L}^{jet}(HAD) + b \quad (4.5)$$

For a given jet at detector level the corrected energy is then obtained by inverting this function:

$$E_{T,L}^{jet}(COR) = \frac{E_{T,L}^{jet}(CAL) - b}{m}, \tag{4.6}$$

- The energy loss is not the same for different pseudorapidity regions. Thus, the parametrizations were done separately for each region in $\eta_{\mathrm{L}}^{\mathrm{jet}}$. Fig. 4.11 shows the correlation before any correction for the fourteen $\eta_{\mathrm{L}}^{\mathrm{jet}}$ regions.

- The $E_T^{jet}$ correction was transferred from the laboratory frame to the Breit frame according to the formula:

$$E_{T,\mathrm{B}}^{\mathrm{jet}}(CORR) = E_{T,\mathrm{B}}^{\mathrm{jet}}(CAL) \cdot \frac{E_{T,L}^{jet}(CORR)}{E_{T,L}^{jet}(CAL)}. \tag{4.7}$$

This correction procedure was repeated for each jet analysis. In the $\alpha_s$ analysis, it was done separately for each jet radius. Fig. 4.12 shows the profile plots for the detector $E_{T,L}^{jet}$ in terms of the hadron $E_{T,L}^{jet}$ for each of the fourteen regions of $\eta_{\mathrm{L}}^{\mathrm{jet}}$. After the corrections were applied the bias was removed as shown in Fig. 4.13. Although Figs. 4.12 and 4.13 refer to the angular-correlations analysis, very similar results were obtained for the $\alpha_s$ analysis for all the choices of the jet radius.

### 4.4.3 The Breit frame and the cut on $\cos\gamma_h$

The transformation of the UCAL geometry from the laboratory to the Breit frame can result in UCAL cells that are too large in the $\eta - \phi$ plane to allow a good jet reconstruction. A single cell of the UCAL in the Breit frame may extend over a large $\eta - \phi$ region such that an entire jet can be reconstructed from it.

A useful parameter to study the range of transformations into the Breit frame is the angle with which the struck quark in the QPM is ejected with respect to the incoming proton axis, termed $\gamma_h$. The transformation to the Breit is the identity when $\cos\gamma_h = -1$ and the Breit frame coincides with the laboratory frame in this limit. On the other hand, as $\cos\gamma_h$ approaches 1 the cells close to the beampipe expand while the ones in the barrel region contract. A study was made to determine which interval of $\cos\gamma_h$ allows a good jet reconstruction and the corresponding cut in $\cos\gamma_h$ was considered as part of the sample selection.

The appropiate cut on $\cos\gamma_h$ could be determined analytically, but it is simpler and equally valid to obtain it from a comparison between the distribution of $\cos\gamma_h$ at the hadron and detector levels of the Monte Carlo sample. In Fig. 4.14, it is observed that the hadron and detector (reconstructed) distributions in $\cos\gamma_h$ increasingly

differ as $\cos\gamma_h \to 1$, which is where the cells of the UCAL are maximally distorted. This figure shows the region of $\cos\gamma_h$ for which the jet reconstruction becomes inadequate. As $\cos\gamma_h \to -1$, the distributions also increasingly disagree, but this is a reflection of the cut imposed on the electron candidate's energy $E'_e > 10$ GeV. Thus, the appropriate range for $\cos\gamma_h$ was obtained from Fig. 4.14 and applied as part of the selection criteria of the NC DIS sample for both analyses, in order to ensure a good reconstruction of jets in the Breit frame. This range was found to be $-0.65 \leq \cos\gamma_h \leq 0.65$ and is part of the phase-space region selection we have mentioned earlier in this Chapter.

It is desirable to perform all the kinematic cuts in the Breit frame since a cut applied on variables in the laboratory frame would affect the selection in a kinematical-dependent way. The reconstruction of jets with $\eta_{\mathrm{L}}^{\mathrm{jet}} > 2$ in the laboratory frame is not adequate due to the proximity of the jet to the beam pipe. In this region part of the jet might go undetected. Thus, events containing jets with $\eta_{\mathrm{L}}^{\mathrm{jet}} > 2$ need to be discarded. The correlation between $\eta_{\mathrm{L}}^{\mathrm{jet}}$ and $\eta_{\mathrm{B}}^{\mathrm{jet}}$ after the cut on $\cos\gamma_h$ was used to determine which cut on $\eta_{\mathrm{B}}^{\mathrm{jet}}$ corresponds to a cut of $\eta_{\mathrm{L}}^{\mathrm{jet}} > 2$. Fig. 4.15 shows that a cut of $\eta_{\mathrm{L}}^{\mathrm{jet}} > 2.5$ in the laboratory frame corresponds to a cut of $\eta_{\mathrm{B}}^{\mathrm{jet}} > 1.5$ in the Breit frame. This cut is also part of the selection criteria mentioned earlier in the Chapter.

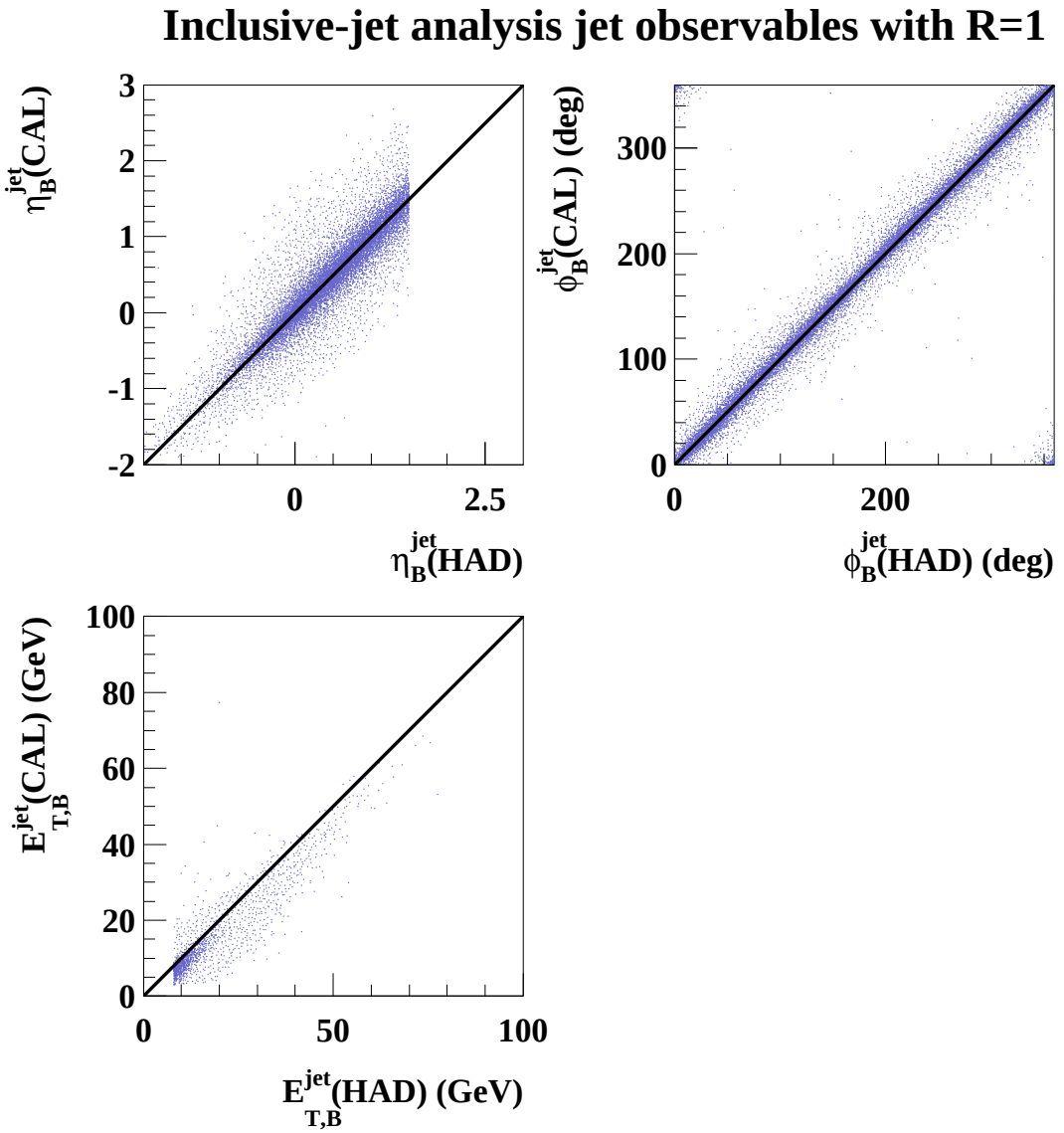


Figure 4.1: Correlations between detector and hadron levels for the jet variables $E_{T,\mathrm{B}}^{\mathrm{jet}}$, $\phi_B^{jet}$ and $\eta_{\mathrm{B}}^{\mathrm{jet}}$ for the inclusive-jet sample based on CDM using jet radius R=1.0.

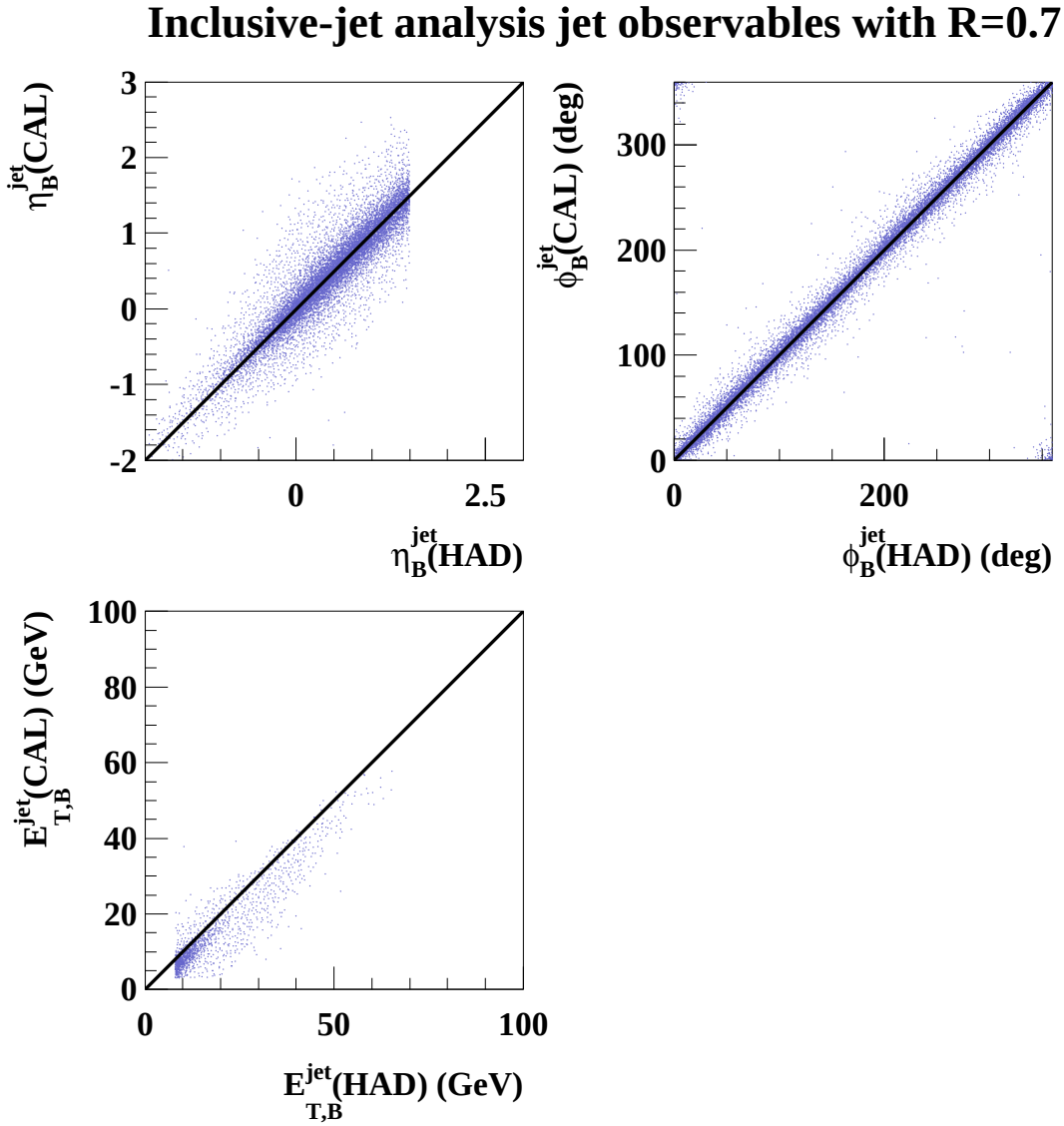


Figure 4.2: Correlations between detector and hadron levels for the jet variables $E_{T,\mathrm{B}}^{\mathrm{jet}}$, $\phi_B^{jet}$ and $\eta_{\mathrm{B}}^{\mathrm{jet}}$ for the inclusive-jet sample based on CDM using jet radius R=0.7

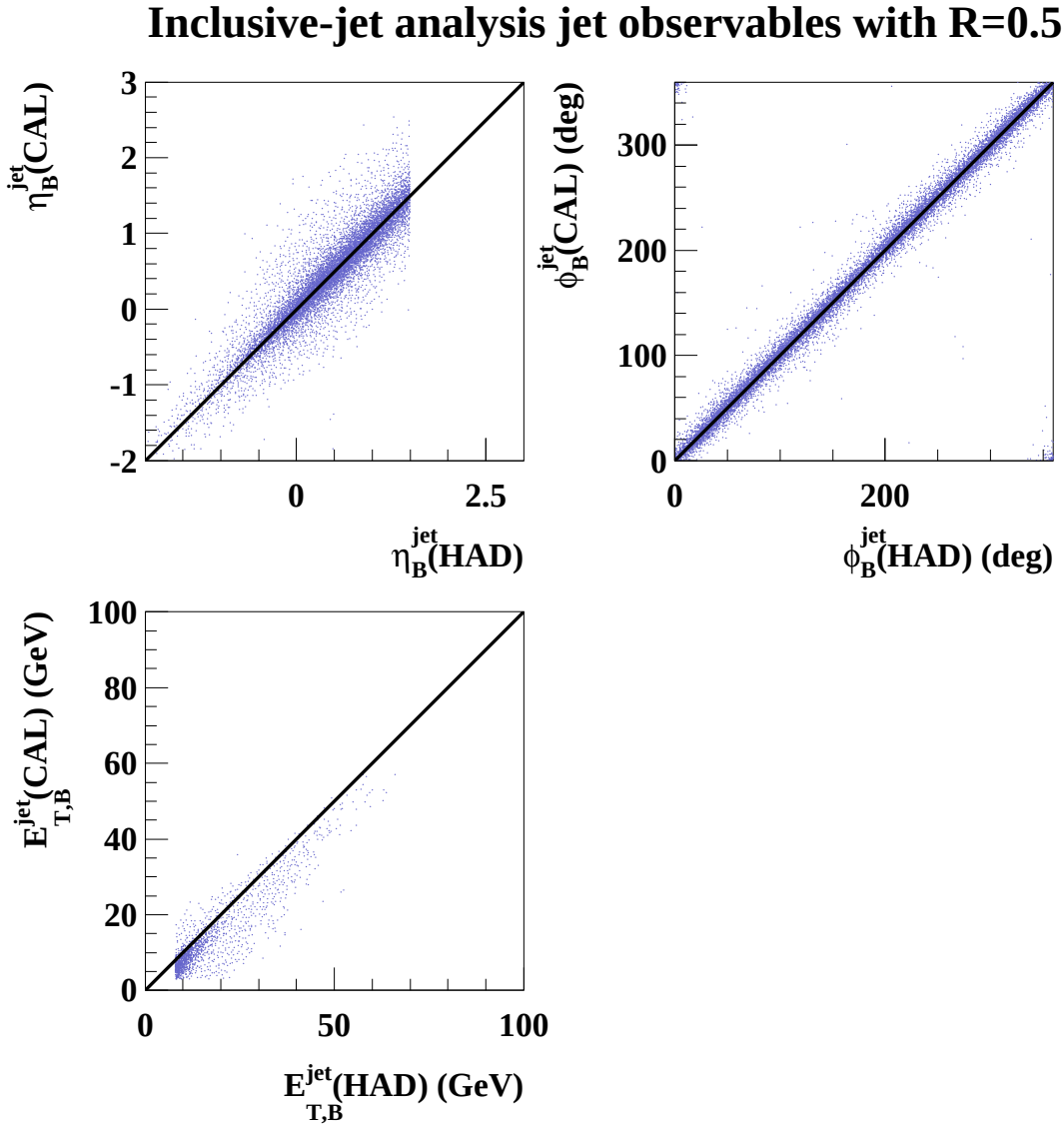


Figure 4.3: Correlations between detector and hadron levels for the jet variables $E_{T,\mathrm{B}}^{\mathrm{jet}}$, $\phi_B^{jet}$ and $\eta_{\mathrm{B}}^{\mathrm{jet}}$ for the inclusive-jet sample based on CDM using jet radius R=0.5

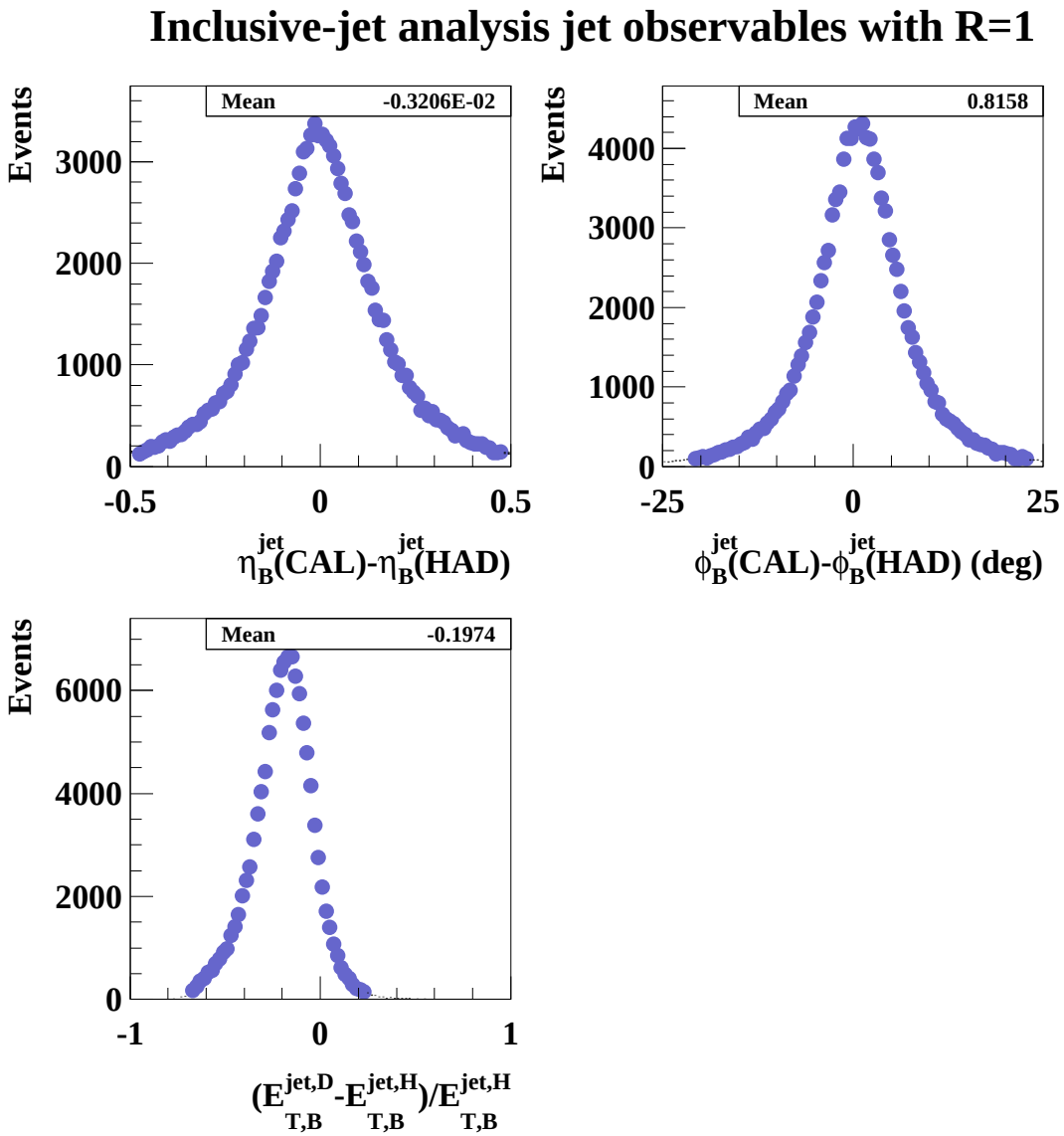


Figure 4.4: Differences between detector and hadron levels for the jet variables $E_{T,\mathrm{B}}^{\mathrm{jet}}$, $\phi_B^{jet}$ and $\eta_{\mathrm{B}}^{\mathrm{jet}}$ for the inclusive-jet sample based on CDM using jet radius R=1.0.

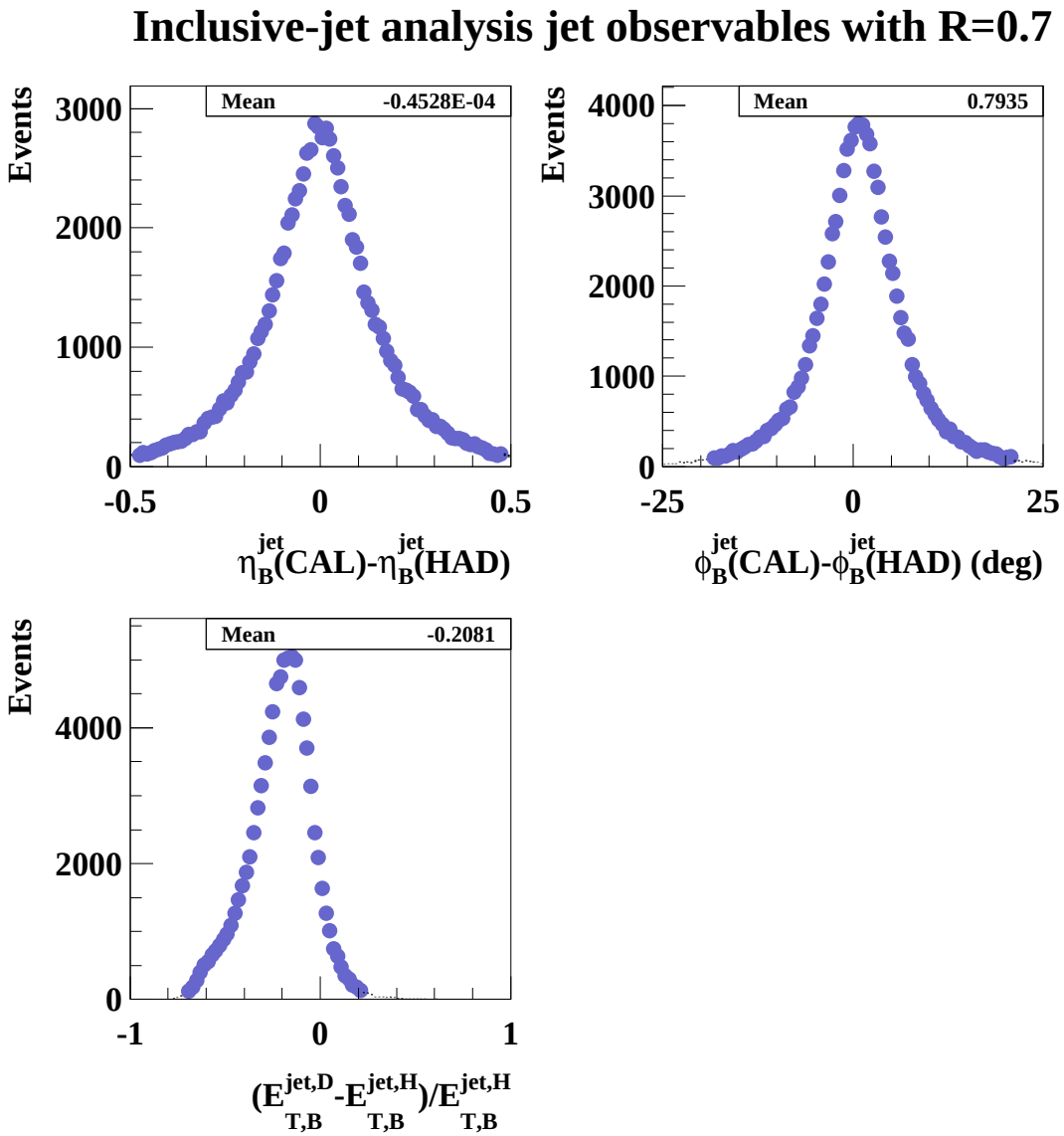


Figure 4.5: Differences between detector and hadron levels for the jet variables $E_{T,\mathrm{B}}^{\mathrm{jet}}$, $\phi_B^{jet}$ and $\eta_{\mathrm{B}}^{\mathrm{jet}}$ for the inclusive-jet sample based on CDM using jet radius R=0.7

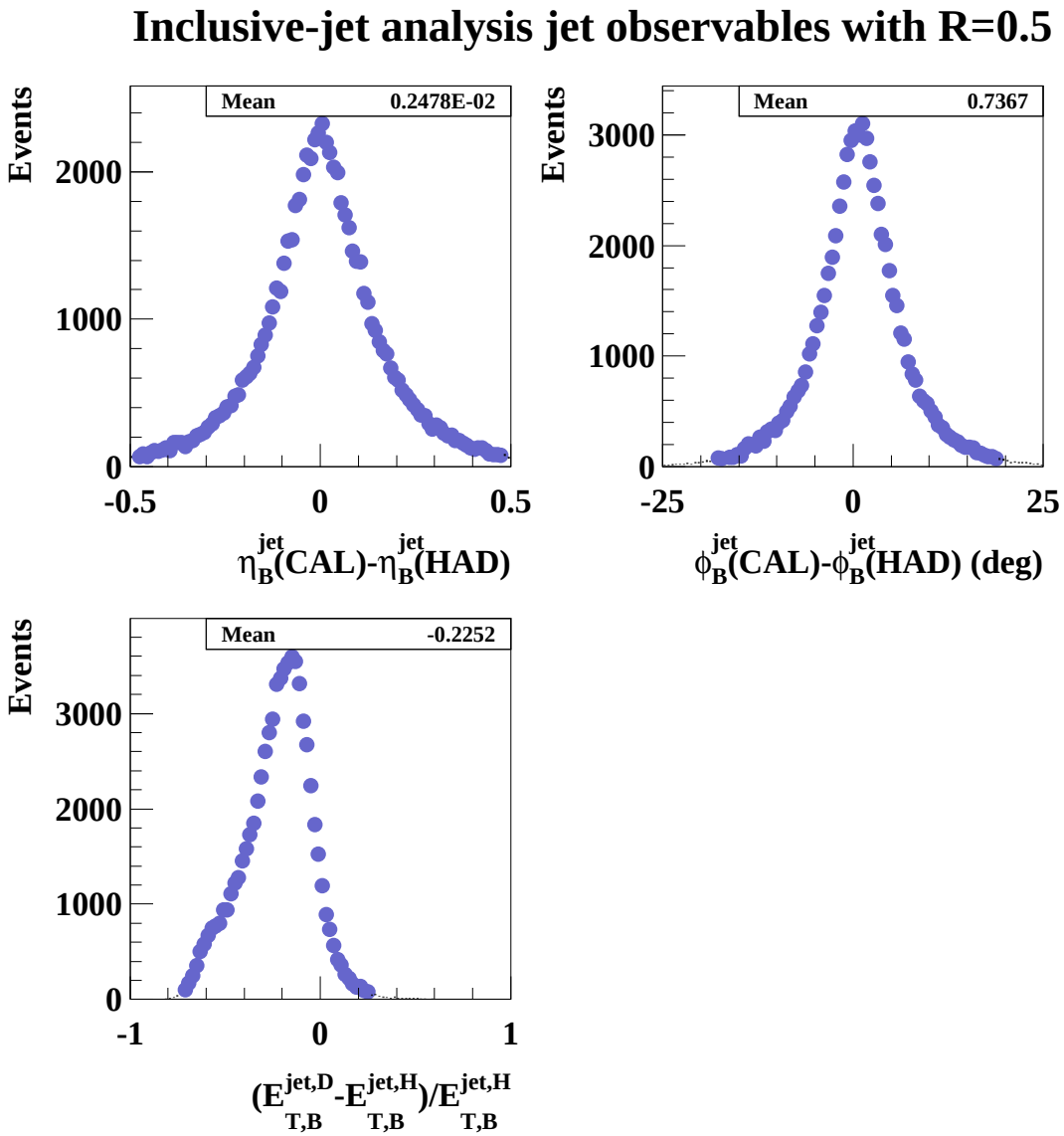


Figure 4.6: Differences between detector and hadron levels for the jet variables $E_{T,\mathrm{B}}^{\mathrm{jet}}$, $\phi_B^{jet}$ and $\eta_{\mathrm{B}}^{\mathrm{jet}}$ for the inclusive-jet sample based on CDM using jet radius R=0.5

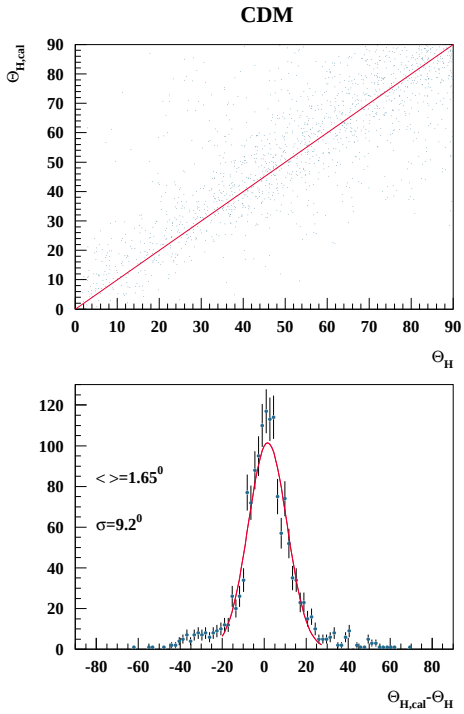


Figure 4.7: Correlation and difference between detector and hadron levels for the angular-correlation variable $\Theta_H$.

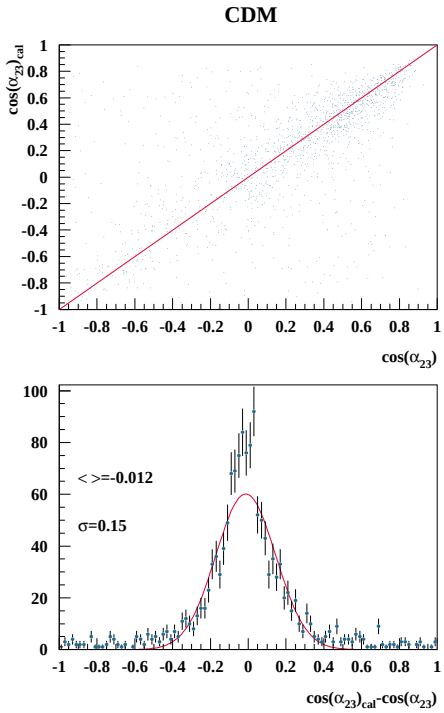


Figure 4.8: Correlation and difference between detector and hadron levels for the angular-correlation variable $\cos\alpha_{23}$.

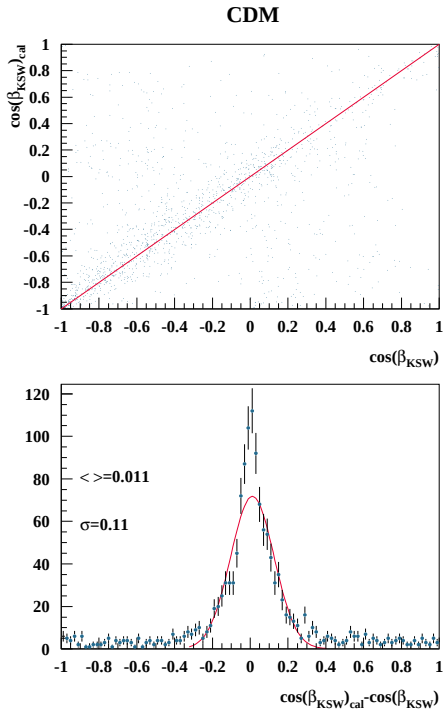


Figure 4.9: Correlation and difference between detector and hadron levels for the angular-correlation variable $\cos\beta_{ksw}$.

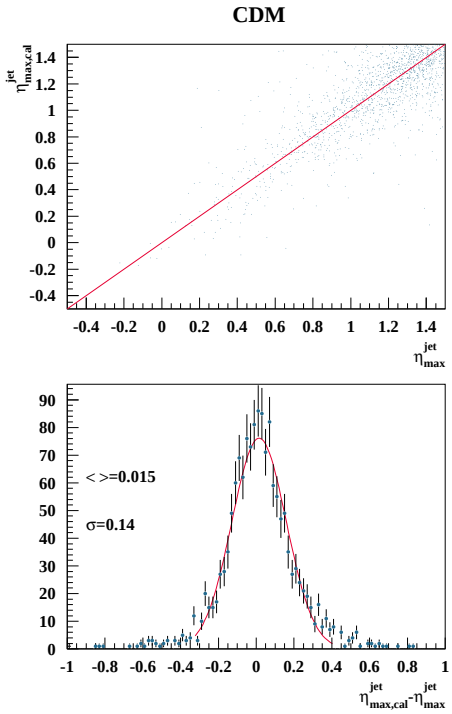


Figure 4.10: Correlation and difference between detector and hadron levels for the angular-correlation variable $\eta^{jet}_{max}$.

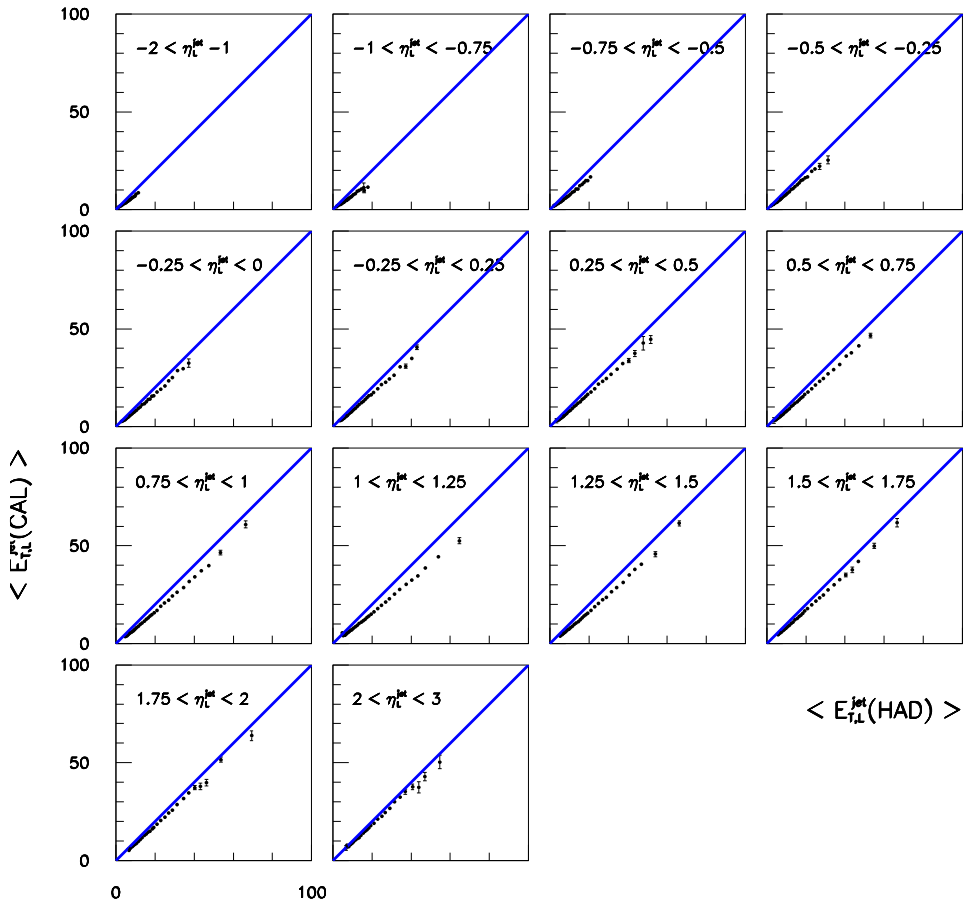


Figure 4.11: $< E_{T,L}^{jet}(CAL) >$ as a function of $E_{T,L}^{jet}(HAD)$ in each region of $\eta_{\mathrm{L}}^{\mathrm{jet}}$ using the MC simulations based on CDM.

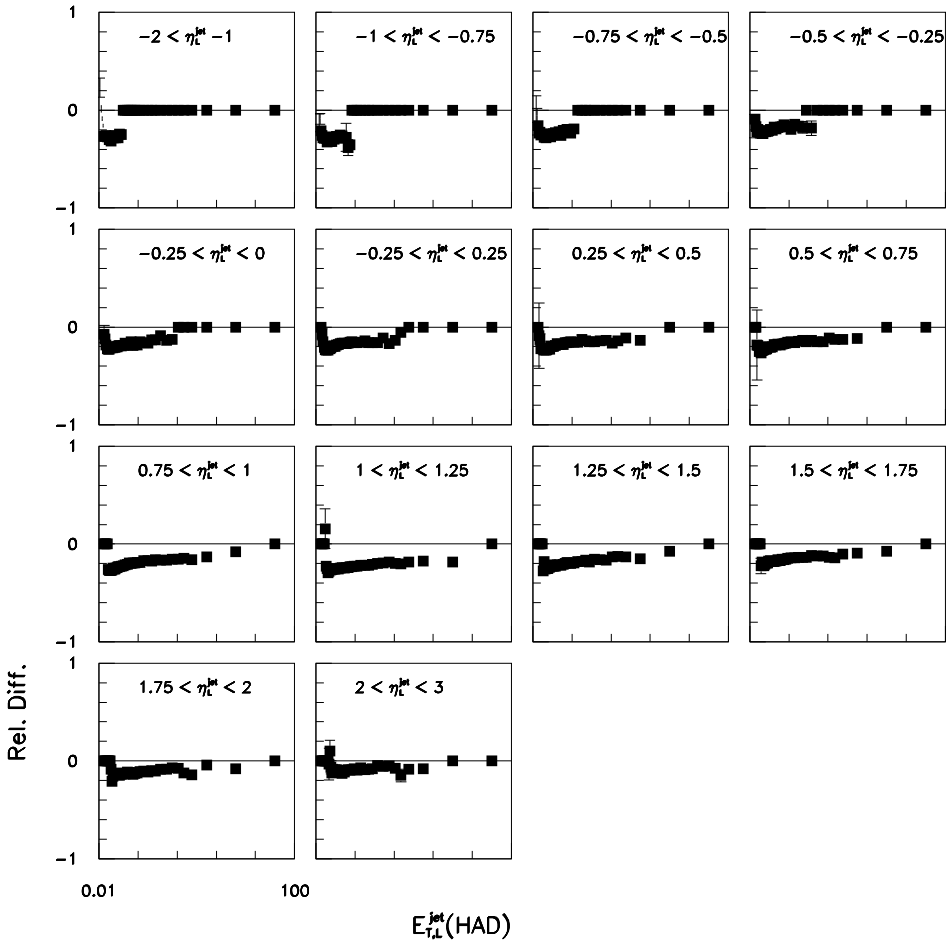


Figure 4.12: The relative difference $< (E^{jet}_{T,L}(CAL) - E^{jet}_{T,L}(HAD))/E^{jet}_{T,L}(HAD) >$ as a function of $E^{jet}_{T,L}(HAD)$ in each region of $\eta^{\rm jet}_{\rm L}(HAD)$ using the MC simulations based on CDM.

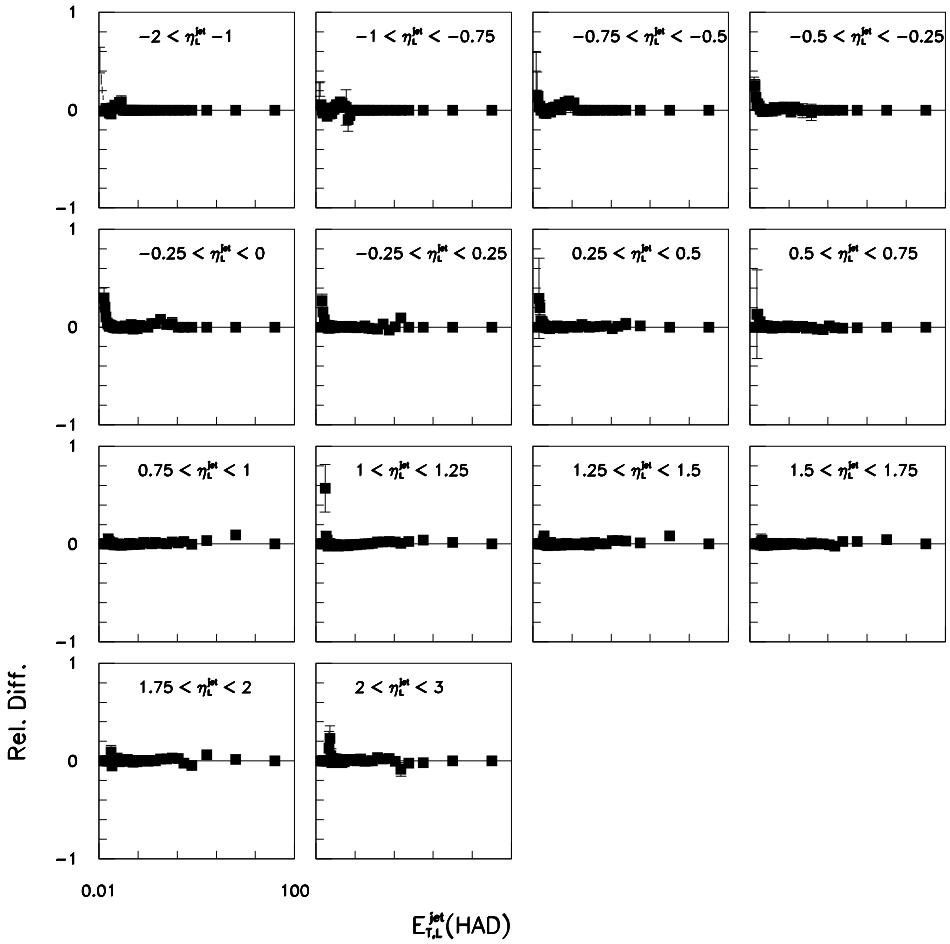


Figure 4.13: The relative difference $< (E_{T,L}^{jet}(CORR) - E_{T,L}^{jet}(HAD))/E_{T,L}^{jet}(HAD) >$ as a function of $E_{T,L}^{jet}(HAD)$ in each region of $\eta_{\mathrm{L}}^{\mathrm{jet}}(HAD)$ using the MC simulations based on CDM.

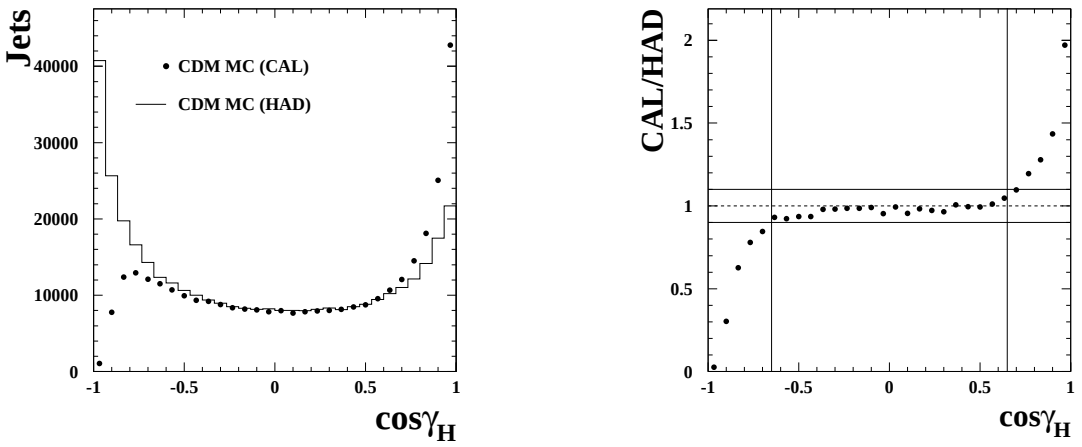


Figure 4.14: Distributions in $\cos\gamma_h$ at the hadron and detector levels in the MC simulation (left). The ratio of the detector- and hadron-level distributions as a function of $\cos\gamma_h$ (right).

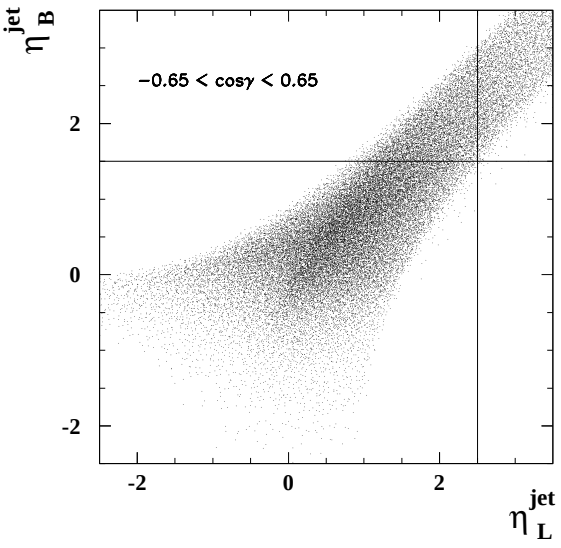


Figure 4.15: Correlation between $\eta_{\mathrm{L}}^{\mathrm{jet}}$ and $\eta_{\mathrm{B}}^{\mathrm{jet}}$ after imposing the $\cos\gamma_h$ cut.

## 4.5 Data and Monte Carlo distributions

The validity of the correction factors and reconstruction studies shown so far relies on the fact that the MC simulation is able to properly describe the distributions in the data sample for all the variables used. This section includes all the comparisons of the data distributions to those of the MC simulation for the different analyses. In the plots shown here the distributions in the MC sample were normalized to those in the data. Both for the data and the MC simulations the distributions are those obtained after the entire selection described earlier in this chapter is applied.

### 4.5.1 Comparisons of data and MC for the $\alpha_s$ analysis using HERA I data

For the $\alpha_s$ analysis using HERA I data the comparisons included in this section show that both MC simulations (CDM and MEPS) are able to reproduce the distributions in the data. For example, Fig. 4.16 shows a comparison of the total $E_T$, $y_{jb}$, the missing $p_T$ and the energy in the FCAL distributions. The variable $y_{jb}$ was reconstructed using the Jacquet-Blondel method:

$$y_{jb} = \frac{\sum_h (E - p_z)_h}{2E_e} \tag{4.8}$$

where the sum runs over all the UCAL cells not associated to the electron candidate. Note that the simulation of the energy distribution in the FCAL is somewhat shifted to higher energies with respect to the data. This known discrepancy does not, however, affect our jet analyses since at the end, as we will show, the jet variables are well described and this energy distribution is not actually being used.

Fig. 4.17 shows the energy in the RCAL, in the BCAL and the $E_{T,\mathrm{B}}^{\mathrm{jet}}$ and $\eta_{\mathrm{B}}^{\mathrm{jet}}$ distributions (with a finer binning than that used for the cross section measurements). The RCAL energy distribution has a sharp peak corresponding to the scattered electron's energy contribution. The $\eta_{\mathrm{B}}^{\mathrm{jet}}$ and $E_{T,\mathrm{B}}^{\mathrm{jet}}$ particularly show the jets being mostly in the forward region and their $E_{T,\mathrm{B}}^{\mathrm{jet}}$ decreasing as a power function of $E_T$. Fig. 4.18 displays the $P_T(HAD)$ of the hadronic system, the number of bad and good tracks, and the $\frac{P_T}{\sqrt{E_T}}$ distributions.

The electron candidate's energy, its polar angle, $x_{DA}$ and $Q^2_{DA}$ distributions of the events in the sample are shown in Fig. 4.19. The variable $x$ was reconstructed using the double-angle method according to the formula:

$$x_{DA} = \frac{E_e}{E_p} \cdot \frac{\sin\gamma_h + \sin\theta_e + \sin(\theta_e + \gamma_h)}{\sin\gamma_h + \sin\theta_e - \sin(\theta_e + \gamma_h)} \tag{4.9}$$

There we show that the electron's energy sharply peaks at a value $\sim 27$ GeV, which means the selection cut on $E'_e > 10$ GeV does not have a big impact on the efficiency

of the selection. In terms of the polar angle, the electron tends to be found, as would be expected, at large angles with respect to the proton direction, which corresponds to the RCAL or backward region. The $x_{DA}$ and $Q^2_{DA}$ distributions are shown with a finer binning than that used for cross-section measurements. The distribution in $x_{DA}$ for this sample peaks at $x \sim 10^{-2}$.

The description of the $Q^2_{DA}$ distribution in the data can be further improved for both the MEPS and CDM simulations. For this purpose a re-weighting function in terms of $Q^2_{generated}$ was obtained. All the MC distributions shown in this chapter have been re-weighted with such a function. While the description of the $Q^2_{DA}$ distribution improves, the rest of the distributions are still well described.

Fig. 4.20 shows the distributions for $y_{DA}$ and the z-vertex. The variable $y$ was reconstructed using the double-angle method according to the formula:

$$y_{DA} = \frac{\sin\theta_e(1-\cos\gamma_h)}{\sin\gamma_h + \sin\theta_e - \sin(\theta_e+\gamma_h)} \tag{4.10}$$

Fig. 4.21 shows the distributions for $Q^2_{DA}$, $E^{\rm jet}_{T,\rm B}$ and $\eta^{\rm jet}_{\rm B}$ with the binning that corresponds to the cross-section measurements. As can be seen, the jet distributions in $Q^2_{DA}$, $E^{\rm jet}_{T,\rm B}$ and $\eta^{\rm jet}_{\rm B}$ are well described by both CDM and MEPS; for this reason the average of both simulations was used to obtain the correction factors to be applied to the data as discussed in the next chapter.

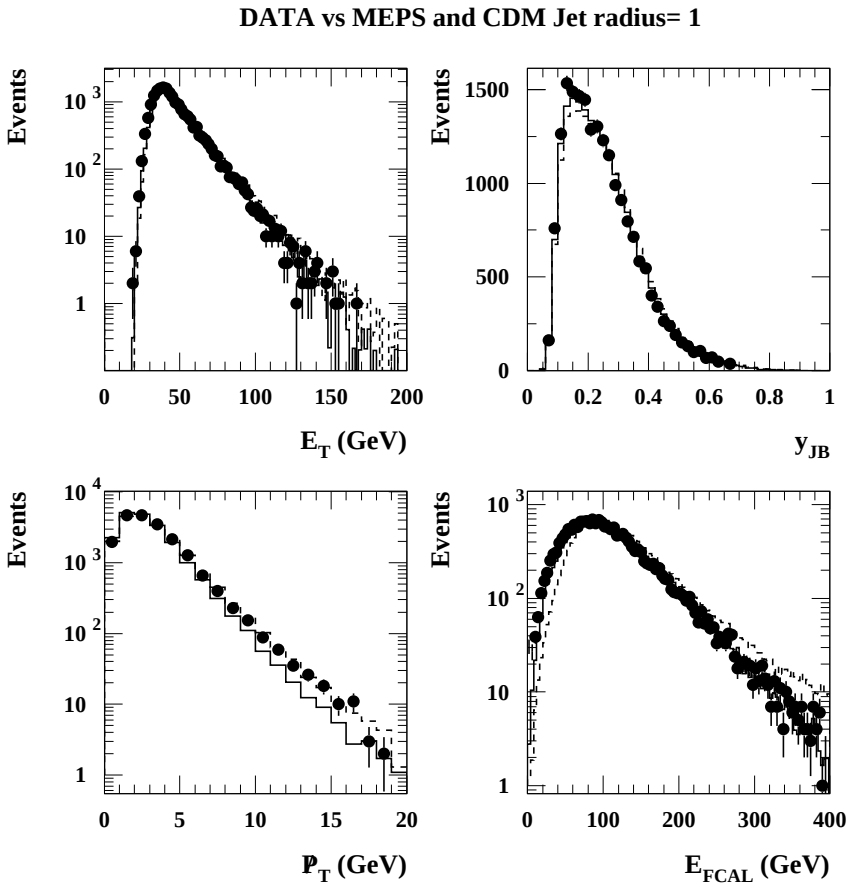


Figure 4.16: Comparison of the MC simulations based on CDM (dashed) and MEPS (solid) to the distributions in the data (dots) for the total $E_T$ of the event in the laboratory frame, the $y_{jb}$ variable, the missing $p_T$ and the energy in the FCAL.

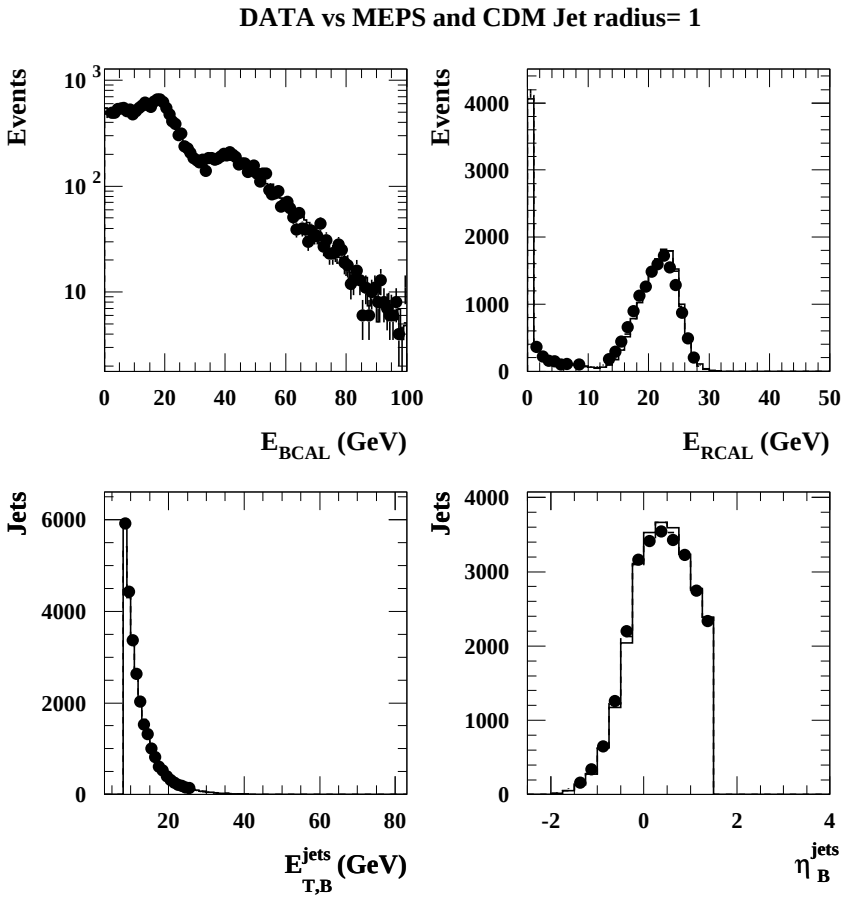


Figure 4.17: Comparison of the MC simulations based on the CDM (dashed) and MEPS (solid) to the distributions in the data (dots) for the energy in the RCAL, the BCAL, and the $E^{\rm jet}_{T,\rm B}$ and $\eta^{\rm jet}_{\rm B}$ distributions with a finer binning than that used for the cross section measurements.

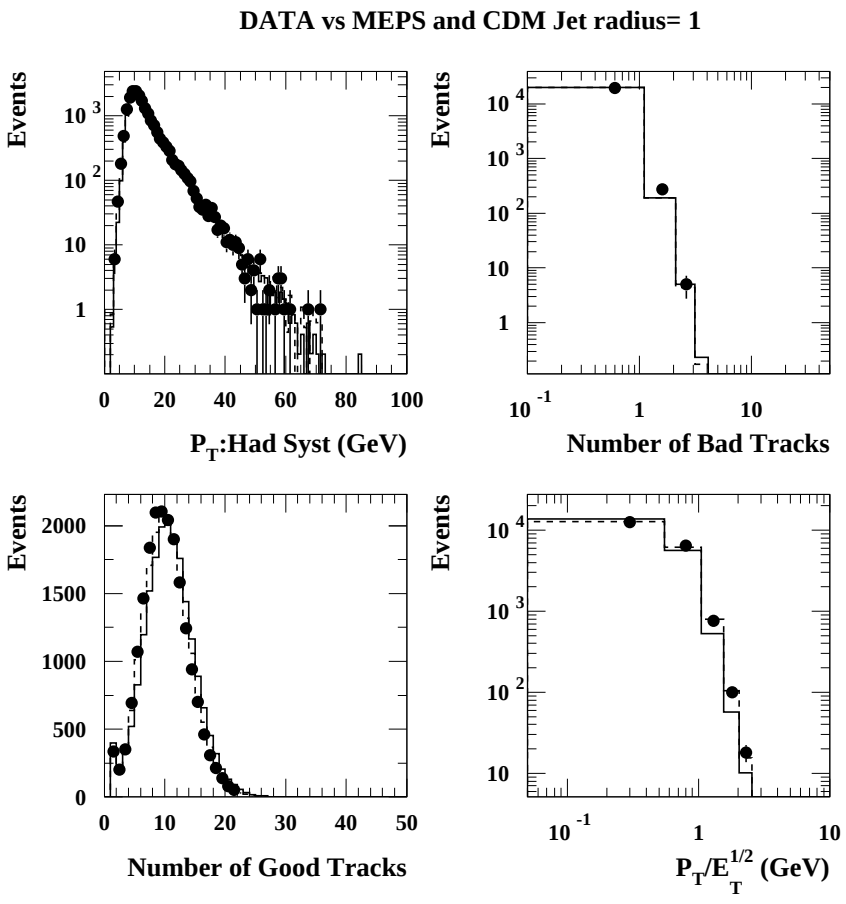


Figure 4.18: Comparison of the MC simulations based on the CDM (dashed) and MEPS (solid) to the distributions in the data (dots) for the $P_T$ of the hadronic system, the number of bad tracks, the number of good tracks and the $\frac{P_T}{\sqrt{E_T}}$ variable.

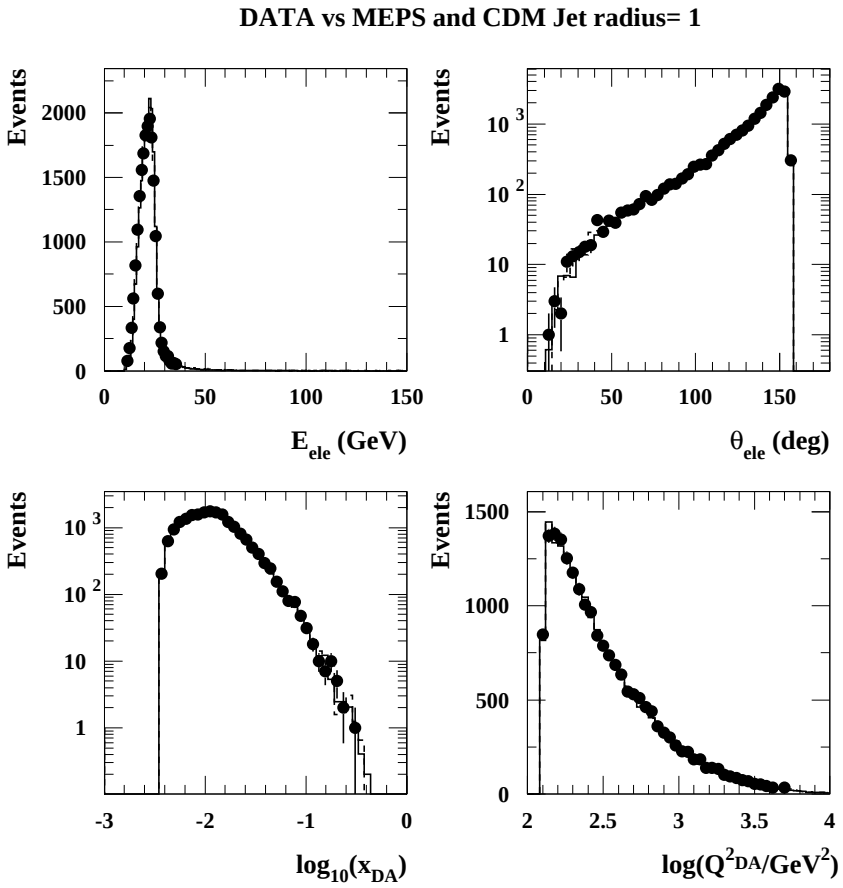


Figure 4.19: Comparisons of the MC simulations based on the CDM (dashed) and MEPS (solid) to the distributions in the data (dots) for the electron candidate's energy, its polar angle, $x_{DA}$ and $Q^2_{DA}$.

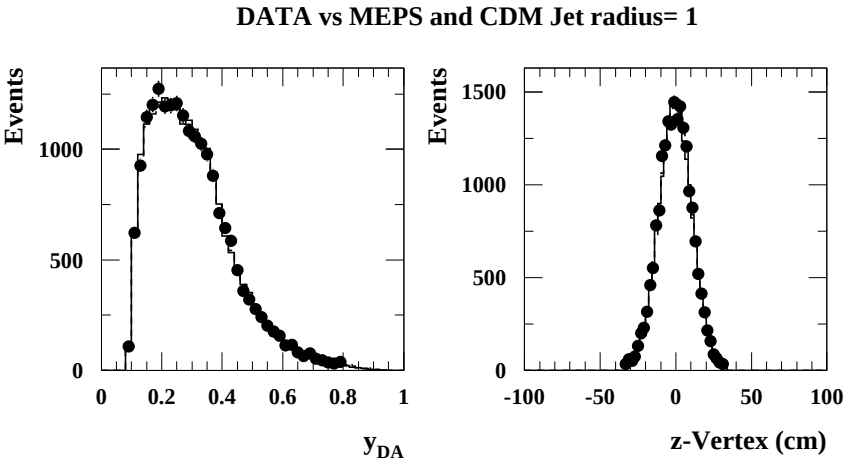


Figure 4.20: Comparisons of the MC simulations based on the CDM (dashed) and MEPS (solid) to the distributions in the data (dots) for $y_{DA}$ and the z-vertex.

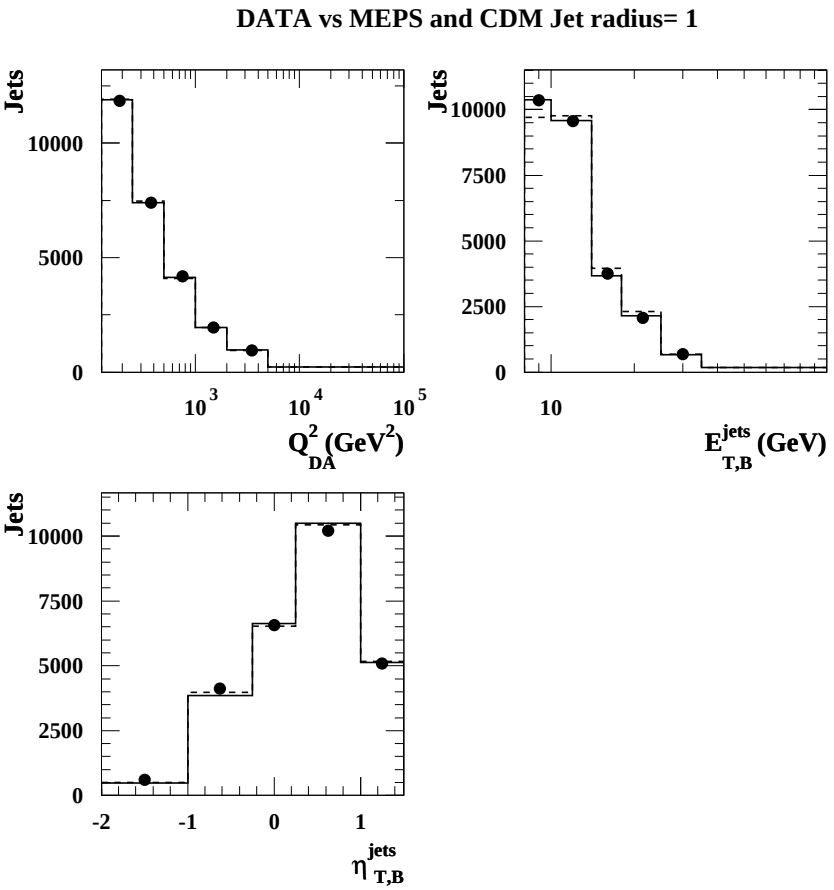


Figure 4.21: Comparison of the MC simulations based on the CDM (dashed) and MEPS (solid) to the distributions in the data (dots) for the $Q^2_{DA}$, $E^{\rm jet}_{T,\rm B}$ and $\eta^{\rm jet}_{\rm B}$ variables with the same binning as the cross-section measurements with jet-radius R=1.

**Distributions in jet variables for jet-radii $R = 0.7$ and $R = 0.5$**

The distributions shown for the inclusive-jet sample with R=1 were also obtained for $R = 0.7$ and $R = 0.5$. The results are very similar in the sense that all the distributions are well described by both the CDM and MEPS simulations. For this reason, they are not all shown again except for the $Q^2_{DA}$, $E^{\text{jet}}_{T,\text{B}}$, and $\eta^{\text{jet}}_{\text{B}}$ distributions, which are shown in Figs. 4.22 and 4.23. These correspond to the same jet variables as in Fig. 4.21. As expected, the total number of events that pass the selection cuts decreases roughly linearly as one decreases the jet radius. This is because decreasing the jet radius tends to break the jets apart into more jets of lower $E^{\text{jet}}_{T,\text{B}}$, making it less probable for the event to pass the high $E^{\text{jet}}_{T,\text{B}}$ cuts and be included in the sample. We see, however, that the jet variables for $R = 0.7$ and $R = 0.5$ are nevertheless well described by the CDM and MEPS simulations.

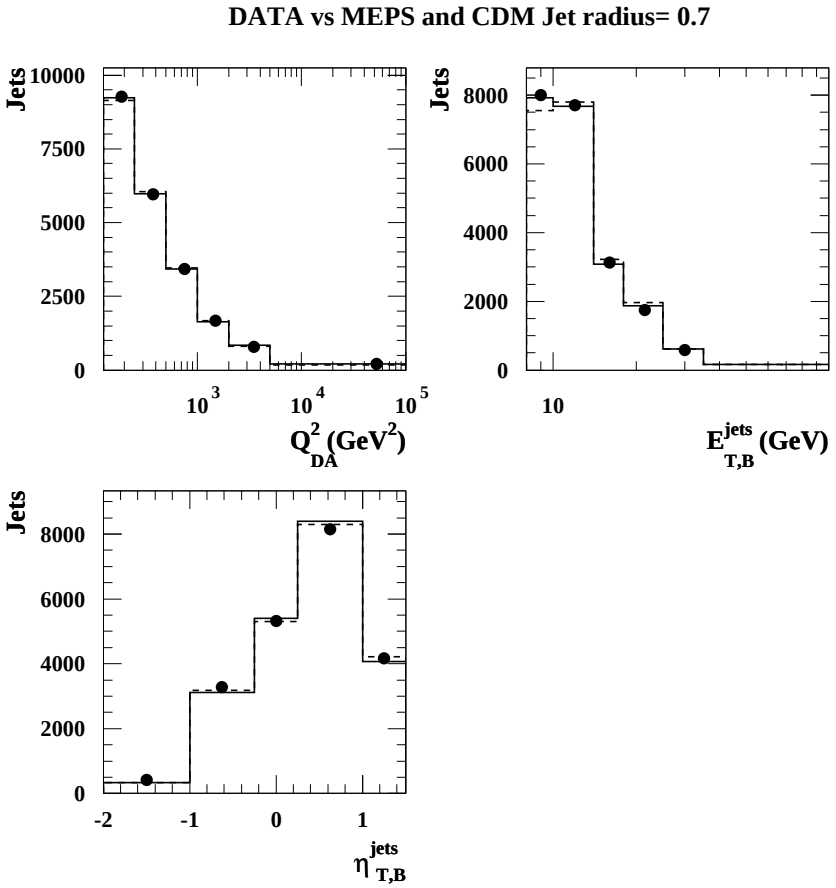


Figure 4.22: Comparison of the MC simulations based on the CDM (dashed) and MEPS (solid) to the distributions in the data (dots) for the $Q^2_{DA}$, $E^{\rm jet}_{T,\rm B}$ and $\eta^{\rm jet}_{\rm B}$ variables with the same binning as the cross-section measurements with jet-radius R=0.7

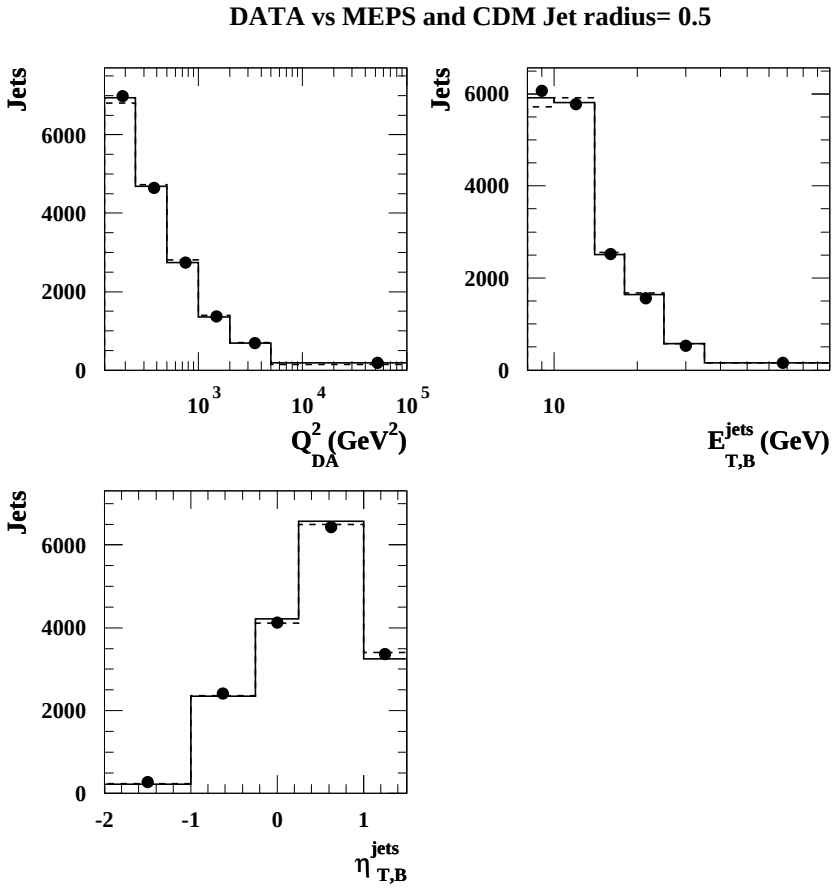


Figure 4.23: Comparison of the MC simulations based on the CDM (dashed) and MEPS (solid) to the distributions in the data (dots) for the $Q^2_{DA}$, $E^{\rm jet}_{T,\rm B}$ and $\eta^{\rm jet}_{\rm B}$ variables with the same binning as the cross-section measurements with jet-radius R=0.5

### 4.5.2 Comparisons between data and MC for three-jet angular-correlation distributions

Comparisons of data and MC simulations for three-jet NC DIS are shown in this section. Only the distributions of the angular-correlation variables are shown. The comparisons for the other distributions are very similar to those already shown. Both MC samples describe the data reasonably well, although it is found that the simulation using the MEPS model provides a better description of the data, as can be seen in Figs. 4.24 and 4.25. The figures show that this is generally the case for both the phase-space region of $Q^2 > 125$ GeV$^2$ and that of $500 < Q^2 < 5000$ GeV$^2$. The MEPS simulation was used to obtain the correction factors to be applied to the data, as shown in the next chapter.

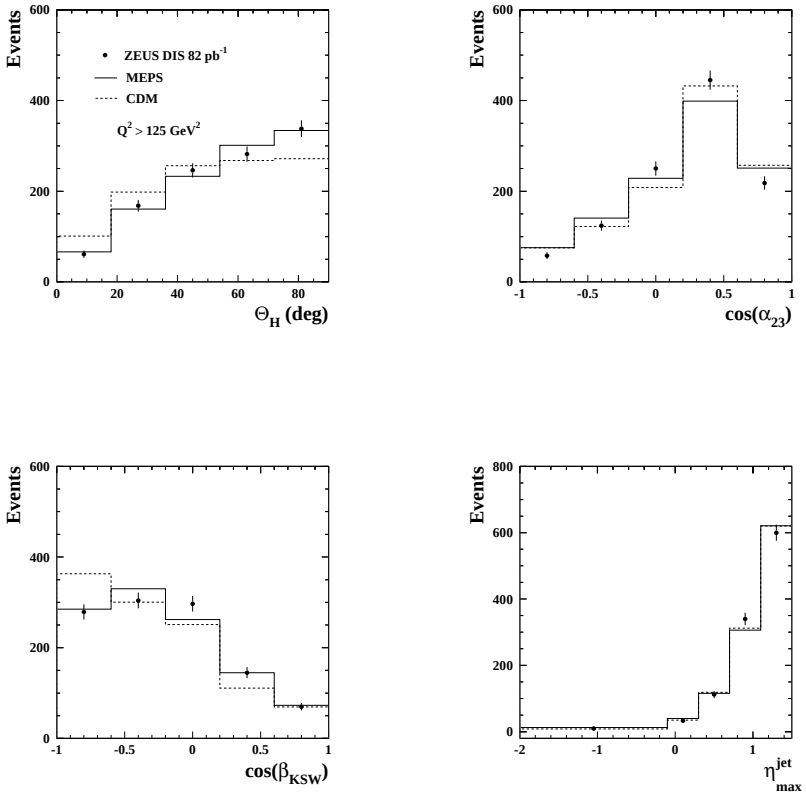


Figure 4.24: Comparison of the MC simulations using MEPS (solid) and CDM (dashed) with the distributions in the data (dots) for the angular-correlation variables $\Theta_H$, $\cos\alpha_{23}$, $\cos\beta_{ksw}$ and $\eta^{jet}_{max}$ for the region of $Q^2 > 125$ GeV$^2$.

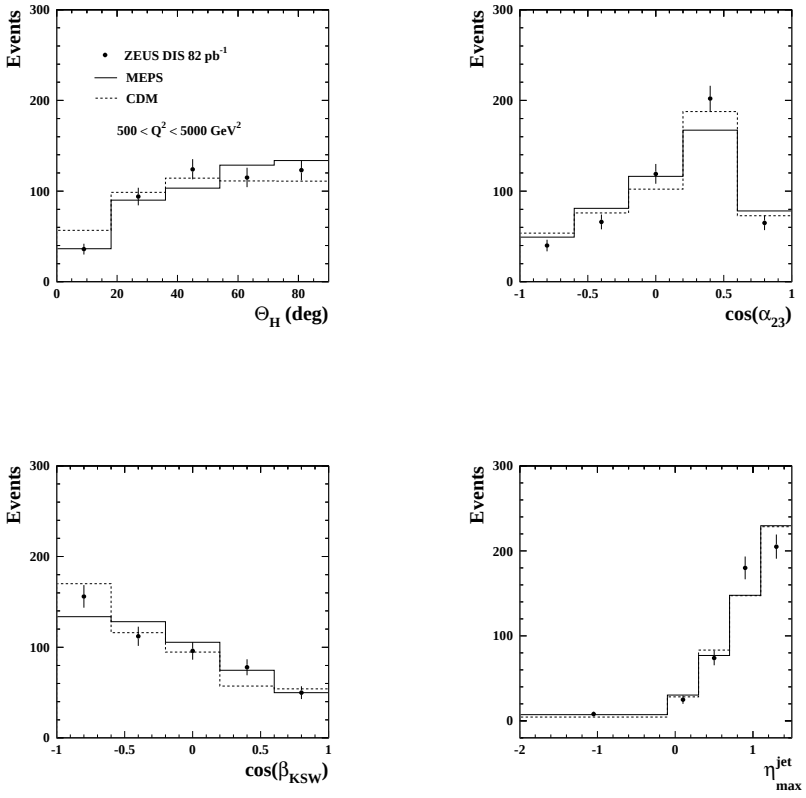


Figure 4.25: Comparison of the MC simulations using MEPS (solid) and CDM (dashed) with the distributions in the data (dots) for the angular-correlation variables $\Theta_H$, $\cos\alpha_{23}$, $\cos\beta_{ksw}$ and $\eta^{jet}_{max}$ for the region of $500 < Q^2 < 5000$ GeV$^2$.

### 4.5.3 Comparisons of data and MC for the $\alpha_s$ analysis using HERA II data

The HERA II running period (2004-2007) offers increased statistics and it is therefore desirable to perform the jet analysis including HERA II data. Presently only a reduced number of studies have been made using HERA II data and the MC simulations are not yet properly understood to the level achieved for HERA I. The $\alpha_s$ analysis published using HERA I data was repeated using HERA II in order to gain an initial view into this new running period. For this purpose, new MC samples with increased statistics were generated and similar criteria were used to select a NC DIS inclusive-jet sample both in the data and in the MC. One of the goals of this effort is to reproduce the $\alpha_s$ analysis with both HERA running periods combined.

For brevity, only the most relevant problems initially encountered in the HERA II data analysis are shown here. Fig. 4.26 shows that the distribution in the number of tracks has significantly changed from HERA I to HERA II. More importantly the available MC simulations are not yet able to reproduce this change properly. Fig. 4.27 shows that the shape of the distribution in $x_{DA}$ has not changed and is well reproduced by the MC simulations. Figs. 4.28 through 4.30 show the distributions of the jet variables. The comparison of HERA II with HERA I shows that these distributions have not significantly changed. Nevertheless, there is a problem in the HERA II MC simulation regarding the $E_{T,\mathrm{B}}^{\mathrm{jet}}$ and $\eta_{\mathrm{B}}^{\mathrm{jet}}$ distributions. In $\eta_{\mathrm{B}}^{\mathrm{jet}}$ the simulation predicts more forward jets than the data, a discrepancy which is not yet understood. A full analysis of inclusive-jet measurements and determinations of $\alpha_s(M_Z)$ demands better simulations to improve upon the precision achieved so far with HERA I data. For this reason the rest of the results obtained from the HERA II running period, such as cross sections and extractions of $\alpha_s$ are not shown in this document, although they have been found to be consistent with those of HERA I.

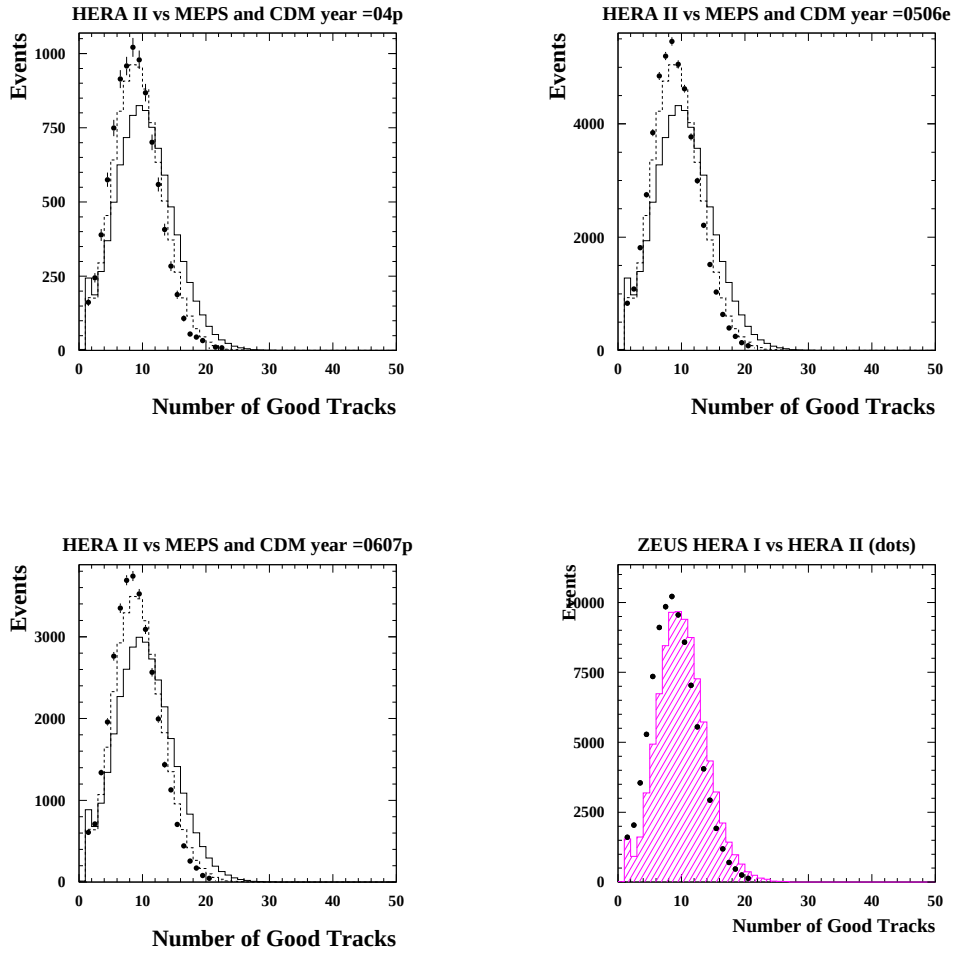


Figure 4.26: Comparison of the MC simulations based on MEPS (solid) and CDM (dashed) with the distributions of the number of good tracks in the HERA II data (dots): (a) 2004 $e^+p$, (b) 2005-2006 $e^-p$ and (c) 2006-2007 $e^+p$. The lower right plot shows the distribution in the data for the HERA I runnning period (histogram) vs that for the entire HERA II runnning period (dots).

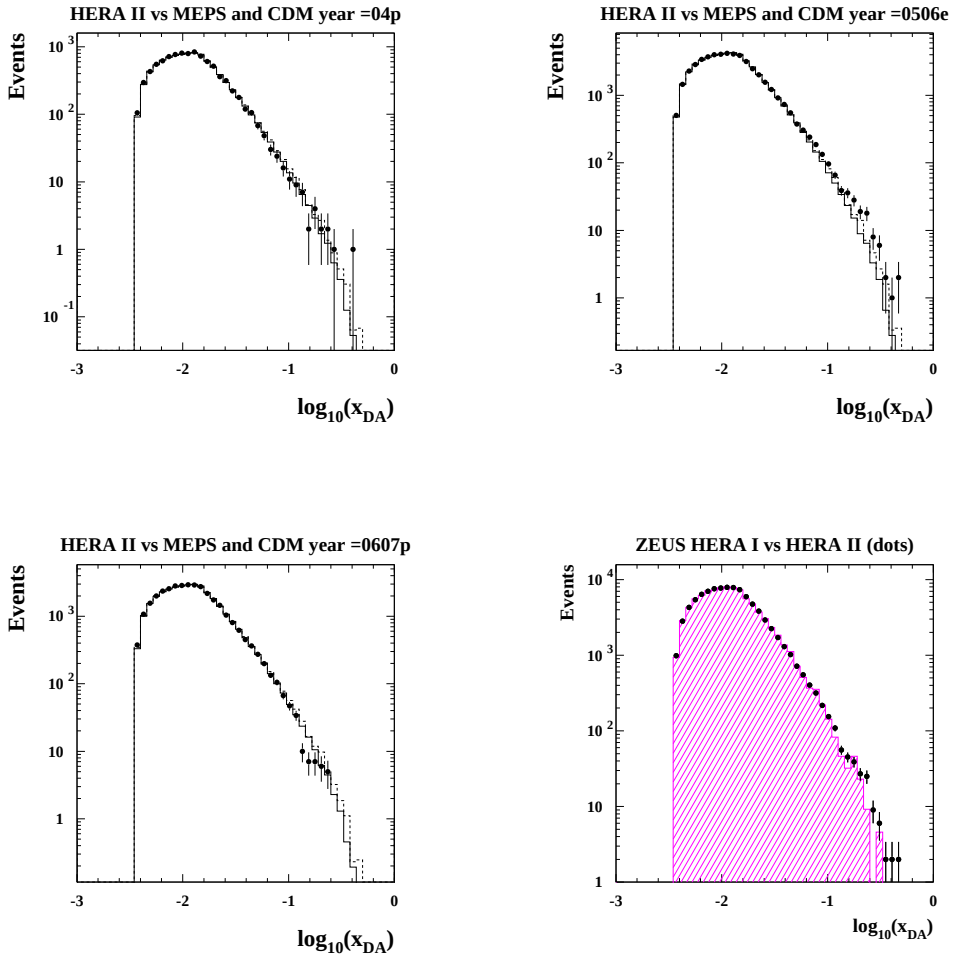


Figure 4.27: Comparison of the MC simulations based on MEPS (solid) and CDM (dashed) with the distributions of $log(x_{DA})$ in the HERA II data (dots): (a) 2004 $e^+p$, (b) 2005-2006 $e^-p$ and (c) 2006-2007 $e^+p$. The lower right plot shows the distribution in the data for the HERA I runnning period (histogram) vs that for the entire HERA II runnning period (dots).

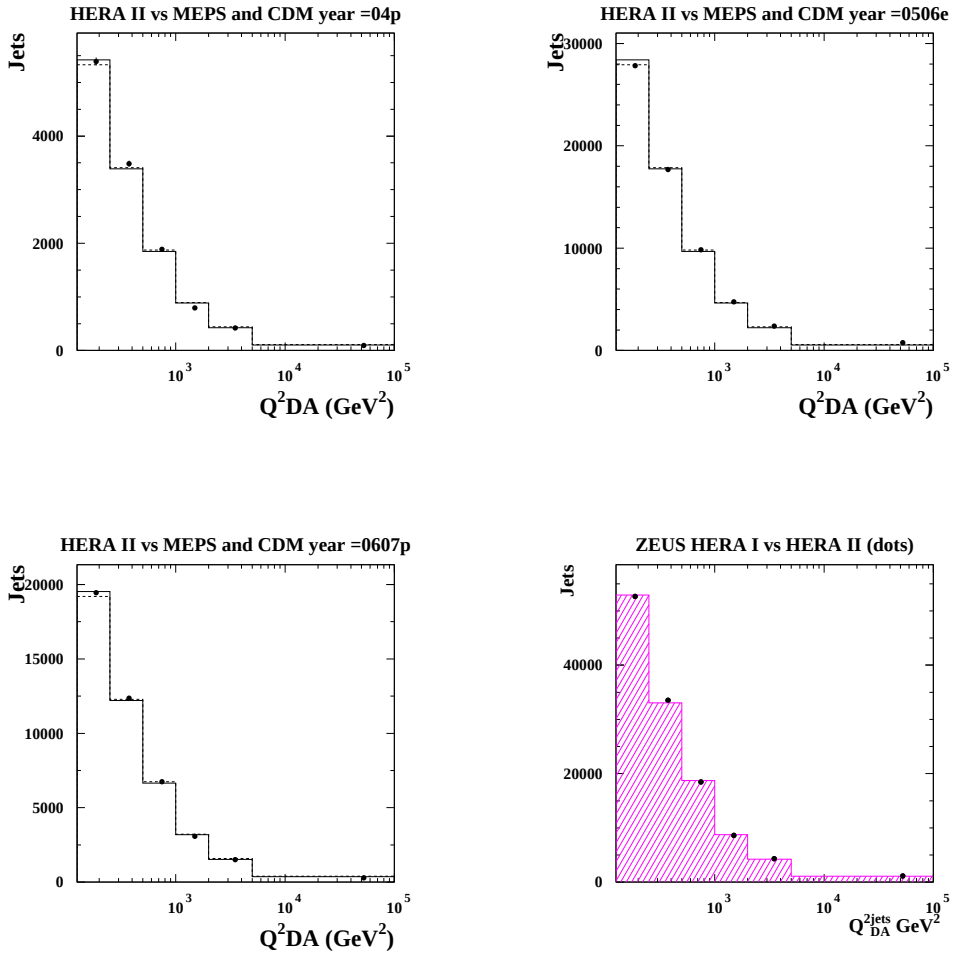


Figure 4.28: Comparison of the MC simulations based on MEPS (solid) and CDM (dashed) with the distributions of $Q^2_{DA}$ in the HERA II data (dots): (a) 2004 $e^+p$, (b) 2005-2006 $e^-p$ and (c) 2006-2007 $e^+p$. The lower right plot shows the distribution in the data for the HERA I runnning period (histogram) vs that for the entire HERA II runnning period (dots).

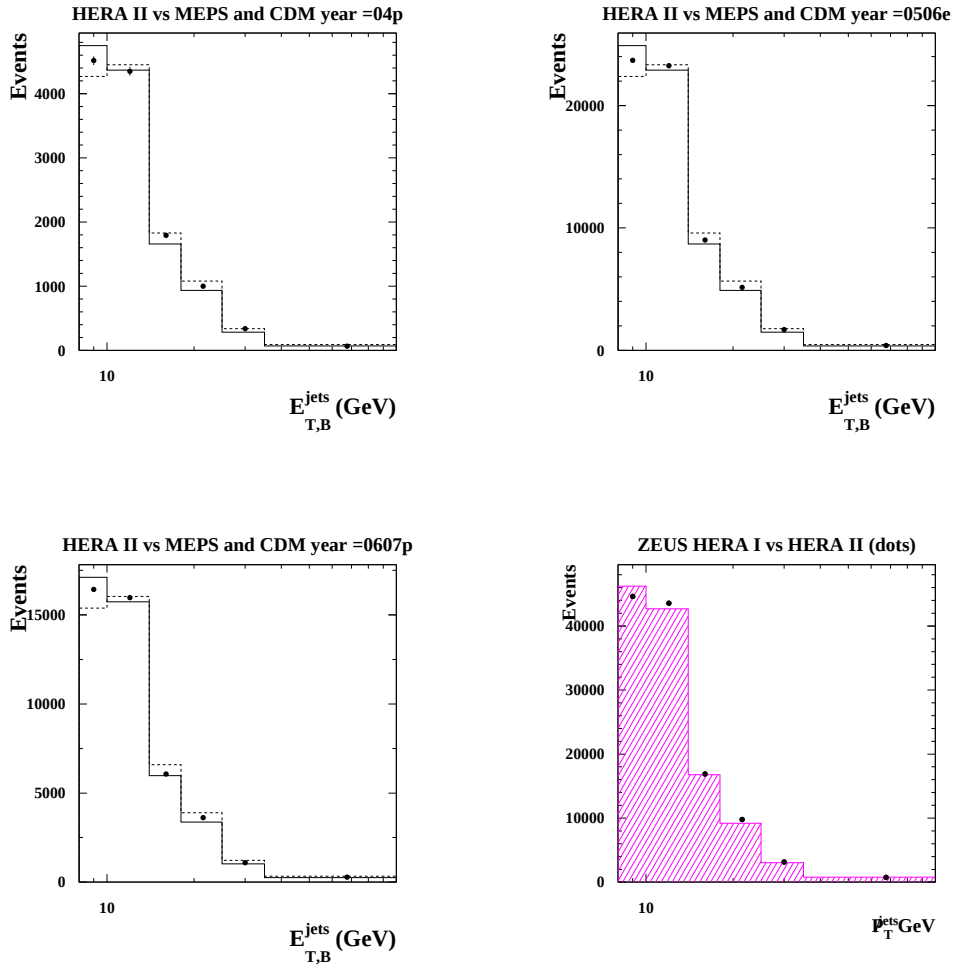


Figure 4.29: Comparison of the MC simulations based on MEPS (solid) and CDM (dashed) with the distributions of $E^{\rm jet}_{T,\rm B}$ in the HERAII data (dots): (a) 2004 $e^+p$, (b) 2005-2006 $e^-p$ and (c) 2006-2007 $e^+p$. The lower right plot shows the distribution in the data for the HERA I runnning period (histogram) vs that for the entire HERA II runnning period (dots).

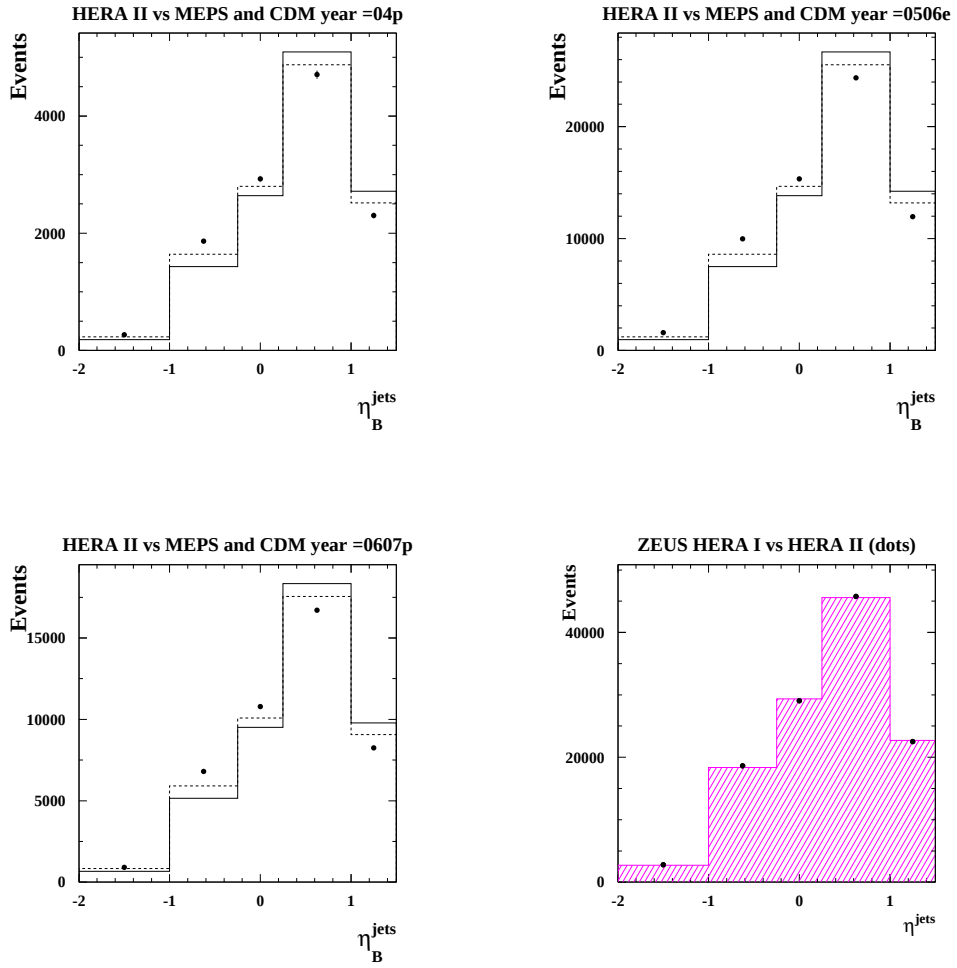


Figure 4.30: Comparison of the MC simulations based on MEPS (solid) and CDM (dashed) with the distributions of $\eta_{\mathrm{B}}^{\mathrm{jet}}$ in the HERA data (dots): (a) 2004 $e^+p$, (b) 2005-2006 $e^-p$ and (c) 2006-2007 $e^+p$. The lower right plot shows the distribution in the data for the HERA I runnning period (histogram) vs that for the entire HERA II runnning period (dots).

**Jet profiles using HERA II**

In order to determine whether a MC simulation for a jet analysis is valid it is also important to check, apart from the $Q^2$, $E^{\rm jet}_{T,\rm B}$ and $\eta^{\rm jet}_{\rm B}$ distributions of the jets, that the core and the energy flow within the jets are also well simulated. This check was done in the past using HERA I data and is presented here for the HERA II samples. This check consists of making what are called 'jet profiles'. The jet profiles are defined as follows:

- Divide the jets in the sample according to their $\eta^{\rm jet}_{\rm L}$ into three regions:$-1 < \eta^{\rm jet}_{\rm L} < 0$, $0 < \eta^{\rm jet}_{\rm L} < 1$ and $1 < \eta^{\rm jet}_{\rm L} < 2$;
- For each region, the mean transverse energy in the UCAL (excluding that associated to the electron) is evaluated as a function of the distance in $\eta$ from the jet axis, taking care that every cell whose distance in $\phi$ is larger than $\pi/2$ is excluded;
- For each region, the mean transverse energy in the UCAL (excluding that associated to the electron) is evaluated as a function of the distance in $\phi$ from the jet axis, taking care that every cell whose distance in $\eta$ is larger than 1 is excluded;

Figs. 4.31 and 4.32 show the jet profiles as functions of the distances $\delta\eta = \eta^{cell} - \eta^{\rm jet}_{\rm L}$ and $\delta\phi = \phi^{cell} - \phi^{jet}_{L}$ from the jet axis. A logarithmic scale was chosen in order to make differences between the data and the simulation more evident. An isotropically noisy UCAL, for example, would manifest itself in these plots as a pedestal. From the jet profiles we can see that the core of the jets is well described by the MC simulation. The asymmetric bump is expected since more hadronic activity takes place in the forward region. Note that there is a small $\sim$ 300 MeV discrepancy between the CDM simulation and the data. A similar discrepancy is observed for the MEPS simulation. This discrepancy is currently under study as part of understanding the HERA II data sample and the MC models.

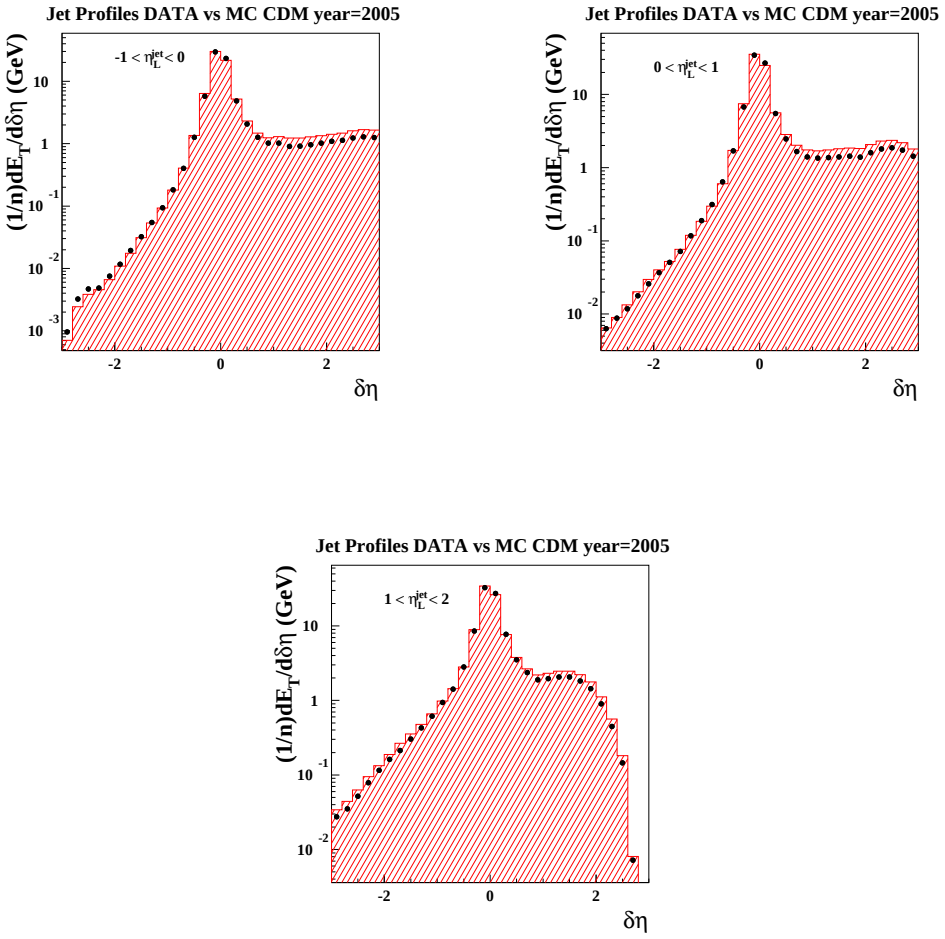


Figure 4.31: Transverse energy profiles as functions of the distance $\delta\eta$ from the jet axis integrated over $|\delta\phi| < \pi/2$ in HERA II data (dots) and the MC simulations based on CDM (histogram).

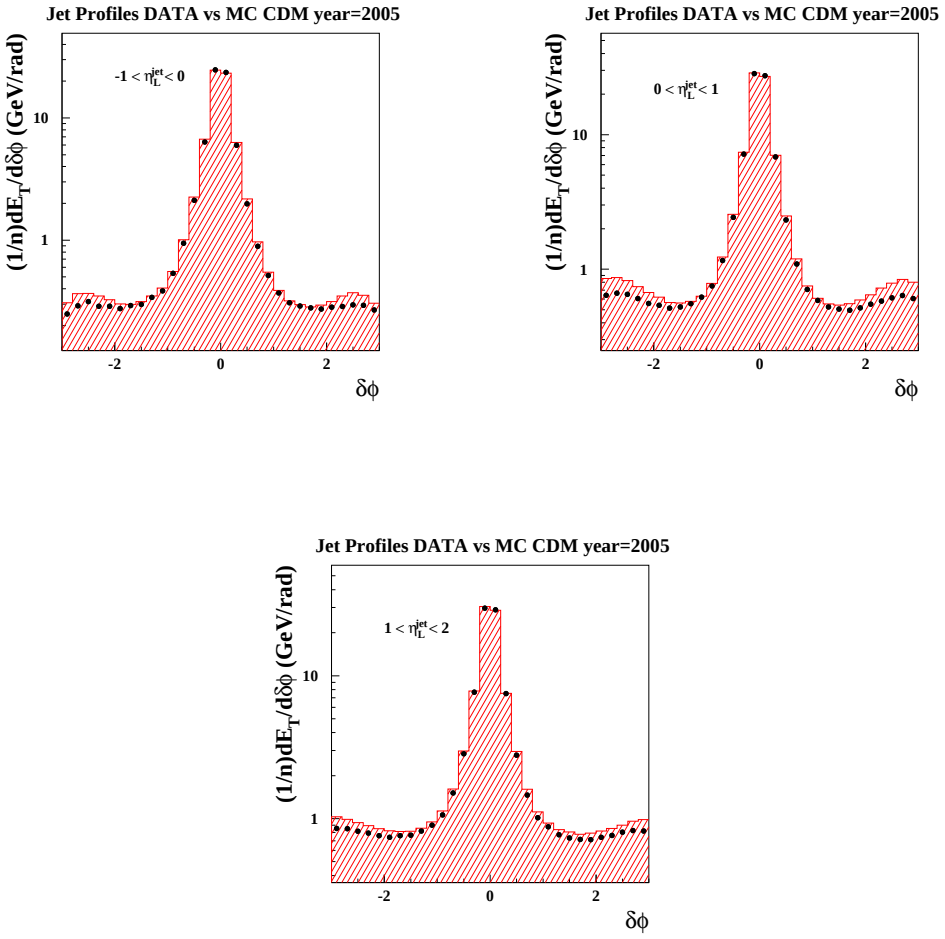


Figure 4.32: Transverse energy profiles as functions of the distance $\delta\phi$ from the jet axis integrated over $|\delta\eta| < 1$ in HERA II data (dots) and the MC simulations based on CDM (histogram).

# Chapter 5

# Correction factors and systematic uncertainties

## 5.1 Correction factors

The cross-section measurements made for the $\alpha_s$ and the angular-correlations analyses were corrected for detector effects that took into account the efficiency of the trigger, the selection criteria and the purity and efficiency of the jet reconstruction. The correction factors were applied using the bin-by-bin method which relies on a good description of the data by the MC simulation. These correction factors are obtained from the simulations after $E_{T,\mathrm{B}}^{\mathrm{jet}}$ corrections are applied to the jets as explained in Chapter 4.

The fixed-order calculations discussed in Chapter 2 only have partons as their final state. An accurate comparison with the measured cross sections necessitates that the fixed-order pQCD calculations be supplemented with hadronization correction factors. Moreover, since the calculations also did not take into account the NC contribution from $Z^0$-exchange nor QED effects due to the running of $\alpha_{QED}$ and intial and final-state QED radiation, either the predictions or the data had to be corrected for these effects to render a comparison possible.

The legitimacy of using the MC simulations for obtaining correction factors to the data or the theory rests on how well the MC is able to describe the distributions it aims to correct. In Chapter 4 we showed comparisons of the distributions of the data with the MC simulations at the detector level. The MEPS simulation was able to reproduce the distributions in the data, while CDM although agreeing with MEPS for the $Q^2$, $\eta_{\mathrm{B}}^{\mathrm{jet}}$ and $E_{T,B}^{jet}$ predictions, gave a poorer description of the angular-correlation variables.

In Chapter 3 we showed comparisons of the MC simulations using both the MEPS

and CDM parton-cascade models to the $O(\alpha_s^2)$ and $O(\alpha_s^3)$ pQCD calculations. There we saw that the MEPS simulation was able to reproduce the $O(\alpha_s^2)$ and $O(\alpha_s^3)$ pQCD calculations, while CDM although agreeing with MEPS for the inclusive-jet cross section predictions, gave a poorer description for the angular-correlation variables.

Identifying and quantifying possible sources of systematic uncertainty is a necessary component of any measurement. The conventional approach is to vary the assumptions by reasonable amounts (such as their known uncertainty) and estimate the impact of such variations on the final results. Ideally the analysis should be insensitive to small variations in quantities whose exact values are assumed or otherwise not fully known by the experimentalist, such as background subtraction cuts, the choice for the parton-cascade model or the energy scale of the jets. The analysis is carried through with independent variations and the corresponding changes in the final results are added in quadrature and are taken as the overall systematic uncertainty. These systematic checks often result in a simple variation of the acceptance correction factor applied to the data, and are presented in the second part of this chapter.

### 5.1.1 Acceptance correction factors

The $E_{T,B}^{jet}$, $Q^2$ and angular-correlation distributions in the data were corrected for detector effects using bin-by-bin correction factors determined with the MC samples. For the $E_{T,B}^{jet}$ and $Q^2$ distributions in the $\alpha_s$ analysis, it is shown in Chapter 4 (Figs. 4.21 through 4.23) that both the MEPS and CDM MC simulations provide a good description of the data. For this reason the average between the acceptance-correction values obtained with CDM and MEPS was used to correct the data to the hadron level. The deviations in the results obtained by using either CDM or MEPS to correct the data from their average were taken to represent systematic uncertainties on the modelling of the parton cascade in the corrections, as discussed later. As shown in Figs. 5.1 through 5.3, the acceptance-correction factors differed from unity by typically less than 10% for all choices of the jet radius. The same applies to Fig. 5.4, which shows the acceptance correction factors used to correct the $E_{T,\mathrm{B}}^{\mathrm{jet}}$ distributions in different regions of $Q^2$.

The acceptance correction factors ($C_{ACC}$) are defined as $C_{ACC} = \frac{purity}{efficiency}$, where efficiency (purity) is the fraction of generated (reconstructed) events for a given bin that are reconstructed (generated) in that same bin:

$$C_{ACC} = \frac{N_{HAD}}{N_{DET}} = \frac{P}{E} = \frac{(N_{GEN} \bigcap N_{REC})/N_{REC}}{(N_{GEN} \bigcap N_{REC})/N_{GEN}} = \frac{N_{GEN}}{N_{REC}} \tag{5.1}$$

Since the $C_{ACC}$ factor corrects for purity and efficiency in the selection of the data sample, here 'generated' stands for the MC hadronic level, whereas 'reconstructed'

refers to the MC detector level. In other words, distributions of the variables in the data sample are 'corrected' to the hadron level by multiplying them by $C_{ACC}$:

$$\sigma_i = \frac{N^{DATA}_{REC,i}}{(\Delta x)L} \cdot \frac{N^{MC}_{GEN,i}}{N^{MC}_{REC,i}} \tag{5.2}$$

where $\sigma_i$ is the cross section for a given variable range (i.e. histogram bin), $\Delta x$ is the bin width and $L$ is the luminosity. The closer the distribution in the MC simulation is to the data, the more reliable this procedure is.

Figs. 5.8 and 5.9 show the acceptance correction factors applied to the angular-correlation distributions for the region $Q^2 > 125$ GeV$^2$. Figs. 5.10 and 5.11 show the acceptance correction factors applied to the angular-correlation distributions for the region $500 < Q^2 < 5000$ GeV$^2$. In Chapter 4 (see Figs. 4.24 and 4.25) we showed that in this case MEPS provides a better description of the angular-correlation distributions in the data. For this reason only MEPS was used to obtain the acceptance correction factors in this case, and the CDM simulation was used to estimate the systematic uncertainty on the modelling of the parton cascade in the corrections, as discussed later in this chapter.

### 5.1.2 QED correction factors

The fixed-order pQCD calculations carried out with DISENT or NLOJET++ do not include the effect of the runnning of $\alpha_{QED}$ nor the radiative corrections needed to describe processes such as the radiation of photons by the initial- or final-state electron. Thus, the calculations needed to be supplemented with QED correction factors ($C_{QED}$). It is inconsequent whether the correction factors are applied to the data or the predictions, provided the inverse of one is applied to the other. These correction factors were applied to the data and were obtained by generating a MC sample with the same settings as the MEPS sample used to obtain the detector corrections but without QED radiative processes. The factor obtained in each bin had the form

$$C_{QED,i} = \frac{N^{MC-DET}_{NO-QED,i}}{N^{MC-DET}_{QED,i}}, \tag{5.3}$$

where $C_{QED,i}$ is the QED correction factor to be applied to the differential cross section in bin $i$ obtained by means of eq. 5.2. Figs. 5.1 through 5.11 show the QED correction factors applied to the data. As can be seen, they show a reasonably flat distribution that is close to unity.

### 5.1.3 $Z^0$-exchange corrections

The fixed-order pQCD calculations carried out with DISENT or NLOJET++ do not include the contribution from $Z^0$-mediated NC DIS processes. Thus, it was necessary to supplement the pQCD calculations with $Z^0$-exchange correction factors. A sample as the one used for the acceptance correction factors was generated but without $Z^0$ exchange. The correction factors obtained were applied to the theoretical predictions and had the following form:

$$C_{Z^0,i} = \frac{N^{HAD}_{Z^0,i}}{N^{HAD}_{NO-Z^0,i}}. \tag{5.4}$$

Figs. 5.1 through 5.3 and 5.6 show the QED correction factors applied to the data for the $\alpha_s$ analysis. The correction factors are very close to unity. The $Z^0$ correction factors for the angular-correlation distributions were combined with those for the hadronization, as discussed next, and are shown in Figs. 5.8 through 5.11.

### 5.1.4 Parton-to-hadron corrections

In order to improve on the comparison of the hadronic jet cross sections with the fixed-order pQCD calculations, hadronization correction factors ($C_{HAD}$) were obtained and applied to the DISENT and NLOJET++ predictions. The parton-to-hadron corrections were obtained using the Monte Carlo samples without the $Z^0$-exchange. It is inconsequent whether the correction factors are applied to the data or the predictions, provided the inverse of one is applied to the other. In this case the correction factors were applied to the predictions and had the following form:

$$C_{HAD,i} = \frac{N^{MC}_{HAD,i}}{N^{MC}_{PAR,i}} \tag{5.5}$$

As can be seen from Figs. 5.1, 5.2, and 5.3, the deviation of $C_{HAD}$ from unity increases as the jet radius decreases. This is expected since the hadronization tends to 'smear' the energy of the jet. One of the objectives of the $\alpha_s$ analysis was to determine a region of validity for the jet radius. The hadronization correction factor imposes a lower constraint on the jet radius, since large values of $C_{HAD}$ spoil the connection between the measured hadronic final state and the hard interaction for jet analyses. Fig. 5.12 shows the hadronization correction factors as a function $Q^2$ for R values in the range $0.3 < R < 1.2$. It becomes evident that for values lower than R=0.5, the correction factors decrease below 0.5 and make the less analysis less precise. For the angular-correlation variables, $C_{Z^0}$ and $C_{HAD}$ were combined into a single correction factor as shown in Figs. 5.8 through 5.11. These correction factors may appear to deviate from unity substantially for some regions, but the situation

improves when the cross sections are normalized. The lower region of $\eta^{jet}_{max}$, as we showed in Chapter 3 (Figs. 3.39 and 3.40), has a relatively large uncertainty on the modelling of the parton cascade. Moreover, we see that the hadronization correction is large, a reason for which this region might be excluded in a future fit to the color factors.

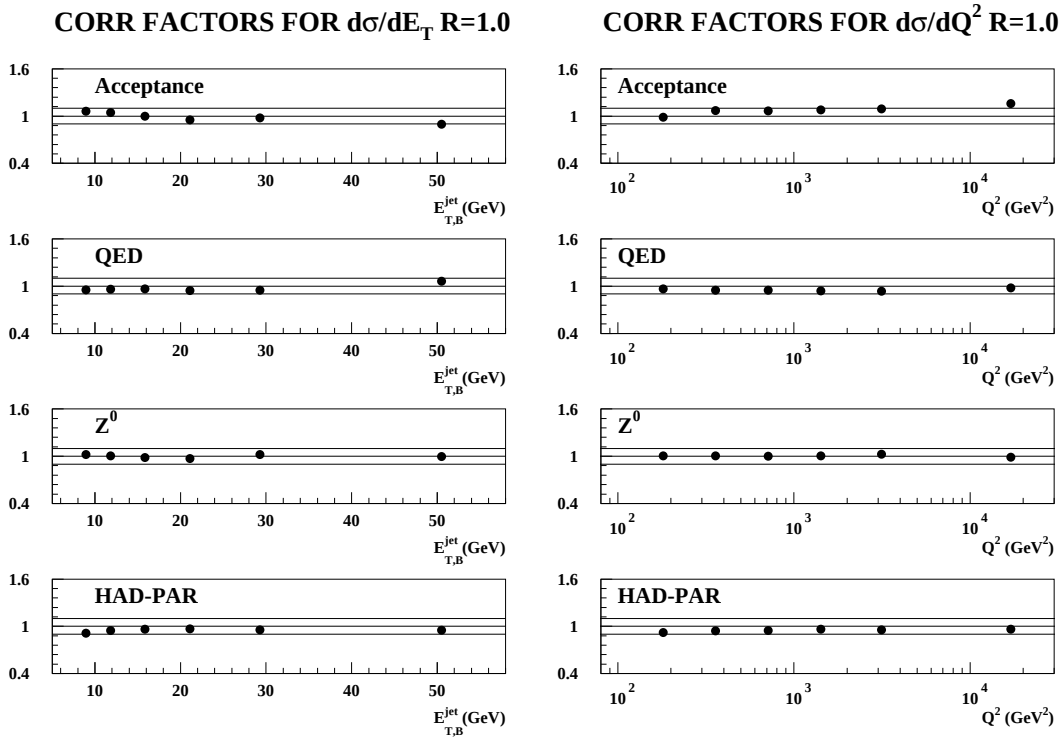


Figure 5.1: $C_{ACC}$, $C_{QED}$, $C_{Z^0}$ and $C_{HAD}$ factors applied to the data (ACC and QED) and to the fixed-order pQCD calculations ($Z^0$ and HAD) for the $E^{jet}_{T,B}$ (left) and $Q^2$ (right) distributions in the $\alpha_s$ analysis with jet-radius R=1.0. In all cases the factors deviate less than 10% from unity.

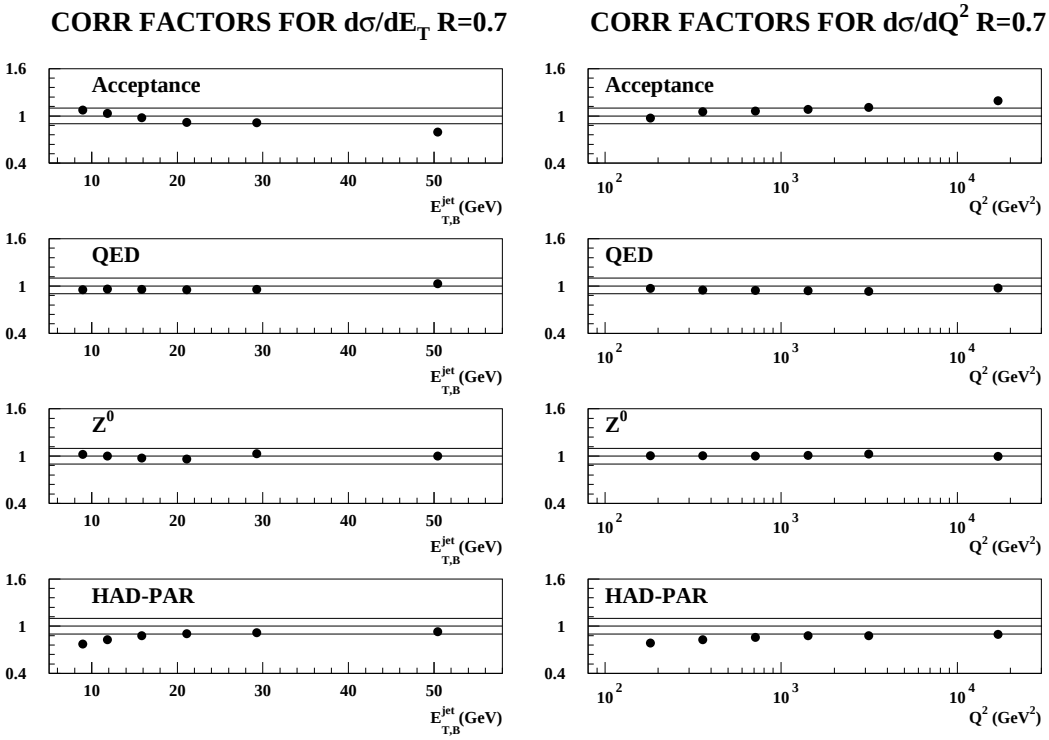


Figure 5.2: $C_{ACC}$, $C_{QED}$, $C_{Z^0}$ and $C_{HAD}$ factors applied to the data (ACC and QED) and to the fixed-order pQCD calculations ($Z^0$ and HAD) for the $E^{jet}_{T,B}$ (left) and $Q^2$ (right) distributions in the $\alpha_s$ analysis with jet-radius R=0.7. In all cases the factors deviate less than 10% from unity.

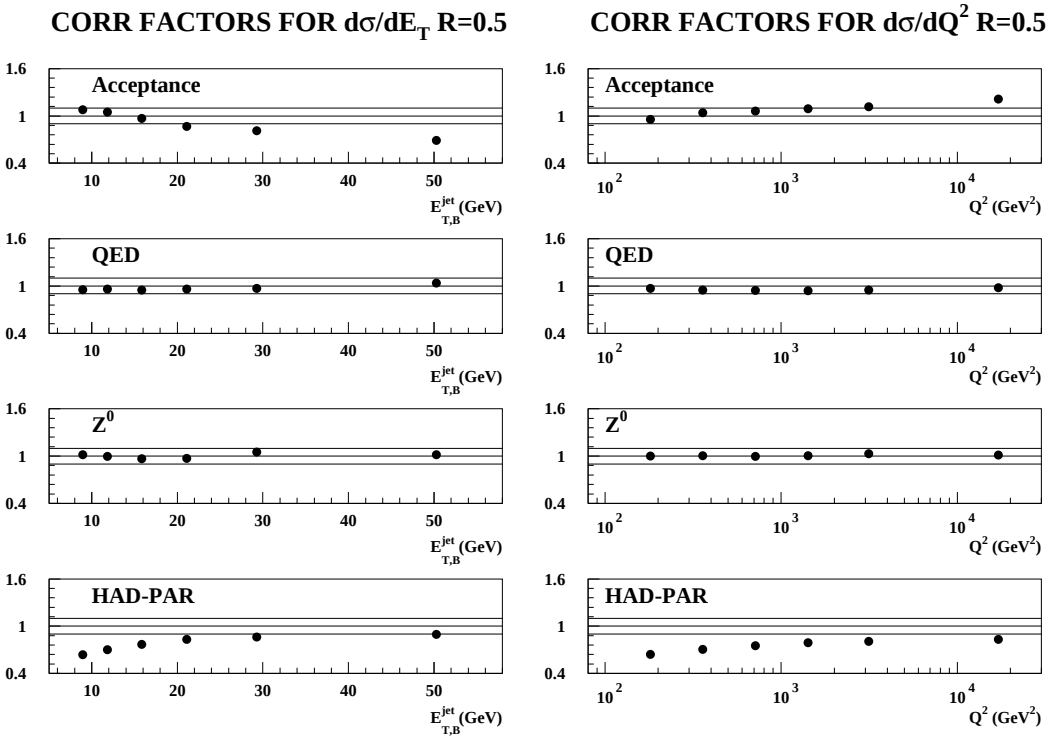


Figure 5.3: $C_{ACC}$, $C_{QED}$, $C_{Z^0}$ and $C_{HAD}$ factors applied to the data (ACC and QED) and to the fixed-order pQCD calculations ($Z^0$ and HAD) for the $E^{jet}_{T,B}$ (left) and $Q^2$ (right) distributions in the $\alpha_s$ analysis with jet-radius R=0.5. In all cases the factors deviate less than 10% from unity.

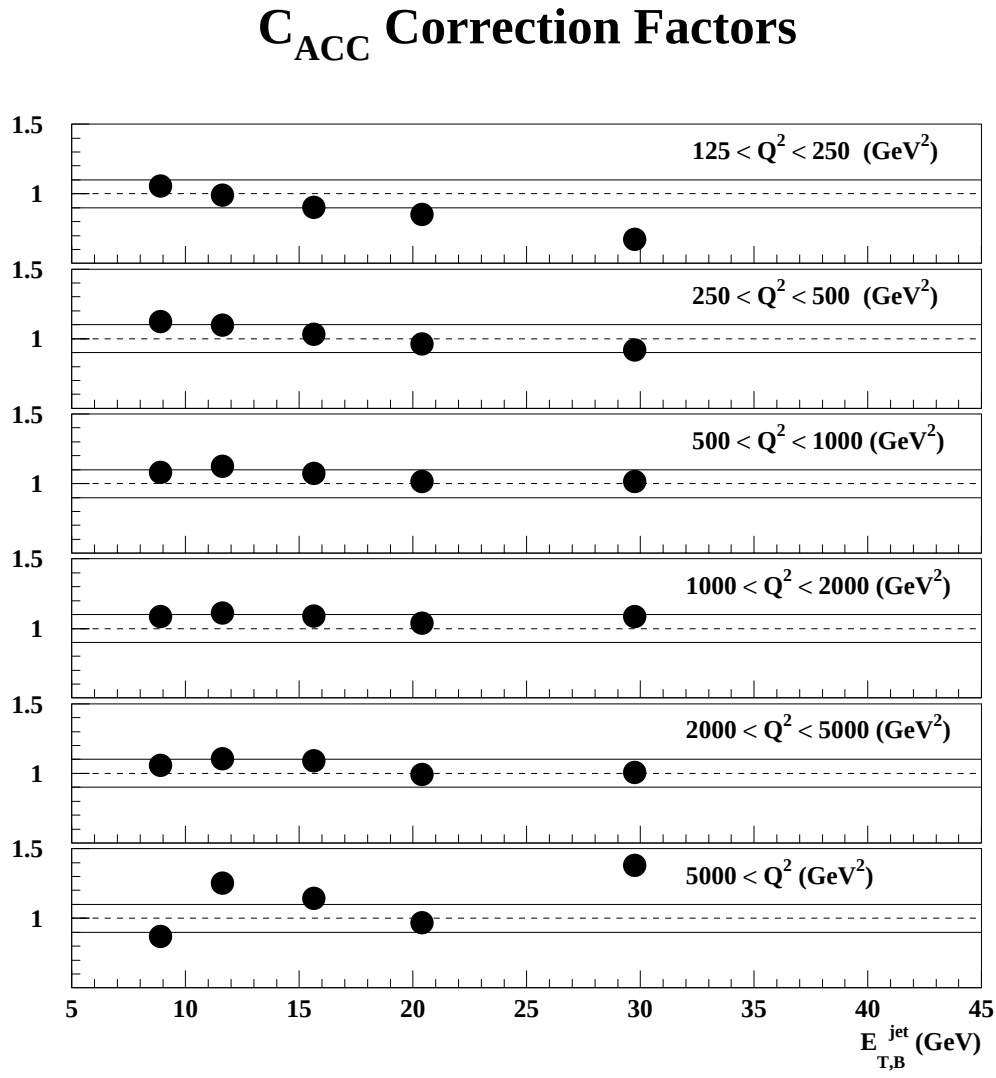


Figure 5.4: $C_{ACC}$ factors applied to the data for the $E_{T,B}^{jet}$ distributions in different regions of $Q^2$.

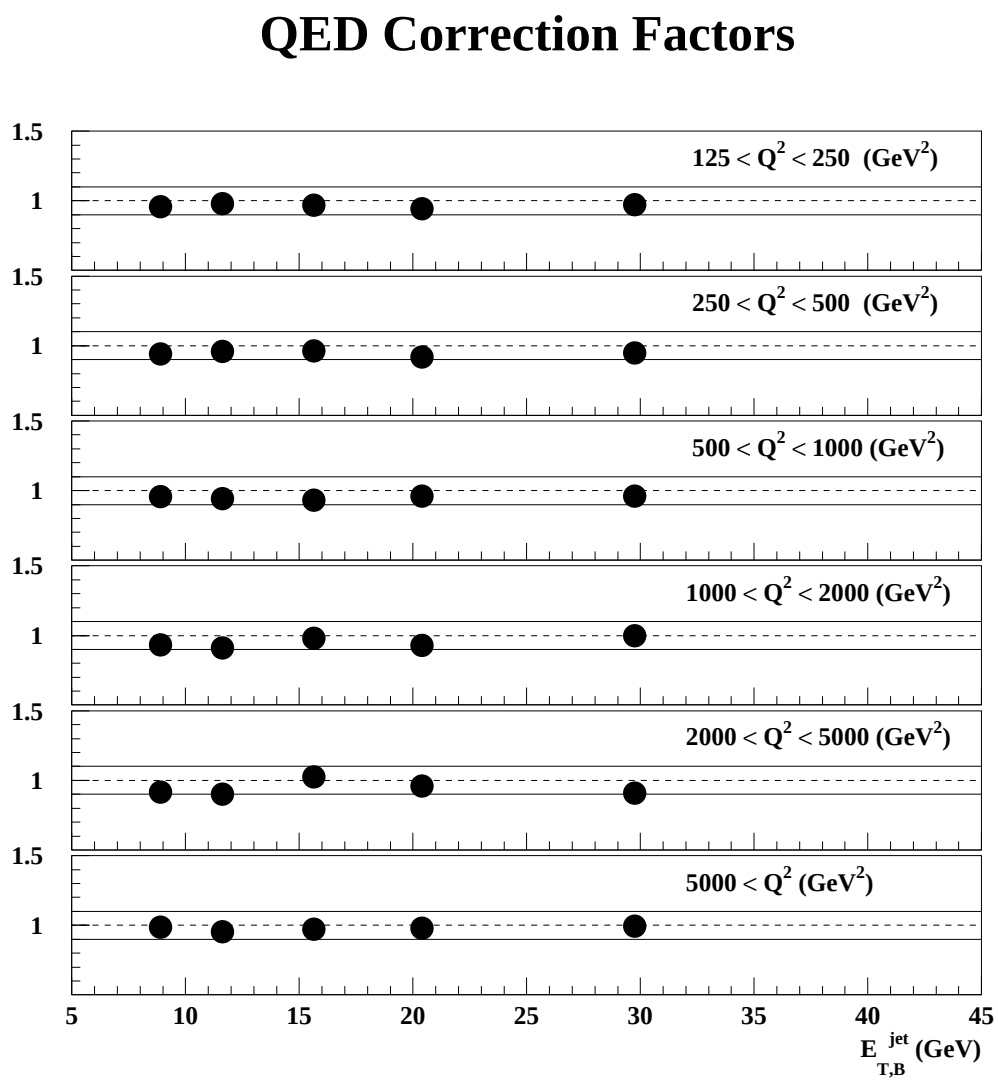


Figure 5.5: $C_{QED}$ factors applied to the data for the $E_{T,B}^{jet}$ distributions in different in regions of $Q^2$.

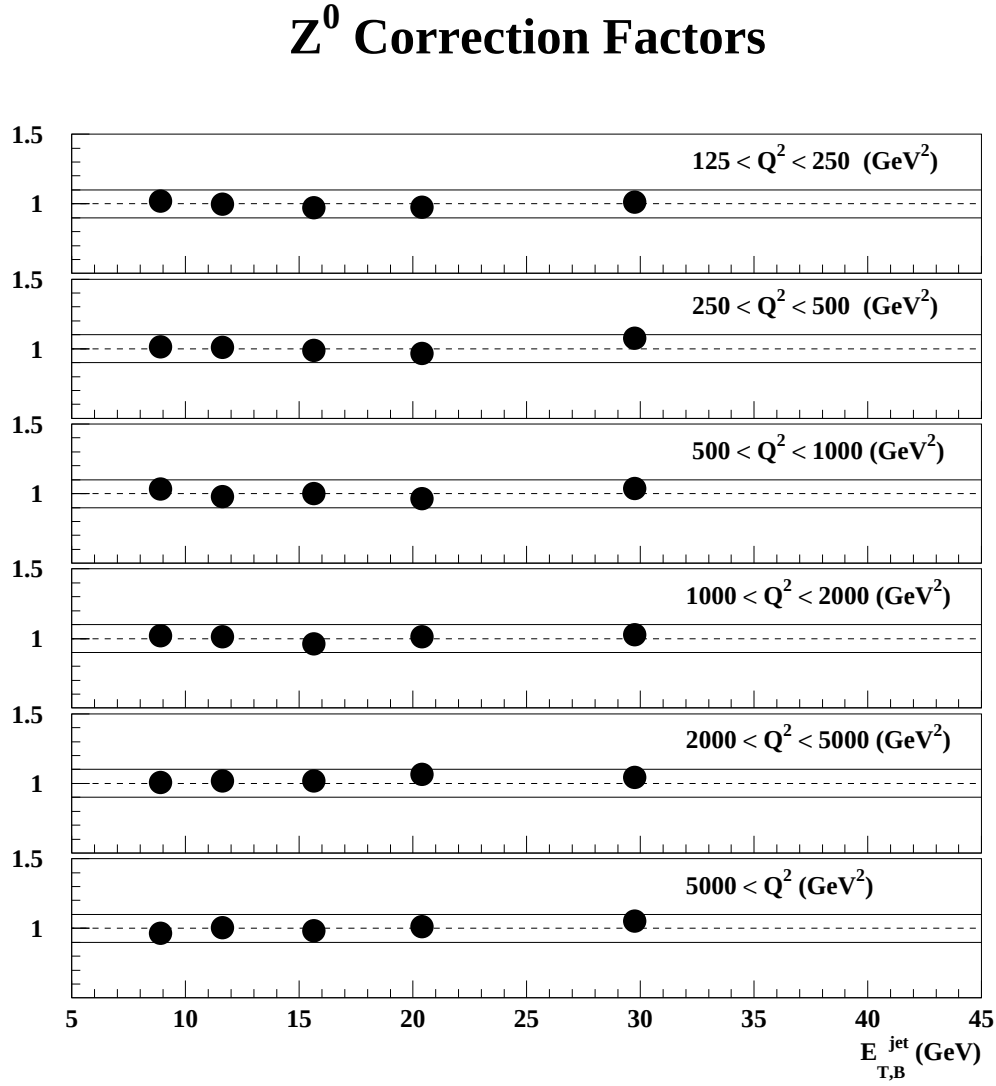


Figure 5.6: $C_{Z^0}$ factors applied to the fixed-order caculations for the $E_{T,B}^{jet}$ distribution in different regions of $Q^2$.

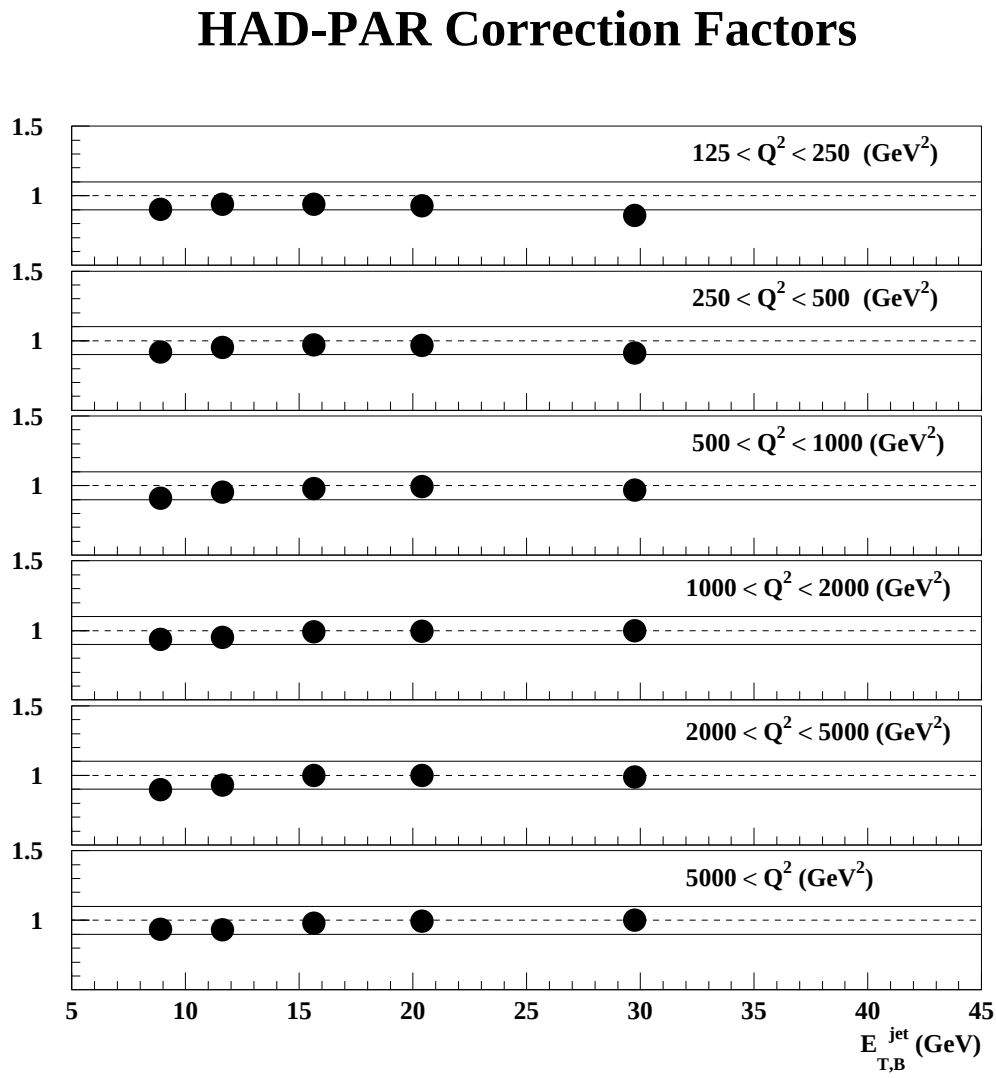


Figure 5.7: $C_{HAD}$ factors applied to the fixed-order calculations for the $E_{T,B}^{jet}$ distribution in different regions of $Q^2$.

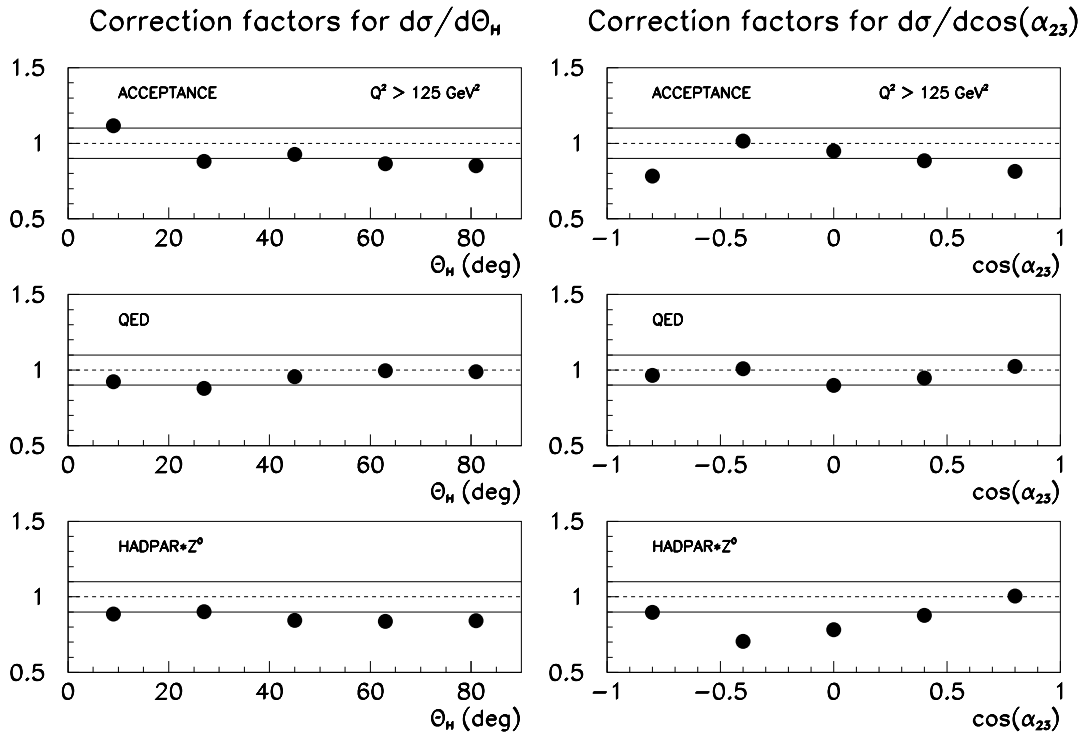


Figure 5.8: $C_{ACC}$, $C_{QED}$ and $C_{Z^0} \cdot C_{HAD}$ factors applied to the data (ACC and QED) and to the fixed-order pQCD calculations ($Z^0$ and HAD) for the $\Theta_H$ and $\cos\alpha_{23}$ distributions in the region of $Q^2 > 125$ GeV$^2$. The factors shown here were applied to the cross-sections before calculating the normalized cross section.

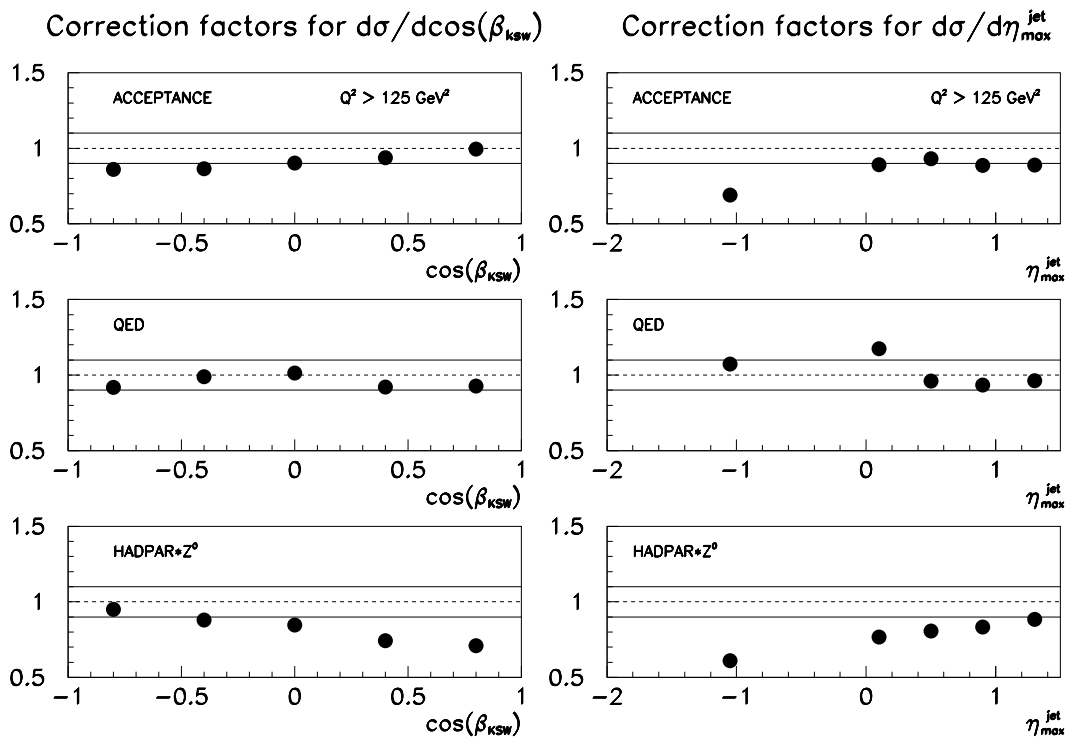


Figure 5.9: $C_{ACC}$, $C_{QED}$ and $C_{Z^0} \cdot C_{HAD}$ factors applied to the data (ACC and QED) and to the fixed-order pQCD calculations ($Z^0$ and HAD) for the $\Theta_H$ and $\cos\alpha_{23}$ distributions in the region of $Q^2 > 125$ GeV$^2$. The factors shown here were applied to the cross-sections before calculating the normalized cross section.

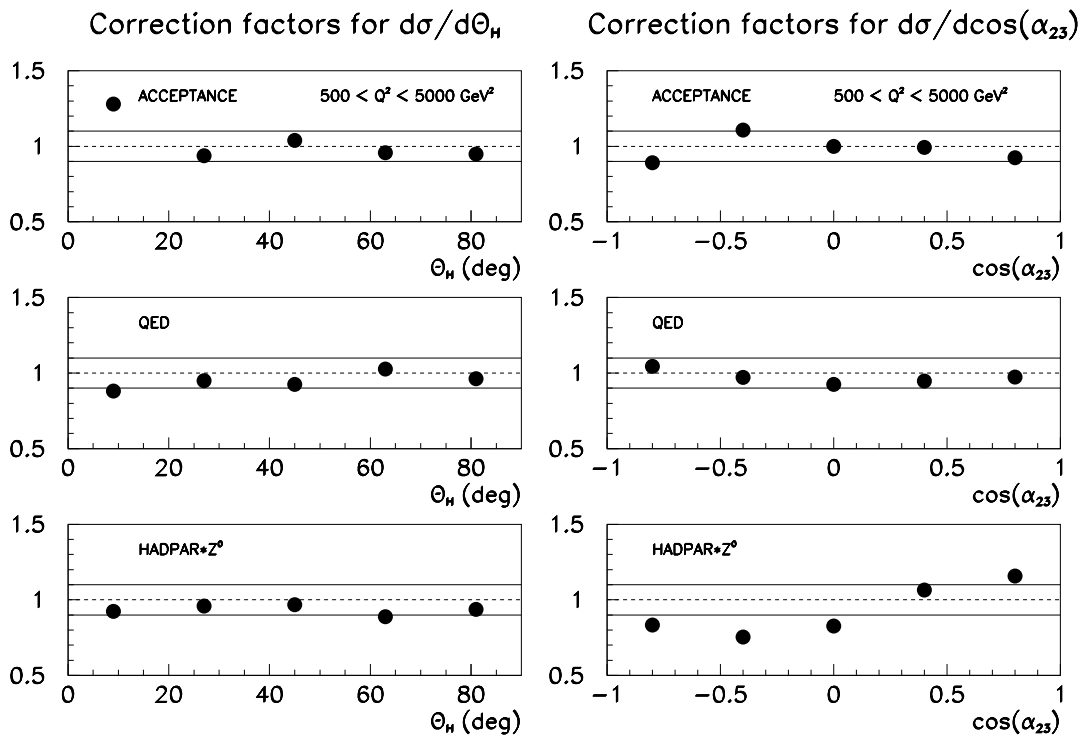


Figure 5.10: $C_{ACC}$, $C_{QED}$ and $C_{Z^0} \cdot C_{HAD}$ factors applied to the data (ACC and QED) and to the fixed-order pQCD calculations ($Z^0$ and HAD) for the $\Theta_H$ and $\cos\alpha_{23}$ distributions for the region of $500 < Q^2 < 5000$ GeV$^2$. The factors shown here were applied to the cross-sections before calculating the normalized cross section.

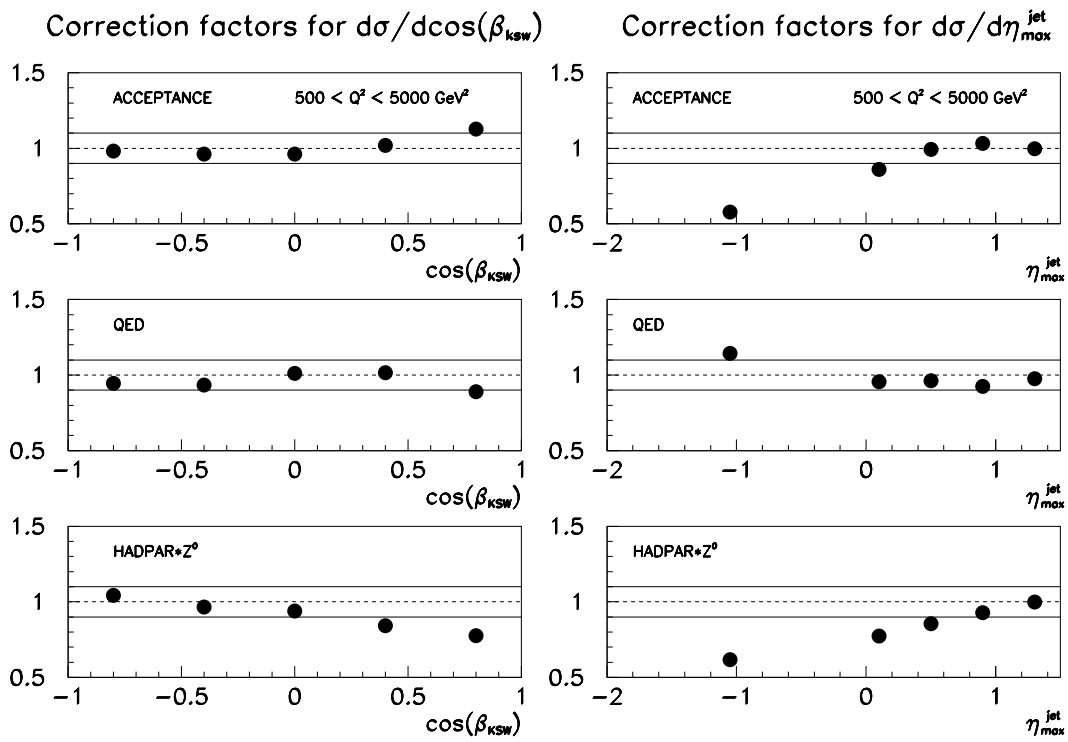


Figure 5.11: $C_{ACC}$, $C_{QED}$ and $C_{Z^0} \cdot C_{HAD}$ factors applied to the data (ACC and QED) and to the fixed-order pQCD calculations ($Z^0$ and HAD) for the $\Theta_H$ and $\cos\alpha_{23}$ distributions for the region of $500 < Q^2 < 5000$ GeV$^2$. The factors shown here were applied to the cross-sections before calculating the normalized cross section.

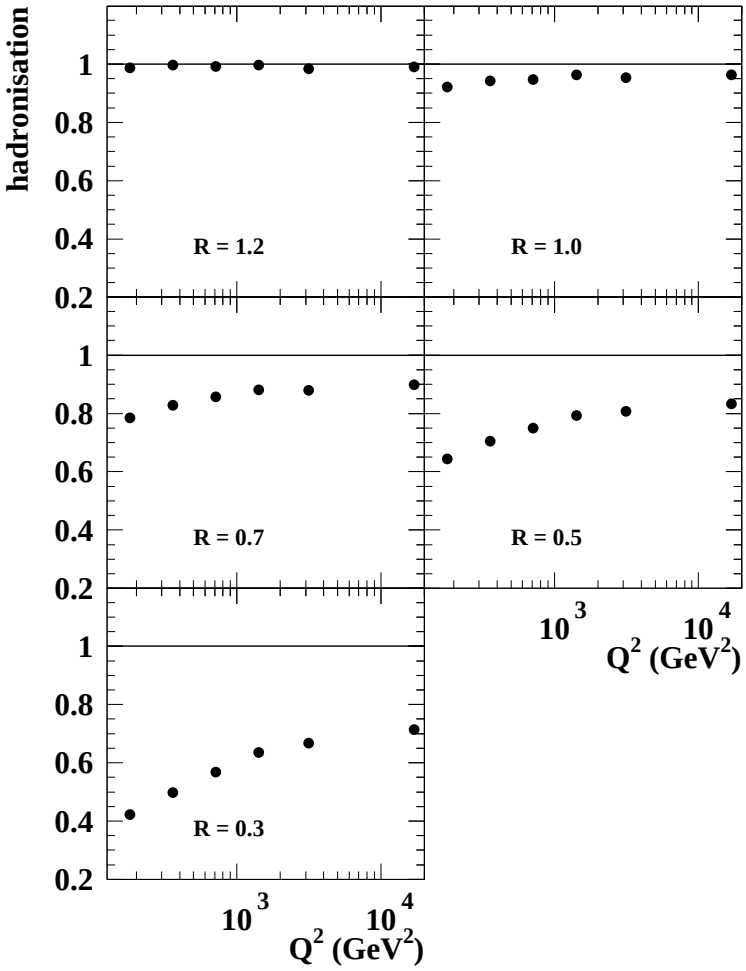


Figure 5.12: $C_{HAD}$ as a function of $Q^2$ for the jet radius R in the range $0.3 < R < 1.2$.

## 5.2 Experimental uncertainties

There are two types of experimental uncertainty associated to the measurements-systematic and statistical. For the statistical uncertainty, the number of events is assumed to have an underlying Poisson probability distribution. For this type of distribution the mean number of events is equal to the variance, and therefore $\sigma = \sqrt{N}$ is the $1\sigma$ spread assummed in the data. Especial care needs to be taken in the case of jet measurements. In this case, the Poisson distribution still applies to the number of events and not to that of the jets. A single event can contribute with more than one jet in a bin or with jets in different bins in the case of, say, an $E^{\rm jet}_{T,{\rm B}}$ distribution. Thus, in some cases there is a statistical correlation among different bins. This effect was taken into account for the analyses presented here and the statistical uncertainties shown are the correct ones for the jet analyses. Figs. 5.13 through 5.15 show the statistical uncertainties in the measurements of the jet cross sections. As expected from the steep fall-off of the distributions of the jets with increasing $Q^2$ and $E^{\rm jet}_{T,{\rm B}}$, the statistical uncertainties increase for higher energy scales. Figs. 5.16 through 5.19 show the statistical uncertainties for the angular-correlation normalized cross sections for the region $Q^2 > 125$ GeV$^2$. Figs. 5.20 through 5.23 show the statistical uncertainties for the angular-correlation normalized cross sections for the region $500 < Q^2 < 500$ GeV$^2$. Note that $\sim 1/2$ of the events are lost by restricting the phase-space region in $Q^2$, which is the price paid in order to minimize the dependence on $\alpha_s(\mu_R)$.

The following sources of systematic uncertainty were considered for the measured inclusive-jet cross sections:

- the uncertainty in the absolute energy scale of the electron candidate was estimated to be $\pm 1\%$. The resulting uncertainty in the cross sections was below $\pm 1\%$;
- the differences in the results obtained by using either ARIADNE-CDM or LEPTO-MEPS to correct the data for detector effects were taken to represent systematic uncertainties. The resulting uncertainty was typically below $\pm 3\%$;
- the $E^{jet}_{T,LAB}$ cut was raised to 4 GeV. The resulting uncertainty was smaller than $\pm 1\%$;
- the cut in $\eta^{jet}_{LAB}$ used to suppress the contamination due to photons falsely identified as jets in the Breit frame was set to -3 and to -1.5. The resulting uncertainty was below $\pm 1\%$;
- the $E - P_Z$ cut was raised and lowered by 3%. The resulting uncertainty was smaller than $\pm 1\%$;

- the uncertainty in the boost to the Breit frame was estimated by reconstructing the momentum of the exchanged boson using CTD information instead of that provided by the UCAL. The resulting uncertainty was less than 1%;
- the uncertainty in the absolute energy scale of the jets was estimated to be $\pm 1\%$ for $E^{jet}_{T,LAB} > 10$ GeV and $\pm 3\%$ for lower $E^{jet}_{T,LAB}$ values. The resulting uncertainty was $\approx \pm 5\%$;
- the uncertainty in the cross sections due to that in the simulation of the trigger was below 0.5%.

In addition, there was an overall normalization uncertainty of 2.2% from the luminosity determination.

Figs. 5.13 through 5.15 show the uncertainties listed above for the inclusive-jet cross sections. An important point to note from these plots is that the experimental uncertainties do not increase significantly anywhere in the jet-radius range of $0.5 < R < 1.0$. The uncertainties for the differential cross-section measurements with respect to $E^{\rm jet}_{T,\rm B}$ for different regions of $Q^2$ where similar in magnitude to those listed above.

The same sources of experimental uncertainty were considered for the angular-correlations analysis. Figs. 5.16 through 5.23 show the systematic uncertainties for the angular-correlation cross sections. Notably the largest contribution to the total systematic uncertainty in this case arises from that on the modelling of the parton-cascade. The angular correlations in the simulations rely on the parton cascade since the MC simulations available for these processes only contain pQCD calculations to $O(\alpha_s)$ and, therefore, it is not surprising that there is a relativey strong dependence of the acceptance correction factors (and thus of the cross section) on the parton-cascade model. As we showed in Chapter 4 (Figs. 4.24 and 4.25), the CDM model provides a somewhat poorer description of the distributions in the data than MEPS. For this reason the default used to correct the cross sections was MEPS and CDM was used to estimate this uncertainty.

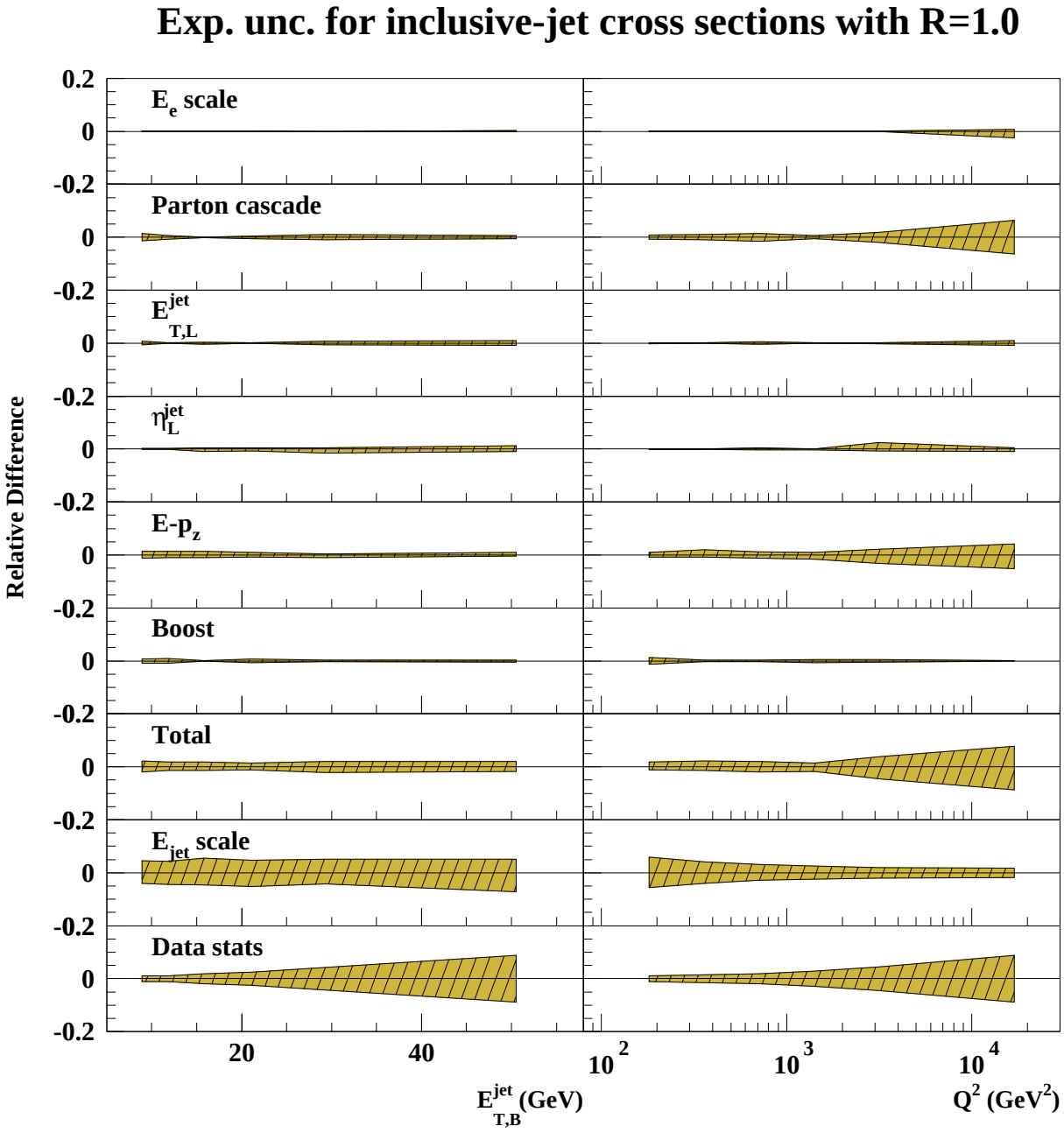


Figure 5.13: Relative systematic uncertainties with largest contributions to the overall experimental uncertainty of the inclusive-jet cross-section measurements of $d\sigma/dE^{jet}_{T,B}$ (left) and $d\sigma/dQ^2$ (right) with jet radius R=1.0.

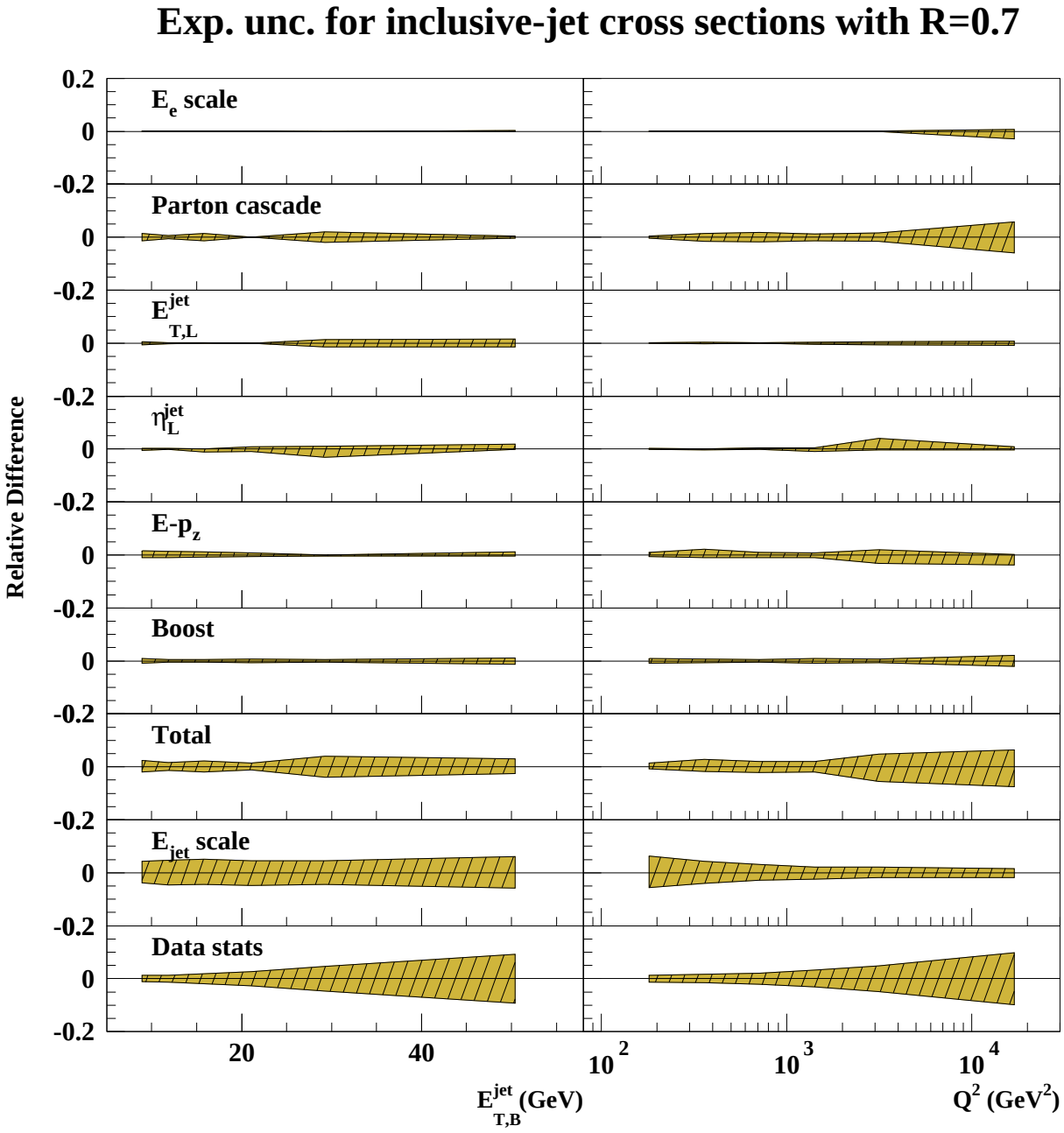


Figure 5.14: Relative systematic uncertainties with largest contributions to the overall experimental uncertainty of the inclusive-jet cross-section measurements of $d\sigma/dE^{jet}_{T,B}$ (left) and $d\sigma/dQ^2$ (right) with jet radius R=0.7.

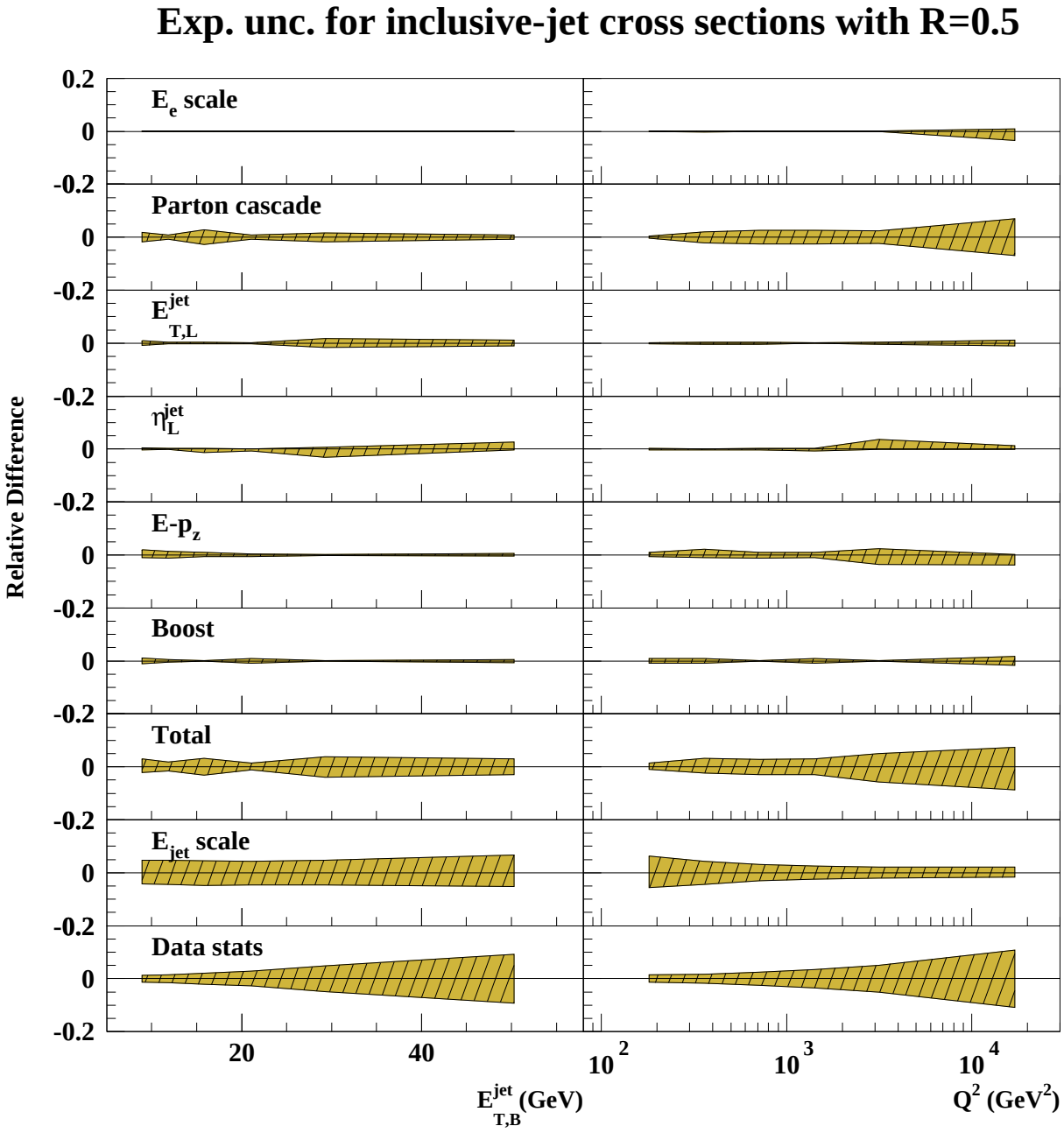


Figure 5.15: Relative systematic uncertainties with largest contributions to the overall experimental uncertainty of the inclusive-jet cross-section measurements of $d\sigma/dE^{jet}_{T,B}$ (left) and $d\sigma/dQ^2$ (right) with jet radius R=0.5.

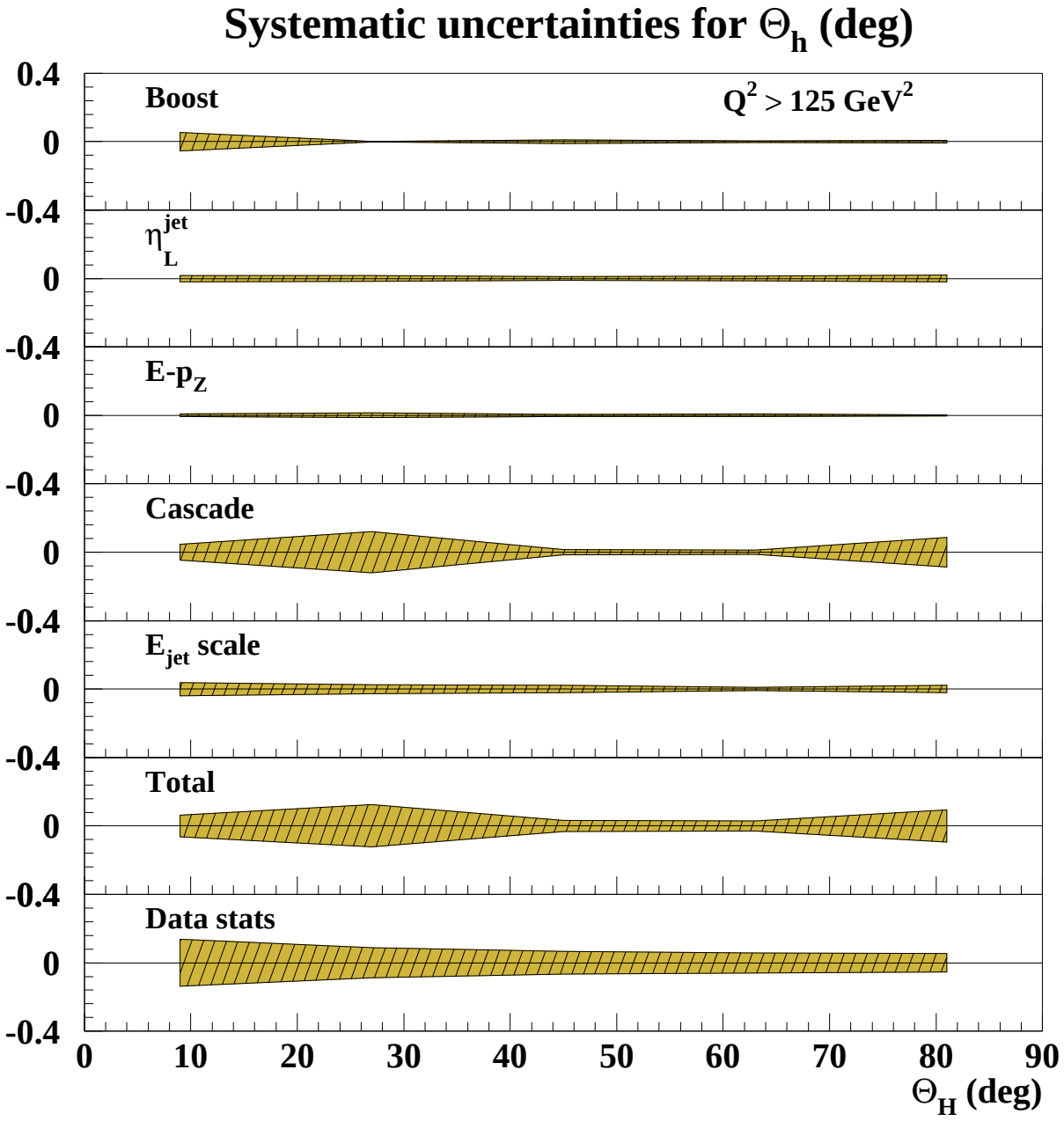


Figure 5.16: Relative systematic uncertainties with largest contributions to the overall experimental uncertainty of the normalized three-jet cross-section measurement of $(\frac{1}{\sigma})d\sigma/d\Theta_H$.

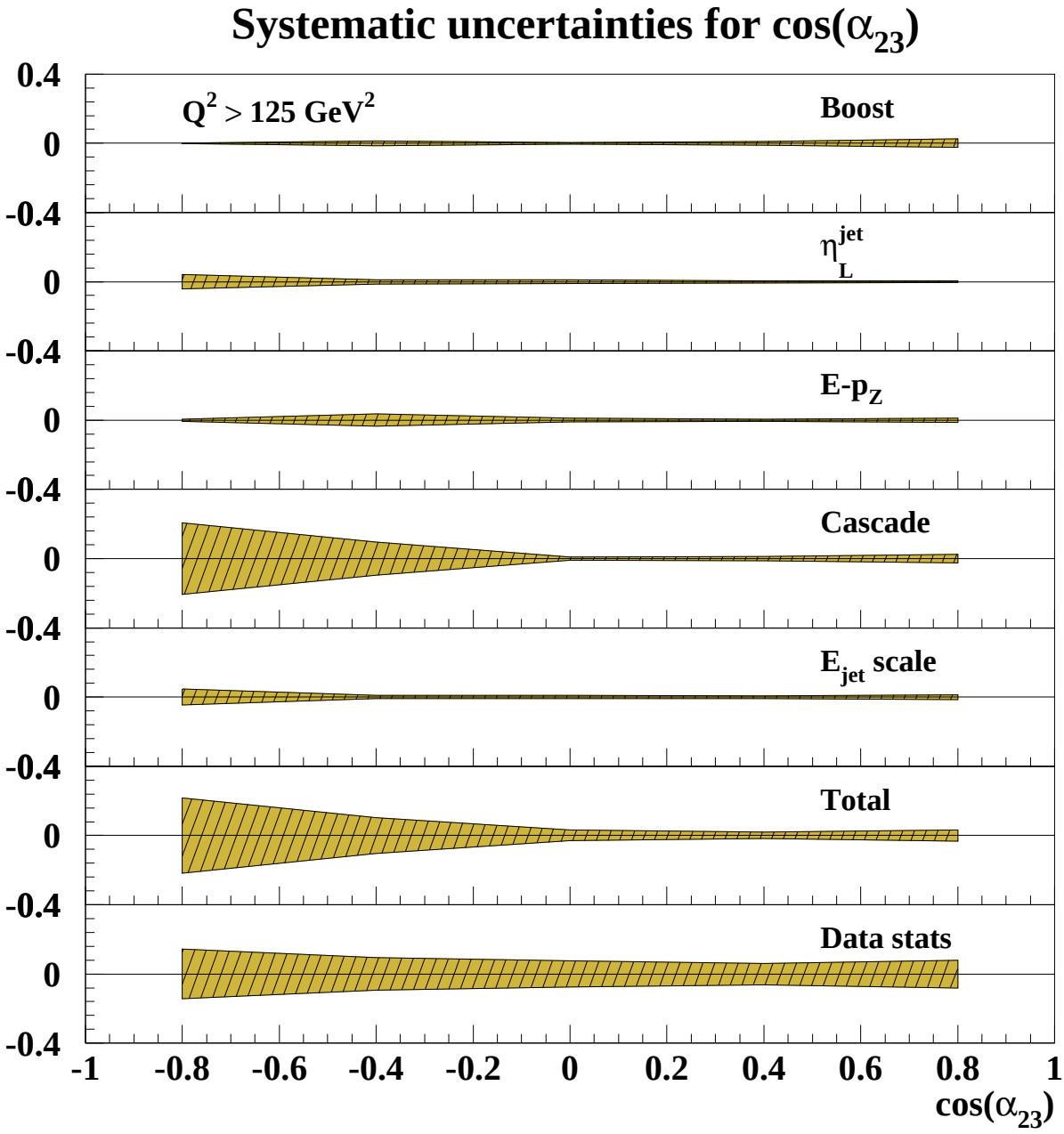


Figure 5.17: Relative systematic uncertainties with largest contributions to the overall experimental uncertainty of the normalized three-jet cross-section measurement of $(\frac{1}{\sigma})d\sigma/d\cos\alpha_{23}$.

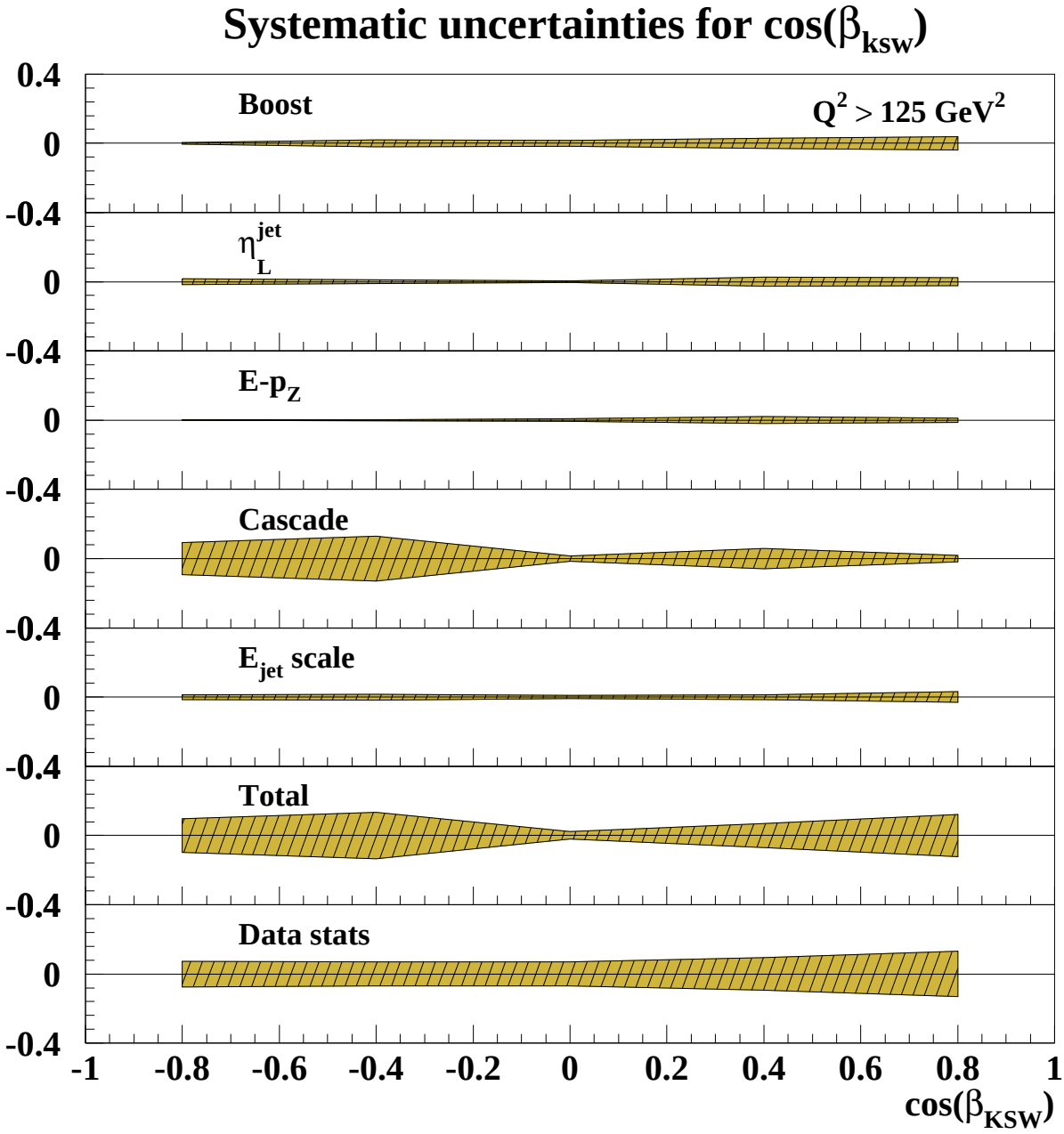


Figure 5.18: Relative systematic uncertainties with largest contributions to the overall experimental uncertainty of the normalized three-jet cross-section measurement of $(\frac{1}{\sigma})d\sigma/d\cos\beta_{ksw}$.

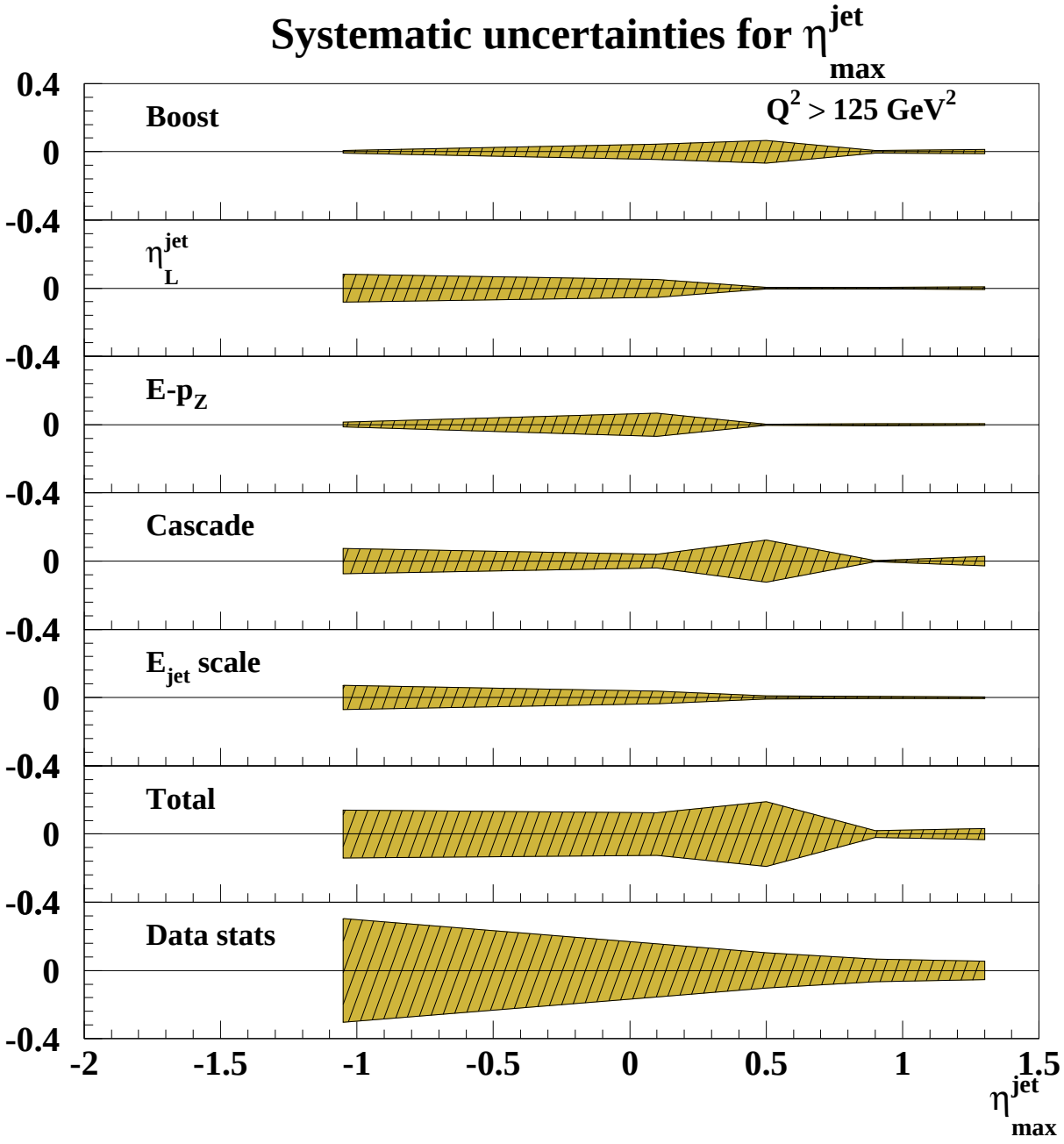


Figure 5.19: Relative systematic uncertainties with largest contributions to the overall experimental uncertainty of the normalized three-jet cross-section measurement of $(\frac{1}{\sigma})d\sigma/d\eta^{jet}_{max}$.

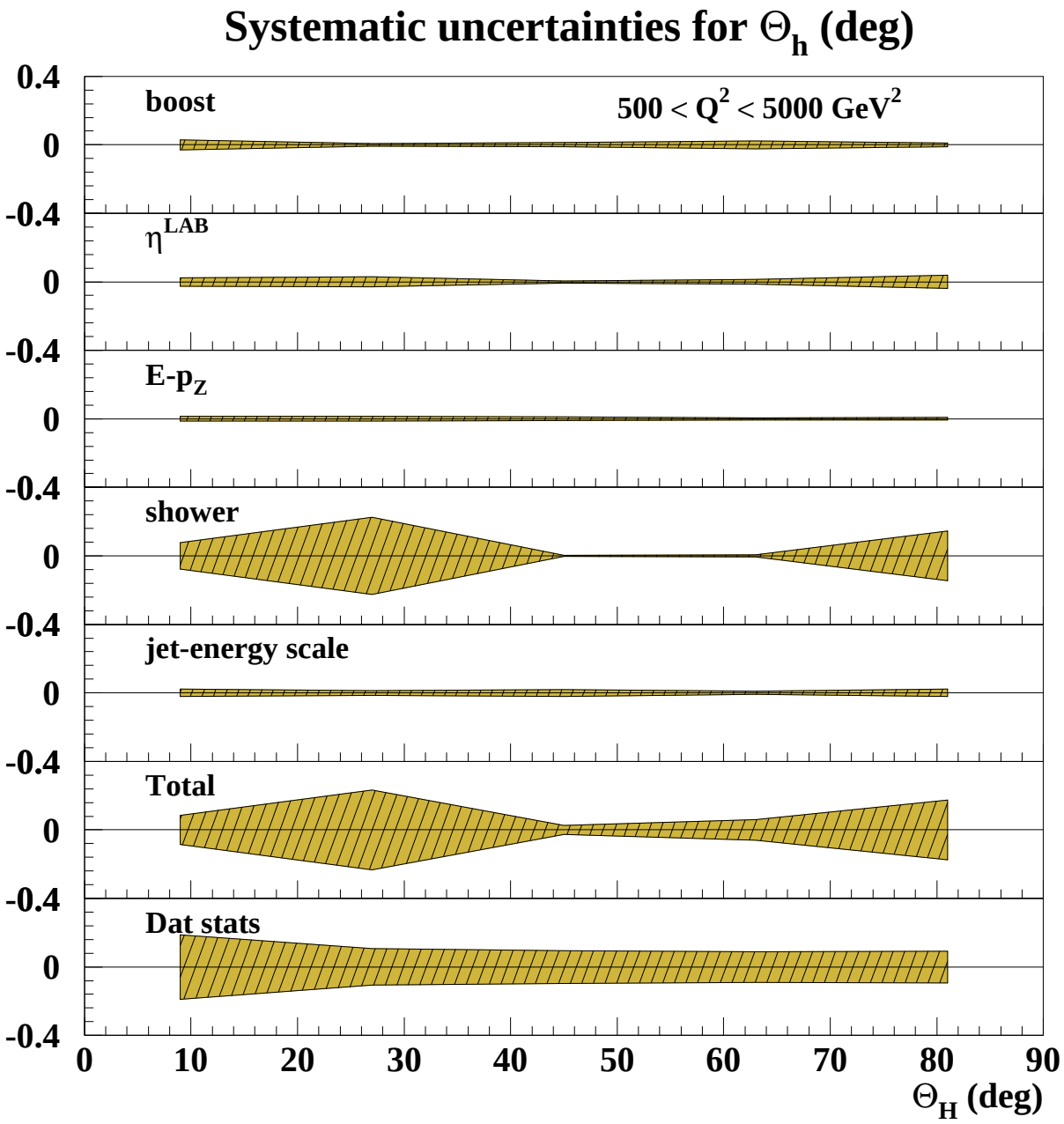


Figure 5.20: Systematic uncertainties with largest contributions to the overall experimental uncertainty of the normalized three-jet cross-section measurement of $(\frac{1}{\sigma})d\sigma/d\Theta_H$.

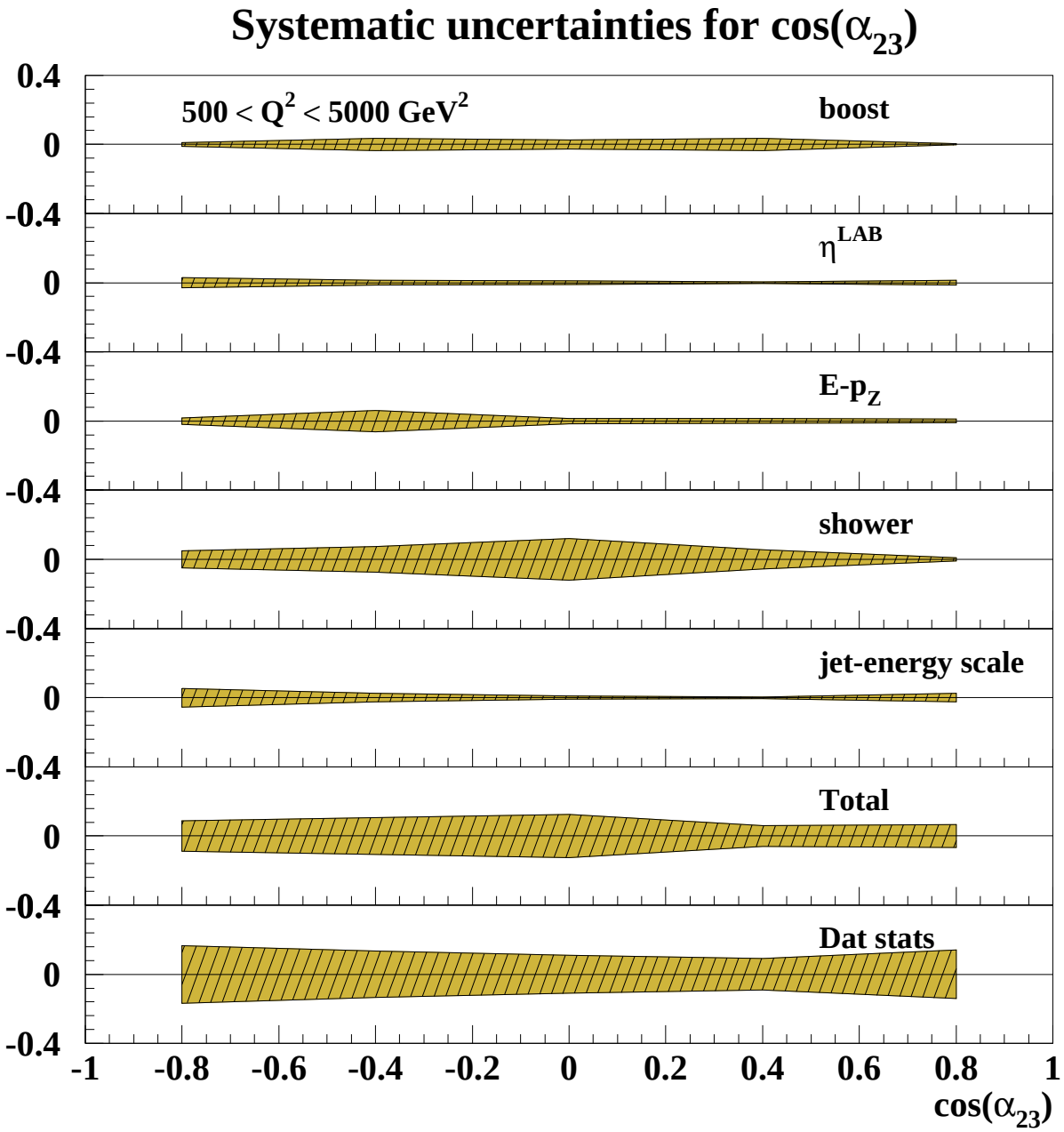


Figure 5.21: Systematic uncertainties with largest contributions to the overall experimental uncertainty of the normalized three-jet cross-section measurement of $(\frac{1}{\sigma})d\sigma/d\cos\alpha_{23}$.

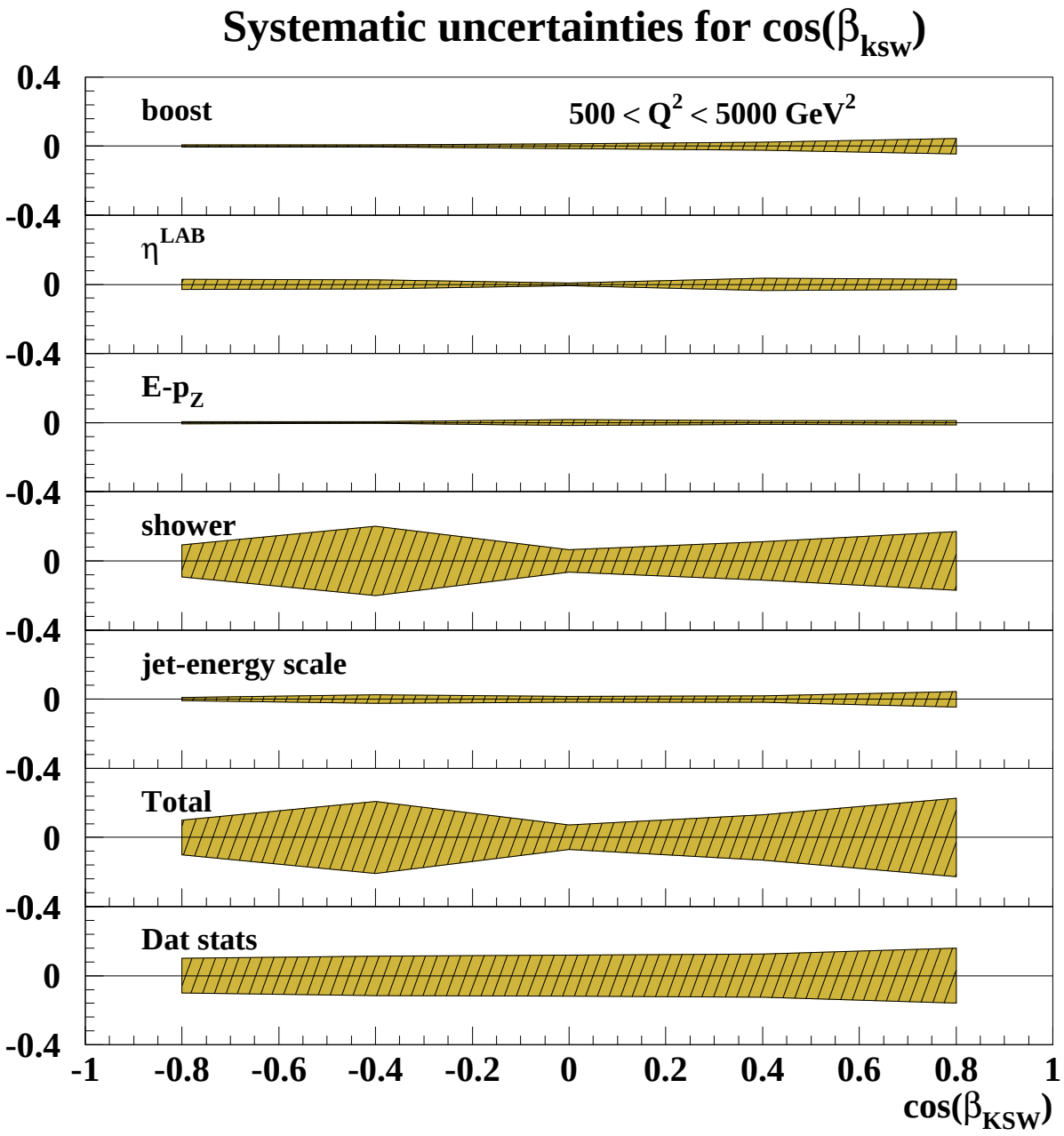


Figure 5.22: Systematic uncertainties with largest contributions to the overall experimental uncertainty of the normalized three-jet cross-section measurement of $(\frac{1}{\sigma})d\sigma/d\cos\beta_{ksw}$.

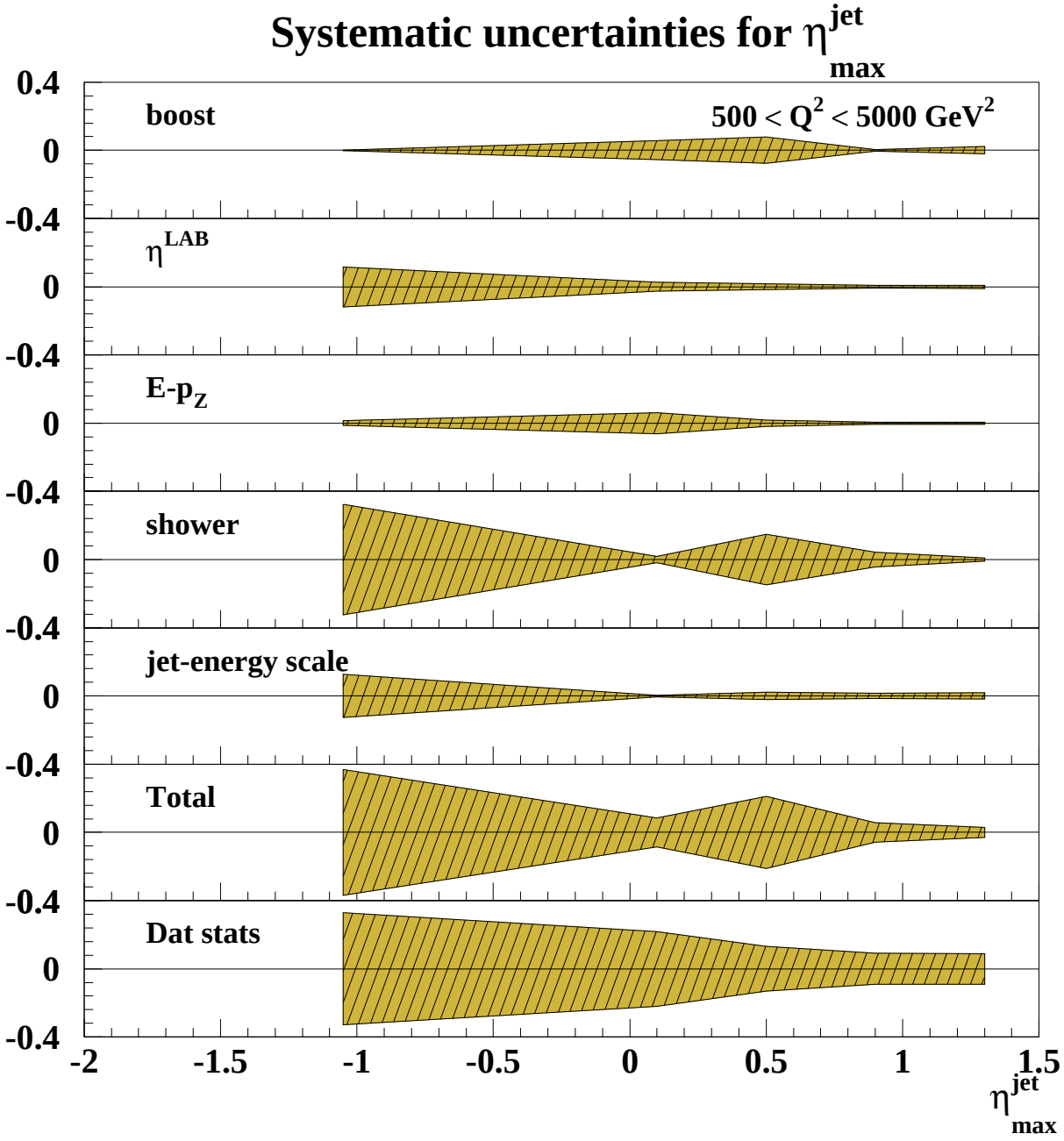


Figure 5.23: Systematic uncertainties with largest contributions to the overall experimental uncertainty of the normalized three-jet cross-section measurement of $(\frac{1}{\sigma})d\sigma/d\eta^{jet}_{max}$.

# Chapter 6

# Results: Jet radius dependence of inclusive-jet cross sections in DIS at HERA

## 6.1 Introduction

In preceding chapters we have shown how the inclusive-jet data sample has been selected and corrected with the aid of MC simulations. We have also made a detailed estimation of the theoretical and experimental uncertainties associated with these measurements. This chapter presents the final results of the $\alpha_s$ analysis, which are:

- Measurements of differential cross sections as functions of $Q^2$ and $E^{\rm jet}_{T,\rm B}$ and $d\sigma/dE^{jet}_{T,B}$ for different $Q^2$ regions in NC DIS for $Q^2 > 125$ GeV$^2$ using an integrated luminosity of 81.7pb$^{-1}$;
- Study of the dependence of the cross sections on the jet-radius parameter in the $k_T$ cluster algorithm;
- Measurement of the dependence on R of the inclusive-jet cross section for $Q^2 > 125$ and 500 GeV$^2$;
- Extraction of $\alpha_s(M_Z)$ from different $d\sigma/dE^{jet}_{T,B}$ and $d\sigma/dQ^2$ regions, among which is the most precise to date using ZEUS data alone: $\alpha_s(M_Z) = 0.1207 \pm 0.0014(\text{stat.}) \,^{+0.0035}_{-0.0033}(\text{exp.}) \,^{+0.0022}_{-0.0023}(\text{th.})$;
- Comparison of the measured inclusive-jet differential cross sections and of the running of $\alpha_s(E^{\rm jet}_{T,\rm B})$ and $\alpha_s(Q)$ with those predicted by QCD.

As discussed along this chapter, these measurements tested the characteristic aspects of pQCD and are expected to improve the determination of the proton PDFs

when included in future global QCD fits. Moreover, when combined with similar H1 measurements they yielded a determination of $\alpha_s$ with an overall experimental plus theoretical uncertainty of $\sim 2.7\%$, the most precise determination of $\alpha_s(M_Z)$ obtained at HERA thus far.

## 6.2 Differential inclusive-jet cross sections in NC DIS

**The measured cross sections**

The inclusive-jet cross sections were measured in the kinematic region $Q^2 > 125$ GeV$^2$ and $|\cos\gamma_h| < 0.65$. These cross sections include every jet of hadrons in the event with $E_{T,\mathrm{B}}^{\mathrm{jet}} > 8$ GeV and $-2 < \eta_{\mathrm{B}}^{\mathrm{jet}} < 1.5$ and were corrected for detector and QED radiative effects and the running of $\alpha_{em}$. The measurements of the inclusive-jet differential cross sections as functions of $E_{T,\mathrm{B}}^{\mathrm{jet}}$ and $Q^2$ are presented in Fig. 6.1. Each data point is plotted at the abscissa at which the NLO QCD differential cross section was equal to its bin-averaged value. The figures show a steep fall-off over three (five) orders of magnitude for the $d\sigma/dE_{T,B}^{jet}$ ($d\sigma/dQ^2$) over the measured range. The measurements are shown for different choices of the jet radius R=0.5, 0.7 and 1, and compared to $O(\alpha_s^2)$ calculations (solid line) using the ZEUS-S proton PDF set with $\mu_R = E_{T,\mathrm{B}}^{\mathrm{jet}}$. The values obtained with each jet radius choice have been scaled by the factor indicated in brackets to aid visibility. The inner error bars in the data (dots) represent the statistical uncertainty, while the outer error bars are the total experimental uncertainty excluding that due to the energy scale, which is represented as a band. The explicit values of the results shown in Fig. 6.1 are shown in Tables 6.1 and 6.2.

Fig. 6.2 shows the inclusive-jet differential cross sections with respect to $E_{T,\mathrm{B}}^{\mathrm{jet}}$ in different regions of $Q^2$ for R=1. The steep fall-off in the cross section with increasing $E_{T,\mathrm{B}}^{\mathrm{jet}}$ flattens out at higher $Q^2$ regions, a phenomenon well reproduced by pQCD, as shown in the figure. The explicit values of the results shown in Fig. 6.2 are shown in Table 6.3

The dependence of the total inclusive-jet cross sections with the jet radius parameter was also measured and is shown in Fig. 6.3. The measurements were made for $E_{T,\mathrm{B}}^{\mathrm{jet}} > 8$ GeV and $-2 < \eta_{\mathrm{B}}^{\mathrm{jet}} < 1.5$ in the kinematic range given by $|\cos\gamma_h| < 0.65$ integrated above $Q^2_{min} = 125$ and 500 GeV$^2$ for different jet radii. The measured cross section, $\sigma_{jets}$, increases linearly with R in the range between 0.5 and 1. The increase of $\sigma_{jets}$ as R increases can be understood as the result of more transverse energy being gathered in a jet so that a larger number of jets has $E_{T,\mathrm{B}}^{\mathrm{jet}}$ exceeding the threshold of 8 GeV. The explicit values of the results shown in Fig. 6.3 are shown in Table 6.4

**The comparison with fixed-order QCD calculations**

The inclusive-jet measurements were compared in detail to the $O(\alpha_s^2)$ QCD calculations obtained using the program DISENT as described in Chapter 3. The default calculations used the ZEUS-S parametrization of the proton PDFs (except in Fig. 6.2 in which CTEQ6 was used) with $\mu_R = E_{T,\mathrm{B}}^{\mathrm{jet}}$ and $\mu_F = Q$. The fractional differences between the measured $d\sigma/dE_{T,B}^{jet}$ and the QCD prediction are shown for the three choices of the jet radius in Fig. 6.4. There the hatched bands display the total theoretical uncertainty and the error bars in the data are as for Fig. 6.1. The figure shows $O(\alpha_s^2)$ QCD calculations provide a good description of the data within the small theoretical and experimental uncertainties. Similar comparisons with the pQCD predictions obtained using the MRST2001 and CTEQ6 parametrizations of the proton PDFs are shown in Fig. 6.5. The differences among the predictions due to the choice of proton PDFs used are contained within the uncertainties due to that of the PDFs themselves shown in Fig. 3.8, showing that there is no tension among the different sets for these observables. The figures also show that the overall theoretical and experimental uncertainties increase with increasing $E_{T,\mathrm{B}}^{\mathrm{jet}}$. Although the uncertainty from higher orders decreases with the increasing scale $E_{T,\mathrm{B}}^{\mathrm{jet}}$, the PDF related uncertainties of Fig. 3.8 increase, resulting in an overall increasing theoretical uncertainty. The experimental uncertainties increase due to the smaller statistics available with increasing $E_{T,\mathrm{B}}^{\mathrm{jet}}$. Notice, however, that the uncertainties are similar and so is the agreement between theory and data for all the choices of the jet radius considered here. Thus, it is concluded that $O(\alpha_s^2)$ QCD provides predictions with comparable precision in the range R=0.5-1.

Figs. 6.6 and 6.7 show similar comparisons between the measured $d\sigma/dQ^2$ and the $O(\alpha_s^2)$ QCD calculations. In this case the overall theoretical uncertainty decrases with increasing $Q^2$, as expected from a decreasing $\mu_R$ dependence and a decreasing PDF uncertainty at higher scales (refer to Fig. 3.8). Fig. 6.8 shows the comparison with the default prediction for the measured differential cross section as a function of $E_{T,\mathrm{B}}^{\mathrm{jet}}$ in different regions of $Q^2$ for R=1. For the $d\sigma/dQ^2$ case, pQCD provides a good description of the data despite the steep fall-off of the measurement and the small uncertainty involved in the comparison. In the case of Fig. 6.8, pQCD is able to reproduce well the flattening of the fall-off of $d\sigma/dE_{T,B}^{jet}$ with increasing $Q^2$ observed in the data.

Fig. 6.9 is similar to Figs. 6.4 and 6.6, but here the theoretical predictions have been obtained using $\mu_R = Q$ instead of $\mu_R = E_{T,\mathrm{B}}^{\mathrm{jet}}$. As can be seen, the difference between the predictions obtained with different choices of $\mu_R$ is in general within the theoretical uncertainties and is under $\sim 5\%$, except for the very high $Q^2$ region.

For the total cross section as a function of R the comparison with $O(\alpha_s^2)$ calcula-

tions is shown in Fig. 6.3. The figures demonstrate that the $O(\alpha_s^2)$ calculations are able to reproduce the linear dependence of the inclusive-jet cross section on the jet radius. The sub-plots contained in the figures show the LO and NLO predictions for this dependence. At LO ($O(\alpha_s)$), there are only two back-to-back partons with high $E_{T,\mathrm{B}}^{\mathrm{jet}}$ in Breit frame. Reducing the jet radius in this case will not have an effect on the final state in terms of jets and the total cross section shows no dependence on the jet radius parameter. At NLO the transverse energy is shared among the three partons. Decreasing the jet radius will tend to break the event into more jets with reduced transverse momentum for each jet, making it less probable for a single jet to pass the $E_{T,\mathrm{B}}^{\mathrm{jet}} > 8$ GeV cut. Thus, the cross section is reduced with decreasing jet radius as shown both by the predictions and the measurements.

**Conclusions regarding the measured jet cross sections**

Here is an outline of the conclusions regarding the inclusive-jet cross section measurements:

- They probe an extended kinematic regime with respect to previous analyses due to the increase in the proton beam energy;
- The improved experimental uncertainties and the precision of the predictions in this regime provide a compelling test of pQCD;
- It is concluded that NLO QCD provides predictions with comparable precision in the range $R = 0.5 - 1$. For larger values of $R$, e.g. $R = 1.2$, it was estimated that the uncertainty on the NLO QCD calculations due to terms beyond NLO increases up to about 10% for high $Q^2$ values (see Fig. 3.1). On the other hand, the hadronisation correction estimated for the cross sections with smaller radii, e.g. $R = 0.3$, increases up to about 40% (see Fig. 5.12). It has been shown that the quality of the description of the data by pQCD does not depend on the jet radius for the range of R considered, meaning that $0.5 < R < 1$ is a valid range for the $k_T$ clustering algorithm.
- The improvement in the experimental uncertainties obtained will facilitate a more precise determination of the gluon density in the proton at high $x$. This is evidenced by Fig. 3.9, where it is shown that the gluon fraction becomes substantial in the lower $Q^2$ region for these measurements, and Fig. 3.3, which shows that the uncertainties in the prediction coming from that in the PDFs is large and in fact dominant in some regions.
- The small uncertainties in the measurements yield small uncertainties in the determinations of $\alpha_s$. This topic and the next are the subject of the next

section;

- The wide range in $E_{T,\mathrm{B}}^{\mathrm{jet}}$ and $Q^2$ allows for a test of the pQCD scale dependence of $\alpha_s$.

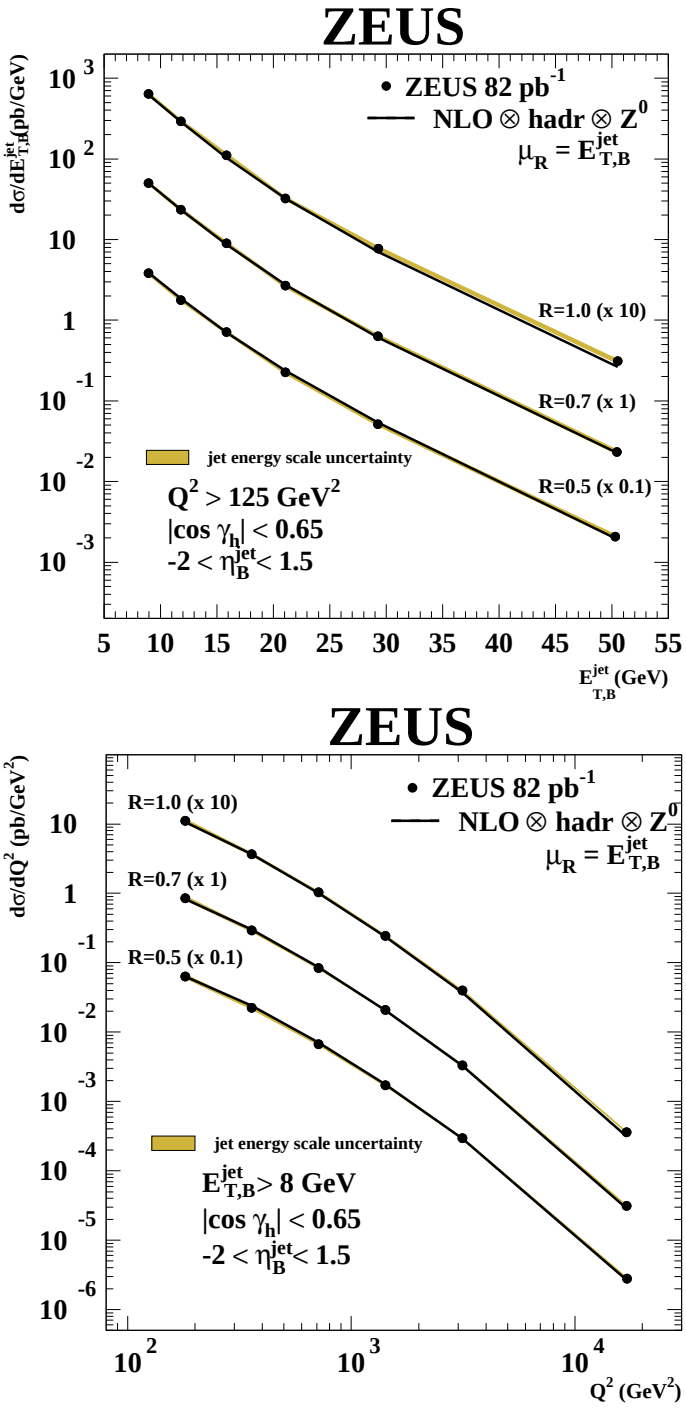


Figure 6.1: The measured $d\sigma/dE^{jet}_{T,B}$ and $d\sigma/dQ^2$ (dots) for different jet radii. The $O(\alpha_s^2)$ QCD calculations with $\mu_R = E^{\rm jet}_{T,\rm B}$ (solid lines) obtained using the ZEUS-S parametrisations of the proton PDFs are also shown. The inner error bars show the statistical uncertainty. The outer error bars show the statistical and systematic uncertainties, not associated with the uncertainty in the absolute energy scale of the jets (shaded bands), added in quadrature.

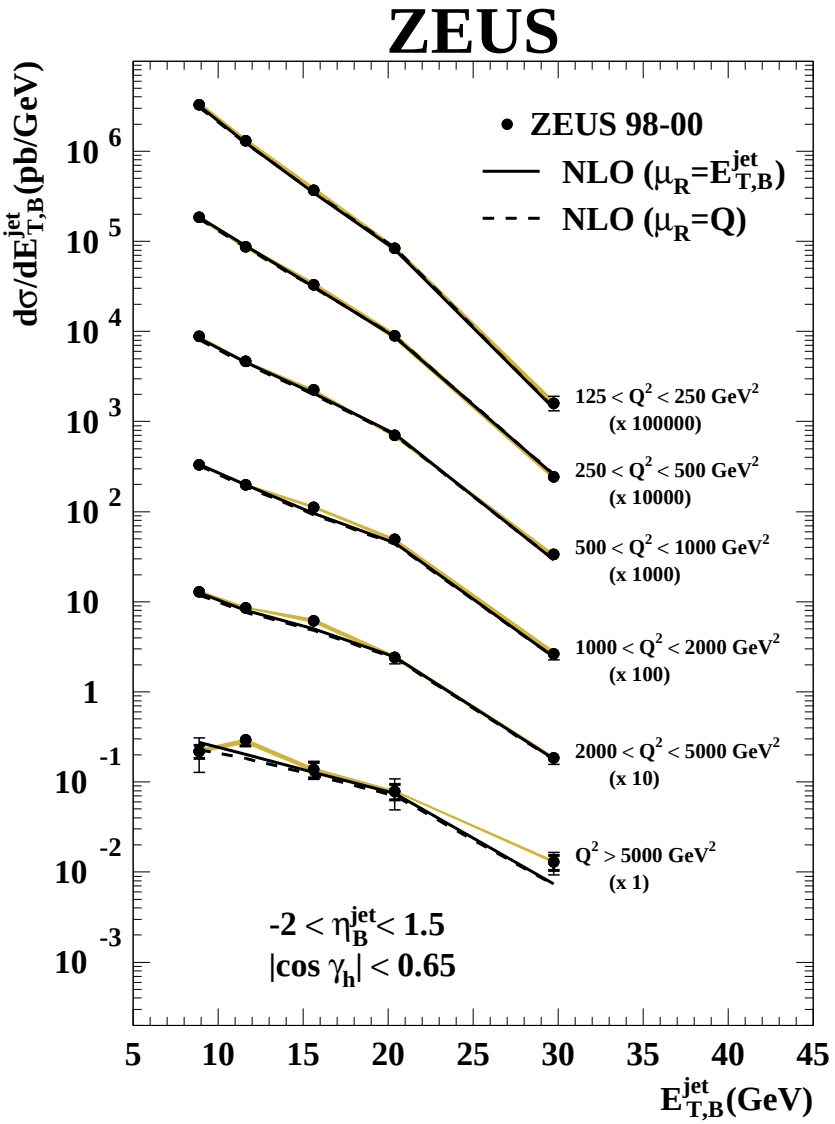


Figure 6.2: The measured differential cross section $d\sigma/dE^{jet}_{T,B}$ for inclusive-jet production with $E^{\rm jet}_{T,\rm B} > 8$ GeV and $-2 < \eta^{\rm jet}_{\rm B} < 1.5$ in different regions of $Q^2$ (dots). The $O(\alpha_s^2)$ QCD calculations with $\mu_R = E^{\rm jet}_{T,\rm B}$ (solid lines) and $\mu_R = Q$ (dashed lines) corrected for hadronization and $Z^0$ effects and using the CTEQ6 parametrizations of the proton PDFs are also shown. Other details as in the caption to Fig. 6.1.

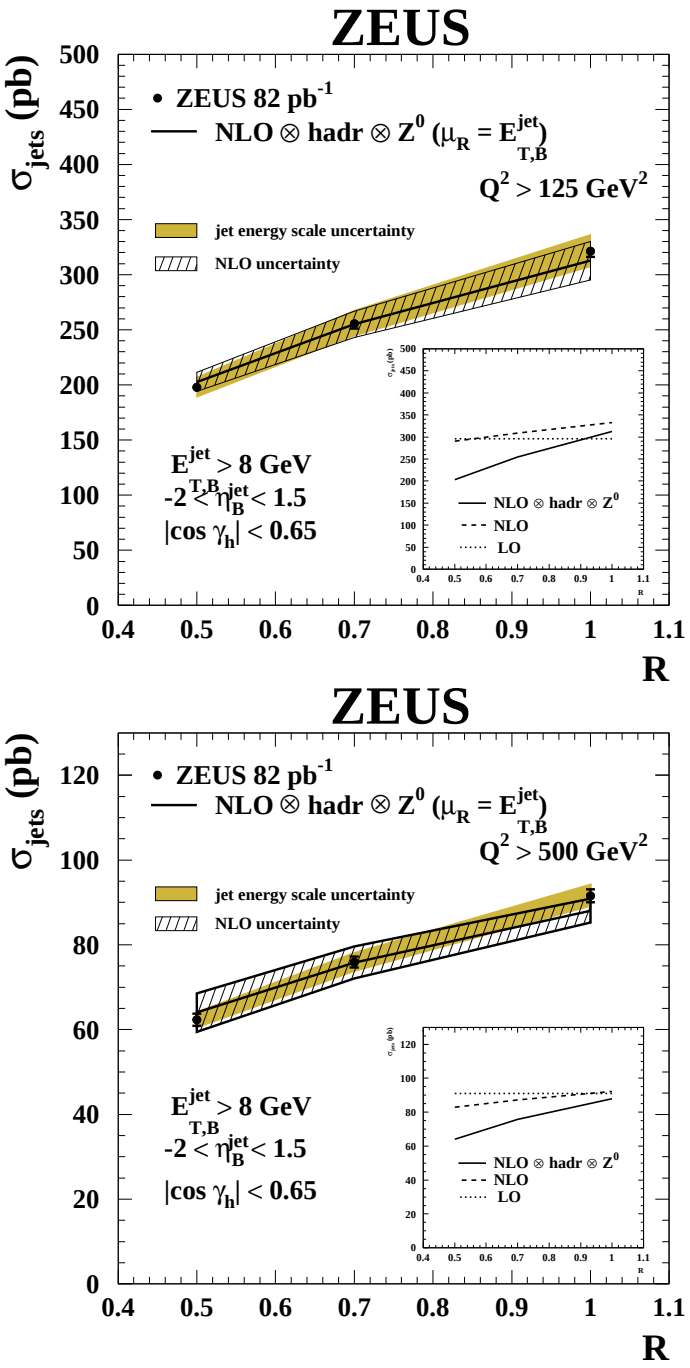


Figure 6.3: The measured inclusive-jet cross-section $\sigma_{jets}$ as a function of the jet radius for inclusive-jet production with $E^{\rm jet}_{T,\rm B} > 8$ GeV and $-2 < \eta^{\rm jet}_{\rm B} < 1.5$ (dots), in the kinematic range given by $|\cos\gamma_h| < 0.65$ and $Q^2 > 125$ GeV$^2$ (top) and $Q^2 > 500$ GeV$^2$ (bottom). The insets show the LO (dotted lines) and NLO (dashed lines) QCD calculations done using the ZEUS-S PDFs. The NLO QCD calculations corrected to include hadronisation and $Z^0$ effects are shown as solid lines. Other details as in the caption to Fig. 6.1.

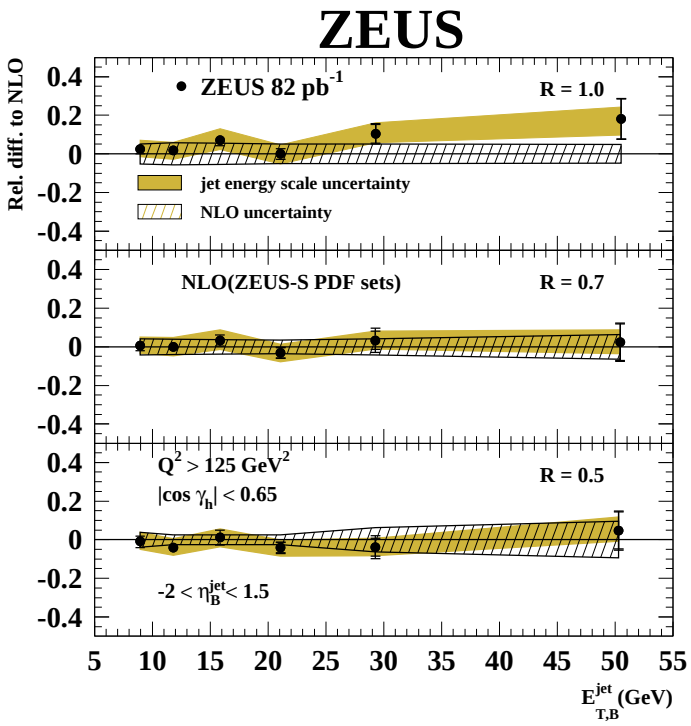


Figure 6.4: The fractional differences between the measured $d\sigma/dE^{jet}_{T,B}$ and the NLO QCD calculations using the ZEUS-S parametrizations of the proton PDFs; the hatched bands display the total theoretical uncertainty. Other details as in the caption to Fig. 6.1.

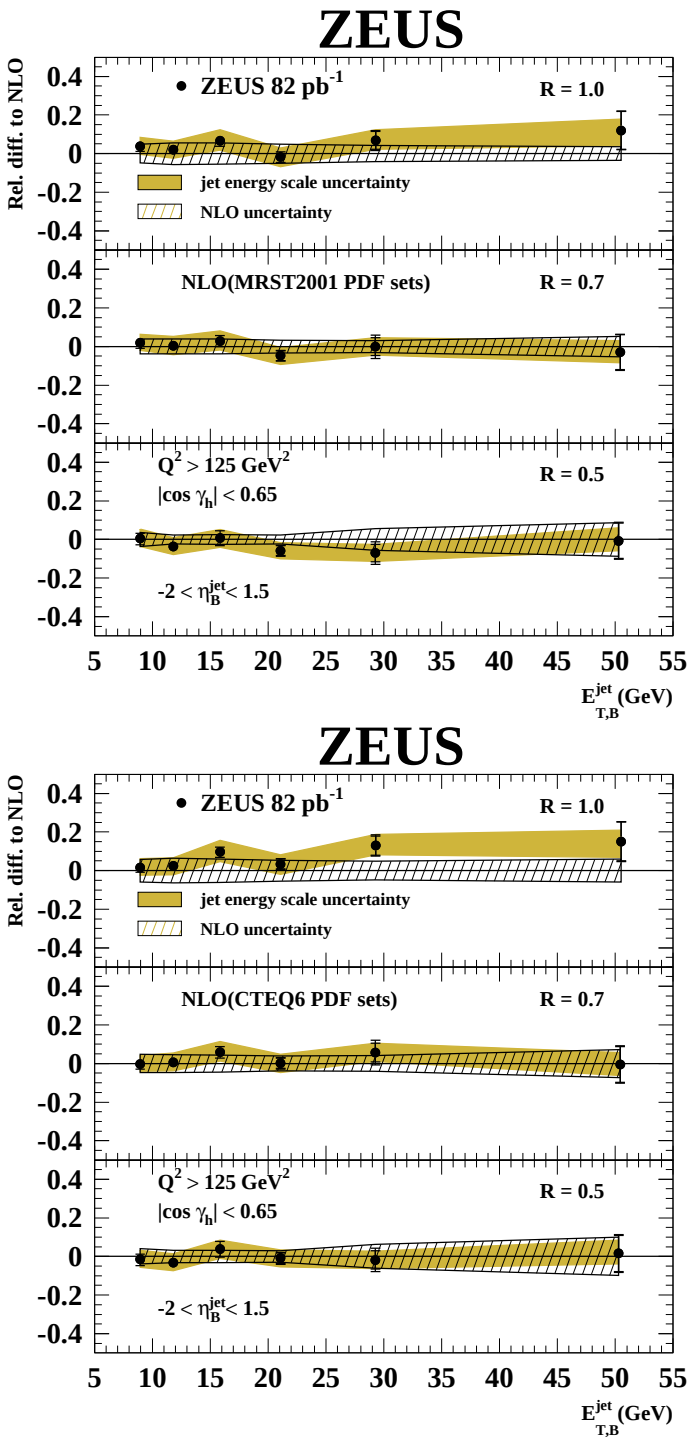


Figure 6.5: The fractional differences between the measured $d\sigma/dE^{jet}_{T,B}$ and the NLO QCD calculations using the MRST2001 (top) and CTEQ6 (bottom) parametrizations of the proton PDFs; the hatched bands display the total theoretical uncertainty. Other details as in the caption to Fig. 6.1.

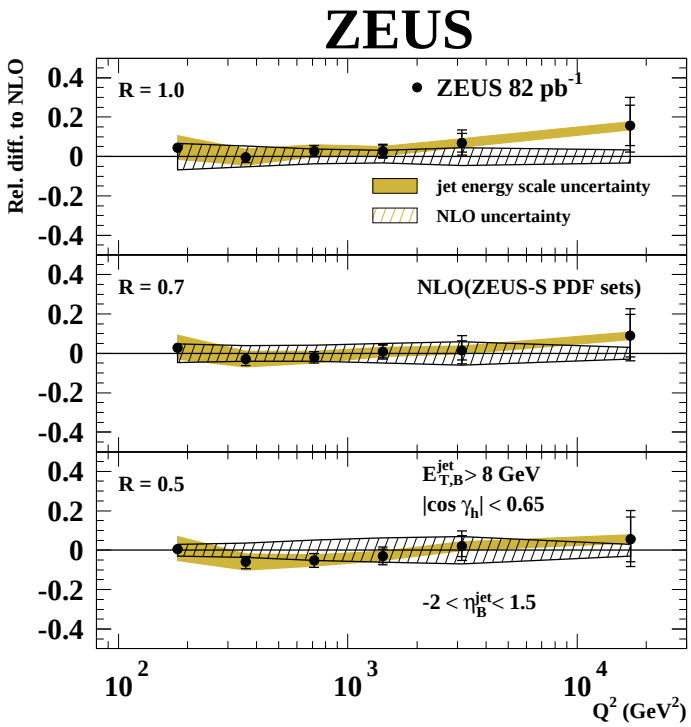


Figure 6.6: The fractional differences between the measured $d\sigma/dQ^2$ and the NLO QCD calculations using the ZEUS-S parametrizations of the proton PDFs; the hatched bands display the total theoretical uncertainty. Other details as in the caption to Fig. 6.1.

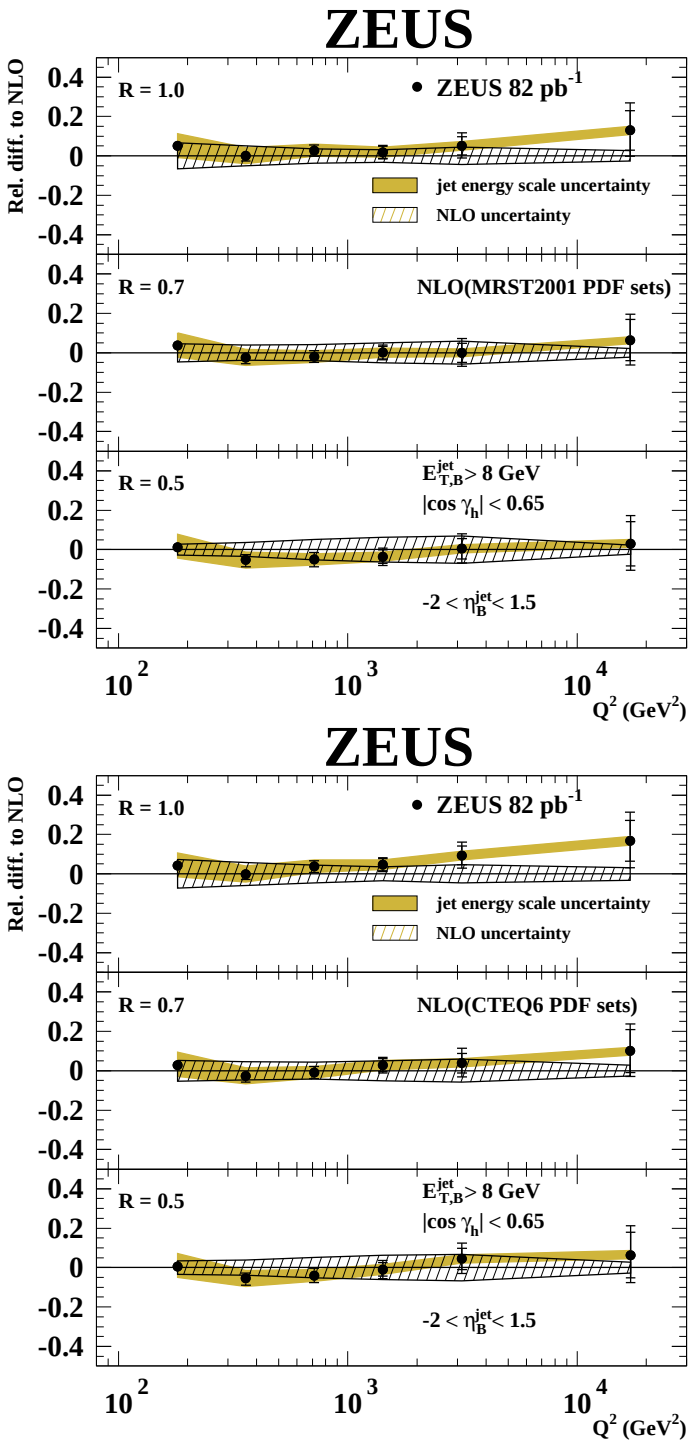


Figure 6.7: The fractional differences between the measured $d\sigma/dQ^2$ and the NLO QCD calculations using the MRST2001 (top) and CTEQ6 (bottom) parametrizations of the proton PDFs; the hatched bands display the total theoretical uncertainty. Other details as in the caption to Fig. 6.1.

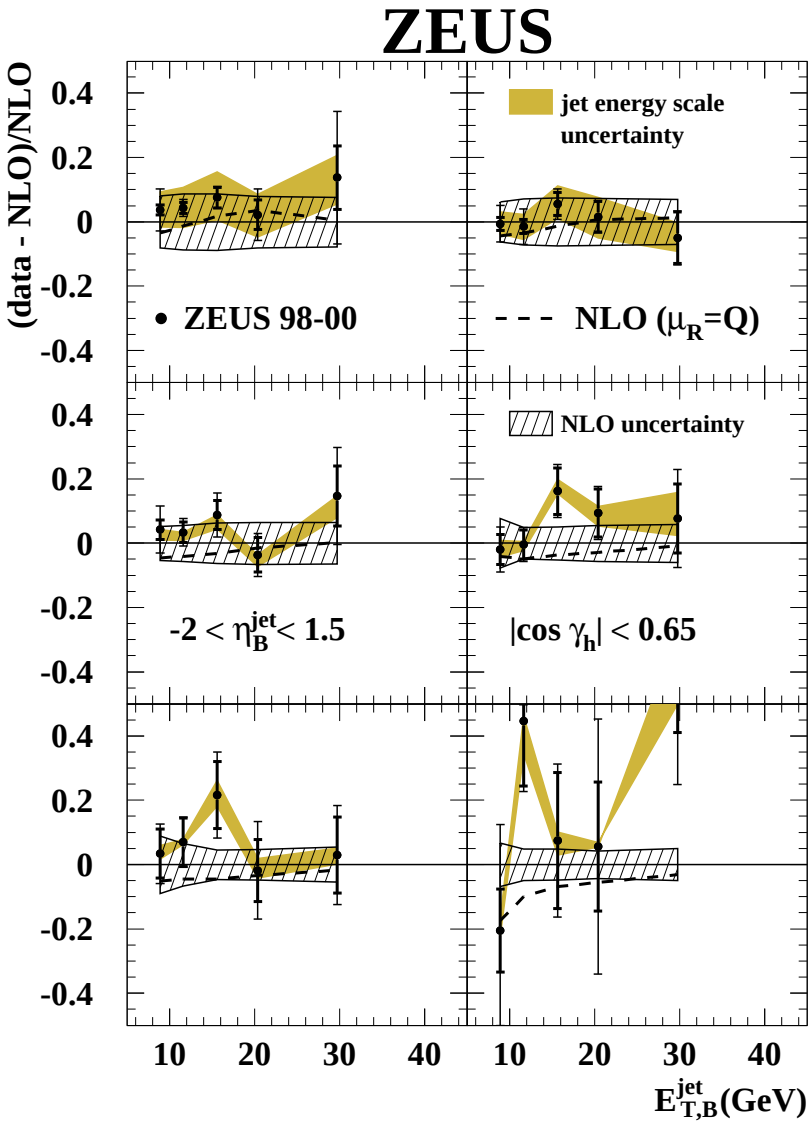


Figure 6.8: The fractional differences between the measured $d\sigma/dE^{jet}_{T,B}$ in different regions of $Q^2$ and the NLO QCD calculations using the CTEQ6 parametrizations of the proton PDFs and $\mu_R = E^{\rm jet}_{T,\rm B}$; the hatched bands display the total theoretical uncertainty. The relative differences between the NLO QCD calculations with $\mu_R = Q$ and those with $\mu_R = E^{\rm jet}_{T,\rm B}$ are also as dashed lines. Other details as in the caption to Fig. 6.1.

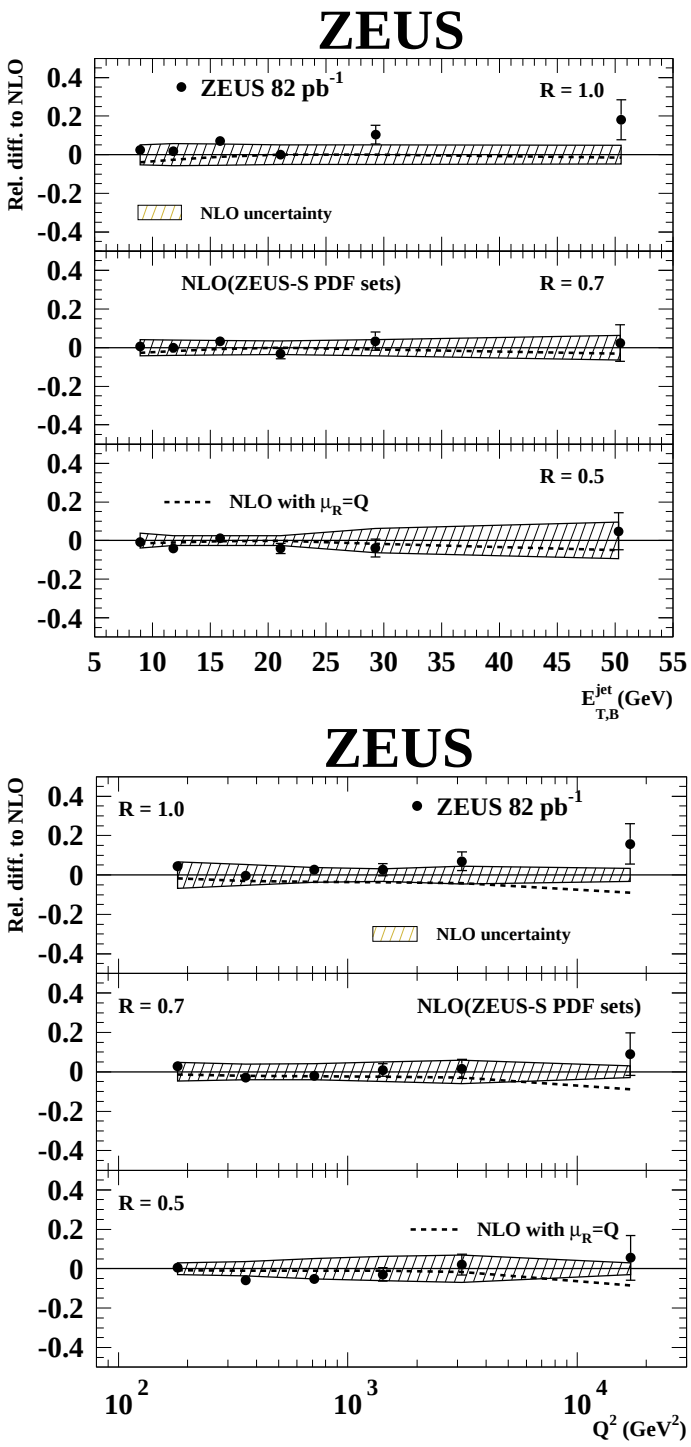


Figure 6.9: The fractional differences between the measured $d\sigma/dQ^2$ and the NLO QCD calculations done with the CTEQ6 proton PDFs; the hatched bands display the total theoretical uncertainty. The error bars represent the statistical uncertainty. The shaded bands display the uncertainty due to the absolute energy scale of the jets. The relative differences between the NLO QCD calculations with $\mu_R = Q$ and those with $\mu_R = E^{\rm jet}_{T,\rm B}$ are also as dashed lines.

## 6.3 Determinations of $\alpha_s(M_Z)$

### 6.3.1 The extraction of $\alpha_s(M_Z)$ from the inclusive-jet cross section measurements

The measured differential cross sections presented in the previous section were used to determine values of $\alpha_s(M_Z)$ using the method described in Chapter 1. The idea is to parametrize the dependence of the prediction on the assumed value of $\alpha_s(M_Z)$ (both in the matrix elements and in the PDF sets) and then use this parametrization to obtain the value of $\alpha_s(M_Z)$ that reproduces the measured cross section. Here is an outline of the method used:

- As shown in Fig. 1.19, the calculations are repeated using an NLO program such as DISENT, assuming different values of $\alpha_s(M_Z)$ both in the matrix elements and in the proton PDF set. Note that this procedure limits the amount of calculations that can be made since there are only a limited amount of PDF parametrizations available with different assumed values of $\alpha_s(M_Z)$.
- For the case of the ZEUS-S PDF sets, five [1] predictions were obtained for each inclusive-jet cross section with $\alpha_s(M_Z) = 0.115$, 0.117, 0.119, 0.121, and 0.123.
- These predictions lie in a curve like Fig. 1.19 which symbolizes the dependence of the cross section on the value of $\alpha_s(M_Z)$ assumed.
- These five predictions were then fitted with a simple polinomial

$$\left[\frac{d\sigma}{dA}\right]_i (\alpha_s(M_Z)) = C_1^i \alpha_s(M_Z) + C_2^i \alpha_s^2(M_Z), \tag{6.1}$$

  which represents the dependence of the theorical prediction on $\alpha_s(M_Z)$. Here the $C_1^i$ and $C_2^i$ are the parameters that are determined from a $\chi^2$ fit to the five points (corrected for hadronization and $Z^0$-exchange effects).
- Once the dependence of the prediction on $\alpha_s(M_Z)$ is obtained, the value of $\alpha_s(M_Z)$ obtained from a measurement of a cross section is simply that which reproduces that measurement.

Several cross-section measurements can also be combined to obtain a single value of $\alpha_s(M_Z)$. This yielded more precise determinations since the same value of $\alpha_s(M_Z)$ must simultaneously describe several measurements. In this case first the parametrization of the dependence of each cross section prediction on $\alpha_s(M_Z)$ was

[1] Note that for other PDF parametrizations there are more (or less) sets available with alternate values of $\alpha_s(M_Z)$ assumed in the fits. For example for the CTEQ6AB (MRST2001) there are 10(3) different available sets.

obtained, and then the value of $\alpha_s(M_Z)$ was extracted from the data by a simultaneous $\chi^2$ fit to the measured $d\sigma/dE^{jet}_{T,B}(d\sigma/dQ^2)$ for several regions of the variable $E^{\rm jet}_{T,\rm B}(Q^2)$ using the parametrizations.

Using this method a value of $\alpha_s(M_Z)$ was obtained from the various differential cross sections and jet radii. It was found that the combined region of $Q^2 > 500$ GeV$^2$ with R=1 yielded the smallest theoretical and experimental uncertainties for the value of $\alpha_s(M_Z)$:

$$\alpha_s(M_Z) = 0.1207 \pm 0.0014(\text{stat.})^{+0.0035}_{-0.0033}(\text{exp.})^{+0.0022}_{-0.0023}(\text{th.}) \qquad (6.2)$$

This value is consistent with previous values obtained at HERA and with the world average ($\alpha_s^{\rm worldaverage} = 0.1189 \pm 0.0010$) [66]. It has an overall uncertainty of $\sim 3.7\%$, making it one of the most precise extractions for this value to date. It should be noted that the there are regions of phase-space where the experimental (theoretical) uncertainties for this extraction can be reduced at the expense of increased theoretical (experimental) uncertainties. The experimental and theoretical uncertainties associated to the extractions of $\alpha_s(M_Z)$ are discussed in detail in the next sections.

Fig. 6.10 shows the values of $\alpha_s(M_Z)$ obtained using the method outlined above from each of the measured $d\sigma/dQ^2$ data points and for the combined region of $Q^2 > 500$ GeV$^2$. The values shown in the figure correspond to the three choices of the jet radius. The abscissas are the mean $Q^2$ of the events in each bin of the inclusive-jet cross section from which the values of $\alpha_s(M_Z)$ where extracted. The inner error bars denote the statistical uncertainties, while the outer error bars are the statistical and systematic uncertainties added in quadrature. The theoretical uncertainties are shown as a solid vertical line next to each value of $\alpha_s(M_Z)$. The horizontal line represents the world average with its uncertainty.

Figs. 6.11 and 6.12 show the values of $\alpha_s(M_Z)$ obtained having used the MRST2001 and CTEQ6AB sets to obtain the dependence of the predictions on the value of $\alpha_s(M_Z)$, respectively. The values obtained are consistent with those of Fig. 6.10. The values in Fig. 6.10 were used as the default values. This choice is explained in the next section, regarding the theoretical uncertainty in the extracted value of $\alpha_s(M_Z)$ due to that on the proton PDFs.

Since the values of $\alpha_s(M_Z)$ were obtained at different energy scales, the fact that they agree when evolved down to the $M_Z$ implies that the measured energy scale dependence agrees with that of pQCD. The values of $\alpha_s(M_Z)$ extracted from the $d\sigma/dE^{jet}_{T,B}$ measurements are plotted in Fig. 6.13 at the average $E^{\rm jet}_{T,\rm B}$ values corresponding to the $E^{\rm jet}_{T,\rm B}$ bins from which they were obtained, $\alpha_s(< E^{\rm jet}_{T,\rm B} >)$. These plots make the test of the scale dependence of $\alpha_s$ as predicted by pQCD visually evident. The error bars are as those for the previous figures. The plots show that the measured scale dependence of $\alpha_s$ is in agreement with that predicted by pQCD

and illustrate the asymptotic freedom property of QCD. Since the particular scale dependence of $\alpha_s$ for a gauge theory is determined by the color factors, this also constitutes a test of the underlying symmetry group assumption of pQCD. The explicit values of the results shown in Fig. 6.13 are shown in Table 6.5 Overall these plots represent a compelling and precise test of the validity of pQCD as the theory for the strong interactions.

**Conclusions regarding the determinations of $\alpha_s(M_Z)$**

Here is an outline of the conclusions regarding the determinations of $\alpha_s(M_Z)$:

- Extractions of $\alpha_s$ have been obtained from improved measurements of inclusive-jet cross sections with respect to $E^{\text{jet}}_{T,\text{B}}$ and $Q^2$. All the values are consistent among themselves as well as with the world average;
- The agreement of the $\alpha_s(M_Z)$ values obtained from different energy scales represents a compelling test of the energy-scale dependence of $\alpha_s$ predicted by pQCD. Since the shape of $\alpha_s(\mu_R)$ is governed by the color factors as discussed in Chapter 1, these values test directly the underlying symmetry group assumption of pQCD;
- Moreover, the agreement of the values of $\alpha_s(M_Z)$ obtained using different jet-radius assumptions shows that a consistent analysis can be made varying the value of R within the range $0.5 < R < 1$;
- A single value obtained from the combined region $Q^2 > 500$ GeV$^2$ yielded the highest precision to date in the determination of $\alpha_s$ using ZEUS data alone. This value will help constrain the uncertainty in the world average when included;
- The precision of these extractions signals the best venue to follow for a HERA combined value of $\alpha_s(M_Z)$. As will be discussed at the end of this section, such a value has been obtained by combining the ZEUS $d\sigma/dQ^2$ measurements with similar measurements from the H1 Collaboration.

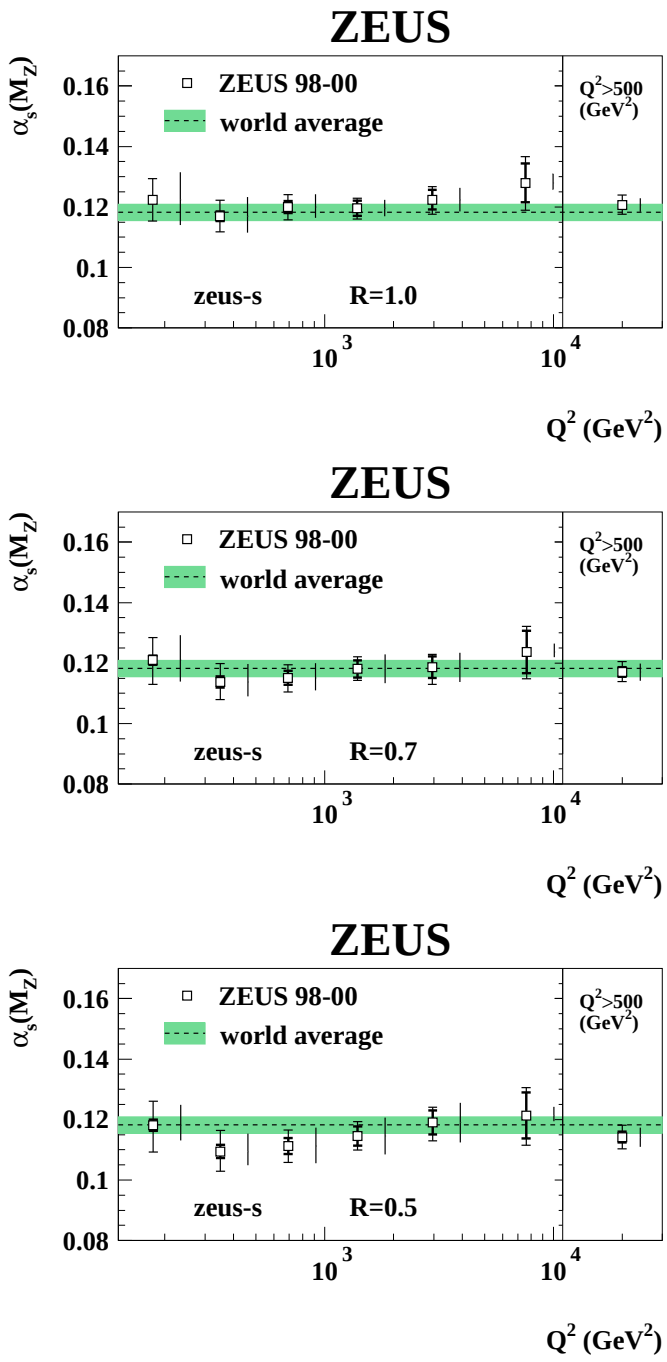


Figure 6.10: The values of $\alpha_s(M_Z)$ determined from the measured $d\sigma/dQ^2$ using the ZEUS-S PDF set for R=1, 0.7 and 0.5. The value of $\alpha_s(M_Z)$ obtained from the combined region of $Q^2 > 500$ GeV$^2$ is also shown. The inner error bars denote the statistical uncertainty, while the outer error bars are the statistical and systematic uncertainties added in quadrature. The theoretical uncertainties are shown as a solid vertical line next to each value of $\alpha_s(M_Z)$. The horizontal line represents the world average with its uncertainty.

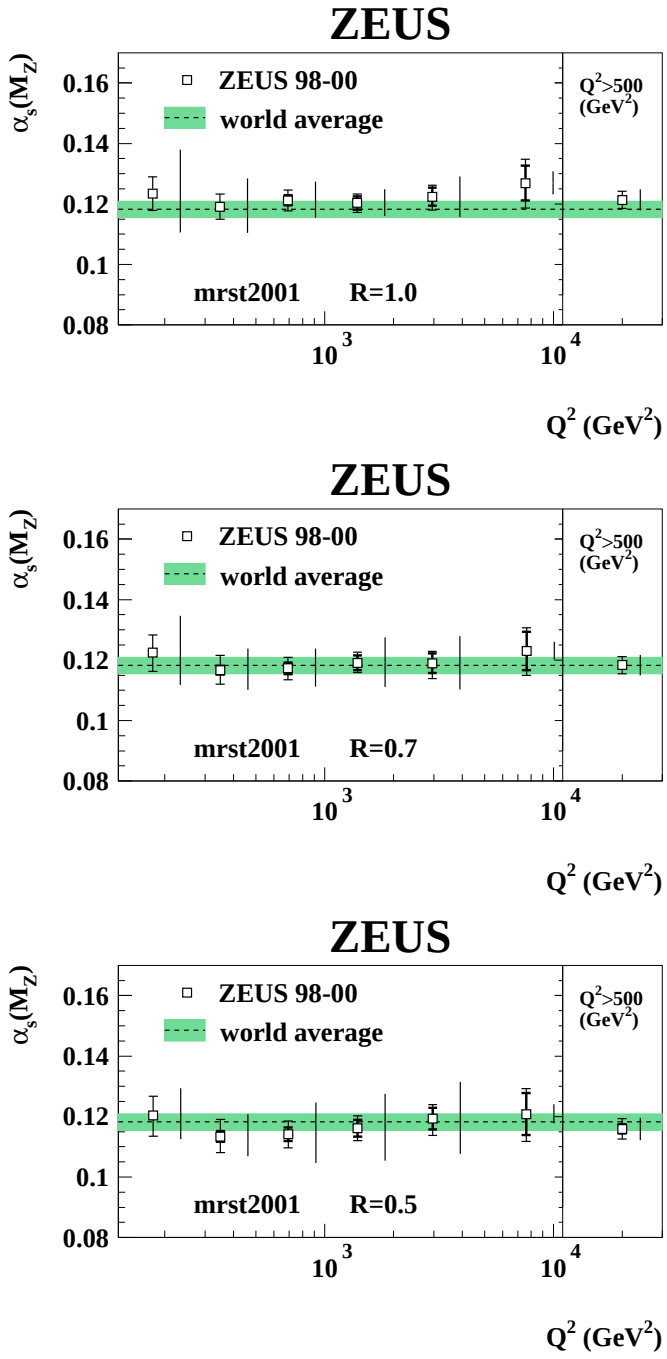


Figure 6.11: The values of $\alpha_s(M_Z)$ determined from $d\sigma/dQ^2$ using the MRST2001 PDFs and R=1, 0.7 and 0.5. The value of $\alpha_s(M_Z)$ obtained from the combined region of $Q^2 > 500$ GeV$^2$ is also shown. The inner error bars denote the statistical uncertainty, while the outer error bars are the statistical and systematic uncertainties added in quadrature. The theoretical uncertainties are shown as a solid vertical line next to each value of $\alpha_s(M_Z)$. The horizontal line represents the world average with its uncertainty.

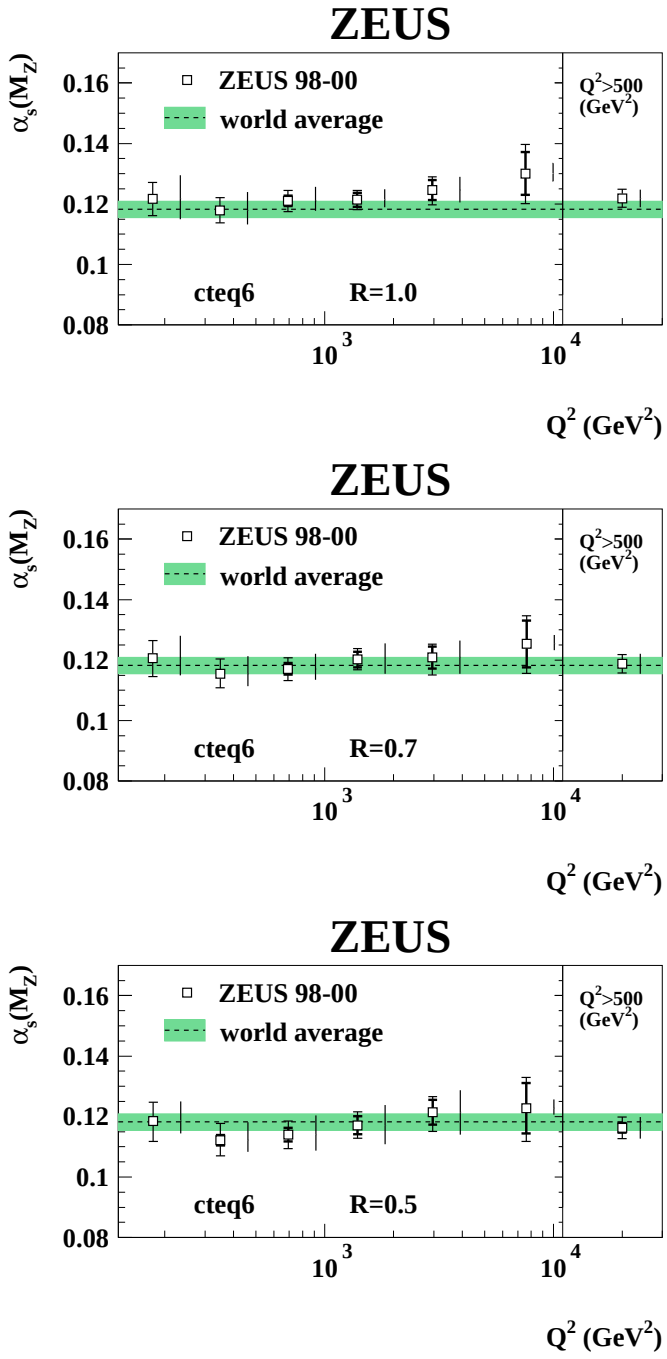


Figure 6.12: The values of $\alpha_s(M_Z)$ determined from $d\sigma/dQ^2$ using the CTEQ6 PDFs and R=1, 0.7 and 0.5. The value of $\alpha_s(M_Z)$ obtained from the combined region of $Q^2 > 500$ GeV$^2$ is also shown. The inner error bars denote the statistical uncertainty, while the outer error bars are the statistical and systematic uncertainties added in quadrature. The theoretical uncertainties are shown as a solid vertical line next to each value of $\alpha_s(M_Z)$. The horizontal line represents the world average with its uncertainty.

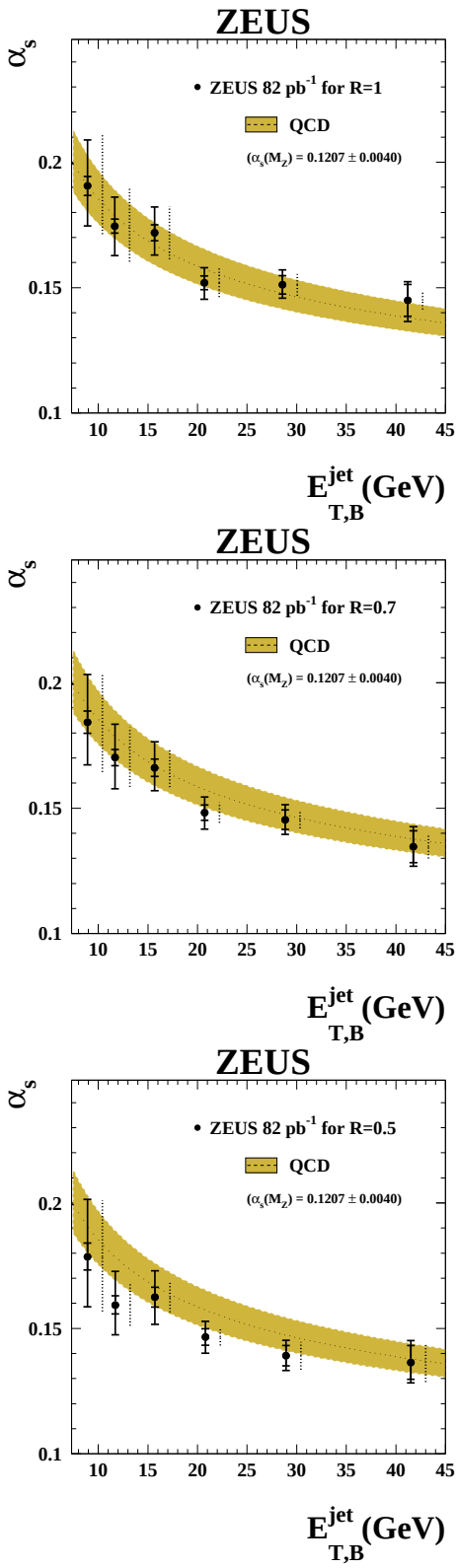


Figure 6.13: Energy scale dependence of $\alpha_s$ as a function of $E^{jet}_{T,B}$ having used the ZEUS-S PDF set and R=1, 0.7 and 0.5. The error bars are as those in the caption to Fig. 6.10. The measurements are compared to the predicted running of $\alpha_s$ using the extracted $\alpha_s(M_Z)$ value from the combined region of $Q^2 > 500$ GeV$^2$.

**Experimental uncertainties in the extracted values of $\alpha_s(M_Z)$**

The uncertainties on the extracted values of $\alpha_s(M_Z)$ due to the experimental systematic uncertainties were evaluated by repeating the analysis for each systematic check of the inclusive-jet cross section measurements. Fig. 6.14 shows the most significant sources of systematic uncertainty considered for the determination of $\alpha_s(M_Z)$. The overall normalization uncertantinty from the luminosity determination was also considered. The largest contribution to the experimental uncertainty comes from the jet energy scale and amounts to $\pm 2\%$ on $\alpha_s(M_Z)$. Due to the larger data sample available, the statistical uncertainties were reduced substantially with regards to previous measurements. Figs. 6.15 and 6.16 show the experimental uncertainties for the jet-radius choices R=0.7 and 0.5. The experimetantal uncertainties do not show a dependency on the choice of the jet radius for $0.5 < R < 1$.

**Theoretical uncertainties in the extracted values of $\alpha_s(M_Z)$**

The theoretical uncertainties considered are listed in this section. The uncertainty due to terms beyond $O(\alpha_s^2)$ was estimated by using the method proposed by Jones et al. **??**, and amounted to $\pm 1.5\%$. This method has the advantage of minimizing the influence of the statistics in the data on the estimation of the theoretical uncertainties. It basically consists of three steps:

- Obtaining the dependence of the prediction on $\alpha_s(M_Z)$ as described above;
- Obtaining the theoretical prediction for the inclusive-jet cross sections with the conventional variation on $\mu_R$ between $E^{\rm jet}_{T,\rm B}/2$ and $2 \cdot E^{\rm jet}_{T,\rm B}$;
- The minimum variation of $\alpha_s(M_Z)$ such that the predictions with $\mu_R = E^{\rm jet}_{T,\rm B}$ reach those with $\mu_R = 2E^{\rm jet}_{T,\rm B}$ or $\mu_R = E^{\rm jet}_{T,\rm B}/2$ is taken as the uncertainty in $\alpha_s(M_Z)$.

The uncertainty due to that in the proton PDFs was $\pm 0.7\%$. This uncertainty was estimated in the same way as described for the inclusive-jet cross section theoretical predictions in Chapter 3. Essentially, the extraction of $\alpha_s(M_Z)$ was repeated for each possible variation of the parameters in the PDF parametrizations and then eq. 3.3 was used to obtain the total error from that in the PDFs. Note that the ZEUS-S PDF sets were chosen as the default sets. This is because, as already mentioned in Chapter 3, tensions among the data sets from different experiments spoil a rigorous statistical treatment of the uncertainties in the MRST2001 and CTEQ6 parametrizations. For the ZEUS-S PDF set, all the data included in the QCD fit is well understood and a rigorous statistical treatment is possible. Note that the jet data were not used in the determination of the ZEUS-S PDF set. Fig. 6.17 shows a

comparison of the uncertainties on the extracted values of $\alpha_s(M_Z)$ stemming from those in the PDFs. The use of CTEQ6 results in an uncertainty which is about double that resulting from using the MRST2001 or ZEUS-S PDF sets. This is expected, since the tolerance parameter used in their statistical treatment is larger than that for the other two sets.

Finally, the uncertainty arising from the modelling of the parton cascade in the MC simulation was calculated by using either LEPTO or ARIADNE for the correction of the theoretical calculation and amounted to $\pm 0.8\%$. Figs. 6.18 through 6.20 show the theoretical uncertainties associated to the extraction of $\alpha_s(M_Z)$ separately, as well as the total theoretical uncertainty. The uncertainties on the modelling of the parton cascade increase as the jet radius decreases. As we showed in Chapter 5, the hadronization corrections deviate increasingly from 1 as the jet radius is decreased.

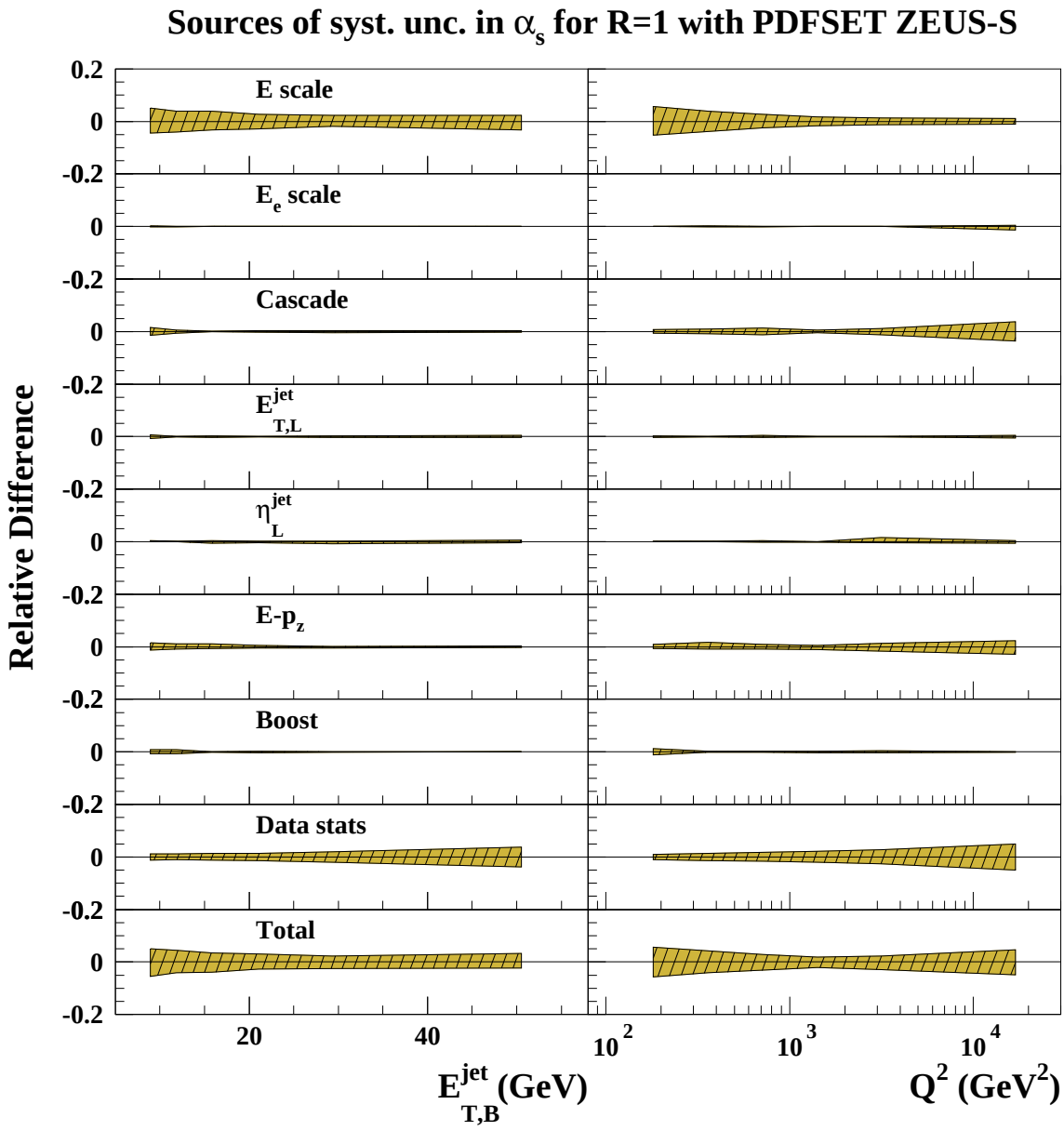


Figure 6.14: Relative systematic uncertainties on the determinations of $\alpha_s(M_Z)$ from the measured $d\sigma/dE^{jet}_{T,B}$ (left) and $d\sigma/dQ^2$ (right) using the jet algorithm with R=1.0 and the ZEUS-S PDFs.

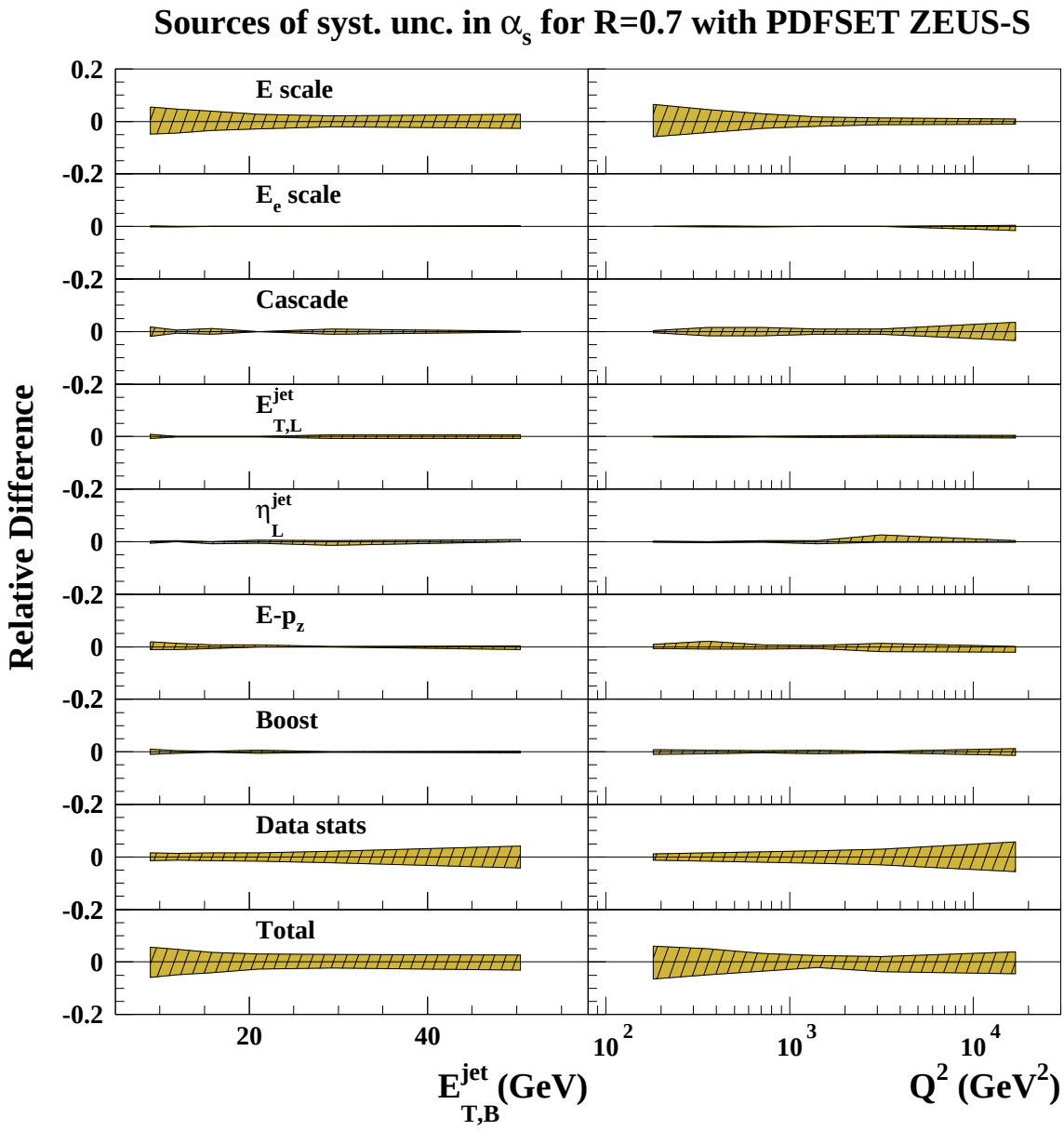


Figure 6.15: Relative systematic uncertainties on the determinations of $\alpha_s(M_Z)$ from the measured $d\sigma/dE^{jet}_{T,B}$ (left) and $d\sigma/dQ^2$ (right) using the jet algorithm with R=0.7 and the ZEUS-S PDFs.

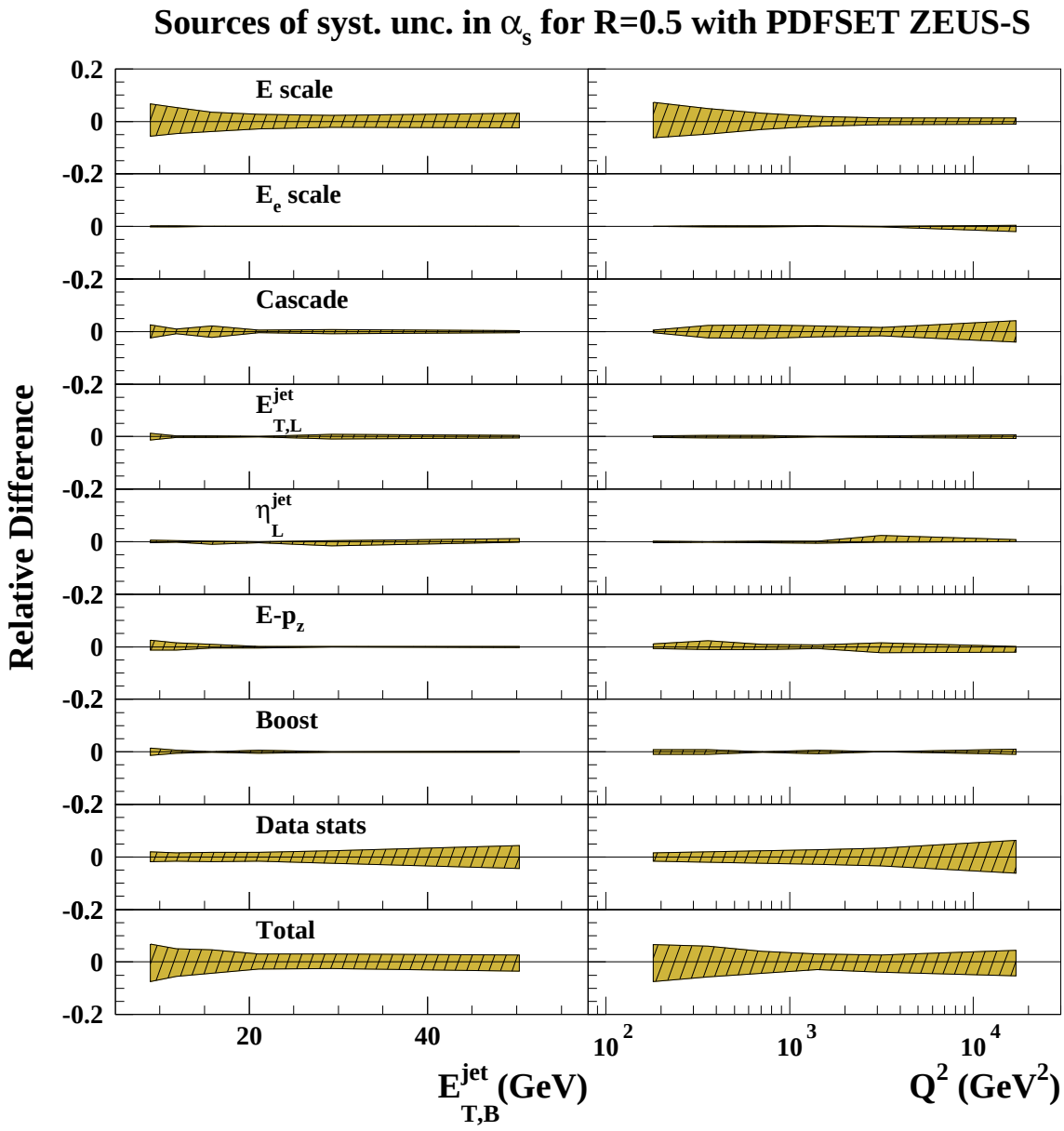


Figure 6.16: Relative systematic uncertainties on the determinations of $\alpha_s(M_Z)$ from the measured $d\sigma/dE^{jet}_{T,B}$ (left) and $d\sigma/dQ^2$ (right) using the jet algorithm with R=0.5 and the ZEUS-S PDFs.

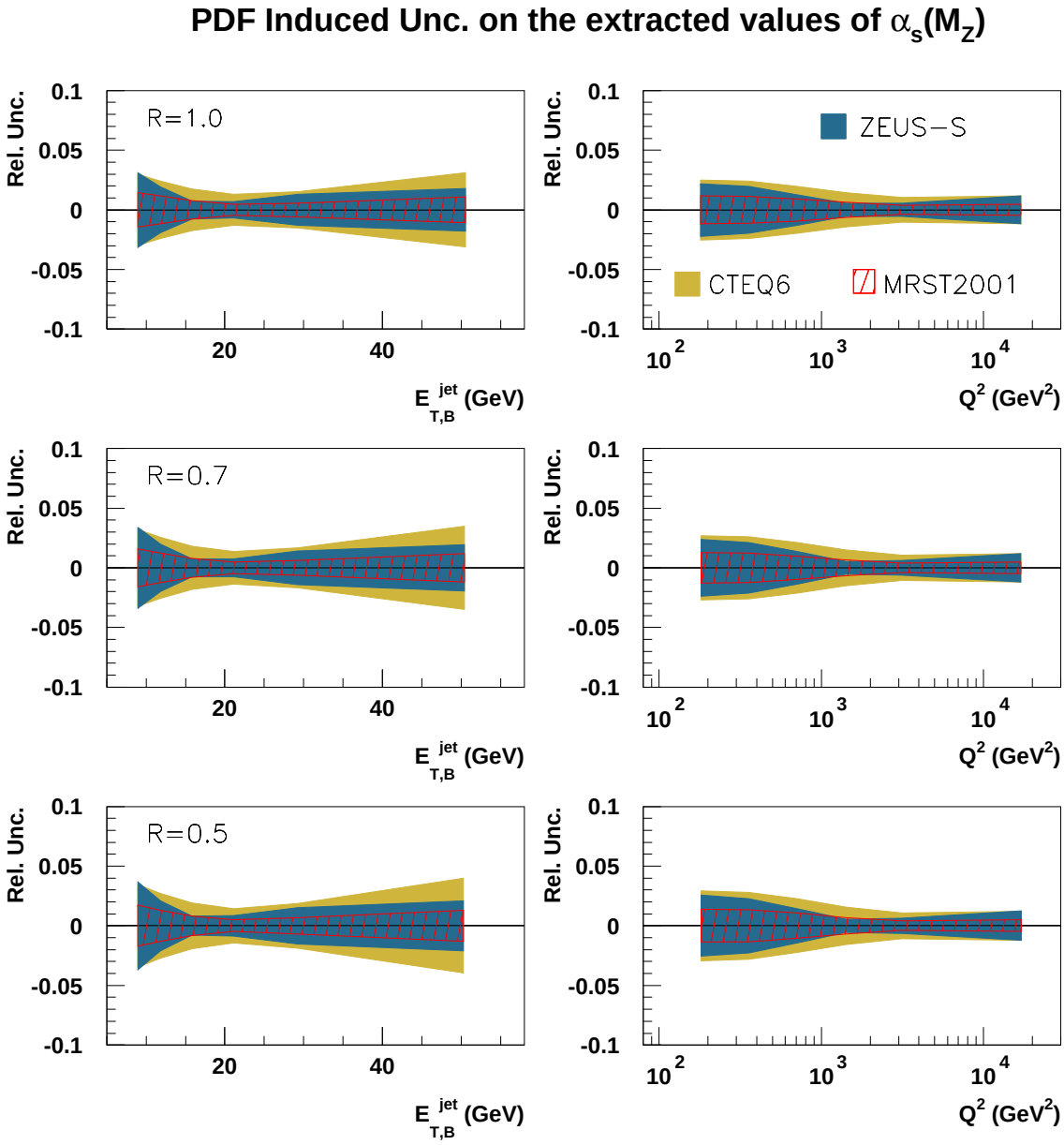


Figure 6.17: Relative uncertainty on the values of $\alpha_s(M_Z)$ extracted from the measured differential cross section $d\sigma/dE^{jet}_{T,B}$ (left) and $d\sigma/dQ^2$ (right) coming from the uncertainty in the PDFs as estimated by using the ZEUS-S, MRTST2001 or CTEQ6 sets of PDFs.

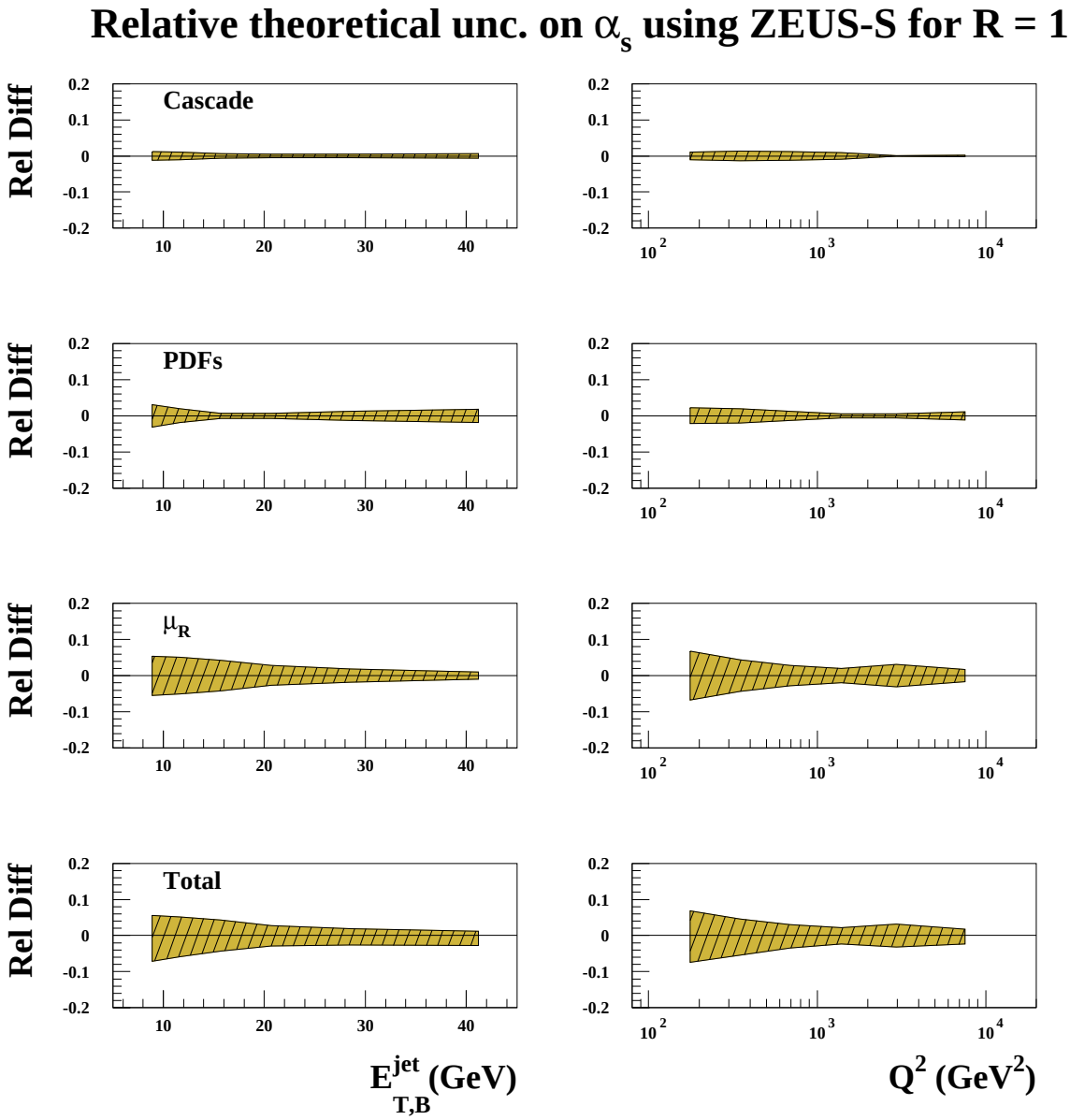


Figure 6.18: Relative theoretical uncertainties on the extracted values of $\alpha_s(M_Z)$ from the measured differential cross section $d\sigma/dE^{jet}_{T,B}$ (left) and $d\sigma/dQ^2$ (right) with R=1 and using the ZEUS-S PDFs.

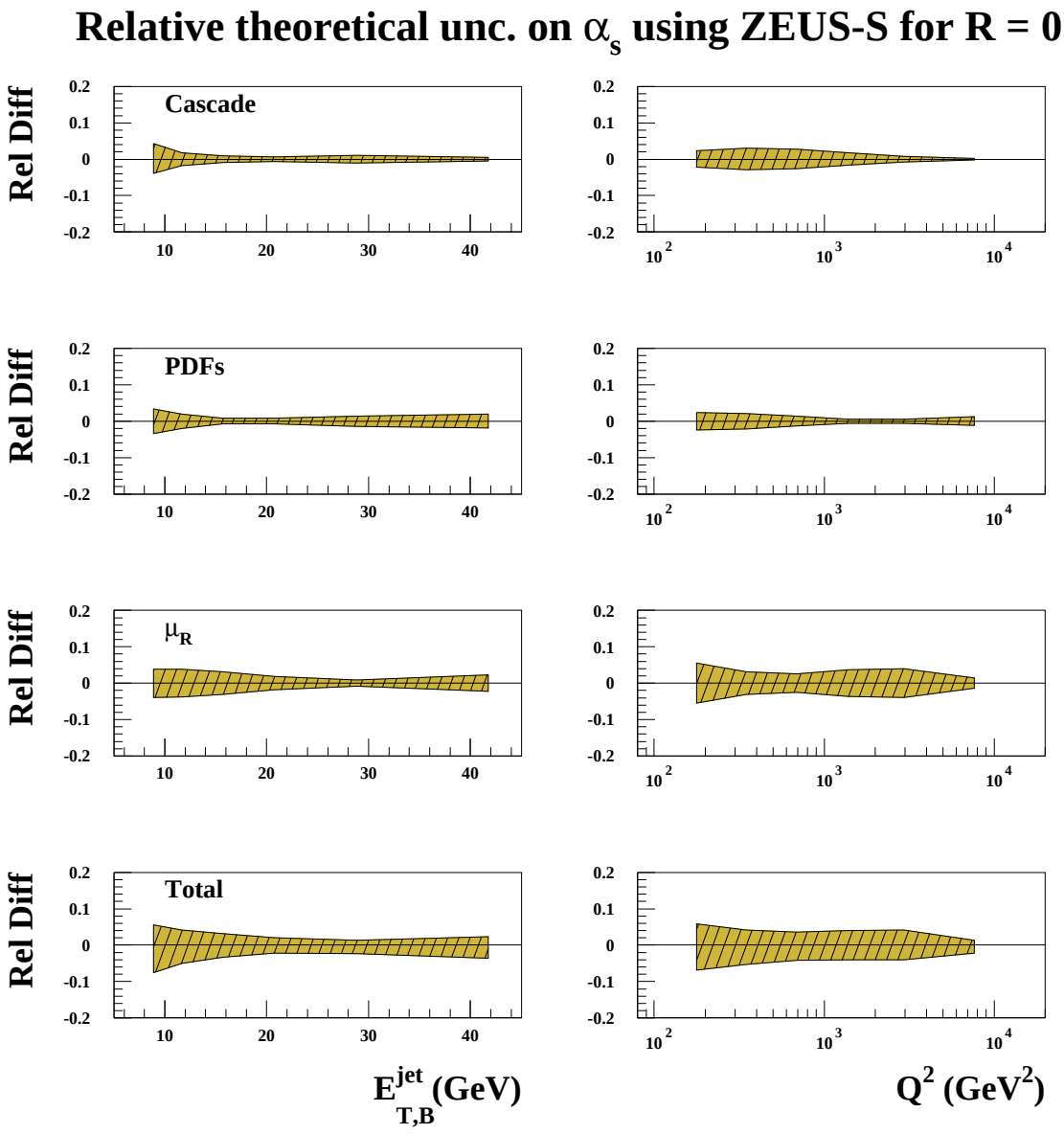


Figure 6.19: Relative theoretical uncertainties on the extracted values of $\alpha_s(M_Z)$ from the measured differential cross section $d\sigma/dE^{jet}_{T,B}$ (left) and $d\sigma/dQ^2$ (right) with R=0.7 and using the ZEUS-S PDFs.

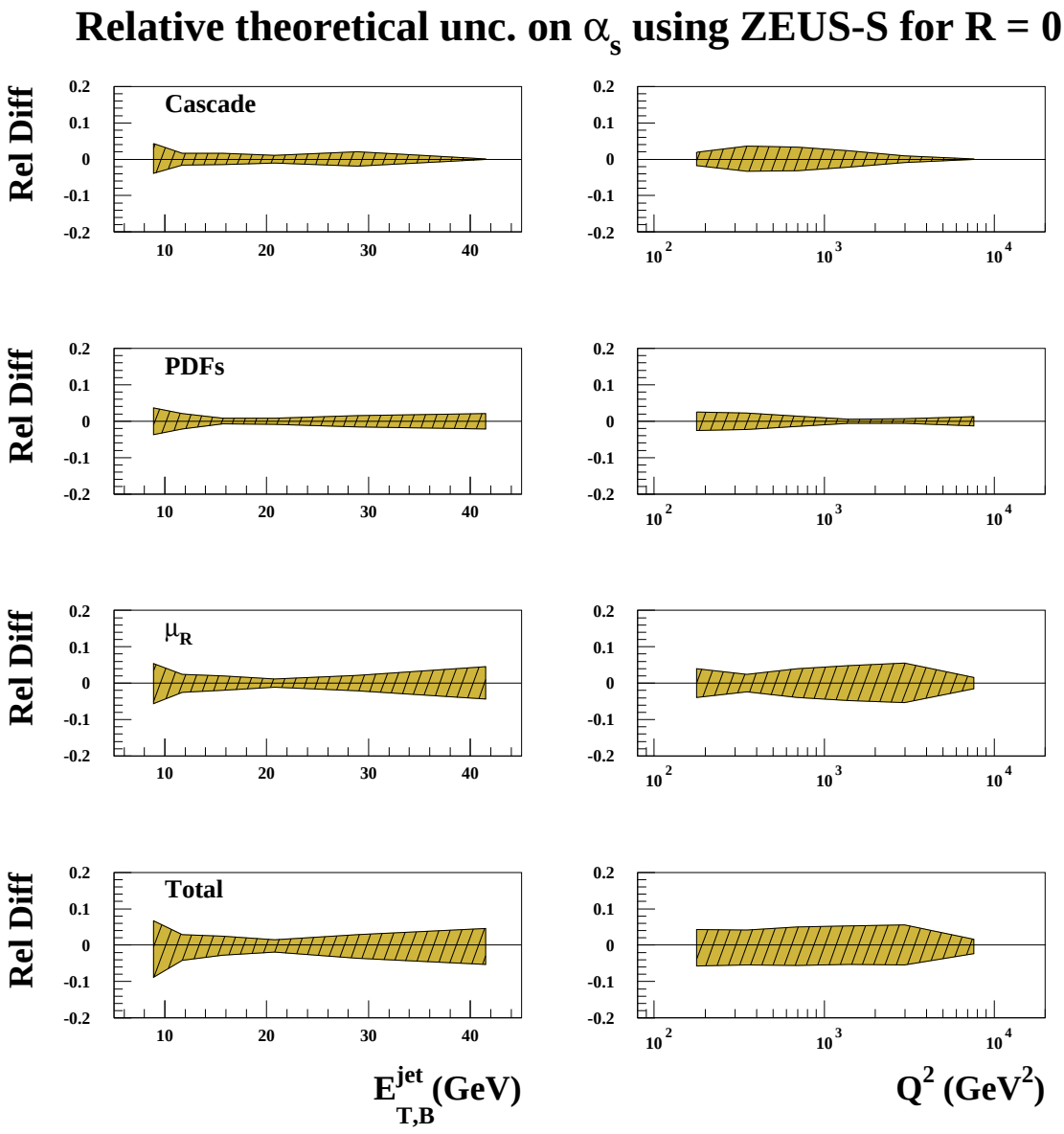


Figure 6.20: Relative theoretical uncertainties on the extracted values of $\alpha_s(M_Z)$ from the measured differential cross section $d\sigma/dE^{jet}_{T,B}$ (left) and $d\sigma/dQ^2$ (right) with R=0.5 and using the ZEUS-S PDFs.

**A combined HERA determination of $\alpha_s(M_Z)$**

The inclusive-jet cross section measurements were also used to obtain the first combined HERA extraction of $\alpha_s(M_Z)$. The six data points of the inclusive-jet differential cross section with respect to $Q^2$ for R=1 shown in Fig. 6.1 were used together with the twenty-four data points of inclusive-jet differential cross sections with respect to $E_{T,\mathrm{B}}^{\mathrm{jet}}$ for different regions of $Q^2$ from the H1 Collaboration. A simultaneous fit was done on all 30 data points in the same way as described above. The calculations were done at $O(\alpha_s^2)$ using the program DISENT. In this case the PDF set used was that of MRST2001. From Fig. 6.17 we have shown that the uncertainties in the extraction of $\alpha_s(M_Z)$ for this choice are similar to those using the ZEUS-S PDFs. The rest of the parameters in the theoretical calculations were as those for the extractions mentioned earlier.

Measurements and theory predictions are used to calculate a $\chi^2(\alpha_s(M_Z))$ function with the Hessian method, where parameters representing systematic shifts of detector related observables are left free in the fit. The sources of systematic uncertainty were treated as correlated for measurements within one experiment, but as uncorrelated between the two experiments. It was checked that the model dependence, which in principle could be correlated between experiments, had a negligible effect whether it was treated as correlated or uncorrelated.

The $\chi^2$ function was defined as

$$\chi^2 = \vec{V}^T \cdot M^{-1} \cdot \vec{V} + \sum_k \epsilon_k^2, \tag{6.3}$$

where the covariance matrix $M$ is composed of contributions from the statistical and uncorrelated systematical errors, $M = M^{\mathrm{stat}} + M^{\mathrm{uncor}}$. An element $M_{ij}$ of each of the matrices denotes the covariance between bins $i$ and $j$. It is noted that $M^{\mathrm{uncor}}$ is diagonal, while for the present analysis $M^{\mathrm{stat}}$ is not. The latter is due to the fact the H1 data were measured differentially in $E_T$, which introduces a statistical correlation between different $E_T$ bins in the same $Q^2$ bin due to multijet events.

The vector $\vec{V}$ is defined as

$$V_i = \sigma_i^{\mathrm{exp}} - \sigma_i^{\mathrm{theo}}(1 - \sum_k \delta_{ik}\epsilon_k), \tag{6.4}$$

with $\sigma_i^{\mathrm{exp}}$ ($\sigma_i^{\mathrm{theo}}$) the measured (predicted) cross section of bin $i$, which depends on the free parameter $\alpha_s(M_Z)$ of the fit. $\delta_{ik}$ denotes the correlated systematic error for bin $i$ associated to source $k$. The systematic uncertainties are symmetric by definition. The $\epsilon_k$ are Gaussian random variables and may be interpreted as pulls, i.e. shifts caused by the systematics normalised to their uncertainty estimates. They are determined in the $\chi^2$ fit but are not counted in the list of free parameters because they are determined according to the Gaussian law hypothesis.

The experimental uncertainty of the free parameter in the fit, i.e. $\alpha_s(M_Z)$, is defined by that change in $\alpha_s(M_Z)$ which gives an increase in $\chi^2$ of one unit with respect to the minimal value. The $\chi^2$ minimisation using MINUIT for the combined fit yields

$$\alpha_s(M_Z) = 0.1198 \pm 0.0019 \text{ (exp)}, \tag{6.5}$$

with $\chi^2/\text{ndf} = 27.4/29$.

Several checks were performed to ascertain the stability of the fit due to the use of the Hessian method to estimate the experimental uncertainty. The contribution to the $\chi^2$ in the simultaneous fit of each of the 30 data points and of each systematic source was determined. Most of the points were found to cluster around one unit of $\chi^2$, so there is no strong tension in the simultaneous fit to both data sets from the different experiments. Another check performed quantified the constraint provided by one data set on the other regarding the correlated systematic uncertainties. It was found that there is no significant change in the mean value of a given correlated source and only a small constraint is observed to be given by the data set of the other experiment when performing the simultaneous fit.

The sources of theoretical uncertainty considered include terms beyond NLO, the factorisation scale and the uncertainties coming from the PDFs and the hadronisation models. The uncertainty on $\alpha_s(M_Z)$ coming from each source amounts to:

- the uncertainty coming from terms beyond NLO was estimated by varying the renormalisation scale by factors 0.5 and 2 in the calculations and using the method of Jones et al. The uncertainty on the value of $\alpha_s(M_Z)$ is 0.0021.

- the effect of the uncertainty due to the value of the factorisation scale was estimated by varying $\mu_F$ by factors 0.5 and 2 in the calculations and repeating the fit to the data; it gave a contribution of 0.0010 to the uncertainty on $\alpha_s(M_Z)$;

- the uncertainty due to those of the PDFs was estimated by repeating the calculations using 30 additional sets from the MRST2001 analysis, which takes into account the statistical and correlated systematic experimental uncertainties of each data set used in the extraction of the PDFs. The resulting uncertainty on $\alpha_s(M_Z)$ was 0.0010;

- the uncertainty due to that on the hadronisation correction was estimated by using different models of the parton cascade to correct the NLO calculations for hadronisation effects. The resulting uncertainty on $\alpha_s(M_Z)$ was 0.0004.

The combined value of $\alpha_s(M_Z)$ was:

$$\alpha_s(M_Z) = 0.1198 \pm 0.0019(\text{exp.}) \pm 0.0026(\text{theo.}) \tag{6.6}$$

The combined experimental and theoretical uncertainty for this extraction is $\sim 2.7\%$, which is the smallest achieved at HERA thus far. Fig. 6.21 shows the best values obtained by the ZEUS and the H1 Collaborations alone, compared with the HERA average, the HERA combined value and the world average. All the HERA values are consistent with each other and will help reduce the uncertainty in the world average.

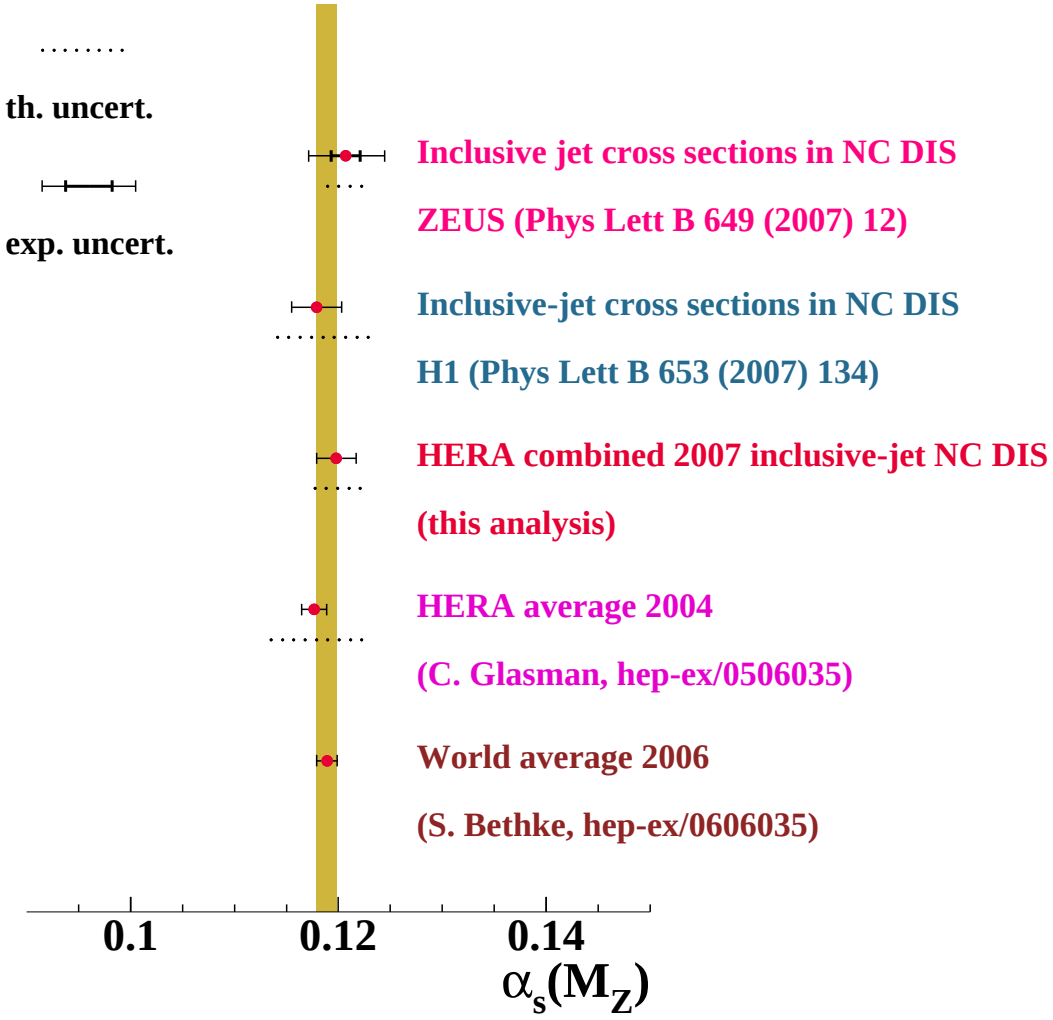


Figure 6.21: Combined HERA value of $\alpha_s(M_Z)$ compared to the ZEUS and H1 values, the HERA average 2004 and the world average.

| $E_{T,\mathrm{B}}^{\mathrm{jet}}$ bin (GeV) | $d\sigma/dE_{T,\mathrm{B}}^{\mathrm{jet}}$ (pb/GeV) | $\delta_{\mathrm{stat}}$ | $\delta_{\mathrm{syst}}$ | $\delta_{\mathrm{ES}}$ | $C_{\mathrm{QED}}$ | $C_{\mathrm{had}}$ |
|---|---|---|---|---|---|---|
| $R = 1$ | | | | | | |
| 8-10 | 63.98 | 0.68 | $^{+1.20}_{-1.39}$ | $^{+2.84}_{-2.56}$ | 0.95 | 0.91 |
| 10-14 | 29.29 | 0.34 | $^{+0.37}_{-0.52}$ | $^{+1.25}_{-1.31}$ | 0.96 | 0.95 |
| 14-18 | 11.07 | 0.20 | $^{+0.15}_{-0.20}$ | $^{+0.61}_{-0.50}$ | 0.96 | 0.96 |
| 18-25 | 3.234 | 0.080 | $^{+0.036}_{-0.045}$ | $^{+0.156}_{-0.167}$ | 0.94 | 0.97 |
| 25-35 | 0.773 | 0.033 | $^{+0.016}_{-0.015}$ | $^{+0.040}_{-0.033}$ | 0.95 | 0.95 |
| 35-100 | 0.0312 | 0.0027 | $^{+0.0005}_{-0.0006}$ | $^{+0.0015}_{-0.0022}$ | 1.06 | 0.95 |
| $R = 0.7$ | | | | | | |
| 8-10 | 50.09 | 0.60 | $^{+0.93}_{-1.19}$ | $^{+2.16}_{-1.94}$ | 0.95 | 0.77 |
| 10-14 | 23.38 | 0.30 | $^{+0.30}_{-0.38}$ | $^{+1.11}_{-1.06}$ | 0.96 | 0.83 |
| 14-18 | 8.97 | 0.18 | $^{+0.17}_{-0.19}$ | $^{+0.47}_{-0.41}$ | 0.96 | 0.88 |
| 18-25 | 2.659 | 0.071 | $^{+0.031}_{-0.038}$ | $^{+0.120}_{-0.126}$ | 0.95 | 0.91 |
| 25-35 | 0.631 | 0.029 | $^{+0.024}_{-0.025}$ | $^{+0.028}_{-0.026}$ | 0.96 | 0.92 |
| 35-100 | 0.0237 | 0.0022 | $^{+0.0006}_{-0.0007}$ | $^{+0.0015}_{-0.0016}$ | 1.03 | 0.93 |
| $R = 0.5$ | | | | | | |
| 8-10 | 38.25 | 0.52 | $^{+0.85}_{-1.11}$ | $^{+1.81}_{-1.60}$ | 0.95 | 0.64 |
| 10-14 | 17.78 | 0.26 | $^{+0.26}_{-0.30}$ | $^{+0.85}_{-0.77}$ | 0.96 | 0.70 |
| 14-18 | 7.09 | 0.15 | $^{+0.22}_{-0.23}$ | $^{+0.32}_{-0.33}$ | 0.95 | 0.77 |
| 18-25 | 2.257 | 0.063 | $^{+0.027}_{-0.032}$ | $^{+0.096}_{-0.103}$ | 0.96 | 0.83 |
| 25-35 | 0.514 | 0.025 | $^{+0.020}_{-0.020}$ | $^{+0.024}_{-0.024}$ | 0.97 | 0.86 |
| 35-100 | 0.0208 | 0.0019 | $^{+0.0006}_{-0.0006}$ | $^{+0.0014}_{-0.0011}$ | 1.04 | 0.90 |

Table 6.1: Inclusive jet cross-sections $d\sigma/dE_{T,\mathrm{B}}^{\mathrm{jet}}$ for jets of hadrons in the Breit frame selected with the longitudinally invariant $k_T$ cluster algorithm for different values of $R$ (Fig. 6.1). The statistical, uncorrelated systematic and jet-energy-scale (ES) uncertainties are shown separately. The multiplicative corrections applied to the data to correct for QED radiative effects, $C_{\mathrm{QED}}$, and the corrections for hadronisation effects to be applied to the parton-level NLO QCD calculations, $C_{\mathrm{had}}$, are shown in the last two columns.

| $Q^2$ bin ($GeV^2$) | $d\sigma/dQ^2$ (pb/$GeV^2$) | $\delta_{\rm stat}$ | $\delta_{\rm syst}$ | $\delta_{\rm ES}$ | $C_{\rm QED}$ | $C_{\rm had}$ |
|---|---|---|---|---|---|---|
| $R = 1$ | | | | | | |
| 125-250 | 1.106 | 0.012 | $^{+0.013}_{-0.020}$ | $^{+0.066}_{-0.062}$ | 0.97 | 0.92 |
| 250-500 | 0.3671 | 0.0053 | $^{+0.0048}_{-0.0078}$ | $^{+0.0153}_{-0.0149}$ | 0.95 | 0.94 |
| 500-1000 | 0.1037 | 0.0020 | $^{+0.0020}_{-0.0021}$ | $^{+0.0033}_{-0.0029}$ | 0.95 | 0.95 |
| 1000-2000 | 0.02439 | 0.00072 | $^{+0.00039}_{-0.00033}$ | $^{+0.00059}_{-0.00058}$ | 0.94 | 0.96 |
| 2000-5000 | 0.00396 | 0.00017 | $^{+0.00017}_{-0.00015}$ | $^{+0.00008}_{-0.00008}$ | 0.94 | 0.95 |
| 5000-100000 | 0.000036 | 0.000003 | $^{+0.000003}_{-0.000003}$ | $^{+0.000001}_{-0.000001}$ | 0.98 | 0.96 |
| $R = 0.7$ | | | | | | |
| 125-250 | 0.855 | 0.010 | $^{+0.007}_{-0.012}$ | $^{+0.054}_{-0.048}$ | 0.97 | 0.79 |
| 250-500 | 0.2913 | 0.0046 | $^{+0.0053}_{-0.0079}$ | $^{+0.0124}_{-0.0119}$ | 0.95 | 0.83 |
| 500-1000 | 0.0840 | 0.0018 | $^{+0.0017}_{-0.0017}$ | $^{+0.0026}_{-0.0024}$ | 0.95 | 0.86 |
| 1000-2000 | 0.02079 | 0.00066 | $^{+0.00041}_{-0.00043}$ | $^{+0.00046}_{-0.00049}$ | 0.94 | 0.88 |
| 2000-5000 | 0.00332 | 0.00016 | $^{+0.00018}_{-0.00016}$ | $^{+0.00007}_{-0.00006}$ | 0.93 | 0.88 |
| 5000-100000 | 0.000031 | 0.000003 | $^{+0.000002}_{-0.000002}$ | $^{+0.000001}_{-0.000001}$ | 0.97 | 0.90 |
| $R = 0.5$ | | | | | | |
| 125-250 | 0.6344 | 0.0088 | $^{+0.0058}_{-0.0092}$ | $^{+0.0406}_{-0.0357}$ | 0.97 | 0.64 |
| 250-500 | 0.2246 | 0.0040 | $^{+0.0053}_{-0.0069}$ | $^{+0.0097}_{-0.0097}$ | 0.95 | 0.70 |
| 500-1000 | 0.0672 | 0.0016 | $^{+0.0020}_{-0.0019}$ | $^{+0.0021}_{-0.0020}$ | 0.94 | 0.75 |
| 1000-2000 | 0.01709 | 0.00060 | $^{+0.00049}_{-0.00051}$ | $^{+0.00043}_{-0.00042}$ | 0.94 | 0.79 |
| 2000-5000 | 0.00296 | 0.00015 | $^{+0.00016}_{-0.00015}$ | $^{+0.00006}_{-0.00006}$ | 0.95 | 0.81 |
| 5000-100000 | 0.000028 | 0.000003 | $^{+0.000002}_{-0.000002}$ | $^{+0.000001}_{-0.000000}$ | 0.98 | 0.83 |

Table 6.2: Inclusive jet cross-sections $d\sigma/dQ^2$ for jets of hadrons in the Breit frame selected with the longitudinally invariant $k_T$ cluster algorithm for different values of $R$ (Fig. 6.1). Other details as in the caption to Table 6.1.

| $E^{\rm jet}_{T,\rm B}$ bin (GeV) | $d\sigma/dE^{\rm jet}_{T,\rm B}$ (pb/GeV) | $\delta_{\rm stat}$ | $\delta_{\rm syst}$ | $\delta_{\rm ES}$ | $C_{\rm QED}$ | $C_{\rm had}$ |
|---|---|---|---|---|---|---|
| $125 < Q^2 < 250$ GeV$^2$ | | | | | | |
| 8-10 | 32.97 | 0.49 | $^{+1.21}_{-1.21}$ | $^{+1.81}_{-1.69}$ | 0.96 | 0.90 |
| 10-14 | 13.00 | 0.22 | $^{+0.19}_{-0.19}$ | $^{+0.79}_{-0.75}$ | 0.98 | 0.94 |
| 14-18 | 3.71 | 0.11 | $^{+0.15}_{-0.15}$ | $^{+0.28}_{-0.24}$ | 0.97 | 0.94 |
| 18-25 | 0.835 | 0.037 | $^{+0.013}_{-0.012}$ | $^{+0.051}_{-0.056}$ | 0.94 | 0.93 |
| 25-100 | 0.0160 | 0.0014 | $^{+0.0027}_{-0.0027}$ | $^{+0.0010}_{-0.0011}$ | 0.97 | 0.86 |
| $250 < Q^2 < 500$ GeV$^2$ | | | | | | |
| 8-10 | 18.40 | 0.38 | $^{+0.74}_{-0.74}$ | $^{+0.68}_{-0.60}$ | 0.94 | 0.92 |
| 10-14 | 8.74 | 0.19 | $^{+0.30}_{-0.30}$ | $^{+0.33}_{-0.35}$ | 0.96 | 0.95 |
| 14-18 | 3.30 | 0.11 | $^{+0.15}_{-0.15}$ | $^{+0.18}_{-0.14}$ | 0.96 | 0.97 |
| 18-25 | 0.889 | 0.042 | $^{+0.041}_{-0.041}$ | $^{+0.052}_{-0.057}$ | 0.92 | 0.97 |
| 25-100 | 0.0242 | 0.0020 | $^{+0.0005}_{-0.0005}$ | $^{+0.0012}_{-0.0011}$ | 0.95 | 0.91 |
| $500 < Q^2 < 1000$ GeV$^2$ | | | | | | |
| 8-10 | 8.79 | 0.26 | $^{+0.34}_{-0.34}$ | $^{+0.26}_{-0.15}$ | 0.96 | 0.91 |
| 10-14 | 4.69 | 0.14 | $^{+0.19}_{-0.19}$ | $^{+0.11}_{-0.13}$ | 0.94 | 0.95 |
| 14-18 | 2.239 | 0.093 | $^{+0.137}_{-0.137}$ | $^{+0.091}_{-0.074}$ | 0.93 | 0.98 |
| 18-25 | 0.701 | 0.039 | $^{+0.051}_{-0.051}$ | $^{+0.026}_{-0.026}$ | 0.96 | 0.99 |
| 25-100 | 0.0335 | 0.0027 | $^{+0.0018}_{-0.0018}$ | $^{+0.0019}_{-0.0019}$ | 0.96 | 0.97 |
| $1000 < Q^2 < 2000$ GeV$^2$ | | | | | | |
| 8-10 | 3.30 | 0.16 | $^{+0.14}_{-0.14}$ | $^{+0.09}_{-0.08}$ | 0.93 | 0.93 |
| 10-14 | 1.985 | 0.091 | $^{+0.077}_{-0.077}$ | $^{+0.017}_{-0.037}$ | 0.91 | 0.95 |
| 14-18 | 1.115 | 0.069 | $^{+0.056}_{-0.056}$ | $^{+0.034}_{-0.008}$ | 0.98 | 0.99 |
| 18-25 | 0.492 | 0.034 | $^{+0.039}_{-0.039}$ | $^{+0.009}_{-0.018}$ | 0.93 | 0.99 |
| 25-100 | 0.0263 | 0.0026 | $^{+0.0043}_{-0.0043}$ | $^{+0.0020}_{-0.0013}$ | 1.00 | 1.00 |
| $2000 < Q^2 < 5000$ GeV$^2$ | | | | | | |
| 8-10 | 1.292 | 0.095 | $^{+0.120}_{-0.120}$ | $^{+0.033}_{-0.022}$ | 0.92 | 0.90 |
| 10-14 | 0.858 | 0.060 | $^{+0.024}_{-0.024}$ | $^{+0.007}_{-0.006}$ | 0.90 | 0.93 |
| 14-18 | 0.612 | 0.052 | $^{+0.070}_{-0.070}$ | $^{+0.023}_{-0.017}$ | 1.02 | 1.00 |
| 18-25 | 0.242 | 0.024 | $^{+0.028}_{-0.028}$ | $^{+0.009}_{-0.006}$ | 0.96 | 1.00 |
| 25-100 | 0.0185 | 0.0021 | $^{+0.0023}_{-0.0023}$ | $^{+0.0004}_{-0.0005}$ | 0.91 | 0.99 |
| $5000 < Q^2 < 100000$ GeV$^2$ | | | | | | |
| 8-10 | 0.225 | 0.037 | $^{+0.091}_{-0.091}$ | $^{+0.011}_{-0.006}$ | 0.99 | 0.93 |
| 10-14 | 0.267 | 0.037 | $^{+0.022}_{-0.023}$ | $^{+0.003}_{-0.019}$ | 0.96 | 0.93 |
| 14-18 | 0.122 | 0.024 | $^{+0.017}_{-0.017}$ | $^{+0.003}_{-0.005}$ | 0.97 | 0.98 |
| 18-25 | 0.070 | 0.013 | $^{+0.019}_{-0.019}$ | $^{+0.001}_{-0.000}$ | 0.98 | 0.99 |
| 25-100 | 0.0114 | 0.0022 | $^{+0.0042}_{-0.0042}$ | $^{+0.0003}_{-0.0001}$ | 0.99 | 1.00 |

Table 6.3: Inclusive jet cross-sections $d\sigma/dE^{\rm jet}_{T,\rm B}$ for jets of hadrons in the Breit frame selected with the longitudinally invariant $k_T$ cluster algorithm in different regions of $Q^2$ (see Fig. 6.2). Other details as in the caption to Table 6.1.

| $R$ | $\sigma_{\rm jets}$ ($pb^{-1}$) | $\delta_{\rm stat}$ | $\delta_{\rm syst}$ | $\delta_{\rm ES}$ | $C_{\rm QED}$ | $C_{\rm had}$ |
|---|---|---|---|---|---|---|
| $Q^2 > 125$ $^{-1}$ | | | | | | |
| 0.5 | 197.8 | 1.9 | $^{+3.3}_{-4.1}$ | $^{+9.3}_{-8.6}$ | 0.96 | 0.70 |
| 0.7 | 255.6 | 2.1 | $^{+3.3}_{-4.4}$ | $^{+11.9}_{-11.1}$ | 0.96 | 0.82 |
| 1.0 | 321.5 | 2.4 | $^{+4.2}_{-5.4}$ | $^{+14.8}_{-14.1}$ | 0.96 | 0.94 |
| $Q^2 > 500$ $^{-1}$ | | | | | | |
| 0.5 | 62.3 | 1.1 | $^{+1.5}_{-1.4}$ | $^{+1.7}_{-1.7}$ | 0.95 | 0.77 |
| 0.7 | 75.8 | 1.3 | $^{+1.3}_{-1.3}$ | $^{+2.1}_{-2.0}$ | 0.95 | 0.87 |
| 1.0 | 91.6 | 1.4 | $^{+1.6}_{-1.5}$ | $^{+2.6}_{-2.4}$ | 0.95 | 0.95 |

Table 6.4: Inclusive jet cross-sections $\sigma_{\rm jets}$ for jets of hadrons in the Breit frame selected with the longitudinally invariant $k_T$ cluster algorithm for $Q^2 > 125$ and 500 GeV$^2$ (Fig. 6.3). Other details as in the caption to Table 6.1.

| $\langle E^{\rm jet}_{T,{\rm B}} \rangle$ (GeV) | $\alpha_s$ | $\delta_{\rm stat}$ | $\delta_{\rm syst}$ | $\delta_{\rm theor}$ |
|---|---|---|---|---|
| 8.9 | 0.1907 | $^{+0.0038}_{-0.0038}$ | $^{+0.0194}_{-0.0171}$ | $^{+0.0208}_{-0.0192}$ |
| 11.7 | 0.1746 | $^{+0.0028}_{-0.0028}$ | $^{+0.0123}_{-0.0126}$ | $^{+0.0148}_{-0.0142}$ |
| 15.7 | 0.1719 | $^{+0.0032}_{-0.0031}$ | $^{+0.0105}_{-0.0092}$ | $^{+0.0107}_{-0.0105}$ |
| 20.7 | 0.1519 | $^{+0.0028}_{-0.0028}$ | $^{+0.0061}_{-0.0065}$ | $^{+0.0057}_{-0.0057}$ |
| 28.6 | 0.1512 | $^{+0.0037}_{-0.0037}$ | $^{+0.0050}_{-0.0045}$ | $^{+0.0043}_{-0.0044}$ |
| 41.2 | 0.1452 | $^{+0.0064}_{-0.0063}$ | $^{+0.0041}_{-0.0056}$ | $^{+0.0036}_{-0.0036}$ |

Table 6.5: The $\alpha_s$ values determined from a QCD fit of the measured $d\sigma/dE^{jet}_{T,B}$ with $R = 1$ as a function of $E^{\rm jet}_{T,{\rm B}}$ (Fig. 6.13). The statistical, systematic and theoretical uncertainties are shown separately.

# Chapter 7

# Results: Angular correlations in three-jet production in NC DIS at HERA

## 7.1 Introduction

Three-jet angular-correlation variables devised to study the underlying symmetry of the strong interactions in a transparent way in $ep$ scattering were introduced in Chapter 1 and studied in detail in subsequent chapters. By 'transparent' what is meant is that the angular correlations show a sensitivity to the gauge symmetry of the interaction that is independent of the value of $\alpha_s(M_Z)$, the running of $\alpha_s$ or PDF evolution.

As shown in chapter 3 this independence is attained by normalizing the cross sections. Further conditions, such as a restricted $Q^2$ region can be imposed to rid the angular correlations of any residual dependence on the running of $\alpha_s$. In the case of the $\eta^{jet}_{max}$ variable this dependence is still significant at $O(\alpha_s^2)$ even after normalizing the cross sections and therefore an analysis for the restricted $500 < Q^2 < 5000$ GeV$^2$ region has also been fully carried out. In Chapter 3 we also showed how obtaining the predictions at a higher perturbative order, $O(\alpha_s^3)$, lessens the dependence of the correlation variables on the running of $\alpha_s$.

The theoretical and experimental uncertainties involved in the analysis are discussed in detail in Chapters 3 and 4, as well as the correction factors obtained using MC simulations that are applied to correct the data and the predictions for various effects. The current chapter presents the final results for this analysis, which are listed below:

- Measurements of normalized differential three-jet cross sections as functions of

the angular-correlation variables $\Theta_H$, $\cos\alpha_{23}$, $\cos\beta_{ksw}$, and $\eta^{jet}_{max}$ for the region $Q^2 > 125$ GeV$^2$ and $500 < Q^2 < 5000$ GeV$^2$, respectively;

- Measurement of the total three-jet cross section in NC DIS for $Q^2 > 125$ GeV$^2$ and $500 < Q^2 < 5000$ GeV$^2$, respectively.
- Evaluation of the CDM and MEPS models with regards to reproducing the angular correlation distributions in the data;
- Comparison of the measured angular correlations to $O(\alpha_s^2)$ and $O(\alpha_s^3)$ QCD predictions;
- Comparison of the measured angular correlations to the $O(\alpha_s^2)$ predictions using various symmetry groups. The groups considered are SU(3), U(1)$^3$, SU(N) for large N, and the extreme choice $C_F = 0$. A discussion of the potential that the angular correlations have towards an extraction of the color factors is also provided.

The comparison of the data with different models testifies that these observables have the potential to provide a direct extraction of the color factors. By itself, the comparison represents a transparent test of the essential assumption of pQCD, namely that the underlying symmetry of the strong interactions is SU(3).

## 7.2 Comparison to the MC simulations: CDM and MEPS

As discussed in Chapter 3, two different MC simulations were used in this analysis. They are both based on $O(\alpha_s)$ pQCD calculations and for this reason the presence of a third jet is entirely a consequence of the parton cascade. Thus, it is important to compare how well the CDM and the MEPS models describe the angular correlation distributions of the data. This comparison was already shown in Chapter 4, where the aim was to show that it is legitimate to use the MC simulation based on MEPS to obtain the necessary correction factors to be applied to the data or to the predictions. In this section the figures are shown again under a different light. Here the aim is to describe the performance of each of the parton-cascade models in reproducing the angular correlations in the data.

Fig. 7.1 shows the number of events in the data sample found in each bin of each of the four angular correlation variables for the the kinematic region $Q^2 > 125$ GeV$^2$. The distribution of events in the data is compared to each of the MC simulations at the detector level. Here the MC distributions are normalized to the number of events in the data. Both models provide a description of the data which is fairly good. The MEPS model, however, appears to give a slightly better description. This

difference between the models is most significant for the $\Theta_H$ distribution, where the CDM distribution is tilted with respect to the data. For the case of $\cos\beta_{ksw}$ CDM again offers a less adequate description of the data, since it overshoots it in the lowest bin, where again MEPS gives a better description. For the $\cos\alpha_{23}$ and $\eta^{jet}_{max}$ distributions, both models are able to describe the data well in general.

Fig. 7.2 shows the same comparison but for the restricted kinematic region of $500 < Q^2 < 5000$ GeV$^2$. The statistical uncertainties are larger for this data sample since the number of events available is about half as for the $Q^2 > 125$ GeV$^2$ sample. The conclusions are the same, however, with MEPS providing a more adequate description of the data in this region.

In conclusion the MEPS model is able to provide a better description than CDM of the angular correlations for three-jet final states in the kinematic regions under study.

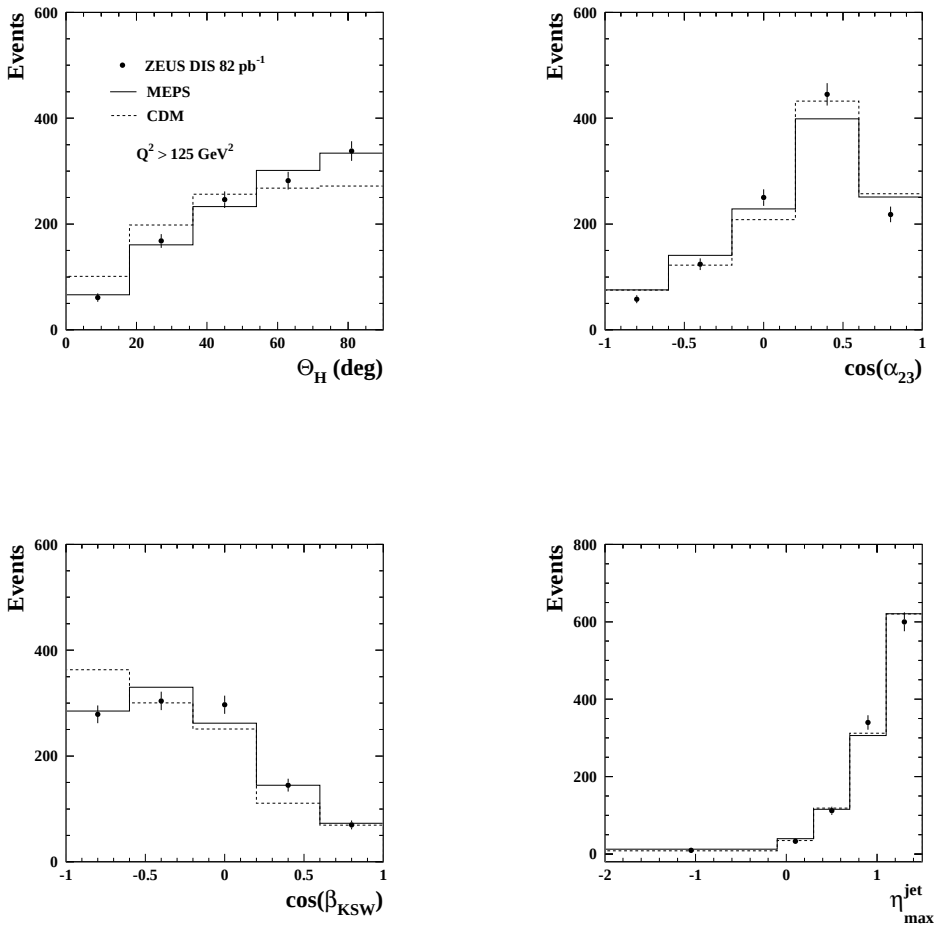


Figure 7.1: Comparison of the MC simulations using the MEPS (solid lines) and CDM (dashed lines) models with the distribution in the data for the angular-correlation variables $\Theta_H$, $\cos\alpha_{23}$, $\cos\beta_{ksw}$ and $\eta^{jet}_{max}$ for the region of $Q^2 > 125$ GeV$^2$. It is found that the MEPS model provides a better general description of the data for these variables.

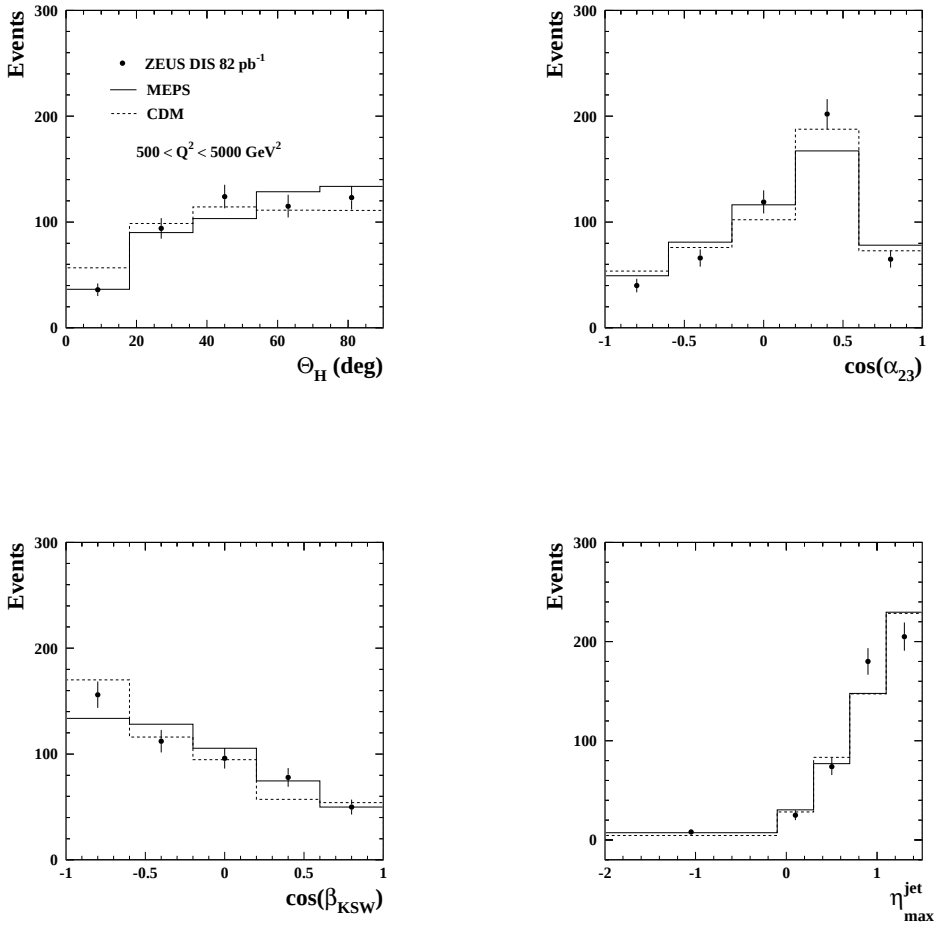


Figure 7.2: Comparison of the MC simulations using the MEPS (solid lines) and CDM (dashed lines) models with the distribution in the data for the angular-correlation variables $\Theta_H$, $\cos\alpha_{23}$, $\cos\beta_{ksw}$ and $\eta^{jet}_{max}$ for the region of $500 < Q^2 < 5000$ GeV$^2$. It is found that the MEPS model provides a better general description of the data for these variables.

## 7.3 Comparison to pQCD at $O(\alpha_s^2)$ and $O(\alpha_s^3)$

Both the program DISENT and NLOJET++ have been used to obtain the $O(\alpha_s^2)$ predictions independently. As discussed in Chapter 3, the program DISENT can perform only up to $O(\alpha_s^2)$ calculations for inclusive three-jet production in the Breit frame and it does not have by default the option to change the color factors. In order to obtain the predictions with different models the color factors had to be identified and disentangled from the calculations to obtain an explicit expression of the form of eq. 1.28. With this expression at hand, the predictions for different groups are straightforward since they involve only a simple change of the color factors. DISENT was originally used for all the calculations in the analysis.

Recently NLOJET++ has become a viable option for three-jet calculations at $O(\alpha_s^3)$. However, obtaining an expression such as eq. 1.28 at $O(\alpha_s^3)$ using NLOJET++ is more involved. The color factors are embedded in the calculations such that it is not possible to disentangle them in the same way as in the DISENT program. It is however possible to carry out calculations with different SU(N) groups. Thus, in order to obtain an equation such as eq. 1.28, enough predictions with different SU(N) assumptions need to be calculated to obtain a set of equations that can solved for the sub-process cross sections. This recipe has been carried out successfully at $O(\alpha_s^2)$ and cross-checked with DISENT. Figs. 7.3 and 7.4 show the $O(\alpha_s^2)$ calculations for SU(2), SU(3), SU(5) and SU(10) from which such a set of equations was solved to get the explicit terms at $O(\alpha_s^2)$ in eq. 1.28. The bottom plots in these figures show the relative differences of the predictions with respect to SU(3). In section 7.5 we will show that the relative differences among the SU(N) predictions are larger at $O(\alpha_s^3)$.

As mentioned, carrying out an analysis at $O(\alpha_s^3)$ has the additional complication that an equation such as eq. 1.28 at $O(\alpha_s^3)$ contains more color-factor combinations than at $O(\alpha_s^2)$, which implies a larger set of equations to be solved using NLOJET++. Moreover, the statistics needed for a good convergence with the NLOJET++ program are significantly larger than with DISENT and are therefore more demanding in terms of CPU time. For these reasons obtaining the predictions for other models such as an Abelian model at $O(\alpha_s^3)$ is still a work in progress. For the time being NLOJET++ has been used at $O(\alpha_s^3)$ to study the impact of the contribution from the higher-order terms to the $O(\alpha_s^2)$ predictions.

For the remainder of this section all the calculations shown are for SU(3). Fig. 7.5 shows the measured normalized differential cross sections for three-jet production in NC DIS (dots) integrated over $E_{T,\mathrm{B}}^{\mathrm{jet}} > 8$ GeV, $E_{T,B}^{jet2,3} > 5$ GeV and $-2 < \eta_{\mathrm{B}}^{\mathrm{jet}} < 1.5$ in the kinematic region given by $Q^2 > 125$ GeV$^2$ and $|\cos\gamma_h| < 0.65$ as functions of $\Theta_H$, $\cos\alpha_{23}$, $\cos\beta_{ksw}$ and $\eta_{max}^{jet}$. The data points are plotted at the bin centers.

The measurements are compared to the $O(\alpha_s^2)$ and $O(\alpha_s^3)$ pQCD calculations made using NLOJET++. The lower part of the figures displays the relative difference to the $O(\alpha_s^3)$ calculations, and the hatched band shows its relative total uncertainty.

The $O(\alpha_s^2)$ predictions are able to provide a consistent description of the data within its uncertainties. However, the $O(\alpha_s^3)$ calculations give a more precise and accurate description everywhere. In the lower $\cos\alpha_{23}$ region the $O(\alpha_s^2)$ prediction differs significantly from the data point (although still within the $O(\alpha_s^2)$ uncertainties). Note that the $O(\alpha_s^3)$ contribution improves the agreement with the data significantly for this region. The description of $\eta_{max}^{jet}$ also improves considerably with the $O(\alpha_s^3)$ predictions. In Fig. 7.6 similar results are shown for the restricted $500 < Q^2 < 5000$ GeV$^2$ region.

In conclusion, both the $O(\alpha_s^2)$ and $O(\alpha_s^3)$ predictions are found to be consistent with the data within their respective theoretical uncertainties. The distributions in the $O(\alpha_s^3)$ predictions, however, have reduced theoretical uncertainties and are found to resemble more closely the data distributions. The impact of the $O(\alpha_s^3)$ contributions to the predictions are found to be significant in some regions.

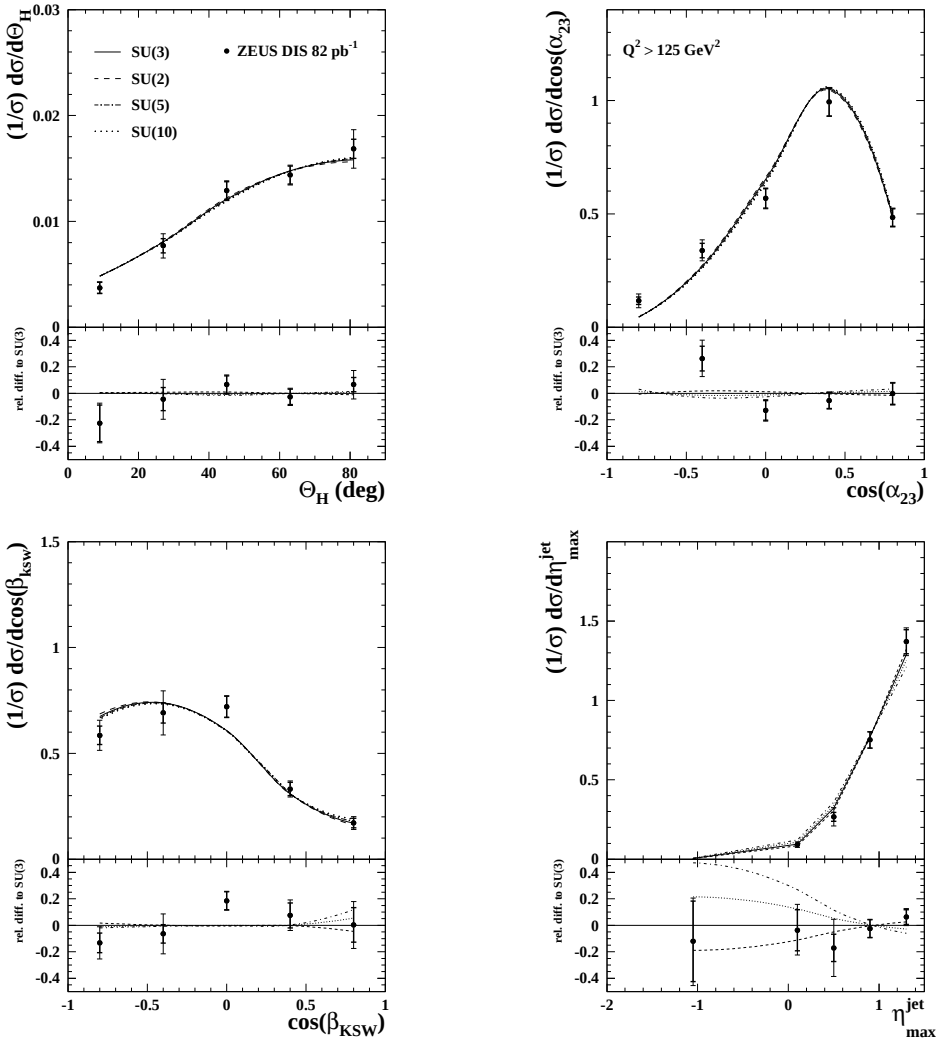


Figure 7.3: Measured normalized differential cross sections compared to the $O(\alpha_s^2)$ predictions for SU(N) with N=2, 3, 5 and 10 made using NLOJET++ for the kinematic region defined by $Q^2 > 125$ GeV$^2$. The lower part of the figures displays the relative difference to the $O(\alpha_s^2)$ calculations based on SU(3). The ZEUS-S PDFs have been used in the calculations.

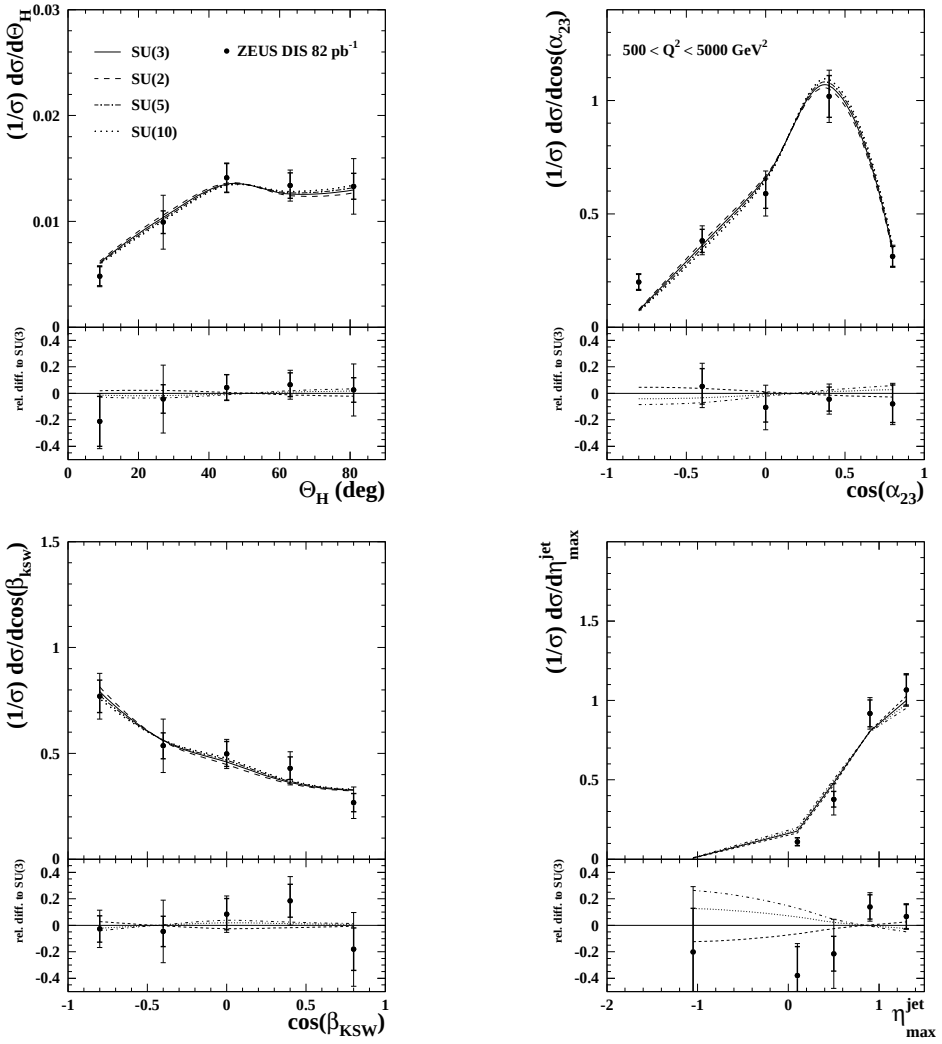


Figure 7.4: Measured normalized differential cross sections compared to the $O(\alpha_s^2)$ predictions for SU(N) with N=2, 3, 5 and 10 made using NLOJET++ for the kinematic region defined by $500 < Q^2 < 5000$ GeV$^2$. The lower part of the figures displays the relative difference to the $O(\alpha_s^2)$ calculations based on SU(3). The ZEUS-S PDFs have been used in the calculations.

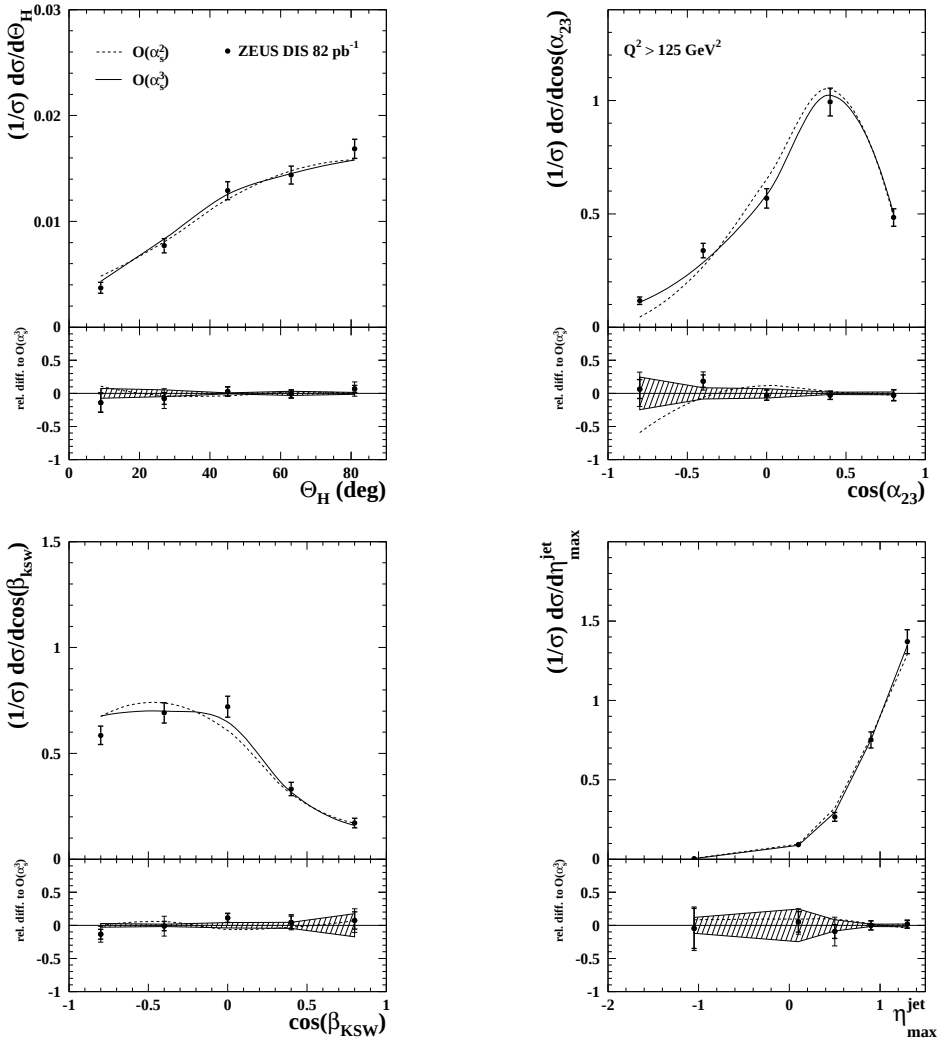


Figure 7.5: Measured normalized differential cross sections compared to the $O(\alpha_s^2)$ and $O(\alpha_s^3)$ pQCD calculations made using NLOJET++ for the kinematic region defined by $Q^2 > 125$ GeV$^2$. The lower part of the figures displays the relative difference to the $O(\alpha_s^3)$ calculations and the hatched band shows their total uncertainty. The ZEUS-S PDFs have been used in the calculations.

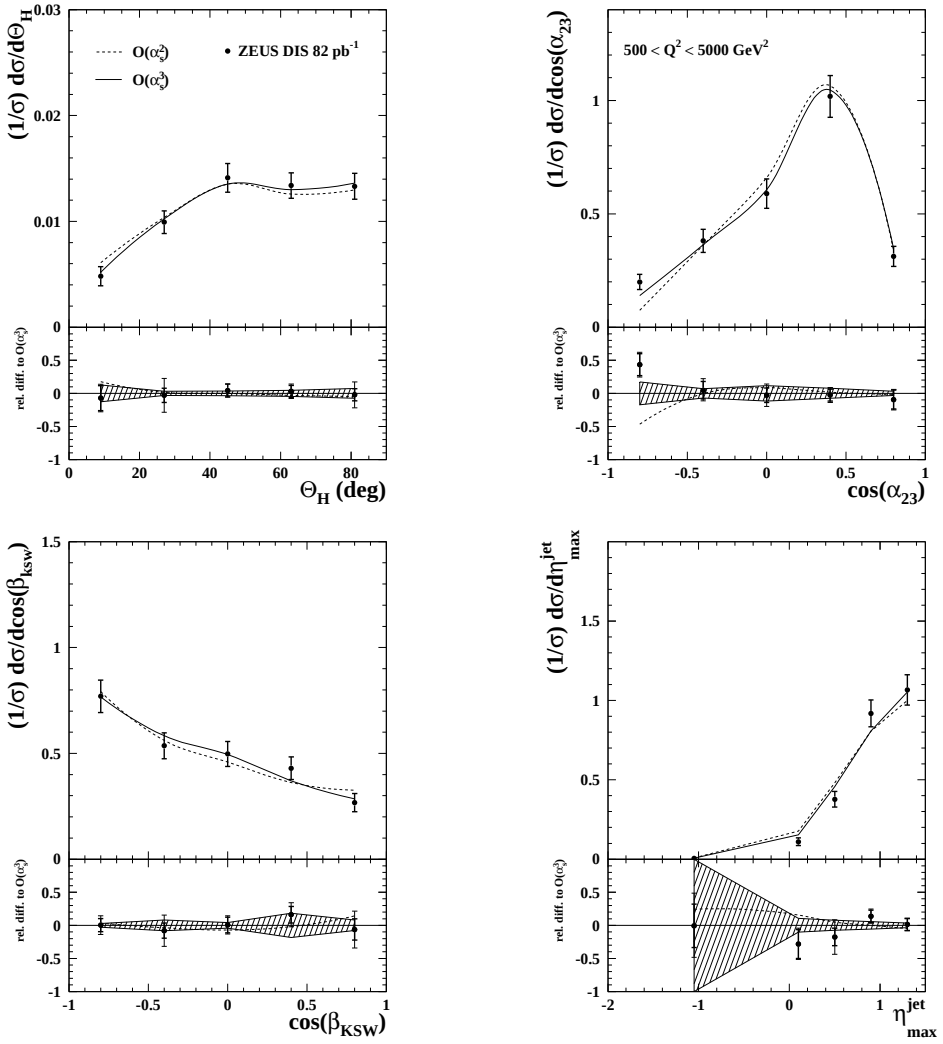


Figure 7.6: Measured normalized differential cross sections compared to the $O(\alpha_s^2)$ and $O(\alpha_s^3)$ pQCD calculations made using NLOJET++ for the kinematic region defined by $500 < Q^2 < 5000$ GeV$^2$. The lower part of the figures displays the relative difference to the $O(\alpha_s^3)$ calculations and the hatched band shows their total uncertainty. The ZEUS-S PDFs have been used in the calculations.

## 7.4 Comparison to $O(\alpha_s^2)$ predictions based on different symmetry groups

The measured normalized cross sections for the angular variables have been compared to the $O(\alpha_s^2)$ predictions based on SU(3) in Fig. 7.5. The symmetry groups to which the measured correlations are compared in this section are (see Fig. 7.7): an Abelian model based on U(1)$^3$, SU(N) for large N, SO(3) and the extreme choice $C_F = 0$. The angular-correlation distributions are discussed separately below:

- $\boldsymbol{\Theta_H}$: The measured angular correlation (dots) is reasonably well described by the $O(\alpha_s^2)$ pQCD prediction (solid line). This variable was designed to be sensitive to the relative contribution of TGV in $\sigma_B$. The figure shows that the difference between the U(1)$^3$ prediction and the SU(3) prediction is only up to $\sim 10\%$. This is due to the fact that $\sigma_B$ has a small contribution to the overall cross-section of $\sim 13\%$, substantially smaller than in $e^+e^-$ annihilation. Thus, the sensitivity of the angular correlations to the TGV is relatively suppressed for *ep* scattering. For the choice $C_F = 0$, however, the relative difference with pQCD goes up to $\sim 20\%$ and is clearly disfavoured by the data;

- $\cos\alpha_{\boldsymbol{23}}$: The measured angular correlation (dots) is reasonably well described by the $O(\alpha_s^2)$ pQCD prediction (solid line). In the first bin the discrepancy is large, but as we showed in Fig. 3.4, so is the theoretical uncertainty. From the figures in the previous section we know that the $O(\alpha_s^3)$ contribution is significant in this region. The Abelian prediction deviates from SU(3) by up to $\sim 10\%$, for the same reason mentioned above;

- $\cos\beta_{\boldsymbol{ksw}}$: The measured angular correlation (dots) is reasonably well described by the $O(\alpha_s^2)$ QCD prediction (solid line). The sensitivy of this angular correlation is similar to the others. Again the Abelian prediction deviates from SU(3) by up to $\sim 10\%$ in some regions, whereas the choice $C_F = 0$ is again clearly disfavoured by the data.

- $\eta^{\boldsymbol{jet}}_{\boldsymbol{max}}$: The measured angular correlation (dots) is reasonably well described by the $O(\alpha_s^2)$ QCD prediction (solid line). For this angular-correlation variable, the sensitivity to the TGV is increased with respect to the rest. The relative difference with the Abelian model goes up to $\sim 30\%$ in some regions, whereas both SU(N) for large N and $C_F = 0$ are clearly disfavoured by the data. The statistical uncertainties, however, increase in the region of $\eta^{jet}_{max}$ where the sensitivity to the TGV is largest.

In general the relative difference between SU(3) and the Abelian model is $\sim 10\%$, except for $\eta^{jet}_{max}$, where it goes up to $\sim 30\%$. The ability of the angular correlations

to discern among different symmetry groups is suppressed by the relatively small contribution from $\sigma_B$ and by the relatively large statistical uncertainties in the region where the sensitivity to the TGV is largest. Nevertheless, the angular correlations show sufficient sensitivity to distinguish between pQCD and the predictions based on $SU(N)$ for large N and $C_F = 0$, especially using the $\eta_{max}^{jet}$ angular-correlation variable.

Fig. 7.8 shows the same type of comparisons for the restricted phase-space region of $500 < Q^2 < 5000$ GeV$^2$. Although the sensitivity of the angular correlations to the color factors has not decreased, the statistical uncertainties for this region are larger, since the data sample is cut almost by half by restricting the $Q^2$ range to this region. All the comments for Fig. 7.7 also apply to this figure. Tables 7.1 through 7.4 contain the actual numbers of the measured normalized cross sections as well as the experimental uncertainties and the correction factors applied to the data and the predictions.

The integrated three-jet cross section in NC DIS for $Q^2 > 125$ GeV$^2$ and $500 < Q^2 < 5000$ GeV$^2$ have also been measured and have been found to be:

$$\sigma_{ep\to 3jets} = 11.48 \pm 0.35(\text{stat.})^{+1.99}_{-1.98}(\text{syst.})\text{pb}$$

and

$$\sigma_{ep\to 3jets} = 5.73 \pm 0.26(\text{stat.})^{+0.56}_{-0.60}(\text{syst.})\text{pb}$$

respectively. The total cross sections reflect the fact that the restricted phase-space has the disadvantage of reducing the statistics by $\sim 1/2$.

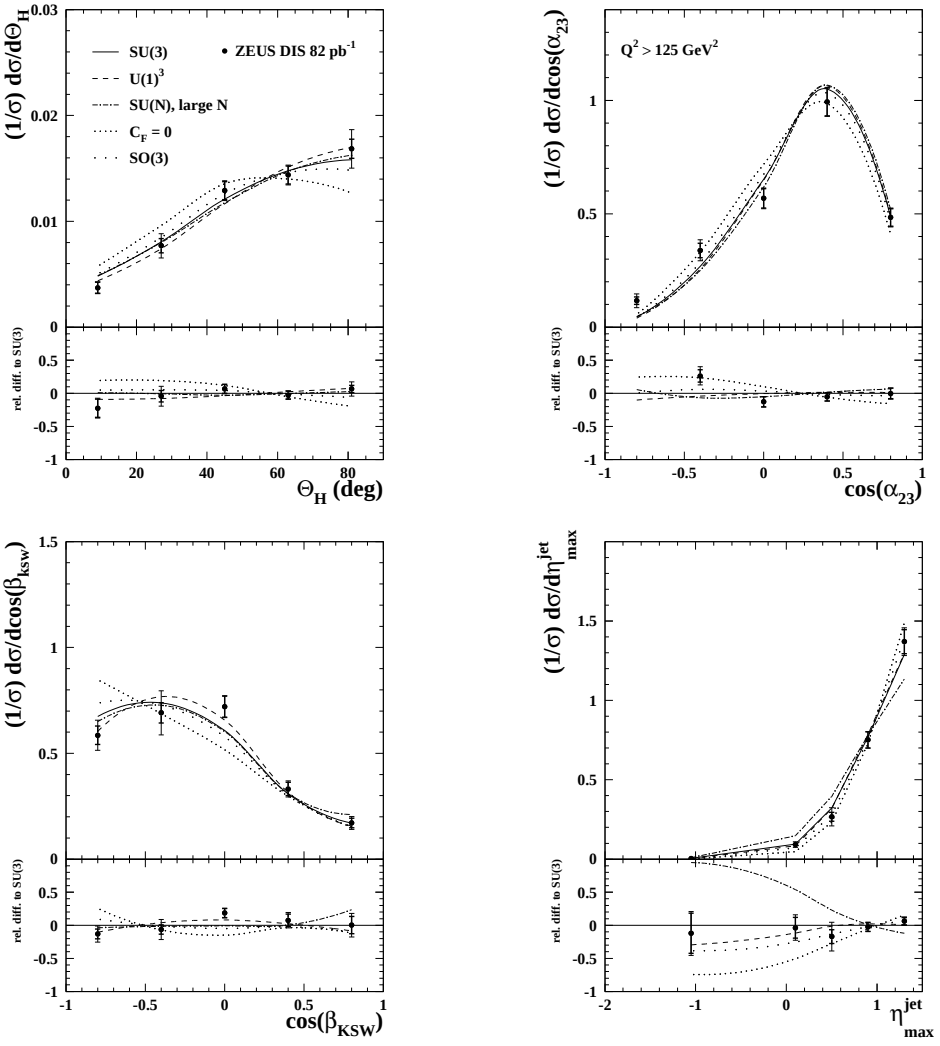


Figure 7.7: Measured normalized differential cross sections for three-jet production in NC DIS (dots) integrated over $E_{T,\mathrm{B}}^{\mathrm{jet}} > 8$ GeV, $E_{T,B}^{jet2,3} > 5$ GeV and $-2 < \eta_{\mathrm{B}}^{\mathrm{jet}} < 1.5$ in the kinematic region given by $Q^2 > 125$ GeV$^2$ and $|\cos\gamma_h| < 0.65$ as functions of $\Theta_H$, $\cos\alpha_{23}$, $\cos\beta_{ksw}$ and $\eta_{max}^{jet}$. The data points are plotted at the bin centers. The error bars are the same as in the caption to Fig. 6.1. For comparison, the $O(\alpha_s^2)$ calculations are shown for different symmetry groups. The lower part of the figures displays the relative difference to the calculations based on SU(3).

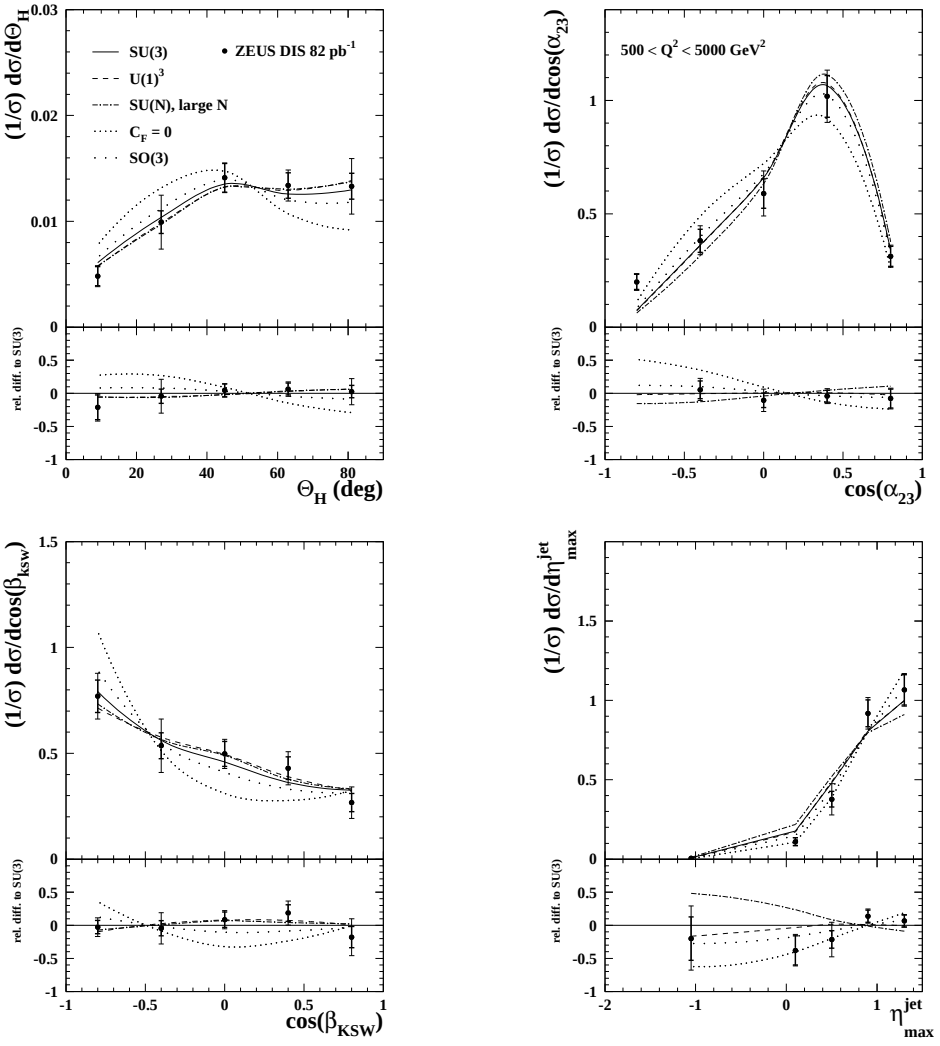


Figure 7.8: Measured normalized differential cross sections for three-jet production in NC DIS (dots) integrated over $E_{T,\mathrm{B}}^{\mathrm{jet}} > 8$ GeV, $E_{T,B}^{jet2,3} > 5$ GeV and $-2 < \eta_{\mathrm{B}}^{\mathrm{jet}} < 1.5$ in the kinematic region given by $500 < Q^2 < 5000$ GeV$^2$ and $|\cos\gamma_h| < 0.65$ as functions of $\Theta_H$, $\cos\alpha_{23}$, $\cos\beta_{ksw}$ and $\eta_{max}^{jet}$. The data points are plotted at the bin centers. The error bars are the same as in the caption to Fig. 6.1. For comparison, the $O(\alpha_s^2)$ calculations are shown for different symmetry groups. The lower part of the figures displays the relative difference to the calculations based on SU(3).

## 7.5 Discussion of an extraction of the color factors and conclusions

One of the aims of studying angular correlations in three-jet production in $ep$ scattering is to make a direct extraction of the color factors from the data. As mentioned in Chapter 1, this has been carried out successfully in the past in $e^+e^-$ annihilation at LEP. The beauty of this approach lies in the fact the underlying gauge symmetry can be observed in a transparent way through the angular correlations. We have seen that this is also possible in $ep$ collisions since it has been shown that the angular correlations show sensitivity to the underlying symmetry, albeit relatively suppressed, in $ep$ scattering.

The extraction procedure is straightforward once a formula of the form of eq. 3.5 is obtained, since then one needs only leave the color factors as free parameters in a fit of the theory to the data. In practice the fit procedure is somewhat complicated by the correlation matrices which enter into the fit of the normalized cross sections. A direct extraction of the color factors using eq. 3.5 at $O(\alpha_s^2)$ has been attempted despite the relatively large statistical uncertainties in the data sample and it has been found that the convergence of the fit is not sufficiently good with the present statistics.

In light of this, several alternate venues have been followed:

- Combinations of the angular-correlation variables have been fitted simultaneously. It was found that the fit is not sufficiently good;
- Double differential cross sections with respect to a pair of angular-correlation variables have been measured and calculated at $O(\alpha_s^2)$ for the different symmetry groups. These two-dimensional surfaces have been scanned for particular regions where the ability to discern among the different groups might be enhanced. No such a region was found such that the enhancement could compensate for the increased statistical uncertainty of restricting the phase-space to such an enhanced region;
- The region of $Q^2 < 125$ GeV$^2$ was scanned for a region where the ability of the correlations to discern among the different symmetry groups might be enhanced. No such a region were found such that the enhancement could compensate for the increased statistical uncertainty of restricting the phase-space to such an enhanced region;
- The analysis has been carried out with jet-radii R=0.7 and R=0.5. It was found that the discernability among the different symmtry groups does not increase with these alternate choices of the jet-radius.

In order to gain sensitivity in the predictions to the underlying gauge group, predictions with different SU(N) choices have been obtained at $O(\alpha_s^3)$. As already discussed, in order to carry out the full analysis at $O(\alpha_s^3)$ it is necessary to obtain the $O(\alpha_s^3)$ version of eq. 1.28, which require enough predictions with different SU(N) assumed groups to solve for the sub-process cross sections. The CPU time required in this case is more demanding, and for this reason this is still a work in progress; however, some predictions at $O(\alpha_s^3)$ have already been obtained. Figs. 7.9 and 7.10 show the $O(\alpha_s^3)$ calculations for SU(2), SU(3), SU(5) and SU(10). The bottom plots in these figures show the relative differences of the predictions with respect to SU(3). Here we observe that the relative differences among the SU(N) predictions are larger at $O(\alpha_s^3)$ than at $O(\alpha_s^2)$.

To summarize, it was found that the present statistical uncertainties in the measurements prevent a direct extraction of the color factors. The logical venue to follow is discussed next. We showed in Chapter 3 that the dependence with the running of $\alpha_s$ decreases significantly by performing the calculations at $O(\alpha_s^3)$. Thus, with this reduced dependence the range of $Q^2$ can be increased and the statistical uncertainties reduced. This seems necessary anyway since the overall description of the data improves by the contribution from $O(\alpha_s^3)$ effects, as shown in Fig. 7.5. Moreover, once the HERA II data is analized the entire data sample for HERA will become available providing a more than 5-fold increase in the luminosity with respect to that used for this analysis. Carrying out the analysis at $O(\alpha_s^3)$ while measuring the angular correlations with the combined HERA I and HERA II data sample is a promising venue to extract the color factors.

The conclusions of the angular-correlations analysis are:

- Angular-correlation observables that show sensitivity to the underlying symmetry structure in a way independent from PDF evolution and the running of $\alpha_s$ in *ep* scattering have been devised;

- Measurements of these angular-correlation variables have been obtained and compared to MC simulations based on the CDM and MEPS models, respectively. It has been found that while both models can generally describe the data well, the MEPS model provides a slightly better description.

- The measurements of the angular correlations have been compared to $O(\alpha_s^2)$ predictions using different symmetry groups. It has been found that the pQCD predictions are always consistent with the data within the uncertainties. The data clearly disfavours some models such as those based on $C_F = 0$ or SU(N) for large N; however, but the ability of the data to distinguish between SU(3) and an Abelian model remains elusive due to the relatively large statistical

uncertainties in the data sample.

- The predictions to $O(\alpha_s^3)$ have been obtained and contrasted with those made at $O(\alpha_s^2)$ in pQCD. It has been found that while the pQCD predictions at $O(\alpha_s^2)$ are always consistent with the data within the uncertainties, the $O(\alpha_s^3)$ predictions do generally better, especially in the lower $\cos\alpha_{23}$ region and in the variable $\eta_{max}^{jet}$.

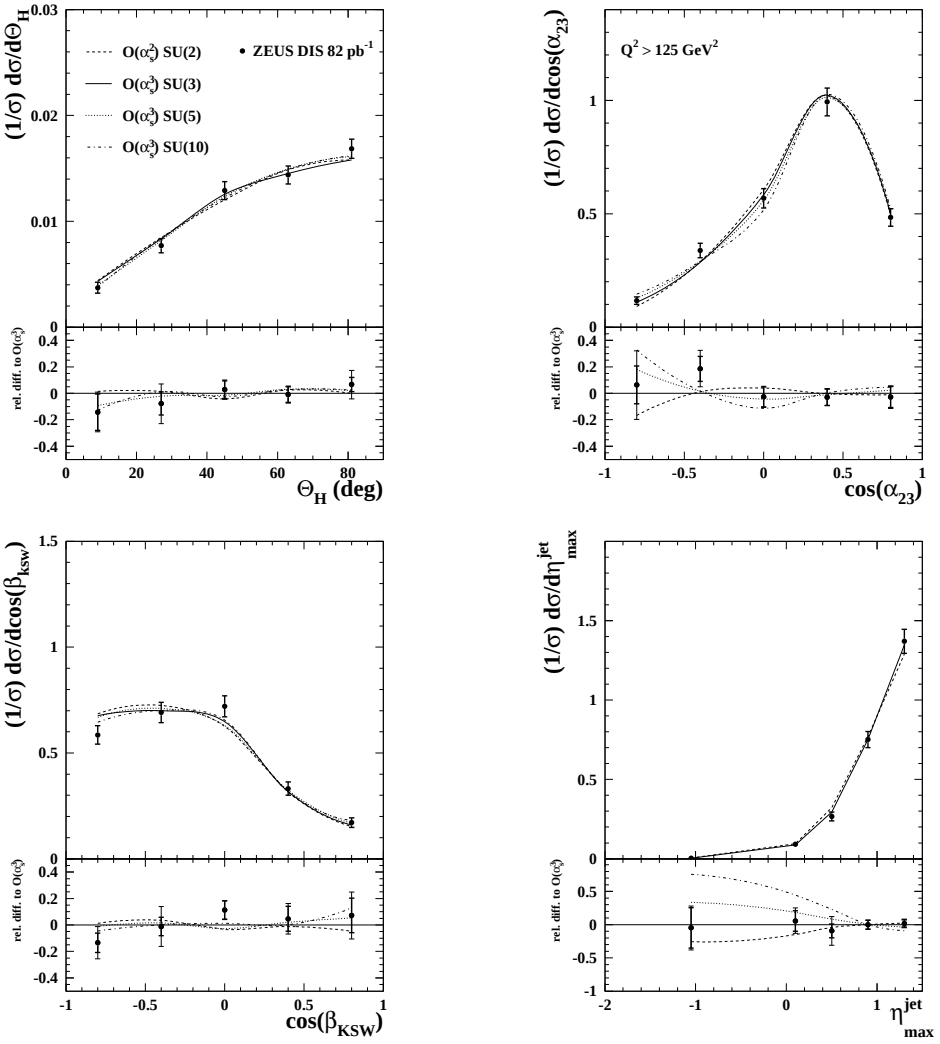


Figure 7.9: Measured normalized differential cross sections compared to the $O(\alpha_s^3)$ predictions for SU(N) with N=2, 3, 5 and 10 made using NLOJET++ for the kinematic region defined by $Q^2 > 125$ GeV$^2$. The lower part of the figures displays the relative difference to the $O(\alpha_s^3)$ calculations based on SU(3). The ZEUS-S PDFs have been used in the calculations.

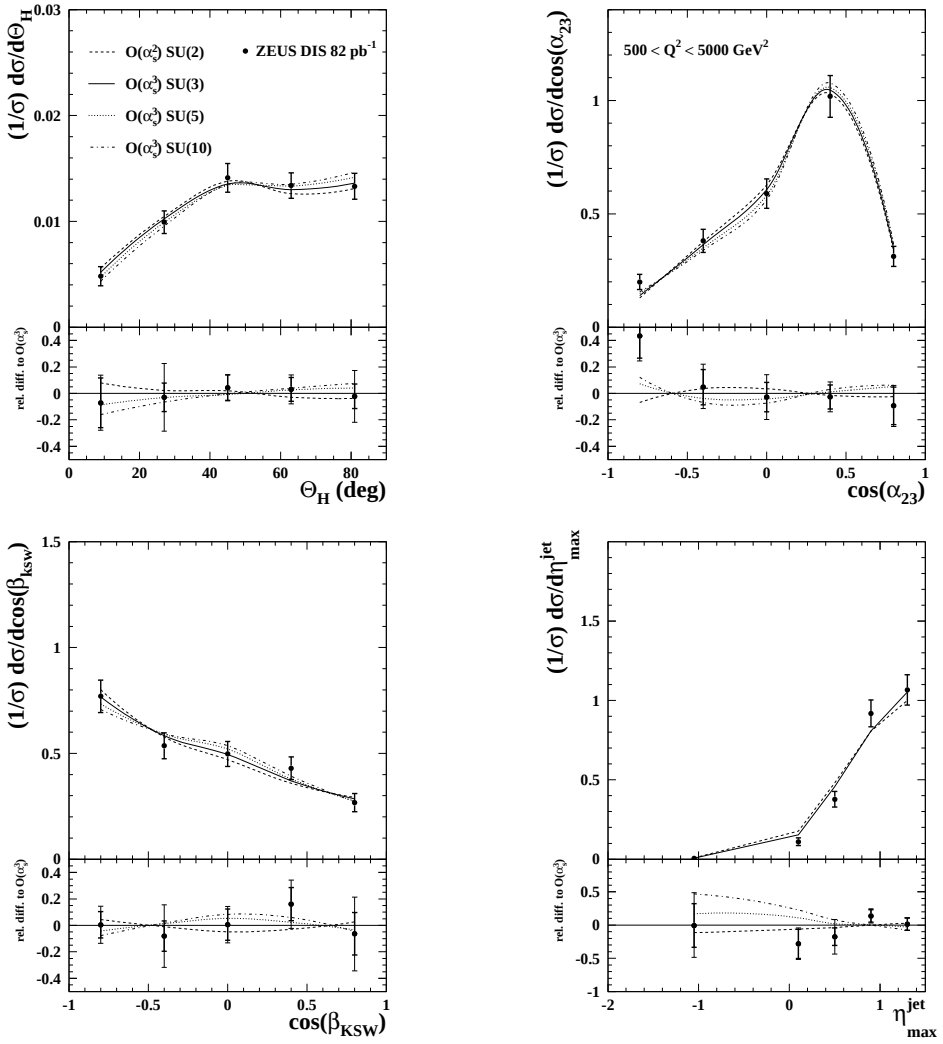


Figure 7.10: Measured normalized differential cross sections compared to the $O(\alpha_s^3)$ predictions for SU(N) with N=2, 3, 5 and 10 made using NLOJET++ for the kinematic region defined by $500 < Q^2 < 5000$ GeV$^2$. The lower part of the figures displays the relative difference to the $O(\alpha_s^3)$ calculations based on SU(3). The ZEUS-S PDFs have been used in the calculations.

| $\Theta_H$ bin (deg) | $(\frac{1}{\sigma})d\sigma/d\Theta_H$ | $\delta_{\rm stat}$ | $\delta_{\rm syst}$ | $\delta_{\rm ES}$ | $C_{\rm QED}$ | $C_{\rm had}$ |
|---|---|---|---|---|---|---|
| $Q^2 > 125$ GeV$^2$ | | | | | | |
| 0-18 | 0.00372 | 0.00051 | $^{+0.00019}_{-0.00019}$ | $^{+0.00014}_{-0.00014}$ | 0.96 | 1.01 |
| 18-36 | 0.00770 | 0.00067 | $^{+0.00093}_{-0.00093}$ | $^{+0.00020}_{-0.00020}$ | 0.91 | 0.99 |
| 36-54 | 0.01291 | 0.00085 | $^{+0.00032}_{-0.00032}$ | $^{+0.00028}_{-0.00025}$ | 0.99 | 1.02 |
| 54-72 | 0.01438 | 0.00085 | $^{+0.00038}_{-0.00039}$ | $^{+0.00015}_{-0.00014}$ | 1.04 | 1.01 |
| 72-90 | 0.01686 | 0.00091 | $^{+0.00155}_{-0.00155}$ | $^{+0.00036}_{-0.00036}$ | 1.03 | 0.98 |
| $500 < Q^2 < 5000$ GeV$^2$ | | | | | | |
| 0.- 18. | 0.00481 | 0.00091 | $^{+0.00039}_{-0.00040}$ | $^{+0.00010}_{-0.00010}$ | 0.92 | 0.96 |
| 18.- 36. | 0.0099 | 0.0011 | $^{+0.0023}_{-0.0023}$ | $^{+0.0001}_{-0.0001}$ | 0.99 | 1.01 |
| 36.- 54. | 0.0141 | 0.0014 | $^{+0.0002}_{-0.0002}$ | $^{+0.0003}_{-0.0003}$ | 0.97 | 1.01 |
| 54.- 72. | 0.0134 | 0.0012 | $^{+0.0008}_{-0.0008}$ | $^{+0.0001}_{-0.0001}$ | 1.07 | 1.02 |
| 72.- 90. | 0.0133 | 0.0012 | $^{+0.0023}_{-0.0023}$ | $^{+0.0003}_{-0.0003}$ | 1.01 | 0.98 |

Table 7.1: Measured normalized differential cross section $(\frac{1}{\sigma})d\sigma/d\Theta_H$ for three-jet production in NC DIS integrated over $E^{\rm jet}_{T,{\rm B}} > 8$ GeV, $E^{jet2,3}_{T,B} > 5$ GeV and $-2 < \eta^{\rm jet}_{\rm B} < 1.5$ in the kinematic region given by $Q^2 > 125$ GeV$^2$ (top) and $500 < Q^2 < 5000$ GeV$^2$ (bottom) and $|\cos\gamma_h| < 0.65$. The statistical, systematic and jet-energy scale uncertainties are showed separately. The multiplicative correction applied to correct for QED radiative effects and for hadronization effects are shown in the last two colums.

| $\cos\alpha_{23}$ | $(\frac{1}{\sigma})d\sigma/d\cos\alpha_{23}$ | $\delta_{\rm stat}$ | $\delta_{\rm syst}$ | $\delta_{\rm ES}$ | $C_{\rm QED}$ | $C_{\rm had}$ |
|---|---|---|---|---|---|---|
| $Q^2 > 125$ GeV$^2$ | | | | | | |
| -1 - -0.6 | 0.117 | 0.017 | $^{+0.025}_{-0.025}$ | $^{+0.005}_{-0.005}$ | 1.01 | 0.93 |
| -0.6 - -0.2 | 0.338 | 0.032 | $^{+0.033}_{-0.035}$ | $^{+0.003}_{-0.003}$ | 1.05 | 0.91 |
| -0.2 - 0.2 | 0.568 | 0.042 | $^{+0.016}_{-0.017}$ | $^{+0.005}_{-0.005}$ | 0.94 | 0.92 |
| 0.2 - 0.6 | 0.993 | 0.061 | $^{+0.016}_{-0.017}$ | $^{+0.007}_{-0.007}$ | 0.99 | 1.02 |
| 0.6 - 1. | 0.484 | 0.039 | $^{+0.014}_{-0.013}$ | $^{+0.007}_{-0.007}$ | 1.07 | 1.17 |
| $500 < Q^2 < 5000$ GeV$^2$ | | | | | | |
| -1.- -0.6 | 0.199 | 0.033 | $^{+0.014}_{-0.014}$ | $^{+0.011}_{-0.011}$ | 1.09 | 0.88 |
| -0.6 - -0.2 | 0.381 | 0.051 | $^{+0.032}_{-0.039}$ | $^{+0.009}_{-0.009}$ | 1.02 | 0.98 |
| -0.2 - 0.2 | 0.589 | 0.065 | $^{+0.073}_{-0.073}$ | $^{+0.006}_{-0.006}$ | 0.97 | 0.92 |
| 0.2 - 0.6 | 1.018 | 0.092 | $^{+0.059}_{-0.060}$ | $^{+0.005}_{-0.005}$ | 0.99 | 1.02 |
| 0.6 - 1. | 0.313 | 0.044 | $^{+0.020}_{-0.020}$ | $^{+0.008}_{-0.008}$ | 1.02 | 1.22 |

Table 7.2: Measured normalized differential cross section $(\frac{1}{\sigma})d\sigma/d\cos\alpha_{23}$ for three-jet production in NC DIS integrated over $E^{\rm jet}_{T,{\rm B}} > 8$ GeV, $E^{jet2,3}_{T,B} > 5$ GeV and $-2 < \eta^{\rm jet}_{\rm B} < 1.5$ in the kinematic region given by $Q^2 > 125$ GeV$^2$ (top) and $500 < Q^2 < 5000$ GeV$^2$ (bottom) and $|\cos\gamma_h| < 0.65$. Other details as in the caption to Table 7.1.

| $\cos\beta_{ksw}$ | $(\frac{1}{\sigma})d\sigma/d\cos\beta_{ksw}$ | $\delta_{\rm stat}$ | $\delta_{\rm syst}$ | $\delta_{\rm ES}$ | $C_{\rm QED}$ | $C_{\rm had}$ |
|---|---|---|---|---|---|---|
| $Q^2 > 125$ GeV$^2$ | | | | | | |
| -1 - -0.6 | 0.585 | 0.043 | $^{+0.056}_{-0.056}$ | $^{+0.008}_{-0.008}$ | 0.95 | 1.06 |
| -0.6 -0.2 | 0.691 | 0.048 | $^{+0.092}_{-0.092}$ | $^{+0.012}_{-0.012}$ | 1.03 | 1.04 |
| -0.2 - 0.2 | 0.720 | 0.049 | $^{+0.013}_{-0.014}$ | $^{+0.006}_{-0.006}$ | 1.05 | 1.00 |
| 0.2 - 0.6 | 0.332 | 0.031 | $^{+0.021}_{-0.023}$ | $^{+0.005}_{-0.005}$ | 0.95 | 0.89 |
| 0.6 - 1 | 0.171 | 0.022 | $^{+0.020}_{-0.020}$ | $^{+0.005}_{-0.005}$ | 0.96 | 0.88 |
| $500 < Q^2 < 5000$ GeV$^2$ | | | | | | |
| -1.- -0.6 | 0.770 | 0.077 | $^{+0.076}_{-0.076}$ | $^{+0.007}_{-0.007}$ | 0.98 | 1.02 |
| -0.6 -0.2 | 0.536 | 0.061 | $^{+0.110}_{-0.110}$ | $^{+0.013}_{-0.013}$ | 0.97 | 1.03 |
| -0.2 - 0.2 | 0.497 | 0.059 | $^{+0.034}_{-0.034}$ | $^{+0.009}_{-0.009}$ | 1.05 | 1.07 |
| 0.2 - 0.6 | 0.430 | 0.054 | $^{+0.056}_{-0.056}$ | $^{+0.008}_{-0.008}$ | 1.06 | 0.98 |
| 0.6 - 1 | 0.267 | 0.043 | $^{+0.059}_{-0.059}$ | $^{+0.012}_{-0.012}$ | 0.93 | 0.85 |

Table 7.3: Measured normalized differential cross section $(\frac{1}{\sigma})d\sigma/d\cos\beta_{ksw}$ for three-jet production in NC DIS integrated over $E^{\rm jet}_{T,{\rm B}} > 8$ GeV, $E^{jet2,3}_{T,B} > 5$ GeV and $-2 < \eta^{\rm jet}_{\rm B} < 1.5$ in the kinematic region given by $Q^2 > 125$ GeV$^2$ (top) and $500 < Q^2 < 5000$ GeV$^2$ (bottom) and $|\cos\gamma_h| < 0.65$. Other details as in the caption to Table 7.1.

| $\eta^{jet}_{max}$ | $(\frac{1}{\sigma})d\sigma/d\eta^{jet}_{max}$ | $\delta_{\rm stat}$ | $\delta_{\rm syst}$ | $\delta_{\rm ES}$ | $C_{\rm QED}$ | $C_{\rm had}$ |
|---|---|---|---|---|---|---|
| $Q^2 > 125$ GeV$^2$ | | | | | | |
| -2 - -0.1 | 0.0042 | 0.0013 | $^{+0.0005}_{-0.0005}$ | $^{+0.0003}_{-0.0003}$ | 1.12 | 0.87 |
| -0.1 - 0.3 | 0.092 | 0.014 | $^{+0.009}_{-0.011}$ | $^{+0.003}_{-0.003}$ | 1.22 | 0.95 |
| 0.3 - 0.7 | 0.267 | 0.028 | $^{+0.051}_{-0.051}$ | $^{+0.003}_{-0.003}$ | 1.00 | 0.97 |
| 0.7 - 1.1 | 0.751 | 0.050 | $^{+0.014}_{-0.013}$ | $^{+0.004}_{-0.004}$ | 0.97 | 0.99 |
| 1.1 - 1.5 | 1.370 | 0.075 | $^{+0.045}_{-0.045}$ | $^{+0.005}_{-0.006}$ | 1.00 | 1.02 |
| $500 < Q^2 < 5000$ GeV$^2$ | | | | | | |
| -2.- -0.1 | 0.0059 | 0.0020 | $^{+0.0021}_{-0.0021}$ | $^{+0.0008}_{-0.0008}$ | 1.20 | 0.70 |
| -0.1 - 0.3 | 0.111 | 0.024 | $^{+0.006}_{-0.009}$ | $^{+0.001}_{-0.001}$ | 1.00 | 0.85 |
| 0.3 - 0.7 | 0.378 | 0.050 | $^{+0.080}_{-0.080}$ | $^{+0.008}_{-0.008}$ | 1.00 | 0.97 |
| 0.7 - 1.1 | 0.918 | 0.085 | $^{+0.050}_{-0.050}$ | $^{+0.015}_{-0.015}$ | 0.97 | 1.05 |
| 1.1 - 1.5 | 1.066 | 0.096 | $^{+0.025}_{-0.025}$ | $^{+0.020}_{-0.020}$ | 1.02 | 1.03 |

Table 7.4: Measured normalized differential cross section $(\frac{1}{\sigma})d\sigma/d\eta^{jet}_{max}$ for three-jet production in NC DIS integrated over $E^{\rm jet}_{T,{\rm B}} > 8$ GeV, $E^{jet2,3}_{T,B} > 5$ GeV and $-2 < \eta^{\rm jet}_{\rm B} < 1.5$ in the kinematic region given by $Q^2 > 125$ GeV$^2$ (top) and $500 < Q^2 < 5000$ GeV$^2$ (bottom) and $|\cos\gamma_h| < 0.65$. Other details as in the caption to Table 7.1.

# Chapter 8

# Summary and Conclusions

This chapter contains a brief summary of the results presented throughout this document.

## 8.1 Inclusive-jet cross sections in NC DIS and determinations of $\alpha_s(M_Z)$

A precise determination of the parton densities of the proton (PDFs) is of essential experimental importance, especially for future hadron collider experiments such as the LHC. The precision of Standard Model predictions relies on the precision with which the PDFs have been determined. In particular, the gluon density in the proton is one of the essential ingredients for predictions of Higgs production in $pp$ collisions. We have discussed in Chapter 1 how the PDFs are obtained through global QCD fits, where inclusive observables such as the measurements of $F_2$ shown in Fig 1.13 have provided most of the information on the PDFs, including that for the gluon PDF in the mid- to high-$x$ region. In this region the slope of $F_2$ is however relatively flat and therefore the resulting uncertainty in the gluon density is larger. In Fig. 1.14 we have shown a global QCD fit carried out by the ZEUS Collaboration using ZEUS data alone, where jet cross-section measurements were included in the fit for the first time to help further constrain the gluon density in the mid- to high-$x$ region. As has been shown in Fig 1.16 the reduction in the uncertainty of the gluon PDF in this region was subtantial. This was one of the motivations for improving the measurements of inclusive-jet cross sections, accomplished by making new measurements with a more than two-fold increase in the statistics with respect to the previous ones.

There are several sources of theoretical uncertainties in pQCD predictions for jet observables, of which the dominant one has typically been that associated to higher-order contributions. This source of uncertainty is reduced by restricting the phase

space to high values of $Q^2$ where the perturbative approach is most reliable. In Chapter 3 (see Figs 3.2 and 3.3) we have shown that inclusive-jet cross sections are affected by a theoretical uncertainty associated to higher-order contributions that is below 5% for $Q^2 > 250$ GeV$^2$. Thus, inclusive-jet cross-section measurements have the advantage that they allow a precision comparison with fixed-order pQCD predictions, serving as another motivation for these measurements.

A data sample was obtained consisting of NC DIS events at high $Q^2$ with at least one high $E_T$ jet in the Breit frame. The sample was based on $81.7 \pm 1.8$ pb$^{-1}$ of integrated luminosity collected with the ZEUS detector during the 1998-2000 (HERA I) running period. The features of the sample where reproduced through the use of MC simulations (see Figs. 4.16 through 4.23), which as we showed in Chapter 4, were used for the study of the reconstruction of the observables with the detector. The MC simulations in combination with espcially selected data samples were used to reduce the dominant experimental uncertainty for this type of measurements, namely that associated with the jet energy scale, to within $\pm 1\%$. We have provided a quantitative estimation of all the sources of systematic uncertainty in the measurements in Chapter 5.

The $k_T$ clustering algorithm is particularly suited for a comparison of the measured hadronic final state with the partonic final state predicted by pQCD. As we showed in Chapter 5 the accuracy of the comparison has been further improved by supplementing the predictions with 'hadronization correction' factors obtained using the MC simulations (see Figs. 5.1 and 5.7).

Chapter 6 contained the final results for this analysis, which are measurements of differential cross sections for inclusive-jet production in $ep$ NC DIS. The cross sections refer to jets of hadrons identified in the Breit frame with the $k_T$ cluster algorithm in the longitudinally invariant inclusive mode. They are given in the kinematic region of $Q^2 > 125$ GeV$^2$ and $|\cos\gamma_h| < 0.65$.

In addition, inclusive-jet measurements were made in different regions of $Q^2$ as functions of $E_{T,\mathrm{B}}^{\mathrm{jet}}$, as shown in Fig. 6.2. The measurements are well described by the NLO QCD predictions. The cross sections in different regions of $Q^2$ are sensitive to the gluon density in the proton. The precise measurements obtained here are therefore of particular relevance for improving the determination of the gluon density in future QCD fits.

NC DIS at HERA provides a well understood environment on which to study the role of the jet-radius parameter of the $k_T$ cluster algorithm. A study of the jet-radius paramater was done by carrying out the inclusive-jet analysis using different values for R. The dependence of the inclusive-jet cross sections on the jet-radius has been presented in Fig. 6.3. There we showed that NLO QCD provides predictions

with comparable precision in the range R=0.5 − 1. Measurements of inclusive-jet differential cross sections for these choices of the jet-radii have been presented (see Fig. 6.1). The NLO QCD calculations provide a good description of the measured inclusive-jet differential cross sections $d\sigma/dE^{jet}_{T,B}$ and $d\sigma/dQ^2$ for R= 0.5, 0.7 and 1. It is observed that the measured inclusive-jet cross section integrated above $Q^2_{\rm min} = 125$ and 500 GeV$^2$ increases linearly with R in the jet-radius range studied.

A third important motivation for these cross-section measurements was that they have been found to yield the most precise extractions of $\alpha_s(M_Z)$ obtained at HERA in the past. Thus, it made sense to pursue an improvement of the determination of $\alpha_s$ through the improved measurements of the cross sections. The values of $\alpha_s$ obtained in this analysis have been shown in Figs. 6.10 through 6.12, as obtained from the $d\sigma/dQ^2$ measurements. The agreement among the extracted values constitutes a precise and compelling test of pQCD, since it implies that the scale dependence predicted by pQCD is in accordance with that found in the data. Fig. 6.13 shows the extractions from the $d\sigma/dE^{jet}_{T,B}$ measurements displayed at the mean $E^{\rm jet}_{T,\rm B}$ of the events in each bin from which they were obtained. This facilitates the visual comparison with the scale-dependence predicted by pQCD.

A QCD fit of the cross-section $d\sigma/dQ^2$ with $R = 1$ for $Q^2 > 500$ GeV$^2$ yielded the determination with smallest uncertainty obtained to date by the ZEUS Collaboration,

$$\alpha_s(M_Z) = 0.1207 \pm 0.0014(\text{stat.})^{+0.0035}_{-0.0033}(\text{exp.})^{+0.0022}_{-0.0023}(\text{theo.})$$

This value is in good agreement with the world and HERA averages. All the extracted values of $\alpha_s$ at different $Q^2$ and $E^{\rm jet}_{T,\rm B}$ are in good agreement with the predicted running of the strong coupling constant over a large range in $Q^2$ and $E^{\rm jet}_{T,\rm B}$.

The measured inclusive-jet differential cross sections have been used together with similar H1 measurements to extract for the first time a combined HERA value of $\alpha_s(M_Z)$. The combined HERA value of $\alpha_s(M_Z)$ is

$$\alpha_s(M_Z) = 0.1198 \pm 0.0019(\text{exp.}) \pm 0.0026(\text{theo.}), \tag{8.1}$$

with an experimental uncertainty of 1.6% and a theoretical uncertainty of 2.2%. It is consistent with previous determinations of $\alpha_s(M_Z)$ made by the H1 and ZEUS Collaborations, and with the world average. By using the new method of combination presented here, no assumption on the correlations had to be made and a significant reduction of the theoretical and experimental uncertainties was achieved by combining observables for which these uncertainties are well under control. A comparison to the most recent value of $\alpha_s(M_Z)$ from LEP [77], $\alpha_s(M_Z) = 0.1211 \pm 0,0010(\text{exp.}) \pm 0.0018(\text{theo.})$, shows that the uncertainty of the HERA combined

2007 value is competitive with LEP, which includes an average of many precise determinations, such as that coming from $\tau$ decays.

## 8.2 Angular correlations in three-jet events in NC DIS

In Chapter 1 it was shown that the underlying symmetry structure of a gauge theory determines many of its properties, such as the relative strengths of its vertices and the evolution of the coupling with the energy scale. In QCD the non-Abelian character of SU(3) leads to asymptotic freedom, a fundamental property the theory needs in order to be able to reproduce the measurements we showed in Fig. 6.13. A symmetry group can be uniquely characterized by its color factors, which in QFT dictate the relative strengths of the different vertices of the theory. The color factors provide a way of studying the underlying symmetry of the strong interactions, since they determine the shapes of the distributions of angular correlations in multijet events. The color factors were measured using four-jet events in $e^-e^+$ annihilation at LEP.

We have shown here that angular correlations that show sensitivity to the underlying symmetry group can also be designed for *ep* scattering using three-jet events in NC DIS (see Fig. 3.11). Moreover, in Chapter 3 we showed that the dependence of the angular correlations on the running of $\alpha_s$ or the PDF evolution can be partially circumvented by normalizing the cross sections and restricting the phase-space region (see Fig. 3.19). This restriction does not affect the sensitivity of the angular-correlations to the underlying group symmetry. Carrying out the analysis at $O(\alpha_s^3)$ also diminishes the dependence on the running of $\alpha_s$, a fact we demonstrated in Fig. 3.20.

The predictions at $O(\alpha_s^2)$ and $O(\alpha_s^3)$ were compared to the MC simulations based on the MEPS and CDM parton cascade models. Figs. 3.35 and 3.36 showed that $O(\alpha_s)$-pQCD-based MC calculations are able to simulate the angular correlations when supplemented by the models.

In this case the data sample used was as subset of that of the inclusive-jet analysis. Measurements of angular correlations in three-jet NC DIS were made using an integrated luminosity of 81 pb$^{-1}$ collected with the ZEUS detector during the HERA I running period. The cross sections refer to jets identified with the $k_T$ cluster algorithm in the longitudinally invariant mode and selected with $E_{T,B}^{jet1} > 8$ GeV, $E_{T,B}^{jet2,3} > 5$ GeV and $-2 < \eta_{\rm B}^{\rm jet} < 1.5$. The measurements were made in the kinematic regions defined by $Q^2 > 125$ GeV$^2$ GeV $^2$ ($500 < Q^2 < 5000$ GeV$^2$) and $|\cos\gamma_h| < 0.65$.

The MC simulations based on MEPS and CDM were also compared to the data

sample as shown in Chapter 4 (see Figs. 4.24 and 4.25) and were found to provide a fair description of the data. The necessary studies of the reconstruction of the observables and the estimation of the systematic uncertainties were carried out using the MC simulations in a similar way as for the inclusive-jet analysis, as has been presented in Chapters 4 and 5. The normalization of the cross sections resulted in a substantial reduction of the theoretical and experimental uncertainties, as we have shown in Chapters 3 and 5.

The final results of this analysis have been presented in Chapter 7. Normalized differential three-jet cross sections were measured as functions of $\Theta_H$, $\cos\alpha_{23}$, $\cos\beta_{ksw}$ and $\eta^{jet}_{max}$ and are shown in Figs. 7.7 and 7.8. Fixed-order calculations separated according to the color configurations were used to study the sensitivity of the angular correlations to the underlying gauge structure (see Figs. 3.11 and 3.21). The predicted distributions of $\Theta_H$, $\cos\alpha_{23}$ and $\cos\beta_{ksw}$ distinguish well the contribution from the triple-gluon coupling in quark-induced processes and $\eta^{jet}_{max}$ distinguishes the TGV contribution coming from gluon induced processes. The variable $\cos\alpha_{23}$ provides additional separation for the other contributions.

The measurements are found to be consistent with the admixture of color configurations as predicted by SU(3). The data clearly disfavour a theory in which $T_F/C_F \sim 0$, as predicted by SU(N) in the limit of large N, or the extreme choice $C_F = 0$.

The data were also compared to the $O(\alpha_s^3)$ pQCD predictions (see Figs. 7.5 and 7.6). It was found that the $O(\alpha_s^3)$ predictions provide a more precise and accurate description of the data than the $O(\alpha_s^2)$ predictions. In some regions, such as the lower $\cos\alpha_{23}$ region, the improvement is substantial.

In conclusion it was found that the relatively large contribution proportional to $T_F C_A$ in SU(3) provides a potential to extract the color factors from these data. However, it was found that the large statistical uncertainties relative to the sensitivity of the angular-correlation variables to the underlying group prevented a fit of the color factors. Thus, the logical venue suggested by this analysis is: to enlarge the data sample both by including the HERA II data, which will constitute a more than five-fold increase in the luminosity; and to carry out the theoretical calculations at $O(\alpha_s^3)$, which will reduce the residual dependence on the running of $\alpha_s$ and allow a less restricted phase space.

# Chapter 9

# Resumen y Conclusiones

Este capítulo contiene un resumen del documento con énfasis en los resultados finales.

## 9.1 Secciones eficaces inclusivas de jets en NC DIS y determinaciones de $\alpha_s(M_Z)$

Obtener una determinación precisa de las densidades partónicas del proton (PDFs) es de importancia fundamental para experimentos futuros de colisiones hadrónicas como el LHC. La precisión de las predicciones teóricas del Modelo Estandar en procesos que involucran hadrones en el estado inicial depende de la precisión a la que han sido determinadas las PDFs. En concreto, la densidad gluónica del protón es uno de los ingredientes esenciales en las predicciones de producción de Higgs en colisiones $pp$.

En el Capítulo 1 hemos visto como se obtienen las PDFs experimentalmente a través de ajustes globales de QCD, en los cuales las medidas de observables inclusivos como las de $F_2$ mostradas en la Figura 1.13 aportan la mayor parte de la información sobre las PDFs, incluyendo la de la PDF gluónica en la región de medio y alto $x$. En esta región, sin embargo, la pendiente de $F_2$ es más pequeña, dando lugar a una incertidumbre mayor en la determinación de la densidad gluónica del protón. La Figura 1.14 muestra un ajuste global de QCD llevado a cabo por la Colaboración ZEUS y haciendo uso sólo de datos obtenidos en el marco de dicha colaboración. En este ajuste fueron incluídas también medidas de secciones eficaces de jets que ayudan a delimitar más aún la densidad gluónica del protón en la región de medio a alto $x$. En la Figura 1.16 hemos mostrado que la reducción de la incertidumbre de la PDF del gluón en esta región debida a las medidas de jets es substancial. Este resultado motivó el llevar a cabo nuevas medidas de secciones eficaces inclusivas

de jets, mejoradas gracias a que se dispone de una muestra con más del doble de luminosidad integrada con respecto a medidas anteriores de este tipo.

Las medidas de secciones eficaces de jets inclusivas tienen además la ventaja de que permiten hacer comparaciones con las predicciones a orden fijo de QCD perturbativo (pQCD) a un nivel alto de precisión. La incertidumbre en la predicción teórica para observables de jets esta típicamente dominada por aquélla asociada a las contribuciones de órdenes más altos. Esta fuente de incertidumbre se ve reducida restringiendo el espacio de fase a un rango de valores grandes de $Q^2$, donde el tratamiento perturbativo de QCD es más fiable. En el Capítulo 3 (ver las Figuras 3.2 y 3.3) hemos demostrado que este tipo de observables tienen una incertidumbre teórica debida a órdenes más altos por debajo del $\pm 5\%$ para valores de $Q^2 > 250$ GeV$^2$. Por lo tanto, otra motivación de las medidas de secciones eficaces de jets presentadas en este documento es que están particularmente dotadas para poner a prueba pQCD.

Para llevar a cabo estas medidas se obtuvo una muestra de eventos de NC DIS con valores grandes de $Q^2$ y que además contuviesen al menos un jet de alto $E_T$ en el sistema de referencia de Breit. La muestra fue basada en $81.7 \pm 1.8$ pb$^{-1}$ de luminosidad integrada proveniente de la toma de datos de 1998-2000 (HERA I) con el detector ZEUS. También se obtuvieron simulaciones de MC de las muestras (ver Figuras. 4.16 a 4.23), que como hemos presentado en el Capítulo 4, fueron utilizadas para estudiar la calidad de la reconstrucción de los observables mediante el detector. Además, las simulaciones de MC también fueron utilizadas para reducir la mayor fuente de incertidumbre experimental para este tipo de medidas, aquélla asociada a la escala de la energía de los jets, que fue reducida por debajo del 1%. En el Capítulo 5 hemos mostrado una estimación detallada de las fuentes de incertidumbre sistemática que afectan a las medidas.

El algoritmo de $k_T$ de reconstrucción de los jets está particularmente dotado para permitir comparar el estado hadrónico que se mide en el detector con el estado partónico calculable en pQCD. La precisión de esta comparación entre las medidas y las predicciones teóricas se ha podido mejorar aún más mediante la implementación de factores de 'corrección por la hadronización', obtenidos a partir de las simulaciones de MC (ver Figuras 5.1 y 5.7).

En el Capítulo 6 hemos presentado los resultados finales de este análisis, que consisten en medidas de secciones eficaces diferenciales de producción de jets inclusiva en colisiones *ep* en el régimen de NC DIS. Las secciones eficaces se refieren a jets de hadrones identificados en el sistema de referencia de Breit con el algoritmo de reconstrucción de los jets de $k_T$. Las medidas se refieren a la región cinemática de $Q^2 > 125$ GeV$^2$ y $|\cos\gamma_h| < 0.65$.

También han sido hechas medidas de producción inclusiva de jets en términos de secciones eficaces como función de $E^{\rm jet}_{T,\rm B}$ para diferentes regiones de $Q^2$. Estas medidas se muestran en la Figura 6.2. Las predicciones teóricas a $O(\alpha_s^2)$ de pQCD son capaces de proporcionar una descripción adecuada de los datos en todo el rango de $E^{\rm jet}_{T,\rm B}$ y $Q^2$ sobre el cual se han llevado a cabo las medidas. Además, las secciones eficaces en regiones diferentes de $Q^2$ son sensibles a la densidad gluónica del protón. Por lo tanto, las medidas son de especial relevancia en términos de proporcionar una determinación más precisa de la densidad del gluón en ajustes globales de QCD en el futuro.

NC DIS en HERA proporciona un entorno adecuado en el cual hacer estudios del parámetro del radio del jet en el algoritmo de $k_T$. Este estudio ha sido llevado a cabo mediante la repetición del analisis usando diferentes valores del radio del jet (R). La dependencia de la sección eficaz inclusiva con el radio del jet R ha sido estudiada de esta manera, como se ha mostrado en la Figura 6.3. Mediante este estudio se ha determinado que QCD a $O(\alpha_s^2)$ proporciona predicciones de precisión comparable en el rango de R=$0.5 - 1$. Las medidas de secciones eficaces diferenciales de jets inclusivas para este rango del radio del jet han sido presentadas en el Capítulo 6. Los cálculos de QCD a $O(\alpha_s^2)$ estan en buen acuerdo con las medidas inclusivas de secciones eficaces differenciales $d\sigma/dE^{jet}_{T,B}$ y $d\sigma/dQ^2$ para valores del radio del jet R= $0.5, 0.7$ y 1. Se ha observado que la sección eficaz inclusiva de jets integrada sobre $Q^2_{\rm min} = 125$ y 500 GeV$^2$ aumenta linealmente con R en el rango estudiado.

Otro motivo importante por el cual se han hecho las medidas de secciones eficaces de jets ha sido que en el pasado éstas han permitido las determinaciones de $\alpha_s(M_Z)$ de mayor precisión en HERA. En las Figuras 6.10 a 6.12 se han presentado los valores de $\alpha_s(M_Z)$ obtenidos a partir de las medidas de secciones eficaces de jets en función de $Q^2$. El acuerdo entre las extracciones obtenidas a partir de un rango grande en $Q^2$ constituye en sí una prueba contundente de la validez de pQCD como la teoría de las interacciones fuertes. La Figura 6.13 muestra un buen acuerdo entre las determinaciones de $\alpha_s$ a partir de medidas de $d\sigma/dE^{jet}_{T,B}$ y la dependencia con la escala de la energía predicha por pQCD.

Un ajuste de la sección eficaz $d\sigma/dQ^2$ con $R = 1$ para la región $Q^2 > 500$ GeV$^2$ ha permitido la determinación más precisa de $\alpha_s$ obtenida hasta el momento por la Colaboración ZEUS,

$$\alpha_s(M_Z) = 0.1207 \pm 0.0014(\text{stat.})^{+0.0035}_{-0.0033}(\text{exp.})^{+0.0022}_{-0.0023}(\text{theo.})$$

Este valor está en buen acuerdo con el promedio mundial y con el promedio de HERA. Todos los valores extraídos de $\alpha_s$ a partir de las medidas de $d\sigma/dQ^2$ y $d\sigma/dE^{jet}_{T,B}$ están en buen acuerdo entre sí así como con la predicción de la dependencia con la escala de la energía predicha por pQCD.

Las medidas de secciones eficaces inclusivas de jets también han sido utilizadas junto con medidas de H1 para extraer por vez primera un valor de $\alpha_s(M_Z)$ combinado de HERA

$$\alpha_s(M_Z) = 0.1198 \pm 0.0019(\text{exp.}) \pm 0.0026(\text{theo.}), \tag{9.1}$$

con una incertidumbre experimental del 1.6% y una incertidumbre teórica del 2.2%. Este valor es consistente con determinaciones previas de $\alpha_s(M_Z)$ hechas independientemente por las Colaboraciones de H1 y ZEUS, así como con el promedio mundial. Con el nuevo método de combinación presentado aquí, no ha sido necesaria ninguna suposición sobre las correlaciones y se ha logrado una reducción significativa de las incertidumbres teóricas y experimentales gracias a la combinación de estos observables cuyas incertidumbres están bajo control. La precisión de esta extracción es comparable, por ejemplo, con la más reciente de LEP [77], $\alpha_s(M_Z) = 0.1211 \pm 0,0010(\text{exp.}) \pm 0.0018(\text{theo.})$, la cual es un promedio hecho sobre muchas determinaciones de gran precisión, como lo son las provenientes de la desintegración del $\tau$.

## 9.2 Correlaciones angulares en sucesos con tres jets en NC DIS

En el Capítulo 1 se ha descrito la manera en la que la simetría subyacente de una teoría gauge determina muchas de sus características, como por ejemplo la fuerza relativa de cada vértice o la dependencia del acoplo con la escala de la energía. En el caso de QCD el carácter no Abeliano de SU(3) implica la libertad asimptótica, una propiedad de la teoría necesaria para describir las medidas que se ha mostrado en la Figura 6.13. Como hemos visto en el primer capítulo, el grupo gauge puede ser caracterizado unívocamente por los factores de color, que son las fuerzas relativas de los diferentes vértices presentes en la teoría. Los factores de color proporcionan una manera independiente de estudiar la simetría subyacente de las interacciones fuertes, ya que determinan las formas de las distribuciones en las variables de correlación angular en sucesos con muchos jets. En eventos de cuatro jets en las aniquilaciones $e^-e^+$ en LEP se han podido extraer los factores de color a partir de medidas de estas correlaciones angulares.

En este documento hemos demostrado que también se pueden obtener variables de correlacion angular en la dispersión de $ep$ que muestran una sensibilidad al grupo gauge subyacente (ver Figura 3.11). La dependencia de las correlaciones angulares con la evolución de $\alpha_s$ o de las PDFs se puede minimizar parcialmente mediante la normalización de las secciones eficaces y lograr que sea despreciable mediante una restricción adecuada del espacio de fase (ver Figura 3.19). También hemos

demostrado (Figura 3.20) que hacer el análisis al siguiente orden en el desarrollo perturbativa ($O(\alpha_s^3)$) reduce todavía más esta dependencia.

Las predicciones a $O(\alpha_s^2)$ y $O(\alpha_s^3)$ han sido comparadas con simulaciones de MC basadas en los modelos de MEPS y CDM para la cascada partonica. En las Figuras 3.35 y 3.36 hemos mostrado cómo los cálculos de MC basados en pQCD a $O(\alpha_s)$ complementados con modelos de la cascada partónica son capaces de reproducir adecuadamente las correlaciones angulares.

La muestra de datos seleccionada para este análisis es un subconjunto de la seleccionada para el análisis de producción inclusiva de jets. Las medidas de correlaciones angulares fueron hechas en el régimen de NC DIS a partir de una luminosidad integrada de 81 pb$^{-1}$, tomada con el detector ZEUS durante el período de HERA I.

Las secciones eficaces se refieren a jets identificados con el algoritmo de $k_T$ y seleccionados con $E_{T,B}^{jet1} > 8$ GeV, $E_{T,B}^{jet1,2} > 5$ GeV y $-2 < \eta_{\rm B}^{\rm jet} < 1.5$. Las medidas fueron hechas en la región cinemática definida por $Q^2 > 125$ GeV$^2$ ($500 > Q^2 > 5000$ GeV$^2$) y $|\cos\gamma_h| < 0.65$.

Las simulaciones de MC basadas en MEPS y CDM también fueron comparadas con la muestra de los datos y proporcionan una buena descripción de los mismos (ver Figuras 4.24 y 4.25).

Los estudios de la reconstrucción de los observables y la estimación de las incertidumbres sistemáticas han sido presentados en los Capítulos 4 y 5. Una ventaja de la normalizacion de las secciones eficaces es la cancelación parcial de las incertidumbres teóricas y experimentales, como se ha puesto de manifiesto en los Capítulos 3 y 5.

Los resultados finales de este análisis han sido presentados en el Capítulo 7. Se trata de medidas de secciones eficaces normalizadas de producción de tres jets en función de $\Theta_H$, $\cos\alpha_{23}$, $\cos\beta_{ksw}$ and $\eta_{max}^{jet}$. Las medidas se han presentado en las Figuras 7.7 y 7.8. Las predicciones a órden fijo fueron separadas en términos de las configuraciones de color usadas para estudiar la sensibilidad de las correlaciones angulares a la estructura gauge subyacente (ver Figuras 3.11 y 3.21). La predicciones de las distribuciones de $\Theta_H$, $\cos\alpha_{23}$ y $\cos\beta_{ksw}$ permiten distinguir bien la contribución del auto-acoplo del gluón en sucesos inducidos por un quark, mientras que la variable $\eta_{max}^{jet}$ es un buen discriminador de dicha contribución proveniente de procesos inducidos por un gluón. La variable $\cos\alpha_{23}$ proporciona una separación adicional de las otras contribuciones.

Se ha encontrado que las medidas son consistentes con la combinación de configuraciones de color predicha por SU(3). Los datos desfavorecen claramente una teoría en la que $T_F/C_F \sim 0$, como es el caso de SU(N) en el límite de N grande, o

la elección $C_F = 0$. La contribución relativamente grande proporcional a $T_F C_A$ en el caso de SU(3) abre la posibilidad de extraer directamente los factores de color de los datos.

Los datos también han sido comparados con las predicciones a $O(\alpha_s^3)$ de pQCD (ver Figuras. 7.5 y 7.6). Se ha mostrado que las predicciones a $O(\alpha_s^3)$ proporcionan una descripción más precisa de los datos que las predicciones a $O(\alpha_s^2)$. En algunas regiones, como en la de valores pequeños de $\cos\alpha_{23}$, la mejora en la descripción de los datos es sustancial. Con respecto a una extracción directa de los factores de color de los datos, hemos hallado que las incertidumbres estadísticas de los datos, en relación a la sensibilidad que muestran las correlaciones angulares a la simetría subyacente, no permiten un ajuste de los factores de color en el momento presente. Por lo tanto, se sugiere como via lógica aumentar la muestra de datos tanto usando la muestra entera de HERA II (que de por sí constituiría un incremento de más de cinco veces la muestra utilizada aquí) así como hacer los cálculos teóricos a $O(\alpha_s^3)$ (esto reduciría la dependencia con la evolución de $\alpha_s$ y por lo tanto permitiría utilizar un espacio de fase menos restringido).

## References


[1] Chekanov, S. and others, Nucl. Phys. **B 765**, 1 (2007).

[2] Chekanov, S. and others, Phys. Lett. **B 649**, 12 (2007).

[3] ZEUS Collaboration, S. Chekanov et al, 'Angular Correlations in Three-Jet Production in ep Collisions at HERA', Contributed paper to the International Europhysics Conference on High Energy Physics (EPS07), Manchester, United Kingdom, 2007.

[4] H1 and ZEUS Collaborations, 'HERA Combined 2007 $\alpha_s$', Contributed paper to the International Europhysics Conference on High Energy Physics (EPS07), Manchester, United Kingdom, 2007.

[5] F. Halzen and A.D. Martin, *Quarks and Leptons: An Introductory Course in Modern Particle Physics*. John Wiley & Sons, Inc, 1984.

[6] J.I. Friedman and H.W. Kendall, Annual Review of Nuclear Science **22**, 203 (1972).

[7] R.K. Ellis, W.J. Stirling and B.R. Webber, *QCD and Collider Physics*, Cambridge Monographs on Particle Physics, Nuclear Physics and Cosmology, Vol. 8. Cambridge University Press, 1996.

[8] M.E. Peskin and D.V. Schroeder, *An Introduction to Quantum Field Theory*. Perseos Books, Cambridge, Massashussets, 1995.

[9] Wunsch, M. Given at 4th San Miniato Topical Seminar on the Standard Model and Just Beyond, San Miniato, Italy, 1-5 Jun 1992.

[10] Barate, R. and others, Z. Phys. **C76**, 1 (1997).

[11] Bravo, S. ALEPH-2001-042.

[12] Heister, A. and others, Eur. Phys. J. **C27**, 1 (2003).

[13] Abreu, P. and others, Z. Phys. **C59**, 357 (1993).

[14] Abreu, P. and others, Phys. Lett. **B414**, 401 (1997).

[15] Akrawy, M. Z. and others, Z. Phys. **C49**, 49 (1991).

[16] Adeva, B. and others, Phys. Lett. **B248**, 227 (1990).

[17] Abreu, P. and others, Phys. Lett. **B449**, 383 (1999).

[18] Akers, R. and others, Z. Phys. **C65**, 367 (1995).

[19] Abbiendi, G. and others, Eur. Phys. J. **C20**, 601 (2001).

[20] Bethke, S. and Ricker, A. and Zerwas, P. M., Z. Phys. **C49**, 59 (1991).

[21] Kluth, S., Nucl. Phys. Proc. Suppl. **133**, 36 (2004).

[22] Yao, W. -M. and others, J. Phys. **G33**, 1 (2006).

[23] Ellis, R. Keith and Georgi, Howard and Machacek, Marie and Politzer, H. David and Ross, Graham G., Nucl. Phys. **B152**, 285 (1979).

[24] Chekanov, S. and others, Phys. Rev. **D67**, 012007 (2003).

[25] Chekanov, S. and others, Eur. Phys. J. **C42**, 1 (2005).

[26] Martin, Alan D. and Roberts, R. G. and Stirling, W. J. and Thorne, R. S., Eur. Phys. J. **C23**, 73 (2002).

[27] Pumplin, J. and Belyaev, A. and Huston, J. and Stump, D. and Tung, W. K., JHEP **02**, 032 (2006).

[28] Bartel, W. and others, Phys. Lett. **B91**, 142 (1980).

[29] ZEUS Coll., J. Breitweg et al., Phys. Lett. **B 507**, 70 (2001).

[30] H1 Coll., C. Adloff et al., Eur. Phys. J. **C 19**, 289 (2001).

[31] ZEUS Coll., S. Chekanov et al., Eur. Phys. J. **C 23**, 13 (2002).

[32] Chekanov, S. and others, Phys. Lett. **B547**, 164 (2002).

[33] Chekanov, S. and others, Phys. Lett. **B551**, 226 (2003).

[34] H1 Coll., C. Adloff et al., Phys. Lett. **B 515**, 17 (2001).

[35] Chekanov, S. and others, Eur. Phys. J. **C44**, 183 (2005).

[36] Catani, S. and Dokshitzer, Yuri L. and Webber, B. R., Phys. Lett. **B285**, 291 (1992).

[37] Prepared for 1996 DPF / DPB Summer Study on New Directions for High-Energy Physics (Snowmass 96), Snowmass, Colorado, 25 Jun - 12 Jul 1996.

[38] Ellis, Stephen D. and Soper, Davison E., Phys. Rev. **D48**, 3160 (1993).

[39] Streng, K. H. and Walsh, T. F. and Zerwas, P. M., Zeit. Phys. **C2**, 237 (1979).

[40] Seymour, Michael H., Z. Phys. **C62**, 127 (1994).

[41] Munoz-Tapia, R. and Stirling, W. James, Phys. Rev. **D52**, 3894 (1995).

[42] HERMES Coll., *Technical Design Report*, 1993.

[43] HERA-B Coll., *Technical Design Report*. DESY-PRC 95/01.

[44] DESY, *Annual Report*, 1994.

[45] ZEUS Coll., *The ZEUS Detector*. Status Report (unpublished), DESY, 1993.

[46] R. Hall-Wilton et al., *The CTD Tracking Resolution* (unpublished). ZEUS-99-024, internal ZEUS-note, 1999.

[47] M. Derrick et al., Nucl. Inst. Meth. **A 309**, 77 (1991).

[48] A. Andresen et al., Nucl. Inst. Meth. **A 309**, 101 (1991).

[49] A. Bernstein et al., Nucl. Inst. Meth. **A 336**, 23 (1993).

[50] H. Bethe and W. Heitler, Proc. Roy. Soc. Lond. **A146**, 83 (1934).

[51] J. Andruskow et al.. DESY 92-066, 1992.

[52] K. Piotrkowski et al.. DESY F35D-93-06, 1993.

[53] C. Youngman, *The ZEUS Data Acquisition System*. DESY 92-150A.

[54] W.H. Smith et al., *The ZEUS Trigger System*. ZEUS-note 89-084.

[55] H. Uigterwall, *The Global Second Level Trigger for ZEUS*. Ph.D. Thesis, University of Amsterdam, 1992.

[56] S.M Fisher et al., *ADAMO: User's guide*. CERN, 1993.

[57] R. Brun et al., GEANT3, Technical Report CERN-DD/EE/84-1, CERN, 1987.

[58] L.A.T. Brauerdick et al.. DESY-95-236, 1995.

[59] Catani, S. and Seymour, M. H., Nucl. Phys. **B485**, 291 (1997).

[60] Nagy, Zoltan and Trocsanyi, Zoltan, Phys. Rev. Lett. **87**, 082001 (2001).

[61] L. Lönnblad, Comp. Phys. Comm. **71**, 15 (1992).

[62] G. Ingelman, A. Edin and J. Rathsman, Comp. Phys. Comm. **101**, 108 (1997).

[63] B. Andersson et al., Phys. Rep. **97**, 31 (1983).

[64] G. Marchesini et al., Comp. Phys. Comm. **67**, 465 (1992).

[65] Ellis, R. Keith and Ross, D. A. and Terrano, A. E., Nucl. Phys. **B178**, 421 (1981).

[66] Bethke, Siegfried, Prog. Part. Nucl. Phys. **58**, 351 (2007).

[67] Martin, A. D. and Roberts, R. G. and Stirling, W. J. and Thorne, R. S., Eur. Phys. J. **C28**, 455 (2003).

[68] Martin, A. D. and Roberts, R. G. and Stirling, W. J. and Thorne, R. S., Eur. Phys. J. **C35**, 325 (2004).

[69] Stump, Daniel and others, JHEP **10**, 046 (2003).

[70] R. Brun et al. GEANT 3.13, CERN DD/EE/84-1 (1987).

[71] A. Kwiatkowski, H. Spiesberger and H.-J. Möhring, Comp. Phys. Comm. **69**, 155 (1992). Also in *Proc. Workshop Physics at HERA*, 1991, DESY, Hamburg.

[72] K. Charchula, G.A. Schuler and H. Spiesberger, Comp. Phys. Comm. **81**, 381 (1994).

[73] T. Sjöstrand, Comp. Phys. Comm. **82**, 74 (1994).

[74] T. Sjöstrand et al., Comp. Phys. Comm. **135**, 238 (2001).

[75] T. Sjöstrand, Comp. Phys. Comm. **39**, 347 (1986).

[76] H. Abramowicz, A. Caldwell and R. Sinkus, Nucl. Inst. Meth. **A 365**, 508 (1995).

[77] S. Kluth. '$\alpha_s$ from LEP'. Talk given in EPS07 (Manchester, England), 2007.

# Acknowledgements

Bueno, es mucha la gente sin la cual este trabajo no hubiera sido posible. Había pensado hacer las menciones usando algún sistema arbitrario, como por ejemplo por orden alfabético. Al final lo haré según me vengan a la mente.

Primero mis directores de tesis: Claudia Glasman y Juan Terrón. Esta tesis ha sido posible sólo gracias a su infatigable apoyo y a su gran destreza profesional. Mi gratitud se extiende al resto del grupo de Altas Energías del Departamento de Física Teórica de la UAM: Fernando Barreiro, Luis Labarga, José del Peso y Mara Soares. Y también a toda la Colaboración ZEUS, que ha proporcionado el ámbito en el cual se ha desarrollado este trabajo.

Ahora los amigos y familiares. A Manolo, por esos gratos paseos por DESY que no olvidaré. A Juan Pedro porque sin él claramente hubiera muerto el primer año de la tesis en Madrid. A Gabriel, con quién aprendí a ir en bici por carreteras heladas. A Elias... vaya... madre mía. A Nidia y a Mer Paz, para que no me puedan decir que no las he mencionado. A Liduam, con quién ojalá comparta mi vejez. A mis padres, que me han dado el interés por la naturaleza y la perseverancia, sin los cuales este trabajo no hubiera sido posible. A mi hermano Fernando, quién me ha proporcionado las huidas necesarias en los momentos claves. A mi hermana María, cuyo amor hacia mí ha sido un pilar necesario todos estos años.

Sabía que esto se iba a poner cursi... Finalmente, doy gracias a todo el resto de los amigos que me han ayudado, de alguna manera u otra, y que he olvidado mencionar, sin duda por despiste.